

**Spectroscopic Analysis and Photostability Assessment of
Lanthanide-Doped Upconverting Nanoparticles Sensitized with
IR820 Derivatives**

Mannu Kaur Maken

A Thesis

In

The Department

of

Chemistry and Biochemistry

Presented in Partial Fulfillment of the Requirements
for the Degree of Doctorate of Philosophy (Chemistry) at

Concordia University

Montreal, Quebec, Canada

October 2023

©Mannu Kaur Maken, 2023

CONCORDIA UNIVERSITY
SCHOOL OF GRADUATE STUDIES

This is to certify that the thesis prepared

By: Mannu Kaur Maken
Entitled: Spectroscopic Analysis and Photostability Assessment of Lanthanide-doped Upconverting Nanoparticles Sensitized with IR820 derivatives and submitted in partial fulfillment of the requirements for the degree of

Doctor Of Philosophy (Chemistry)

complies with the regulations of the University and meets the accepted standards with respect to originality and quality.

Signed by the final examining committee:

_____ Chair
Dr. Peter Darlington

_____ External Examiner
Dr. Stephane Petoud

_____ External to Program
Dr. Yves Gelinis

_____ Examiner
Dr. Rafik Naccache

_____ Examiner
Dr. Christine DeWolf

_____ Thesis Supervisor
Dr. John A. Capobianco

Approved by

_____ Dr. Louis Cuccia, Graduate Program Director

October 23rd, 2023

_____ Dr. Pascale Sicotte, Dean (Faculty of Arts and Science)

ABSTRACT

Spectroscopic Analysis and Photostability Assessment of Lanthanide-doped Upconverting Nanoparticles Sensitized with IR820 derivatives

Mannu Kaur Maken, PhD

Concordia University, 2023

Lanthanide upconverting nanoparticles (LnUCNPs), known for their luminescence when irradiated with near-infrared (NIR) light, often face the challenge of limited absorption capabilities, particularly due to the low absorption cross-section of sensitizer ions like Yb^{3+} . Incorporating NIR dyes has shown promise in enhancing the upconversion luminescence of LnUCNPs by efficiently harnessing NIR light and channeling this energy to the sensitizer ions. The higher absorption cross-section of these NIR dyes, compared to Yb^{3+} , amplifies the LnUCNPs' absorption prowess. However, the inherent photostability of such organic dyes hinders their practical applications, especially when sustained NIR exposure is essential.

Addressing this challenge, this research work delved into improving the photostability of dye-sensitized LnUCNPs. The focus was on IR820 dye, when functionalized with thiophenol groups bearing para substituents of varied electron density, showcased enhanced stability. This enhanced stability was evident when IR820- NO_2 sensitized $\text{NaGdF}_4:\text{Er}^{3+}$, $\text{Yb}^{3+}/\text{NaGdF}_4:\text{Yb}^{3+}$ excited at 808 nm manifested brighter upconversion luminescence due to a better overlap with the Yb^{3+} ion absorption and doubling its photostability duration to 90 minutes. In the process, this research also unearthed certain inconsistencies in the prevalent literature pertaining to the 980 nm and 808 nm wavelengths and the energy back-transfer dynamics from Er^{3+} to the dye.

Progressing further, the IR820-COOH dye was functionalized with APTMS and was incorporated into a silica framework surrounding $\text{NaGdF}_4:\text{Er}^{3+}$, $\text{Yb}^{3+}/\text{NaGdF}_4:\text{Yb}^{3+}$. An in-depth analysis underscored the superior photostability and upconversion luminescence of this embedded system when pitted against covalent surface-linked and electrostatic variants. This optimized embedded system was also examined vis-à-vis Nd^{3+} doped nanoparticles, both being excited at 808 nm. Using the system's enhanced attributes, we adapted it into an 808 nm-responsive Fenton-type catalyst. This adaptation was achieved by coating the system with a wide-pored silica shell that incorporated

hematite nanoparticles. This culminated in an efficient degradation of the Rhodamine B pollutant, a significant environmental menace introduced by the textile sector.

To encapsulate, this thesis paves the way for bolstering the photostability and versatility of dye-sensitized LnUCNPs, employing intricate dye modifications and embedding strategies, heralding new possibilities for applications.

Recognize the entire Human Race as One

-Guru Gobind Singh

Acknowledgements

At the outset of this milestone, I stand with a heart brimming with gratitude, humbly offering my utmost thanks to the Almighty, who has been my guiding light and steadfast protector throughout this journey.

I would like to extend my deepest gratitude to my advisor, Professor Capobianco, whose guidance, support, and expertise have been invaluable throughout this journey. From the outset, boss you offered the ideal balance of freedom and guidance, granting me both the autonomy and the intellectual framework necessary to explore my research interests to their fullest extent. I am particularly grateful for the flexibility and understanding shown during times when external circumstances posed challenges to my research. This empathetic approach to supervision, combined with deep scholarly insight, created a rich and nourishing educational environment. Your mentorship has been a life-changing experience, and I cannot thank you enough for your unwavering belief in me. I feel profoundly privileged to have had you as my supervisor and look forward to carrying the lessons and skills I have gained under your mentorship into the next chapters of my academic and professional life.

A debt of gratitude is owed to my esteemed committee members, Dr. DeWolf and Dr. Naccache. Their insightful feedback, insights, and consistent mentorship have immeasurably enriched my academic odyssey. I would like to extend my most profound appreciation to Dr. DeWolf, from the earliest stages of my project to the final revisions, your keen insights and constructive feedback have been instrumental in shaping this work into its best possible form. Her constant encouragement, especially at times when I encountered obstacles and difficulties, has been both a comfort and a catalyst that propelled me forward. I would like to express my heartfelt gratitude to Dr. Naccache for his invaluable contributions to my research journey. His insightful suggestions and thought-provoking questions have consistently elevated the quality of my work and encouraged me to delve deeper into complex issues. I am particularly indebted to your foundational work in this field. Your pioneering research forms the bedrock upon which our collective projects are built. Your contributions provide a solid and robust framework that has significantly facilitated my own understanding and exploration of the subject matter.

Navigating the intricate tapestry of research has been made so much more rewarding thanks to my dedicated labmates. I cannot let this opportunity pass without extending my warmest gratitude to

Dr. Gabrielle A. Mandl, who has been so much more than a colleague throughout this journey. Gabi, you have been my family at work, providing an atmosphere of camaraderie and comfort that has been invaluable. From the moment I arrived here, you became my first friend, effortlessly making me feel welcomed and included. You have generously lent an empathetic ear to my challenges, both in the research context and in life at large. Your advice, invariably couched in kindness and profound wisdom, has guided me through many an obstacle. You have this extraordinary ability to balance professionalism with genuine care, making you not just an exemplary researcher but an exceptional human being. To say that you are the best colleague anyone could ask for would be an understatement. I cherish our friendship and look forward to many more years of collaboration and mutual support. I'm thankful to Steven L. Maurizio for the countless hours of stimulating discussions and brainstorming sessions and for fostering a nurturing academic ambiance. A heartfelt acknowledgment to Dr. Pedro Alejandro Mena Giraldo, whose constant encouragement has been pivotal in reinforcing my self-belief. His knack for identifying interesting research questions and developing fun projects has added a layer of enjoyment to my scholarly endeavors that I had never thought possible. You have a unique ability to transform complicated challenges into rewarding experiences, and your optimistic outlook has a contagious quality that inspires everyone around you.

On the personal front, I reserve my deepest and most heartfelt thanks for my parents, who are not just the bedrock of my life but my ceaseless source of inspiration. Words fall short to express how immensely grateful I am for the unconditional love, constant support, and endless patience you've showered upon me. Mom and Dad, you've always been the embodiment of love and sacrifice. The decision to uproot your comfortable lives in India for us was not a small one, and yet you made it look so effortless. You've instilled in me a sense of purpose, a strong work ethic, and, most importantly, the courage to face challenges head-on. Every step I take is guided by the values you've instilled in me, and every achievement is a testament to the lessons I've learned at your knees. I realize that everyone believes their parents are the best, but you transcend that belief—you truly are the best. Whether it's your unwavering faith in my abilities or your comforting presence during times of doubt, your support has been my greatest blessing. Your love is the invisible hand that guides me, and your sacrifices are the steppingstones upon which I tread. The journey toward earning this Ph.D. has been arduous, but the load was made lighter knowing you both were there cheering me on, just as you've done all my life. I look forward to a future where I

can make you as proud of me as I am endlessly grateful for you. Thank you, Mom and Dad, for being the amazing parents you are. You are my heroes, my mentors, and my greatest supporters. I love you more than words can express, and I dedicate this achievement to you as a small token of my immense appreciation and love.

My sister, Poonam Kaur, has been the balm to my academic rigors—her innate silliness and unwavering support have been my emotional anchor, reminding me to find joy in the little moments. To Jaysvi and Teghveer, my radiant niece and nephew: your innocent cheerfulness has been a beacon during some of my most challenging days. Massi cherishes every moment with you both and loves you immeasurably. Special appreciation must go to my brother-in-law, who has been the closest thing I've had to a brother. In the intense and often overwhelming whirlpool that is Ph.D. research, finding solace and moments of relaxation can be a luxury. Yet, you've made it possible for me to escape, unwind, and recharge, even when finances were tight. Your generosity knows no bounds—you've not only shared with me the best vacation spots but have also given me a taste of the finer things in life. Thank you for being not just a great brother-in-law but a friend. Your contributions to my life are immeasurable, and I am grateful for every single one.

A special acknowledgment to my confidant and partner in crime, Mohit Sharma. His undying faith in my abilities, even when I doubted myself, has been nothing short of a blessing. His daily reminders to persevere and his indomitable spirit have been instrumental in my journey. Mohit, this achievement is as much yours as it is mine. To Sweta, whose candid conversations and unwavering support have been therapeutic: Thank you for being the ear I needed, reminding me to find joy in the journey, amidst its inevitable highs and lows.

In this profound journey, every word of encouragement, every gesture of support, and every shared dream has left an indelible mark on my heart. Thank you, each and every one of you, for making this dream a shared reality.

Table of Contents

Contribution of Authors	xiii
List of Figures	xv
List of Tables.....	xxv
List of Abbreviations.....	xxvi
List of Equations	xxviii
Chapter 1: Introduction	1
1.1 Luminescence.....	1
1.1.1 Stokes Shift and anti-Stokes shift	1
1.1.2 Photoluminescent nanomaterials	3
1.1.3 Mechanisms of Anti-Stokes Luminescence	4
1.2 Lanthanide Theory	6
1.3 Lanthanide Doped Upconverting Nanoparticles	9
1.3.1 Components of Lanthanide-doped Upconverting Nanoparticles.....	9
1.3.2 Energy Transfer mechanism in Yb ³⁺ -Er ³⁺ pair.....	14
1.4 Strategies for Enhancement of Upconversion Efficiency	16
1.4.1 Core/Shell Architecture.....	16
1.5 Dye Sensitization.....	18
1.5.1 Energy Transfer process.....	19
1.5.2 Cyanine Dyes	23
1.5.3 Method of Dye linking.....	25
1.5.4 Disadvantages of Dye-sensitization.....	28
1.6 State of the Field	30
1.7 Photocatalysis.....	34
1.8 Statement of Problem.....	37
1.9 Project Objectives	38
Chapter 2: On the photostability and luminescence of dye-sensitized upconverting nanoparticles using modified IR820 dyes	40
2.1 Introduction	41
2.2 Experimental Section	44

2.2.1	Material	44
2.2.2	Instrumentation and Method	44
2.2.3	Synthesis of Material	47
2.3	Results and Discussion.....	48
2.3.1	Effects of structural modifications on the photostability of IR820 dye.....	48
2.3.2	Spectroscopic Characterization of dye-LnUCNP nanosystems.....	51
2.4	Conclusion.....	59
2.5	Supporting Information.....	61
2.5.1	Quantification of dye molecules per nanoparticle	61
2.5.2	Photodegradation of IR820 in presence of different assays and in different solvents.	61
2.5.3	Analysis of photodegradation products of IR820 by ESI-MS	63
2.5.4	¹ H-NMR and MALDI-TOF-MS of IR820 derivatives	64
2.5.5	UV-Visible Absorption spectra of IR820 derivatives and corresponding maxima .	66
2.5.6	Analysis of photodegradation of IR820 derivatives by UV-Visible absorption spectroscopy	67
2.5.7	Physical Characterization of core/shell NaGdF ₄ :Yb ³⁺ ,Er ³⁺ /NaGdF ₄ :Yb ³⁺ nanoparticles.....	68
2.5.8	FT-IR spectra for characterization of nanoparticle surface.....	68
2.5.9	Transmission Electron Microscopy images of oleate free nanoparticles.....	69
2.5.10	Calibration curves for quantification of number of dye molecules per nanoparticle	69
2.5.11	Emission Spectra of IR820 and IR820-NO ₂ functionalized LnUCNPs at different dye concentrations	70
2.5.12	Stability study on the electrostatic interaction of IR820-NO ₂ dye with LnUCNP surface	70
2.5.13	Kinetics of IR820-NO ₂ degradation with NaGdF ₄ :Er ³⁺ /Yb ³⁺ and NaYF ₄ :Er ³⁺ /Yb ³⁺	71
2.5.14	Upconversion emission spectra comparisons upon different excitation wavelengths	71
2.5.15	Calibration curves for absorption coefficients at 655 nm.....	72
2.5.16	Quantum Yield measurements	72

Chapter 3: Achieving photostability in dye-sensitized upconverting nanoparticles and their use in Fenton type photocatalysis.....	73
3.1 Introduction	74
3.2 Experimental	75
3.2.1 Material.....	75
3.2.2 Synthesis of NaGdF ₄ :Er ³⁺ (2%), Yb ³⁺ (20%)/NaGdF ₄ : Yb ³⁺ (20%) active core/active shell LnUCNPs	76
3.2.3 Synthesis of NaGdF ₄ :Er ³⁺ , Yb ³⁺ /NaGdF ₄ : Yb ³⁺ / NaGdF ₄ : (10-20%) Nd ³⁺	77
3.2.4 Synthesis of IR820-COOH	77
3.2.5 Synthesis of IR820-APTMS	77
3.2.6 Synthesis of the Surface Silica Linked (SL system).....	77
3.2.7 Synthesis of the Silica Embedded (SE system)	78
3.2.8 Transmission Electron Microscopy (TEM)	78
3.2.9 Energy dispersive X-ray spectroscopy (EDX).....	78
3.2.10 Powder X-ray Diffraction (PXRD).....	78
3.2.11 Upconversion Emission Spectroscopy.....	79
3.2.12 Upconversion Lifetimes.....	79
3.2.13 Upconversion Quantum Yield.....	79
3.2.14 Synthesis of Wide-pored silica shell.....	80
3.2.15 Synthesis and incorporation of α-Fe ₂ O ₃ (hematite) nanoparticles.....	80
3.2.16 Diffuse Reflectance spectroscopy.....	80
3.2.17 Electron Paramagnetic Resonance.....	80
3.2.18 Evaluation of the photocatalytic activity of SE-WP-Fe system.....	81
3.3 Results and Discussion.....	82
3.4 Conclusion.....	93
3.5 Supplementary Information.....	94
3.5.1 Physical and Spectroscopic Characterization of core and core/shell NaGdF ₄ :Yb ³⁺ ,Er ³⁺ /NaGdF ₄ :Yb ³⁺ nanoparticles	94
3.5.2 Characterization of IR820-COOH and IR820-APTMS dye.....	95
3.5.3 Surface Silica linking system.....	98
3.5.4 Surface Embedded System	99

3.5.5	Comparative Analysis of the Spectroscopic Properties and Stability between the SL, SE and Electrostatic system	101
3.5.6	Physical and Spectroscopic Characterization of NaGdF ₄ : Er ³⁺ , Yb ³⁺ /NaGdF ₄ : Yb ³⁺ /NaGdF ₄ : (10-20%) Nd ³⁺	103
3.5.7	Comparative Analysis of Spectroscopic properties of the SE and the optimized Nd ³⁺ system	105
3.5.8	Evaluation and Quantification of Hematite Nanoparticles in the SE-WP System: A Physical and EPR Analysis.....	106
Chapter 4: Conclusion.....		110
Chapter 5: Future Work.....		113
5.1	Short-term fundamental studies	113
5.1.1	Environmental Adaptability	113
5.1.2	Investigating properties under various excitations	114
5.1.3	Exploration of Other Lanthanide Dopants	115
5.2	Long-term Goals in Material Development	116
5.2.1	Scalability and Commercial Viability.....	116
5.2.2	Dye Modification and Multi-dye Integration for Enhanced Photostability and Optical Performance	116
Appendix.....		118
References.....		136

Contribution of Authors

Manuscript 1 (Chapter 2): “On the photostability and luminescence of dye-sensitized upconverting nanoparticles using modified IR820 dyes”¹ (**Published**)

Mannu Kaur: experimental work and manuscript preparation.

Gabrielle A. Mandl: aided in experimental work and manuscript preparation.

Steven L. Maurizio: aided in experimental work.

Gabriella Tessitore: aided in experimental work.

John A. Capobianco: Project Supervisor

Manuscript 2 (Chapter 3): “Achieving photostability in dye-sensitized upconverting nanoparticles and their use in Fenton type photocatalysis”² (**Published with Cover**)

Mannu Kaur: experimental work and manuscript preparation.

Steven L. Maurizio: aided in experimental work and manuscript preparation.

Gabrielle A. Mandl: aided in manuscript preparation.

John A. Capobianco: Project Supervisor

Manuscripts (not included in the thesis)

Manuscript 3: “Near-infrared remote-driven Janus micromotors for transporting cargo and multipurpose upconverting nanoparticles” (**In Review**)

Pedro Alejandro Mena Giraldo: experimental work and manuscript preparation

Mannu Kaur: assisted in experimental work.

Steven L. Maurizio: aided in experimental work and manuscript preparation.

Gabrielle A. Mandl: aided in manuscript preparation.

John A. Capobianco: Project Supervisor

Manuscript 4: “The role of lanthanide luminescence in advancing technology”³ **(Published)**

Gabrielle A. Mandl and Gabriella Tessitore: conceptualized the theme and focus of the review.

Steven L. Maurizio: responsible for sections of Anti-Counterfeiting and assisted in sections for Telecommunication and solar energy conversion.

Mannu Kaur: responsible for sections of telecommunication and solar energy conversion.

John A. Capobianco: Project Supervisor

List of Figures

- Figure 1.1:** Simplified schematic and graphical representation of luminescence processes. (a) Stokes process: Diagram illustrates the absorption of excitation photon (λ_{ex}) and subsequent emission at an increased wavelength (λ_{em}). The accompanying graph showcases the Stokes shift between the absorption and emission wavelengths. (b) Anti-Stokes process: Diagram depicts the absorption λ_{ex} and emission at a decreased wavelength (λ_{em}), made possible through additional energy input. The schematic displays the anti-Stokes shift between the two wavelengths.....2
- Figure 1.2:** Illustrates photoluminescence mechanism in- (a) organic molecules: Jablonski diagram illustrating the energy absorption and release pathways in the molecule; (b) semiconductor and quantum dots: energy level distribution in semiconductors versus semiconductor quantum dots of radius R. When R is less than the Bohr radius, distinct energy levels appear within the band gap; (c) metal ion-based materials: Schematic representation of upconversion through metastable states of an ion that converts low-energy photons to high energy photons.....4
- Figure 1.3:** Schematic representation of the mechanisms a) Single ion X (activator) based excited-state absorption (ESA); b) Sensitizer and activator pair-based energy transfer upconversion (ETU).....6
- Figure 1.4:** Dieke diagram for 4fⁿ energy levels of lanthanide ions in LaCl₃. Diagram obtained from reference 37.....8
- Figure 1.5:** Depiction of a simplified cross-relaxation mechanism among the activator ions doped in a host matrix. Yellow dots represent spectroscopically silent host atoms, blue dots represent dopant ions.....10
- Figure 1.6:** Diagram depicting the energy levels and corresponding energy transfer between Nd³⁺→Yb³⁺ ions under 808 nm excitation.....12
- Figure 1.7:** Schematic representation of the energy transfer process in Yb³⁺-Er³⁺ doped LnUCNPs. On the left, the two-photon upconversion processes produce red and green emissions, while the right showcases the three-photon upconversion process leading to a violet emission.....15

Figure 1.8: Diagram depicting radiative and non-radiative energy transfer pathways from dye to lanthanide. Radiative transfers are characterized by the reabsorption of fluorescent or phosphorescent emissions, while non-radiative transfers originate from the S₁/T₁ excited state of the dye.....19

Figure 1.9: Diagram showcasing the Förster energy transfer method, where electrostatic interactions facilitate the non-radiative transition of excitation energy from the dye to the lanthanide ion.....20

Figure 1.10: Illustration of absorption and fluorescence spectra of a donor (dye)-acceptor (lanthanide) duo. The overlapped area indicates the spectral overlap (*J*) between the dye’s fluorescence and the lanthanide absorption.....21

Figure 1.11: Diagram depicting the Dexter energy transfer, a mutual electron exchange occurs between the dye and lanthanide ion, resulting in a) singlet-singlet and b) triplet–triplet transfer that conserves spin.....22

Figure 1.12: Basic skeleton of a polymethine cyanine dye, x is the number of monomethine unit.....23

Figure 1.13: Commonly used heptamethine cyanine dyes used for dye-sensitization, with tabulated data on their optical properties, anionic groups and potential reactive sites.....24

Figure 1.14: Schematic of different methods of dye linking on the surface on LnUCNP (a) Electrostatic method of direct coordination and encapsulation in (b1) polymer (b2) porous silica shell. Covalent linking by means of (c1) a functionalized silica shell and (c2) polymer coating. Created with BioRender.....28

Figure 1.15: Reaction scheme of indocyanine green with possible cleavage sites undergoing photodegradation at 840 nm. The formation of carbonyl compounds was confirmed by HRMS. Figure modified with permission from reference 123.....29

Figure 1.16: αFe₂O₃ (hematite) nanoparticle upon excitation at 565 and 620 nm, leading to the generation of electrons and holes in conduction (C.B.) and valence (V.B.) respectively, which

subsequently produce superoxide and hydroxide radicals. Created with BioRender.....35

Figure 2.1: (a) Chemical structure of IR820 modified with a thiophenol group and corresponding studied groups placed at the para position. (b) Percentage photodegradation of the IR820 derivatives as a function of irradiation time (808 nm irradiation, 4.5 W/cm²). Errors are established based on three repetitions. (c) Absorption (gray) and emission (blue) of IR820 dye (λ_{max} abs 820 nm, λ_{max} em 849 nm). (d) Absorption (gray) and emission (green) of IR820–NO₂ dye in methanol (λ_{max} abs 837 nm, λ_{max} em 924 nm).....50

Figure 2.2: (a) Integrated emission intensities of the ⁴S_{3/2}→⁴I_{15/2} transition of colloidal dispersions of IR820–NO₂-LnUCNPs (green) and IR820-LnUCNPs (blue) as a function of the number of dye molecules per nanoparticle. (b) Upconversion emission spectra of IR820–NO₂-LnUCNPs and IR820-LnUCNPs (blue) with the optimum number of dye molecules per nanoparticle.....53

Figure 2.3: (a) Schematic of the interactions between the dye, sensitizer, and activator ions upon 808 and 976 nm excitation. (b) Upconversion emission spectra of IR820–NO₂-LnUCNPs and IR820 LnUCNPs upon 976 nm excitation. (c) Upconversion lifetimes of the green (top) and red (bottom) emissions of Er³⁺ in unfunctionalized (black), IR820-functionalized (blue) and IR820–NO₂-functionalized LnUCNPs upon 976 nm excitation.....56

Figure 2.4: (a) Photographs of colloidal dispersions of IR820 LnUCNPs (top) and IR820–NO₂ LnUCNPs (bottom) at 0 and 30 minutes of irradiation with 808 nm excitation. (b) Overall emission intensities of IR820–NO₂-LnUCNPs (green) and IR820-LnUCNPs (blue) as a function of irradiation time upon 808 nm excitation (2.1 W/cm²). Light green and light blue regions around the curves represent the error margins. Errors are based on a minimum of two repetitions.....57

Figure S2.1: a) Percent degradation of IR820 (16μM in DMF) dye versus time in ambient conditions (gray), in the presence of sodium azide (light gray) and under Ar atmosphere (pink). b) Percent degradation of IR820 dye versus time in DMF (gray), ethanol (dark pink), and methanol (light pink). Errors based on a minimum of three repetitions.....61

Figure S2.2: Decrease in absorbance of IR820 with irradiation time in a) DMF b) Ethanol c) Methanol.....	62
Figure S2.3: Absorbance of IR820 in a) air b) Ar atmosphere c) with 50 mM sodium azide added in solution.....	62
Figure S2.4: ESI-MS analysis of non-irradiated IR820 ESI-MS analysis and degradation mechanism of irradiated IR820 (at 808 nm 4.2 W/cm ²).....	63
Figure S2.5: MALDI-TOF analysis of IR820-CH ₃ (MW 915.32), IR820-COOH (MW 945.44), IR820-CF ₃ (MW 969.32) and IR820-NO ₂ (MW 946.4).....	65
Figure S2.6: Absorbance of IR820 and IR820 functionalized with thiophenol with different para substituents: IR820 (black), IR820-NO ₂ (pink), IR820-CF ₃ (light pink), IR820-COOH (light gray), IR820-CH ₃ (gray).....	66
Figure S2.7: Decrease of absorbance of a) IR820-CH ₃ b) IR820-COOH c) IR820-CF ₃ and d) IR820-NO ₂ with irradiation time.....	67
Figure S2.8: a) PXRD pattern of NaGdF ₄ :Er ³⁺ (2%),Yb ³⁺ (20%)/NaGdF ₄ :Yb ³⁺ (20%) (core/shell) and NaGdF ₄ :Er ³⁺ (2%),Yb ³⁺ (20%) (core) nanoparticles. TEM image of b) NaGdF ₄ : Yb ³⁺ ,Er ³⁺ (cores), with inset of size distribution c) NaGdF ₄ :Yb ³⁺ ,Er ³⁺ /NaGdF ₄ :Yb ³⁺ (core/shell) nanoparticles with inset of size distribution.....	68
Figure S2.9: FT-IR of a) oleate capped and oleate free nanoparticles. b) Dye and nanoparticles conjugated with the respective dye.....	68
Figure S2.10: TEM images of a) oleate free LnUCNPs b) IR820-NO ₂ -LnUCNPs, 1 mg/ml dispersion in methanol.....	69
Figure S2.11: Calibration curve of a) IR820 and b) IR820-NO ₂ having 198181 M ⁻¹ cm ⁻¹ and 187143 M ⁻¹ cm ⁻¹ molar extinction coefficients in methanol, respectively.....	69
Figure S2.12: Emission spectra of IR820-NO ₂ (pink) and IR820 (gray) functionalized LnUCNPs (in Methanol) having different dye concentrations and 10mg/ml LnUCNPs excited at 808 nm (2.1 W/cm ²).....	70

Figure S2.13: a) UV-visible absorption spectrum of supernatant collected after 24, 48 and 72 h from a dispersion of IR820-NO₂-LnUCNPs (10 mg/mL) in Methanol. b) Absorption of supernatant of a dispersion of IR820-LnUCNPs at 820 nm and IR820-NO₂-LnUCNPs at 837 nm as a function of time. No leakage of dye from the nanoparticle surface was observed.....70

Figure S2.14: Normalized green emission intensity of LnUCNPs versus irradiation time for IR820-NO₂- NaGdF₄:Er³⁺,Yb³⁺ (gray) and IR820-NO₂- NaGdF₄:Er³⁺,Yb³⁺ (pink) under 808 nm excitation (at 4.2W/cm²).....71

Figure S2.15: a) Upconversion emission spectra of colloidal dispersions of unfunctionalized LnUCNPs (gray), IR820 LnUCNPs (blue) and IR820-NO₂-LnUCNPs (green) upon 808 nm excitation (2.1 W/cm²). b) Upconversion emission spectra of colloidal dispersions of unfunctionalized LnUCNPs (gray) and IR820-NO₂-LnUCNPs (green) upon 980 nm excitation and 808 nm excitation, respectively (both at power densities of 4.2 W/cm²).....71

Figure S2.16: a) Calibration curve for IR820 at 655 nm in methanol b) Calibration curve for IR820-NO₂ at 655 nm in methanol.....72

Figure S2.17: Quantum yields of IR820-NO₂-LnUCNPs (green) and IR820-LnUCNPs (blue) as a function of irradiation time upon 808 nm excitation. Errors for both measurements established based on a minimum of two repetitions.....72

Scheme 3.1: Scheme of the two types of nanoparticle systems investigated in this work, where IR820 is functionalized at the central aryl ring to generate IR820-COOH to generate (a) NaGdF₄:Er³⁺,Yb³⁺/NaGdF₄:Yb³⁺ coated with silica and IR820-COOH linked to the surface *via* the EDC/NHS amide coupling reaction (SL) and (b) the NaGdF₄:Er³⁺,Yb³⁺/NaGdF₄:Yb³⁺ coated with silica and IR820-APTMS embedded into the silica shell (SE). Created with BioRender.....83

Figure 3.1: TEM micrographs of (a) LnUCNPs coated with amine-functionalized-SiO₂ for the SL system (b) LnUCNPs coated with IR820-APTMS embedded in the silica matrix in the SE system.....84

Figure 3.2: Upconversion emission spectra of the (a) SL system with the different number of dye molecules per LnUCNP. b) SE system with different numbers of dye molecules embedded into the silica shell per LnUCNP.....85

Figure 3.3: a) Normalized upconversion emission spectra of the SL and the SE systems under 800 nm excitation. b) Emission intensity of the $^4S_{3/2}, ^2H_{11/2} \rightarrow ^4I_{15/2}$ transition of Er^{3+} in the SL (blue) and SE (green) systems as a function of time under 808 nm excitation.....86

Figure 3.4: Upconversion lifetimes of the $^2H_{11/2} \rightarrow ^4I_{15/2}$ transition of Er^{3+} in (a) the SE system (filled circles) and $NaGdF_4:Yb^{3+}, Er^{3+}/NaGdF_4:Yb^{3+}$ LnUCNPs coated with unfunctionalized silica (outlined circles) under 976 nm excitation. (b) $NaGdF_4:Yb^{3+}, Er^{3+}/NaGdF_4:Yb^{3+}/NaGdF_4:15\% Nd^{3+}$ LnUCNPs (filled circles) and $NaGdF_4:Yb^{3+}, Er^{3+}/NaGdF_4:Yb^{3+}/NaGdF_4$ LnUCNPs (outlined circles) under 976 nm excitation. (c) the SE system (blue) and $NaGdF_4:Yb^{3+}, Er^{3+}/NaGdF_4:Yb^{3+}/NaGdF_4:15\% Nd^{3+}$ LnUCNPs (red) under 808 nm excitation.....88

Figure 3.5: (a) Diffuse reflectance spectra for synthesized hematite nanoparticles and (b) the corresponding Tauc plot to determine the band gap energy. TEM micrographs for the wide-pored silica shell synthesized on the SE nanoparticles (c) before and (d) after the incorporation of hematite nanoparticles. (e) Powder XRD diffractogram and (f) HAADF and EDS mapping of the completed SE-WP-Fe system. (g) Upconversion emission spectra of the completed SE-WP-Fe system with varying concentrations of hematite nanoparticles. (h) Rhodamine B degradation measured from the relative absorbance spectra. (i) Repeated cycles of Rhodamine B photodegradation after 100 min, recycling the SE-WP-Fe system. (j) Photographs of the Rhodamine B solutions, illustrating the degradation of the dye after 100 min. All scale bars are 100 nm.....92

Figure S3.1: TEM micrographs of a) $NaGdF_4:Er^{3+}, Yb^{3+}$ (core nanoparticles) b) $NaGdF_4:Er^{3+}, Yb^{3+}/NaGdF_4:Yb^{3+}$ (active core/active shell nanoparticles) with insets of their respective size distribution. c) Experimental PXRD patterns of $NaGdF_4:Er^{3+}, Yb^{3+}$ (green) $NaGdF_4:Er^{3+}, Yb^{3+}/NaGdF_4:Yb^{3+}$ (red) with a simulated line pattern for hexagonal phase $NaGdF_4$ (bottom plot) is shown for reference (black). d) Upconversion emission spectra of the 2 mg/ml $NaGdF_4:Er^{3+}, Yb^{3+}$ (green) and $NaGdF_4:Er^{3+}, Yb^{3+}/NaGdF_4:Yb^{3+}$ (red) at 976 nm excitation.....94

Figure S3.2: (a) Absorbance and (b) emission spectra of the synthesized IR820-COOH and IR820-APTMS, their comparison with IR820 dye (0.1 mg/ml in methanol).....	95
Figure S3.3: ¹ H NMR spectra of IR820-COOH (top) and IR820-APTMS (bottom) in DMSO-d ₆	96
Figure S3.4: MALDI-TOF analysis of IR820- APTMS (MW=1106.41, top) and IR820-COOH (MW=946.44, bottom).....	97
Figure S3.5: FTIR of amine functionalized SiO ₂ coated active-core/active-shell NPs (black) and IR820-COOH linked with amide coupling on the surface of the silica coated active-core/active-shell NPs (red).....	98
Figure S3.6: (a) UV-Vis absorption spectra for IR820-COOH dye molecules linked in SL system (b) UV-vis calibration curve to quantify the number of dye molecule.....	99
Figure S3.7: (a) UV-Vis absorption spectra for IR820-APTMS dye molecules embedded in SE system (b) UV-vis calibration curve to quantify the number of dye molecules.....	99
Figure S3.8: TEM micrograph of SE systems having varied amounts of dye embedded in the silica matrix with a thickness of a) 4 nmol dye, 4.2±1.2 nm b) 12 nmol dye, 4.0±0.7 nm c) 16 nmol dye, 4.5±1.5 nm d) 25 nmol dye, 5.2±1.0 nm.....	100
Figure S3.9: Photographs of 5 mg/mL solution in methanol of the (left) SL system and (right) SE system, under 808 nm irradiation.....	101
Figure S3.10: Absorbance as a function of incubation time for SE (black), SL (red), and electrostatic (blue) system to monitor leaking of dye from the nanoparticle surface. All samples are 5 mg/mL nanoparticles in methanol.....	101
Figure S3.11: a) Comparison of upconversion luminescence spectra of SL (green) SE (blue) and the electrostatic system (grey) with the dye coordinated to the oleate-free nanoparticle surface upon 808 nm excitation b) Overall emission intensities of SL (green), SE (blue) and electrostatic system (grey) as a function of irradiation time upon 808 nm excitation.....	102

Figure S3.12: TEM micrographs of core, core/shell and core/shell/shell respectively for (a) NaGdF₄:Er³⁺, Yb³⁺/NaGdF₄:Yb³⁺/ NaGdF₄:10%Nd³⁺ (black), NaGdF₄:Er³⁺, Yb³⁺/NaGdF₄:Yb³⁺/ NaGdF₄:15%Nd³⁺ (red), NaGdF₄:Er³⁺, Yb³⁺/NaGdF₄:Yb³⁺/NaGdF₄:20%Nd³⁺ (green).....103

Figure S3.13: PXRD patterns of (a) NaGdF₄:Er³⁺, Yb³⁺ (cores), (b) NaGdF₄:Er³⁺, Yb³⁺/ NaGdF₄: Yb³⁺ (core/shell), (c) NaGdF₄:Er³⁺, Yb³⁺/ NaGdF₄: Yb³⁺/ NaGdF₄: x%Nd³⁺ (core/shell/shell), for 10% (black), 15% (red), 20% (green) Nd³⁺-doped batches.....104

Figure S3.14: Upconversion luminescence spectra under 976 nm excitation of the (a) core and (b) core/shell nanoparticles isolated during the synthesis of (c) core/shell/shell LnUCNPs having 10 (red traces), 15 (blue traces) or 20 (green traces) mol% Nd³⁺ in the outer shell or the core and core/shell samples taken during the synthesis of the SE system (black). An aliquot of the cores and core/shells during the synthesis of the final product was taken and purified to obtain these spectra at 2 mg/mL nanoparticles dispersed in hexanes.....104

Figure S3.15: Normalized upconversion luminescence spectra under 808 nm excitation for a) (core/shell/shell) NaGdF₄:Er³⁺, Yb³⁺/NaGdF₄:Yb³⁺/NaGdF₄: x%Nd³⁺ x = 10, 15 or 20 mol% Nd³⁺ concentrations (hexanes, 2 mg/mL dispersions) b) Upconversion luminescence spectra of oleate-free NaGdF₄:Er³⁺, Yb³⁺/NaGdF₄:Yb³⁺/NaGdF₄: 15% Nd³⁺ and the SE system (2 mg/mL dispersions in methanol).....105

Figure S3.16: Upconversion lifetimes of the ⁴F_{9/2}→⁴I_{15/2} transition of Er³⁺ in (a) the SE system (C/S/SiO₂-Dye, filled) and NaGdF₄:Yb³⁺, Er³⁺/NaGdF₄:Yb³⁺LnUCNPs coated with unfunctionalized silica (C/S/SiO₂, outlined) under 808 nm excitation. (b) NaGdF₄:Yb³⁺, Er³⁺/NaGdF₄:Yb³⁺/NaGdF₄:15% Nd³⁺ LnUCNPs (C/S/NaGdF₄:Nd³⁺, filled circles) and NaGdF₄:Yb³⁺, Er³⁺/NaGdF₄:Yb³⁺/NaGdF₄ LnUCNPs (C/S/NaGdF₄, outlined circles) under 976 nm excitation.....105

Figure S3.17: (a) TEM micrograph with the corresponding inset of the size distribution (15.5 ± 5.7 nm), (b) Experimental PXRD (red) and JCPDS 84-0307 reference pattern (black) of α-Fe₂O₃ nanoparticles.....106

Figure S3.18: (a) Calibration curve generated from absorption spectra of dispersions of α-Fe₂O₃ nanoparticles in ethanol. (b) Absorbance spectrum both used for quantification of the α-Fe₂O₃ nanoparticles inserted into the pores of the SE-WP nanoparticles.....106

Figure S3.19: Electron paramagnetic resonance spectra of the SE-WP-Fe, SE, α -Fe ₂ O ₃ with and without H ₂ O ₂ (red and blue, respectively) with DMPO spin trapping agent with and without 800 nm excitation. All spectra were recorded using 2 mg/mL nanoparticles in methanol.....	107
Figure S3.20: Emission intensity of the $^2H_{11/2} \rightarrow ^4I_{15/2}$ transition of Er ³⁺ in the SE-WP-Fe:0.50 system (2 mg/mL dispersion in methanol) as a function of irradiation time (808 nm excitation) in the presence and absence of H ₂ O ₂	109
Figure A1.1: Schematic illustration of anti-Stokes luminescence by (a) Two-photon absorption and (b) Hot band absorption mechanism.....	119
Figure A2.1: Schematic illustration of triplet-triplet annihilation.....	120
Figure A2.2: Upconversion process by Cooperative Sensitization.....	121
Figure A2.3: Upconversion process by Photon-Avalanche mechanism.....	123
Figure A2.4: Upconversion process by Energy migration mechanism.....	124
Figure A3.1: Quenching mechanism of LnUCNPs in the presence of surface ligands and defects.....	125
Figure A4.1: Diagram depicting the potential mechanism behind the plasmonic amplification of upconversion luminescence.....	128
Figure A5.1: (a) TEM image of NaGdF ₄ undoped nanoparticles of size 36.7±3.5 nm (b)PXRD pattern confirming the hexagonal crystal phase.....	130
Figure A5.2: (a) TEM image of NaYF ₄ undoped nanoparticles of size 26.2±2.5 nm (b)PXRD pattern confirming the hexagonal crystal phase.....	130
Figure A5.3: TEM image of (a) NaGdF ₄ :Er ³⁺ , Yb ³⁺ core nanoparticles of size 18.6±2.5 nm (green) (b) NaGdF ₄ :Er ³⁺ , Yb ³⁺ / NaGdF ₄ :Yb ³⁺ core/shell nanoparticles of size 30.6±3.3 nm (red) (c) NaGdF ₄ :Er ³⁺ , Yb ³⁺ / NaGdF ₄ :Yb ³⁺ /SiO ₂ nanoparticles of size 30.6±3.3 nm with silica shell thickness of 3.5±1.2 nm (d)PXRD pattern confirming the hexagonal crystal phase of core (green) and core/shell (red) corresponding to JCPDS 27-0699.....	131
Figure A5.4: TEM image of (a) NaGdF ₄ :Er ³⁺ , Yb ³⁺ core nanoparticles of size 19.2±1.7 nm (green) (b) NaGdF ₄ :Er ³⁺ , Yb ³⁺ / NaGdF ₄ :Yb ³⁺ core/shell nanoparticles of size 29.8±2.0 nm (red) (c)	

NaGdF₄:Er³⁺, Yb³⁺/ NaGdF₄:Yb³⁺/NaGdF₄ nanoparticles of size 37.6±3.3 nm (blue) (d)PXRD pattern confirming the hexagonal crystal phase of core (green), core/shell (red) and core/shell/shell (blue) corresponding to JCPDS 27-0699.....132

Figure A5.5: (a) TEM image of NaGdF₄ undoped nanoparticles of size 39.5±3.2 nm (b)PXRD pattern confirming the hexagonal crystal phase.....133

Figure A5.6: TEM images of α-Fe₂O₃ nanoparticles synthesized by different trials.....134

Figure A5.7: TEM images of (a) LnUCNP-WP with a large pore size of ~20-25 nm loaded with 30 nm α-Fe₂O₃ (b) LnUCNP coated with mesoporous silica loaded with 15 nm α-Fe₂O₃ nanoparticles.....135

List of Tables

Table S2.1: Quantification of the number of dye molecules linked per nanoparticle.....	61
Table S2.2: Mass-to-charge ratio and molecular weight of peaks determined by ESI-MS analysis.....	63
Table S2.3: Absorbance and fluorescence (λ_{ex} 808 nm) of IR820 and functionalized dyes in methanol.....	66
Table S3.1: Absorbance maximum, emission maximum, and molar extinction coefficients for IR820, IR820-COOH, and IR820-APTMS dyes in methanol.....	95
Table S3.2: Moles of IR820-COOH dye, EDC, and NHS were added to link different numbers of dye molecules in the SL system.....	98
Table S3.3: Moles of IR820-CONH-APTMS dye and TEOS added to embed different numbers of dye molecules in the SE system.....	100
Table S3.4: EPR data corresponding to the spectra presented in Figure S3.19. All samples were recorded in methanol (2 mg/mL dispersions) at room temperature.....	108
TableA5.1: trials for the synthesis of α -Fe ₂ O ₃ nanoparticles.....	134

List of Abbreviations

APTMS	3-aminopropyltrimethoxysilane
CB	Conduction Band
CR	Cross-relaxation
CSU	Cooperative Sensitized Upconversion
CTAC	Hexadecyltrimethylammonium chloride
DHB	2,5-Dihydroxybenzoic Acid
DMF	Dimethylformamide
DMPO	5,5-dimethyl-pyrroline N-oxide
DMSO	Dimethylsulfoxide
EDC	N-(3-dimethylaminopropyl)-N'-ethyl carbodiimide
EDX	Energy Dispersive X-ray Spectroscopy
EMU	Energy Migration Upconversion
EPR	Electron Paramagnetic Resonance
ESA	Excited State Absorption
ESI-MS	Electron-spray Ionization-Mass Spectrometry
ETU	Energy Transfer Upconversion
FDA	U.S. Food and Drug Administration
FRET	Förster Resonance Energy Transfer
FT-IR	Fourier Transform-Infrared
GSA	Ground State Absorption
HAADF-	High-angle Annular Dark Field-Scanning Transmission Electron
STEM	Microscopy
HRMS	High-Resolution Mass Spectroscopy
IC	Internal conversion
ICG	Indocyanine Green
ISC	Intersystem Crossing
IUPAC	International Union of Pure and Applied Chemistry
LnUCNPs	Lanthanide-doped Upconverting nanoparticles

MALDI-MS	Matrix-assisted Laser Desorption Ionization-Mass Spectrometry
NHS	N-hydroxysuccinimide
NIR	Near Infrared
NMR	Nuclear Magnetic Resonance
PA	Photon-Avalanche
PTFE	Polytetrafluoroethylene
PVP	Polyvinylpyrrolidone
PXRD	Powder X-ray Diffraction
QY	Quantum Yield
RE	Rare-Earth
ROS	Reactive Oxygen Species
SE	Silica Embedded System
SE-WP	Silica Embedded Wide Pore system
SL	Surface Silica Linked System
SPR	Surface Plasmon Resonance
TEM	Transmission Electron Microscopy
TEOS	Tetraethylorthosilicate
TPA	Two-photon Absorption
TTA	Triplet-triplet Annihilation
TTET	Triplet-Triplet Energy Transfer
UV	Ultraviolet
VB	Valence Band
WP	Wide-pore silica shell

List of Equations

Equation 1	Multiphonon relaxation constant.....	12
Equation 2	Probability of Förster Energy Transfer	20
Equation 3	Förster Radius.....	21
Equation 4	Overlap Integral.....	21
Equation 5	Probability of Dexter Energy Transfer.....	23
Equation 6	Heavy Atom Effect.....	31

Chapter 1: Introduction

1.1 Luminescence

Luminescence, also referred to as "cold light," is the emission of light, originating from energy sources other than heat.⁴ The term "luminescence" was coined by the German physicist Eilhardt Wiedemann in 1888, who derived it from the Latin word "lumen," meaning "light". Materials that exhibit this phenomenon are known as "luminescent materials".^{5,6}

According to the International Union of Pure and Applied Chemistry (IUPAC), luminescence is defined as the emission of radiation from a species that is either electronically or vibrationally excited.⁷ First, the electronic system of luminescent material is excited to a higher energy state, and then it emits photons of light.⁶ Depending on the mode of excitation, luminescence manifests in various forms such as chemiluminescence, bioluminescence, mechanoluminescence, cathodoluminescence, electroluminescence, photoluminescence, thermoluminescence, radioluminescence, and sonoluminescence.⁸ In the context of this work, the focus will primarily be on photoluminescence.

Photoluminescence can be defined as the process when the luminescent material is excited by absorbing a photon, which brings it to an electronically excited state, with subsequent de-excitation accompanied by the emission of photons. The wavelength of the light emitted through photoluminescence depends on the material's properties, rather than the incident radiation. In this way photoluminescence occurs *via* Stokes or anti-Stokes processes.⁴

1.1.1 Stokes Shift and anti-Stokes shift

In general, most photoluminescent materials exhibit luminescence by the Stokes process, in which the emission wavelength is longer than the absorption wavelength.⁹ This phenomenon was first observed by Sir G. G. Stokes in 1852 at the University of Cambridge.¹⁰ The initial experiments were conducted using relatively basic equipment, sunlight served as the source of ultraviolet (UV) excitation, and a blue glass filter, incorporated into a stained-glass window, selectively transmitted light below 400 nm, which was absorbed by quinine. A yellow glass filter (resembling wine glass material) prevented the incident light from reaching the detector (eye). As a result, the fluorescence of quinine, occurring around 450 nm, was easily visible.¹¹

A schematic for the luminescence process by Stokes and anti-Stokes mechanisms is given in **Figure 1.1**. The absorption and emission processes involve two energy states in which an excitation photon of energy $h\nu_{ex}$ or wavelength λ_{ex} is absorbed and an emitted photon of energy $h\nu_{em}$ or wavelength λ_{em} is released (**Figure 1.1a**). Therefore, a “Stokes shift” can be defined as the increase in wavelength between the light emitted by a molecule and the wavelength at which the molecule was initially excited.^{11,12}

In contrast, the anti-Stokes shift can be defined as a decrease in the emission wavelength relative to the excitation wavelength. Thus, any anti-Stokes exhibiting material is capable of converting low-energy excitation photons ($h\nu_{ex}$) into higher energy photons ($h\nu_{em}$) (**Figure 1.1b**). This wavelength conversion is facilitated by the introduction of additional energy (in the form of heat or an additional excitation photon) during the excitation process.¹³ This process is particularly beneficial for biological applications, since longer wavelengths of light (in particular, near-infrared light) are capable of penetrating deeper into biological tissues, and anti-Stokes shifting of NIR greatly minimizes background fluorescence interference.^{14–16}

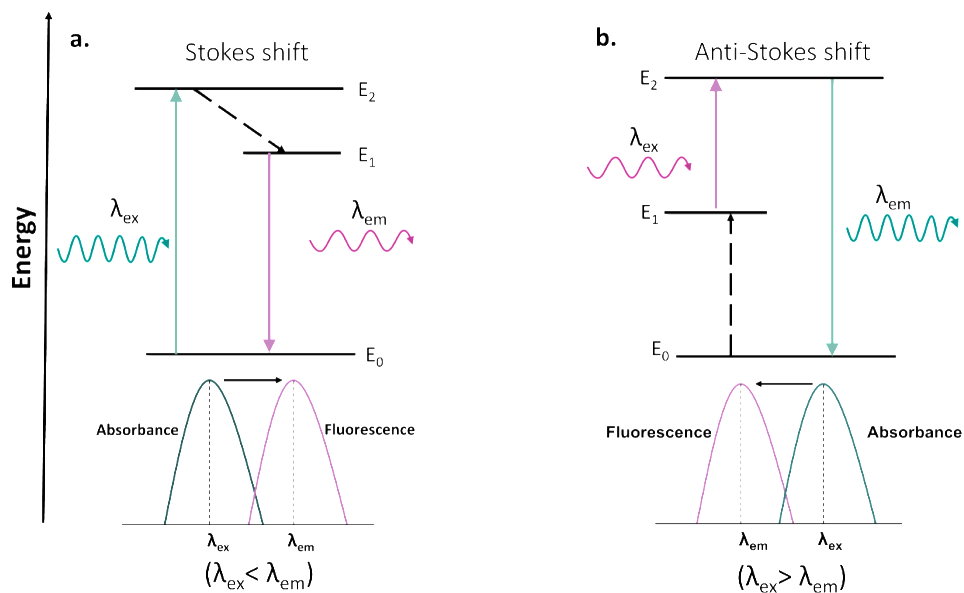


Figure 1.1. Simplified schematic and graphical representation of luminescence processes. (a) Stokes process: Diagram illustrates the absorption of excitation photon (λ_{ex}) and subsequent emission at an increased wavelength (λ_{em}). The accompanying schematic showcases the Stokes shift between the absorbance and emission wavelengths. (b) Anti-Stokes process: Diagram depicts the absorption λ_{ex} and emission at a decreased wavelength (λ_{em}), made possible through additional energy input. The schematic displays the anti-Stokes shift between the two wavelengths.

1.1.2 Photoluminescent nanomaterials

For most luminescent materials, the emission spectrum is mainly centered at a longer wavelength than the excitation spectrum. Most organic dyes, semiconductors, and quantum dots are typical Stokes shift exhibiting materials.⁹ The mechanism of photoluminescence in organic molecules is often explained using the Jablonski diagram, which illustrates the processes occurring between light absorption and emission, as shown in **Figure 1.2a**. This diagram represents the singlet ground state (S_0), the first (S_1), and second (S_2) electronic states in an organic molecule. Each electronic energy level can have various vibrational energy levels (0, 1, 2, etc.). After absorbing light, several processes unfold. In some cases, the organic molecule can relax to a lower excited level (S_1) through a process called internal conversion (IC). From the S_1 state, the organic molecule could relax to the S_0 state by emitting a photon of lower energy as of absorption; this is called fluorescence. Additionally, the same molecule in the excited S_1 state could also undergo electronic spin conversion to the first triplet state (T_1) through intersystem crossing (ISC). The organic molecule from the T_1 state could relax to the S_0 state, emitting a photon of lower energy, this process is called phosphorescence.^{11,17,18}

The photoluminescent properties of semiconductors are defined by a narrow band gap between the valence and the conduction band (**Figure 1.2b**). When a photon is absorbed, it excites an electron from the valence band to the conduction band, leaving a hole behind. These oppositely charged entities can combine and form an exciton, which can diffuse throughout the delocalized conduction and valence bands and can recombine to produce a photon.¹⁹ The excitons are categorized based on size, determined by the Bohr radius.²⁰ In the case of quantum dots, the size of the particles is smaller than the Bohr radius, resulting in the quantum confinement of the excitons. When excitons are confined within a quantum dot, distinct energy states emerge within its energy structure. The number and energy of these states are influenced by the size of the nanoparticles, which, in turn, impacts the absorption and emission properties of the material.²¹

In contrast to organic molecules and semiconductor/quantum dots, some metal ions in a spectroscopically silent host can exhibit a process called upconversion, which has been described as anti-Stokes process.^{9,22} More recently, this relationship between upconversion and the anti-Stokes terminology has come into debate.²³ Upconversion is characterized by the involvement of several metastable energy states, as depicted in **Figure 1.2c** and described here. Starting with the absorption of a low-energy photon, the ground state progresses to excited metastable state 1. This

is then excited to a higher energy level, metastable state 3, by absorbing an additional low-energy photon. After undergoing internal relaxation processes, metastable state 3 relaxes to a lower excited energy state, metastable state 2, before further relaxing to the ground state, emitting a photon. The rest of this thesis is focused on upconversion. The following sections discuss the most prevalent upconversion mechanisms, offering detailed insights into this process.

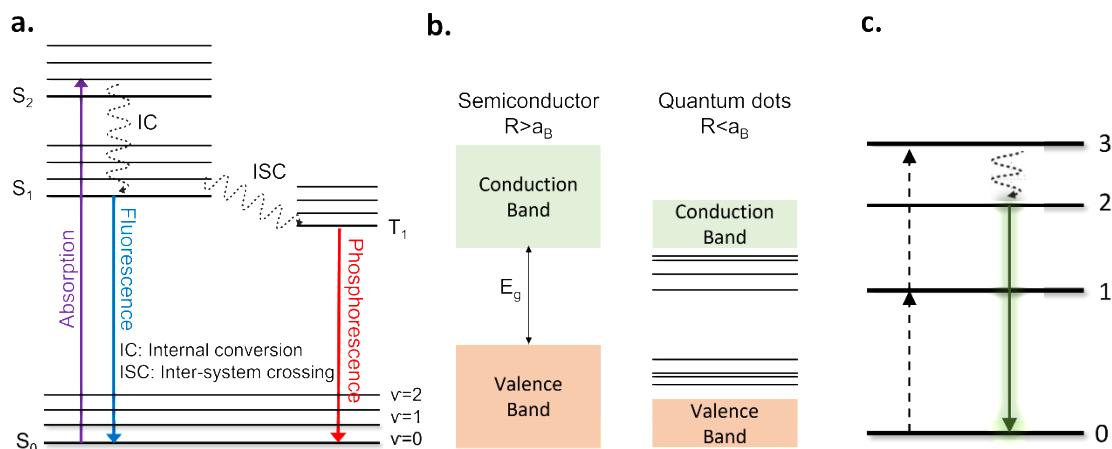


Figure 1.2. Illustrates photoluminescence mechanism in- (a) organic molecules: Jablonski diagram illustrating the energy absorption and release pathways in the molecule; (b) semiconductor and quantum dots: energy level distribution in semiconductors versus semiconductor quantum dots of radius R . When R is less than the Bohr radius, distinct energy levels appear within the band gap; (c) metal ion-based materials: Schematic representation of upconversion through metastable states of an ion that converts low-energy photons to high energy photons.

1.1.3 Mechanisms of Anti-Stokes Luminescence

The mechanism of anti-Stokes luminescence depends on the type of material. Mostly, organic molecules exhibit two-photon absorption (TPA), which involves simultaneous absorption occurring through virtual states.¹³ Photon upconversion is a non-linear process that involves the sequential absorption of two or more photons with a longer wavelength followed by the emission of light with a shorter wavelength.²⁴ In 1959, Bloembergen initially proposed the concept of upconversion,²⁵ and then, in 1966, Auzel, Ovsyankin and Feofilov independently observed the process in action.^{26,27}

Upconversion is reported in both organic and inorganic materials by various mechanisms.¹³ It mostly occurs through triplet-triplet annihilation (TTA) in organic molecules such as polycyclic aromatic hydrocarbons.¹³ In contrast, inorganic materials such as d-block and f-block ions are capable of exhibiting upconversion²⁴ through energy transfer upconversion (ETU), ground state

absorption/excited state absorption (GSA/ESA), two-photon absorption, triplet-triplet annihilation, cooperative sensitization upconversion, photon avalanche, and energy migration upconversion.²⁸ The other mechanisms are discussed in Appendix 1 and 2 for the interested reader.

As mentioned above upconversion can take place by several mechanisms, but for inorganic material, the two most efficient mechanisms are GSA/ESA and ETU.^{28–30} These are the two mechanisms most commonly encountered in the literature for lanthanide-doped upconverting nanoparticles (LnUCNPs) and are of relevance to the work in this thesis.

1.1.3.1 Ground State Absorption/Excited State Absorption

GSA/ESA is a process that involves the sequential absorption of two or more photons by a single ion, causing an ion to transition from its ground state to an excited state. An ion (labeled as X) is initially in its ground state (**Figure 1.3a**) when an incoming photon with a wavelength that matches the energy gap between the ground state (G) and the excited state (E_1) interacts with the ion; it promotes the ion to the E_1 excited state (①, $G \rightarrow E_1$), this is the GSA part of the mechanism. Subsequently, a second pump photon further promotes the ion to an even higher excited state, E_2 (②, $E_1 \rightarrow E_2$), followed by emission and radiative relaxation of the ion back to its ground state. The occurrence of this mechanism is due to the long lifetime of the intermediate-level, E_1 .³¹ Lanthanide ions are ideal for ESA due to their unique $4f$ electronic configurations with abundant discrete energy levels forming a ladder-like energy level structure, often having lifetimes in micro-milliseconds ranges.^{12,32,33}

1.1.3.2 Energy Transfer Upconversion

ETU is quite different from ESA, as ESA occurs within a single ion, while ETU involves two ions of different elements acting as a sensitizer-activator pair (**see section 1.3.1**). In this process, the sensitizer, having a relatively higher absorption cross-section than the activator ion at the excitation wavelength, transfers energy to the activator, from which emission occurs.

A simplified mechanism of ETU is depicted in **Figure 1.3b**. In this process, an incoming pump photon with energy resonant with the gap between states G and E_1 promotes sensitizer ions to the excited state E_1 (S: ①, $G \rightarrow E_1$). In step 2, non-radiative energy transfer occurs from the sensitizer to the activator ion, causing the latter to transition to its excited state E_1 (A: ②, $G \rightarrow E_1$). Subsequently, a second energy transfer event promotes the activator ion to the next excited state E_2 (A: ③, $E_1 \rightarrow E_2$). After energy transfer, the sensitizer relaxes to its ground state, while the

activator ion, now in E_2 , undergoes radiative decay and returns to its ground state ($A: E_2 \rightarrow G$) and results in upconverted emission. Importantly, this process can occur more than twice, leading to 4 or 5 photon processes.^{33–35} The efficiency of ETU depends on the dopant ions' overall concentration, as the proximity of neighboring ion pairs facilitates energy transfer.^{26,29}

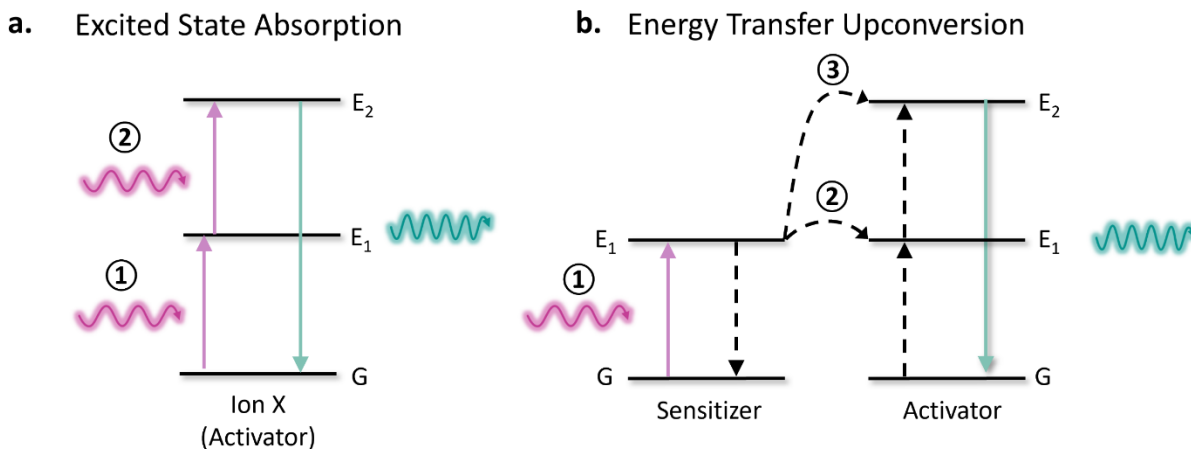


Figure 1.3. Schematic representation of the mechanisms a) Single ion X (activator) based excited-state absorption (ESA); b) Sensitizer and activator pair-based energy transfer upconversion (ETU).

1.2 Lanthanide Theory

The roots of lanthanide chemistry can be found in Scandinavia. In the year 1794, a Finnish scientist named Johann Gadolin discovered an oxide found in a black mineral which was later named as 'gadolinite'. Subsequently, the German chemist Martin Klaproth, the Swedish chemist Jöns Jakob Berzelius and the mineralogist Wilhem Hisinger were able to locate 'ceria' from 'cerite'. But it was only in 1839-1843 that Carl Gustav Mosander was able to accurately separate these substances and detect their individual oxides.³⁶ As the result of his work, ceria was then split into the oxides of lanthanum and cerium, along with an impure oxide known as 'didymia', consisting of metals from Pr to Gd. On the other hand, yttria was also divided into components referred to as 'erbia', 'terbia', and 'yttria'. Subsequently, from 1887 to 1915, Henry Moseley analyzed the X-ray spectra of the elements to confirm the existence of fifteen elements from lanthanum to lutetium.³⁶

The electronic configuration of the lanthanide series ranges from $[Xe]5d^1 6s^2$ for lanthanum to $[Xe] 4f^{14} 5d^1 6s^2$ for lutetium. The most common and stable oxidation state for lanthanides is +3, resulting in trivalent ions with an electronic configuration of $[Xe]4f^n$ (e.g., $[Xe]$ for La, $[Xe] 4f^1$ for Ce, and $[Xe]4f^{14}$ for Lu). The ground state configuration of lanthanide is represented as $[Xe]4f^n$, with n being a value between 0 and 14. This results in a large number of electronic configurations for the

nth electrons in the f orbitals, given by $14! / [n!(14-n)!]$. The poor nuclear shielding ability of the $4f$ electrons causes the outer shell electrons ($5s^2$, $5p^6$) to be more attracted to the nucleus, resulting in the lanthanide contraction effect. Additionally, the $4f$ orbitals are shielded from the external chemical environment by the filled $5s$ and $5p$ orbitals, which extend further from the nucleus than the $4f$ orbitals.³⁷ In other words, the $4f$ electrons are protected from external influences. Due to this shielding property, Lanthanide ions exhibit emission characteristics similar to free ions even when incorporated into a crystal field. Materials containing lanthanide ions often display sharp and narrow emission bands, resembling those observed in gas spectra, because the $4f$ - $4f$ transitions are minimally affected by crystal field splitting.³⁸

In theory, the $4f$ - $4f$ electric dipole transitions for lanthanide ions are forbidden according to Laporte's parity selection rule.³⁸ However, Van Vleck discovered in 1937 that these transitions could occur if the lanthanide ion is present in an asymmetrical crystal field which facilitates an admixture of $4f^{n-1} 5d$ configurations with opposite parity, and relaxes the Laporte selection rule allowing the otherwise forbidden $4f$ - $4f$ electric dipole transitions to take place.³⁹ The $4f$ electronic states in free lanthanide ions follow the Russell Saunders coupling scheme, also known as LS coupling. This scheme describes the coupling of electronic spin and orbital angular momenta. In multi-electron atoms, the orbital angular momenta of individual electrons add up to give the total orbital angular momentum, L ($S=0$, $P=1$, $D=2$, $F=3$, etc.). Similarly, the spin-angular momenta couple to give the total spin angular momentum, S . The total angular momentum, J , is determined by the coupling between L and S and is represented by $J = |L+S|, |L+S-1|, \dots, |L-S|$. The energy levels of the lanthanides are commonly labeled using the Russell Saunders term symbols $^{2S+1}L_J$. Detailed experiments conducted by Dieke and colleagues involved tabulating the energy levels of all trivalent lanthanide ions, as shown in **Figure 1.4**.⁴⁰

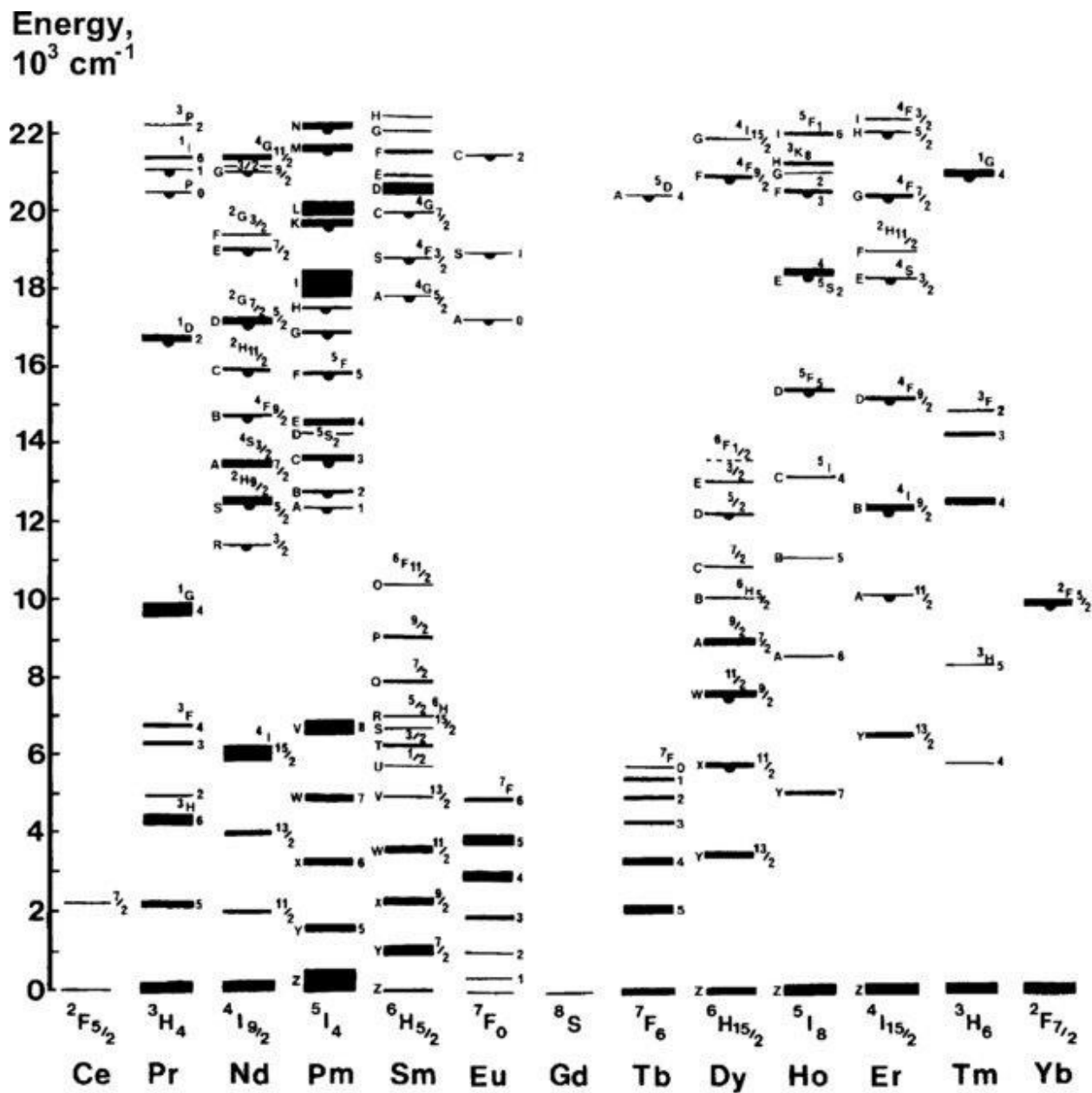


Figure 1.4. Dieke diagram for $4f^n$ energy levels of lanthanide ions in LaCl_3 . Reproduced with permission from reference⁴⁰.

1.3 Lanthanide Doped Upconverting Nanoparticles

LnUCNPs represent specialized inorganic matrices, where lanthanide ions, characterized by a ladder-like arrangement of energy levels, are incorporated within a host lattice.^{15,41} Depending on their precise composition, these structures manifest anti-Stokes luminescence, predominantly *via* the ESA/GSA and/or ETU mechanisms, enabling them to emit UV, visible, or NIR light.^{13,27–29} Though the emission characteristics of LnUCNPs are primarily governed by the specific activator ion, for sensitized luminescence (*via* ETU), the upconversion phenomenon is additionally modulated by the spatial configuration and inter-ionic distance of the dopant ions. These aspects, in turn, are influenced by both the nature of the host structure and the concentration of the embedded dopant ions.^{24,28,29} Consequently, it becomes imperative to understand the components of LnUCNPs.

1.3.1 Components of Lanthanide-doped Upconverting Nanoparticles

1.3.1.1 Activators

The upconversion process necessitates for the activator to have multiple long-lived metastable states.^{12,31} The longer lifetime of a metastable state facilitates the accumulation of a significant transient population, enhancing the likelihood of interaction with subsequent incoming photons.³³ The major known compositions of LnUCNPs usually include lanthanide ions such as Pr³⁺, Nd³⁺, Er³⁺, Tm³⁺, or Ho³⁺ as activator ions; however, there are other elements (transition metals) that can be included as well.^{29,34} The reason why the majority of the research has been focused on lanthanide activators is the high degree of the shielding effect of the *f* and *d* orbitals, leading to sharp and narrow *f-f* transition bands, which are suitable for many applications.⁴²

Certainly, most lanthanide ions are theoretically expected to show upconversion.³⁴ Nonetheless, for practical and efficient upconversion, the energy difference between the two electronic states should be similar to facilitate multiphoton absorption required for the upconversion processes.^{24,29} Er³⁺, Tm³⁺, and Ho³⁺ have been recognized as the most commonly used activators in upconversion phosphors.⁹

Due to the forbidden nature of *4f-4f* transitions in lanthanide ions, they have low absorption cross-section and, consequently, reduced upconversion luminescence efficiencies.⁴³ One straightforward method to enhance this would be increase the concentration of the activator ions.⁴⁴ However, this approach has constraints due to a phenomenon known as concentration quenching, a term coined in 1954 by Dexter and Schulman, which describes the diminishing of luminescence with increased

activator concentration.⁴⁵ At high activator concentrations, the complex ladder-like energy structures of these ions often make them prone to engaging with each other through specific multipolar interactions. This interaction is termed cross-relaxation (CR), and it permits the energy in an excited state to be transferred to the other activator ions.³³ The occurrence of CR at high activator concentrations thereby contributes to the loss of luminescence.

Figure 1.5 illustrates a simplified CR mechanism; in this process, ion 1 transfers a portion of its excited energy to ion 2, as described by the equation $E_2(\text{ion 1}) + G(\text{ion 2}) \rightarrow E_1(\text{ion 1}) + E_1(\text{ion 2})$. Ion 1 and ion 2 are the same, and ion 2 may also be in its excited state.¹⁵ To mitigate the effects of CR, the activator ions are usually employed at concentrations equal to less than 2 mol% for ternary fluoride nanoparticles.⁴⁶

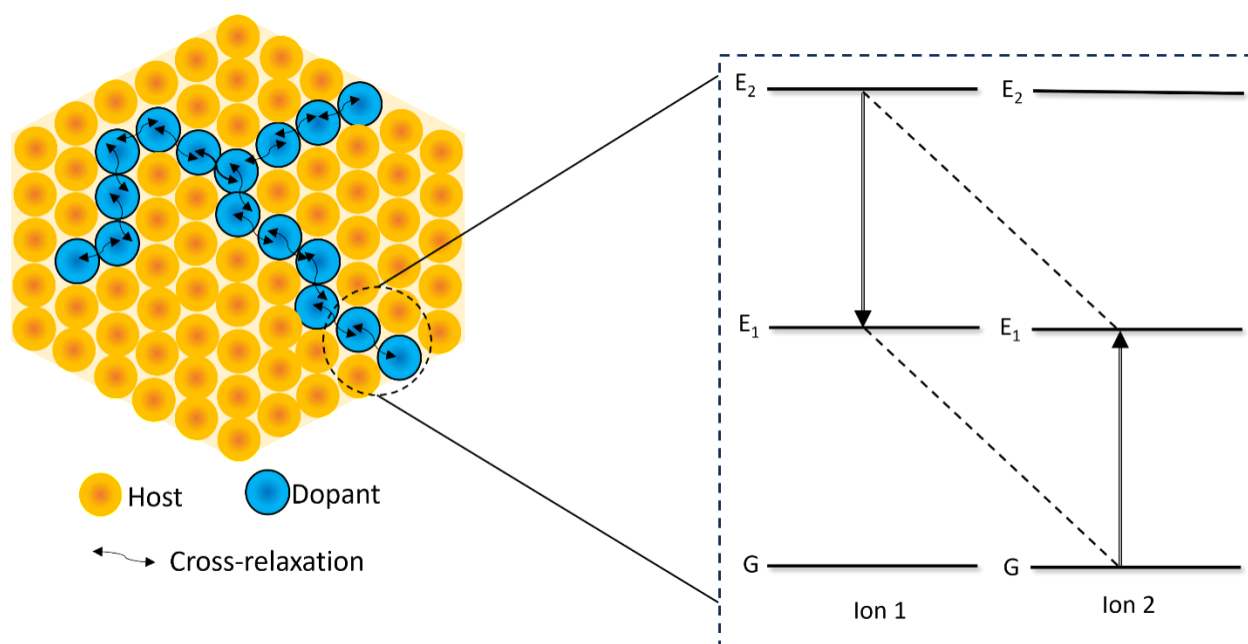


Figure 1.5. Depiction of a simplified cross-relaxation mechanism among the activator ions doped in a host matrix. Yellow dots represent spectroscopically silent host atoms, blue dots represent dopant ions.

1.3.1.2 Sensitizers

Since most lanthanide ions exhibit a low absorption cross-section in the NIR region, they fail to produce efficient upconversion emissions *via* the GSA/ESA mechanism. The efficiency of the upconversion process can, however, be markedly enhanced by the ETU mechanism.^{24,34} This enhancement involves the incorporation of an ion referred to as a sensitizer. The sensitizer ion has a higher absorption cross-section and has the capacity to transfer the absorbed energy to adjacent activator ions embedded in the host crystal lattice.^{24,34,47–49} Through this mechanism, not only is

the inadequate absorptivity of the activator ion relieved, optimal inter-ionic distance among the dopants is also maintained, thereby minimizing the quenching effects frequently triggered by CR events.²⁴

For these reasons, the Yb³⁺ ion is the most frequently used sensitizer; the energy of the electronic transition $^2F_{7/2} \rightarrow ^2F_{5/2}$ energy states are resonant with 976 nm.^{22,28} The absorption band corresponding to this transition exhibits a substantially larger absorption cross-section in the range of $0.29\text{-}1.50 \times 10^{-20}$ cm² compared to all other lanthanide sensitizers.^{34,50} Moreover, the energy difference associated with this transition resonates with numerous *f-f* electronic transitions of lanthanide activator ions (Er³⁺, Tm³⁺, Ho³⁺, etc) employed in upconversion systems, which facilitates effective energy transfer.^{24,47,51} The simple energy level structure of Yb³⁺ facilitates a relatively high concentration (18-20 mol%) of sensitizer ion while the activator concentration is kept low, amounting to 2 mol% or less.⁹ However, the excitation maximum of Yb³⁺ at 980 nm overlaps with the absorption band of water molecules, limiting the applications of Yb³⁺-based LnUCNPs in an aqueous environment. To circumvent these limitations and expand the applicability of LnUCNPs in these environments, Nd³⁺ has also been investigated as a sensitizer ion. It permits photon upconversion using 808 nm excitation, which is within the so-called “optical biological window” where water has an absorption minimum.²⁸ Various studies show the successful use of Nd³⁺ in combination with Yb³⁺-activator pair in a triply-doped system.⁵²⁻⁵⁸ As illustrated in **Figure 1.6**, Nd³⁺ ions under 808 nm excitation exhibit a $^4I_{9/2} \rightarrow ^4F_{5/2}$ transition, followed by a non-radiative transition which relaxes the ion to the $^4F_{3/2}$ excited state. From the $^4F_{3/2}$ state, Nd³⁺ ions non-radiatively transfer energy to the Yb³⁺ ion, resulting in $^2F_{7/2} \rightarrow ^2F_{5/2}$ transition.^{56,57,59} Notably, the absorption cross-section of Nd³⁺ ions at 808 nm is an order of magnitude greater than that of frequently used ions like Yb³⁺.^{60,28,52}

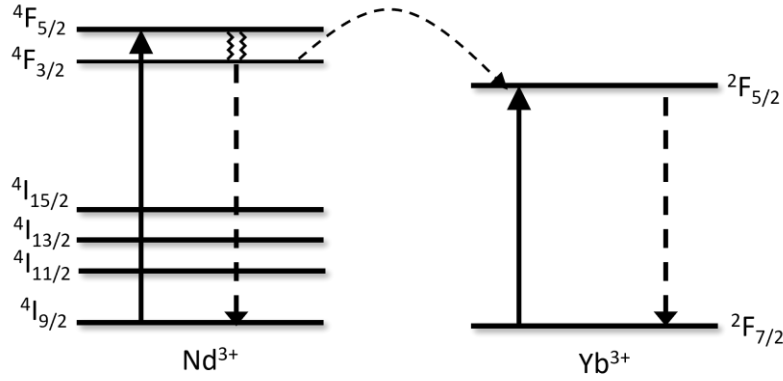


Figure 1.6. Diagram depicting the energy levels and corresponding energy transfer from $\text{Nd}^{3+} \rightarrow \text{Yb}^{3+}$ ions under 808 nm excitation.

1.3.1.3 Host

The host lattice's characteristics as well as its relationship to the dopant ions greatly impact the upconversion process. The host lattice is responsible for the spacing between the dopant ions, spatial position, coordination number, site symmetry, and the anions surrounding the dopant. It is generally necessary for a crystalline host material to possess two important characteristics: a low phonon energy and a minimal lattice mismatch to the doping ions.⁹ The phonon energy of the host can significantly impact the population and depopulation of energy levels of the dopant ions.³¹ Therefore, it is important to understand phonon energy, which is defined as the resonance or vibrational oscillation that occurs at the atomic level in a crystal lattice.³¹ The multi-phonon relaxation constant (k_{nr}) is mathematically given by equation 1:

$$k_{nr} \propto \exp\left(\frac{-\beta\Delta E}{h\omega_{max}}\right) \quad (1)$$

where β is an empirical constant of the host, ΔE is the energy gap between the populated level and the next lower-lying energy level of a lanthanide ion, and $h\omega_{max}$ is the highest energy vibrational mode of the host lattice. If the phonon energy ($h\omega_{max}$) of the host is high, the value of k_{nr} increases, and consequently the non-radiative quenching will be higher.^{9,24,61}

For LnUCNPs, several hosts such as phosphates, vanadates, oxides, and halides have been explored.⁶²⁻⁶⁴ Typically, halides like chlorides, bromides, and iodides have phonon energies below the 300 cm^{-1} . However, due to their hygroscopic nature, they are not widely used. Fluorides, on the other hand, have slightly higher phonon energies, around 350 cm^{-1} , compared to other halide

hosts but exhibit greater chemical stability. This property of fluoride-based hosts makes them a popular choice for hosts in LnUNCs.^{24,47,49}

Thus, much work has been dedicated to preparing binary (REF₃) and ternary (AREF₄, A is an alkali or alkaline earth metal, RE is rare-earth) fluorides with controlled morphology, phase, and narrow size distribution.⁶⁵ Binary rare-earth fluoride nanocrystals, synthesized as they are, demonstrate fascinating self-assembly capability and readily form superlattices.⁶⁶ Ternary fluoride host AREF₄ possesses distinctive luminescent, ferromagnetic, insulating/magnetic, and piezoelectric properties.⁶⁷ Based on the lanthanide dopants used and by manipulating the growth kinetics through changing reaction temperature, time, and solvents, these fluoride hosts can be converted from binary to ternary rare-earth fluorides.^{68,69}

As shown in work done by Mai *et al.*, the rare-earth series was divided into three groups (I: Pr and Nd; II: Sm to Tb; III: Dy to Lu, Y). For group I, as the reaction temperature was increased to 330°C, binary fluorides (PrF₃ and NdF₃) were preferred to form and the product nanoparticles did not have homogenous morphologies. However, as the reaction mixture was heated for a prolonged time, the binary fluorides for this group were partially consumed to produce ternary fluorides. In contrast, group II and group III preferred to form a ternary host; this type of host can form in two different crystal phases: cubic (α -NaREF₄) and hexagonal (β -NaREF₄). Under similar synthesis conditions as group I, the ternary fluoride host doped with group II forms the hexagonal phase, and group III ions form the cubic crystal phase.^{68,69} Between these two crystal phases, the hexagonal phase is a low-symmetry phase that usually produces a crystal field containing more uneven components in the vicinity of lanthanide dopant ions in comparison to the cubic phase, which has high symmetry. These uneven components enhance the electronic coupling between *4f* energy levels and higher electronic configuration and subsequently increase the *f-f* transition probabilities of the dopant ions.⁸ This was confirmed by Heer *et al.* which showed the upconversion efficiency of hexagonal-phase NaYF₄:Yb³⁺, Er³⁺ bulk materials is approximately 10 times higher than that of the cubic phase for this reason.⁶²

Consequently, sodium gadolinium fluoride (NaGdF₄) is considered one of the most efficient host materials due to its high photochemical stability, low phonon energy (350 cm⁻¹), and its ability to facilitate the formation of a hexagonal crystal phase. Furthermore, this host enables precise control

over the size of the nanoparticles by adjusting the reaction temperature.^{31,68,69} For these reasons, NaGdF₄ is the preferred host used throughout this work.

1.3.2 Energy Transfer mechanism in the Yb³⁺-Er³⁺ pair

Under excitation at 980 nm, Yb³⁺ and Er³⁺ co-doped LnUCNPs produce green emissions centered at 525 nm and 542 nm and red emissions at 655 nm. Occasionally, some emission at 415 nm can also be seen.⁷⁰ Conventional intensity vs power studies recorded for NaYF₄: Er³⁺, Yb³⁺ LnUCNPs shows the green and red emissions are two-photon processes and the violet emission at 415 nm is a three-photon process.^{71,72}

As shown in **Figure 1.7**, the Yb³⁺ ions absorb NIR photons, which initiates the ²F_{7/2}→²F_{5/2} electronic transition (ETU figure 1.3b, ① S:G→E₁). As a result of resonance, the excited Yb³⁺ ions non-radiatively transfer their energy to neighboring Er³⁺ ions. This transfer promotes the Er³⁺ ions from ground state ⁴I_{15/2} energy level to the ⁴I_{11/2} energy level (ETU figure 1.3b, ② S:G→E₁—ENERGY TRANSFER→ A:G→E₁).

In the ⁴I_{11/2} state, the excited Er³⁺ can either non-radiatively relax to the ⁴I_{13/2} energy level and subsequently absorb a second photon from an excited Yb³⁺ ion, which promotes it to the ⁴F_{9/2} energy level from which it can radiatively relax to the ground state. This results in the red emission centered at 655 nm attributed to the ⁴F_{9/2}→⁴I_{15/2} transition. Conversely, the excited electrons in the ⁴I_{11/2} energy level are directly promoted to the ⁴F_{7/2} energy level upon a second energy transfer from an excited Yb³⁺ ion (ETU figure 1.3b, S:②G→E₁—ENERGY TRANSFER→ A:E₁→E₂). This leads to the emission of green light at wavelengths of 525 nm and 542 nm, corresponding to the ²H_{11/2}→⁴I_{15/2} and ⁴S_{3/2}→⁴I_{15/2} transitions respectively.^{70,72}

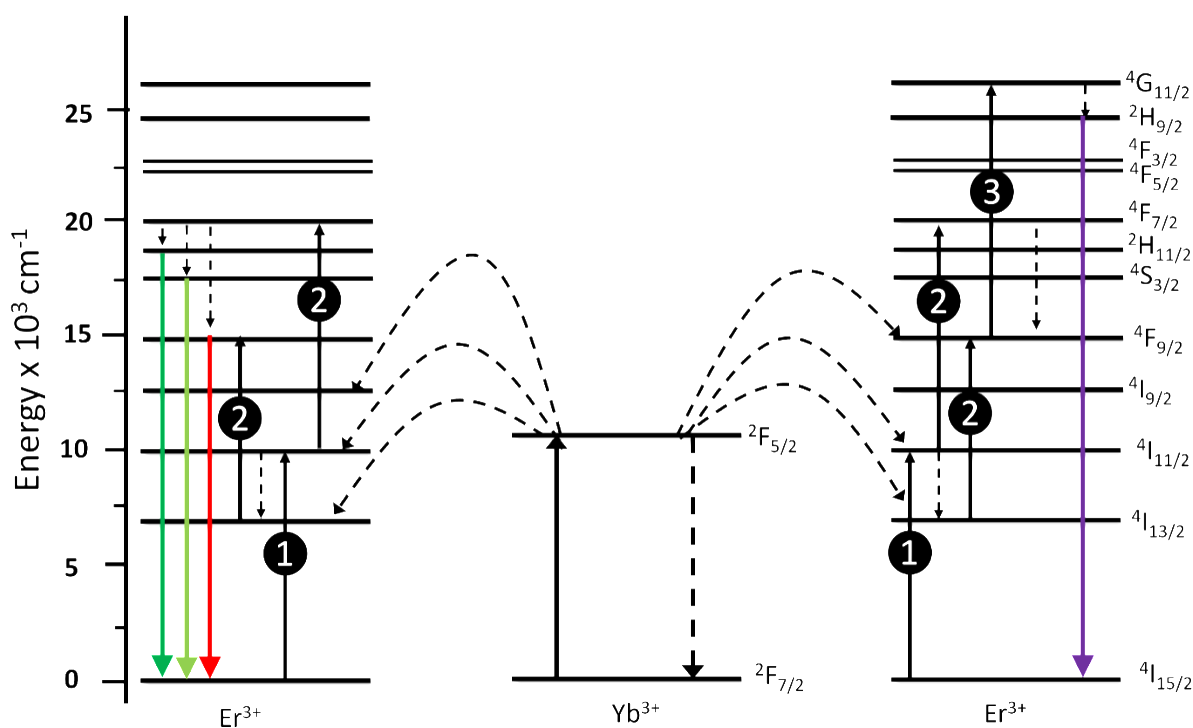


Figure 1.7. Schematic representation of the energy transfer process in Yb³⁺-Er³⁺ doped LnUCNPs. On the left, the two-photon upconversion processes produce red and green emissions, while the right showcases the three-photon upconversion process leading to a violet emission.

The Yb³⁺-Er³⁺ sensitizer-activator pair has proven to be exceptionally effective in various applications, including but not limited to anti-counterfeiting measures, bioimaging, biosensing, and photocatalysis.⁷³⁻⁷⁶ For instance, Lin *et al.* fabricated NaYF₄:Yb³⁺, Er³⁺@CsMnCl₃ nanocomposites for optical anti-counterfeiting applications. They found that these nanocomposites, when used for encryption under UV light and decryption with NIR excitation, provided robust security for sensitive information.⁷³ Li's team developed a unique approach to bioimaging using a phosphatidylcholine-modified NaYF₄:30%Yb³⁺, 1%Nd³⁺, 0.5%Er³⁺/NaYF₄:20%Nd³⁺-based nanocomposite. The nanocomposite generated powerful upconverted luminescent signals in HeLa cells and was also effective in lymphatic imaging applications.⁷⁴ Further, Rabie and colleagues have demonstrated the value of Yb³⁺-Er³⁺ in biosensing. They designed a NIR dopamine sensing platform using Yb/Er/Yb nanostructures as a probe in a core/shell/shell "sandwich" structure. This enabled the precise and sensitive monitoring of dopamine secretion from differentiating stem cells.⁷⁵ In photocatalysis, Liu *et al.* utilized NaYF₄:Yb³⁺, Er³⁺/Au/CdS for H₂ production *via* the photo-reforming of bio-ethanol.

The presence of the Au component in the NaYF₄:Yb³⁺,Er³⁺/Au/CdS structure greatly improved the separation of electron-hole pairs through Förster resonance energy transfer and plasmonic resonance energy transfer. After modification with Au or CdS, the upconversion luminescence of NaYF₄:Yb³⁺,Er³⁺ significantly decreased. This resulted in enhanced NIR light-induced photocatalytic activity in the NaYF₄:Yb³⁺,Er³⁺/Au/CdS structure, which had the highest H₂ yield and H₂ evolution rate under simulated sunlight illumination compared to NaYF₄:Yb³⁺,Er³⁺, NaYF₄:Yb³⁺,Er³⁺/Au, and NaYF₄:Yb³⁺,Er³⁺/CdS.⁷⁶

1.4 Strategies for Enhancement of Upconversion Efficiency

Despite the promising properties of LnUCNPs, their practical applicability is still limited due to inefficient upconversion luminescence. This aspect necessitates improvement in the efficiency of LnUCNPs; in this effort, a range of techniques have been explored by trying to improve the absorption and/or emission characteristics of the nanoparticle. Particularly, core/shell architectures and dye sensitization are two promising routes that have been explored. Other strategies of tailoring the local crystal field and surface plasmon effect are discussed in Appendix 4 for the reader's information.

1.4.1 Core/Shell Architecture

A core/shell system refers to structures where a core luminescent nanoparticle surrounded by additional layers, referred to as the shell layers.⁷⁷ These shell layers are carefully designed to enhance and/or protect the upconversion process.⁷⁸ Due to the high surface-to-volume ratio of the LnUCNPs, the dopants in the core are exposed to surface deactivations caused by surface defects, as well as ligands and solvents that possess high phonon energies. The surface-related deactivation of these dopants occurs through two processes. The first process occurs when photoexcited dopants located on or close to the surface are deactivated from quenching centers nearby (Appendix 3). The second process occurs when the energy from photoexcited dopants located deep in the core of the nanoparticle can migrate to the dopants on the surface or directly to the surface quenching sites (Appendix 3). In order to compensate for these limitations, one approach is to create a protective layer around the core of the upconversion nanoparticles.¹⁵

Depending on the composition and crystal phase of the consecutive shell layers, they are mainly designed to protect and/or enhance the upconversion processes occurring in the core structure. When an epitaxial shell having a well-defined crystal phase or non-epitaxial shell of amorphous

material (SiO₂) or molecular layer (polymer) is coated on the core, it protects the ions from the large vibrational energies of the solvent and surface-associated ligands. As shown by Han *et al.* coating an inert shell of YF₃ on top of YF₃:0.5% Er³⁺, 10% Yb³⁺ core nanoparticles gives five times more intense luminescence.⁷⁹ Similar results were reported by our group, where they compared the emission enhancement of KGdF₄:Tm³⁺, Yb³⁺/KGdF₄ core/shell nanoparticles with KGdF₄:Tm³⁺, Yb³⁺ cores. They reported five times brighter core/shell nanoparticles owing to the protection of the surface dopants by the inert shell from non-radiative decay caused by the surface defects and from vibrational deactivation caused by the solvents or surface-bound ligands.⁸⁰ Since these initial publications, the core/shell strategy has become a widely adopted approach.^{78,81–83}

A sensitizer-doped epitaxial shell serves a twofold purpose. First, it effectively reduces surface-related deactivations, which is comparable to the effects seen in undoped core/shell structures. Second, the presence of the lanthanide sensitizer in the shell synergistically enhances the upconversion luminescence by interacting with the lanthanide dopants situated within the core nanoparticles. The Capobianco group was the first to report such a strategy, demonstrating NaGdF₄:Yb³⁺, Er³⁺/NaGdF₄:Yb³⁺ active shell nanoparticles, that exhibited 4.5- and 9-times enhanced emission when compared to either the NaGdF₄:Yb³⁺, Er³⁺ active-core/NaGdF₄ inert shell or the NaGdF₄:Yb³⁺, Er³⁺ core-only nanoparticles.⁷²

Typically, non-epitaxial shells are applied post-synthetically to core nanoparticles. The primary objective of these shells is to modify the surface of the nanoparticles. This modification serves many purposes, for example, it enhances the dispersibility of the nanoparticles in polar solvents, and, it introduces functional groups on otherwise unfunctionalized positively-charged surface of the fluoride-based LnUCNPs.⁷⁸ LnUCNPs surfaces are often coated with a silica or polymeric shell functionalized by amine, carboxylic, terminal alkyne, or azide. This coating serves dual purposes: it equips the surface with reactive functional groups and notably enhances their dispersibility in aqueous solutions. To illustrate this, Li and Zhang *et al.* synthesized NaYF₄:Er³⁺, Yb³⁺/SiO₂ core-shell nanoparticles featuring a consistent silica layer. This silica shell improved the dispersibility of the system in aqueous solution.^{78,84}

1.5 Dye Sensitization

Several structural manipulations have been studied to improve upconversion luminescence such as controlling the crystal phase of the host lattice, tailoring the local crystal fields, or adopting core/shell structures, which can enhance upconversion luminescence by 10 to 20 times.^{72,82,85} In 1942, Weissmann proposed another promising technique to overcome the inherent low absorption cross-section of the lanthanides by encapsulating them in a suitable organic ligand to harvest the light, which allows for an indirect excitation of the lanthanides ion *via* energy transfer.⁸⁶ In the early 1990s, lanthanide complexes were investigated as luminescent materials, and Lehn proposed that such complexes could be perceived as *light conversion molecular devices* and coined the term *antenna effect*.⁸⁷ This term denotes the absorption, the energy transfer, and the emission sequence involving the ligand and the emitting lanthanide ion, thus surmounting the low absorption cross-section of the lanthanide ions. These lanthanide complexes exhibit unique photophysical properties, including high luminescence intensity and narrow emission bands. These properties make them ideal candidates for a diverse array of applications, such as time-resolved fluorescence assays, luminescent probes in bioimaging, and active elements in optoelectronic devices.⁸⁸⁻⁹⁰ The concepts proposed by Weissmann and Lehn form the basis for the concept of dye-sensitized upconversion for LnUCNPs.

An important component of the dye-sensitized system is the organic dye. In order for these organic dyes to be effective broadband sensitizers, they need to meet three primary criteria. Firstly, they should exhibit high absorption in the NIR region. Secondly, a broad absorption spectrum is desirable. Lastly, the ability to modify the absorption band through molecular bandgap manipulation is crucial. The choice of organic dye depends on the specific lanthanide ion that needs to be sensitized. Many organic dyes used for sensitization exhibit absorption and emission spectra similar to widely used sensitizers like Yb³⁺ and Nd³⁺, offering the potential for efficient energy transfer.

Specifically, heptamethine cyanine dyes possess an absorption wavelength centered beyond 780 nm, with an emission wavelength in the NIR, which can overlap with the absorption bands of Yb³⁺ and Nd³⁺. These dyes exhibit an absorption cross-section ranging from 10⁻¹⁷ to 10⁻¹⁶ cm², which is approximately 1000 to 10,000 times greater than that of a lanthanide ion.⁹¹ Furthermore, dyes can be engineered to attach to the surface of LnUCNPs through electrostatic attraction, physical adsorption, or covalent bonding. However, these dyes are reported to have poor photostability,

which are not adequately addressed in the available literature on dye-sensitized LnUCNPs. Furthermore, the optical properties and photostability of dye-sensitized systems also depend on energy transfer processes, which will be discussed in the next section.

1.5.1 Energy Transfer process

As illustrated in **Figure 1.8**, after the NIR radiation excites the dye from $S_0 \rightarrow S_n$ (absorption). There are a few ways by which the dye could relax (**Figure 1.8**) I) non-radiative internal conversion (IC; $S_n \rightarrow S_1$) (II) radiative relaxation (fluorescence) ($S_1 \rightarrow S_0$), and (III) inter-system crossing (ISC, $S_1 \rightarrow T_1$), from which phosphorescence can occur ($T_1 \rightarrow S_0$). In each scenario, there exists the potential for an energy transfer process between the dye and the lanthanide ion.⁹²

1.5.1.1 Radiative Energy Transfer

As shown in **Figure 1.8**, the fluorescence or phosphorescence ($S_1 \rightarrow S_0$ or $T_1 \rightarrow S_0$ respectively) pathways of de-excitation result in a radiative mechanism. In radiative energy transfer, also known as reabsorption, the dye emits photons that are subsequently absorbed by the lanthanide ion (Yb^{3+} , Nd^{3+}). Therefore, the presence of the lanthanide does not alter the fluorescence lifetime of the dye since the emitted photons are emitted and absorbed in separate steps.

1.5.1.2 Non-radiative energy Transfer

Non-radiative energy transfer comes into play when the dye deactivates through pathways I (IC; $S_n \rightarrow S_1$) and III (ISC, $S_1 \rightarrow T_1$) followed by energy transfer to the lanthanide ion. This type of energy transfer can take place either by Förster or Dexter mechanisms.^{93,94}

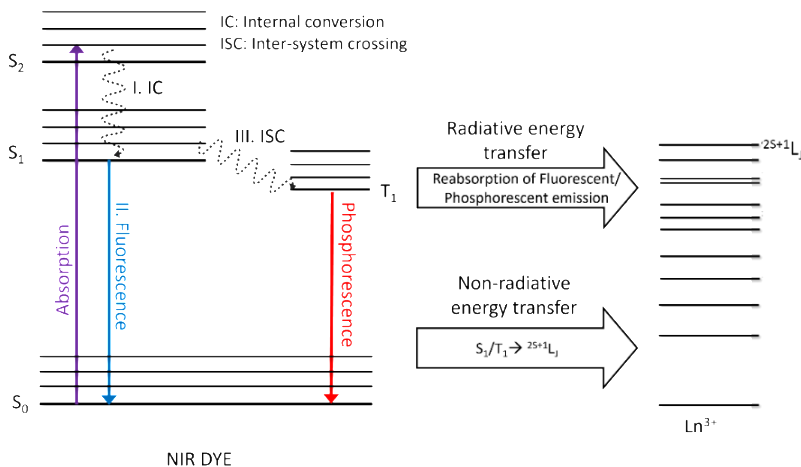


Figure 1.8. Diagram depicting radiative and non-radiative energy transfer pathways from dye to the lanthanide ion. Radiative transfers are characterized by the reabsorption of fluorescent or phosphorescent emissions, while non-radiative transfers originate from the S_1/T_1 excited state of the dye.

Förster resonance energy transfer (FRET) was proposed by Theodor Förster in 1948.⁹³ As shown in **Figure 1.9**, it involves non-radiative energy transfer from an excited donor (I; $S_n \rightarrow S_1$) to a neighboring acceptor lanthanide ion through dipole-dipole interactions. The underlying theory suggests that an excited fluorophore behaves as an oscillating dipole and can exchange energy with another dipole resonating at a similar frequency if the distance between them is sufficiently short. FRET is generally accepted to occur most efficiently between 1-10 nm.^{91,95} The probability of energy transfer through dipole-dipole interactions is given in equation 2⁹³:

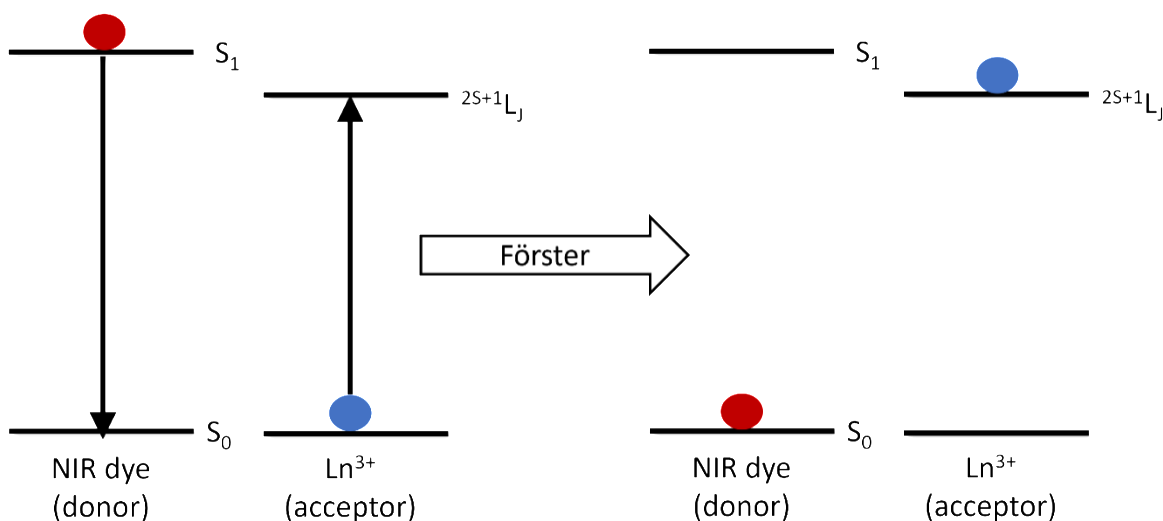


Figure 1.9. Diagram showcasing the Förster energy transfer mechanism, where electrostatic interactions facilitate the non-radiative transition of excitation energy from the dye to the Lanthanide ion.

$$W_{dye-Ln^{3+}} = \left(\frac{1}{\tau_{dye}}\right)\left(\frac{R_0}{R}\right)^6 \quad (2)$$

R is the distance between the dye and the lanthanide ion and τ_{dye} is the lifetime of the excited states of the dye. The Förster radius R_0 (equation 3), is the distance at which 50% of the excitation energy from the dye is transferred to the lanthanide ion. This parameter can be obtained from experimental spectroscopic data as:

$$R_0 = \frac{9 \ln 10}{128\pi^5 N_A} \cdot \frac{k^2 \gamma_D}{n^4} \cdot J \quad (3)$$

Where the refractive index of the environment, denoted by n , the fluorescence quantum yield of Donor γ_D , Avogadro's number, N_A , and the spectral overlap integral, J (equation 4).^{4,29,95,96}

$$J = \frac{\int f_{dye}(\lambda) \epsilon_{Ln}(\lambda) \lambda^4 d\lambda}{\int f_{dye}(\lambda) d\lambda} \quad (4)$$

Therefore, FRET efficiency depends on spectral overlap integral (J), therefore the fluorescence spectrum of the dye molecule should overlap with the absorption the lanthanide ion (**Figure 1.10**), with the extent of overlap referred to as the spectral overlap integral (J).⁹³ The efficiency of spectral overlap is a combination of the degree of overlap between the absorption and emission wavelengths, and also their extinction coefficients.

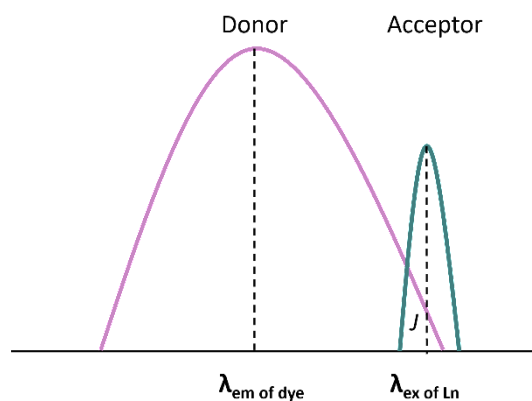


Figure 1.10. Illustration of absorption and fluorescence spectra of a donor (dye)-acceptor (lanthanide) duo. The overlapped area indicates the spectral overlap (J) between the dye's fluorescence and the lanthanide ion absorption.

Dexter energy transfer was formulated by D. L. Dexter in 1953, basing his work on the previous work by Förster.⁹⁴ This energy transfer originates from the exchange of electrons. These interactions come into play when the dye's orbital overlaps with lanthanide energy level and happens at the small distance between the dye and the lanthanide ion (10 Å or less) (**Figure 1.11**).

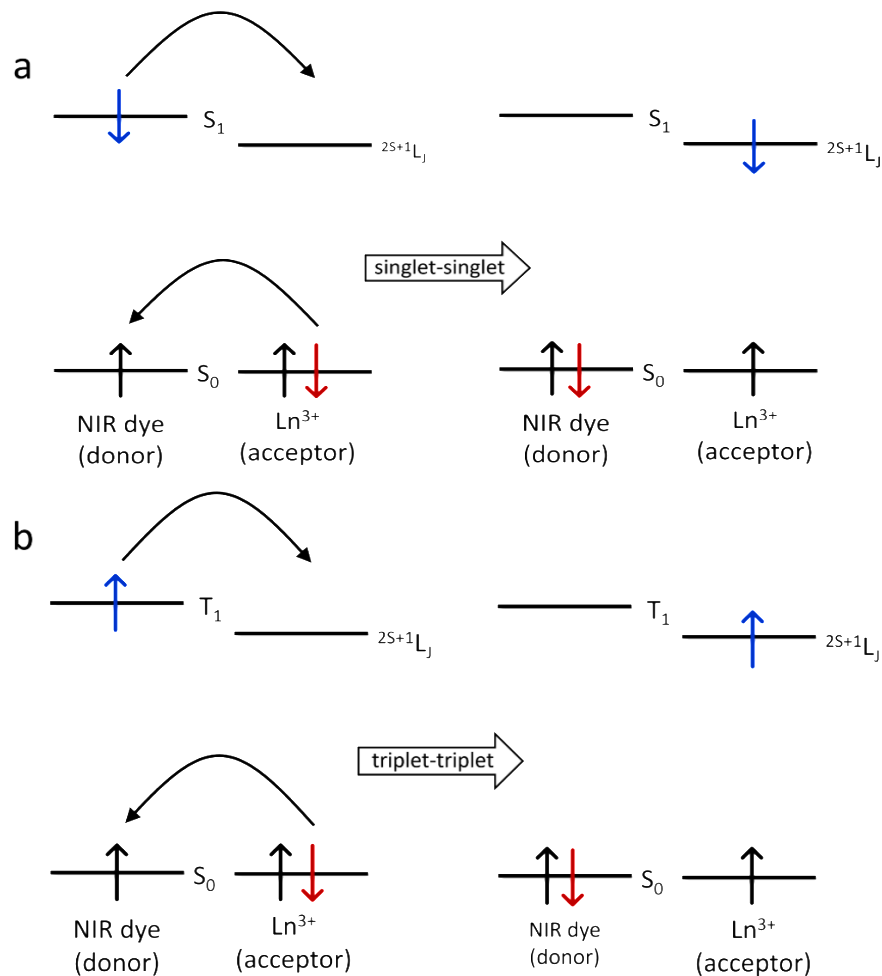


Figure 1.11. Diagram depicting the Dexter energy transfer, a mutual electron exchange occurs between the dye and Ln^{3+} ion, resulting in a) singlet-singlet and b) triplet-triplet transfer.

According to this mechanism, an electron from the excited state of the donor (dye molecule), is exchanged with an electron from the ground state of the lanthanide acceptor ion. The underlying principle of Dexter energy transfer hinges on the overlap of molecular orbitals between the donor and acceptor entities. Specifically, an electron in the excited-state of the donor is transferred to an excited-state of the neighboring lanthanide ion. Concurrently, an electron from the ground-state lanthanide ion backfills the ground state of the donor molecules. This electron exchange can facilitate either a singlet-singlet (**Figure 1.11a**) or a triplet-triplet (**Figure 1.11b**) transition between the involved species. This electron exchange process necessitates a high degree of spatial

proximity between the donor and acceptor, rendering Dexter energy transfer the dominant mechanism at short (10 Å or less) distance.^{29,94,95}

The probability of energy transfer depends on the distance and is given by⁹⁴:

$$W_{dye-Ln^{3+}} = \frac{2\pi}{h} D \cdot J \cdot e^{(-2r/L)} \quad (5)$$

The total distance between the dye and the lanthanide, L , is calculated by adding together the respective van der Waals radii. J is the overlap integral between the two molecules, and D is the challenging to determine Dexter parameter, which is based on the dye and lanthanide experimental spectroscopic data.

1.5.2 Cyanine Dyes

Cyanine dyes are commonly classified on the basis of the number of methine groups in their polymethine chain. Monomethine cyanine dyes ($x=1$, **Figure 1.12**) generally absorb light in the visible region. However, the addition of each methylene unit ($\text{CH}=\text{CH}$) in the polyene chain causes a redshift of approximately 100 nm, resulting in longer wavelengths. For example, a dye with $x=3$ referred to as heptamethine cyanine dye absorbs in the NIR region.⁹⁷⁻⁹⁹

The absorbance maxima of cyanine dyes are a consequence of electron propagation along the polymethine moieties that connect the heterocyclic ring system. The presence of quaternary amines on the rings serves as electron sinks (**Figure 1.12**). One of the unique aspects of cyanine dyes is their flexible chemistry, allowing for modifications at multiple positions on the carbon backbone. The spectral attributes and electronic properties of cyanine dyes can be manipulated by adjusting the length of the polymethine chain and/or by introducing terminal substituents that possess either electron-donating or electron-accepting abilities on the nitrogen heterocycles.^{100,101}

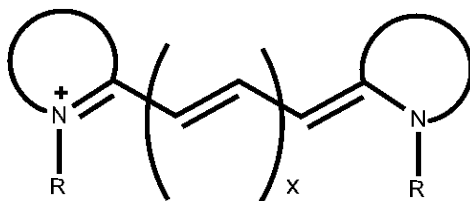


Figure 1.12. Basic skeleton of a polymethine cyanine dye, x is the number of monomethine unit.

1.5.2.1 Heptamethine Cyanine Dyes

Figure 1.13 shows commonly used heptamethine cyanine dyes for dye sensitization. These dyes exhibit absorbance and emission, in the NIR region (700-900 nm). They also possess high absorption coefficients ($\sim 10^{16} \text{ M}^{-1} \text{ cm}^{-1}$).¹⁰² Most of these dyes possess an anionic group and/or reactive site which could be modified to possess an anionic group to coordinate on the positive

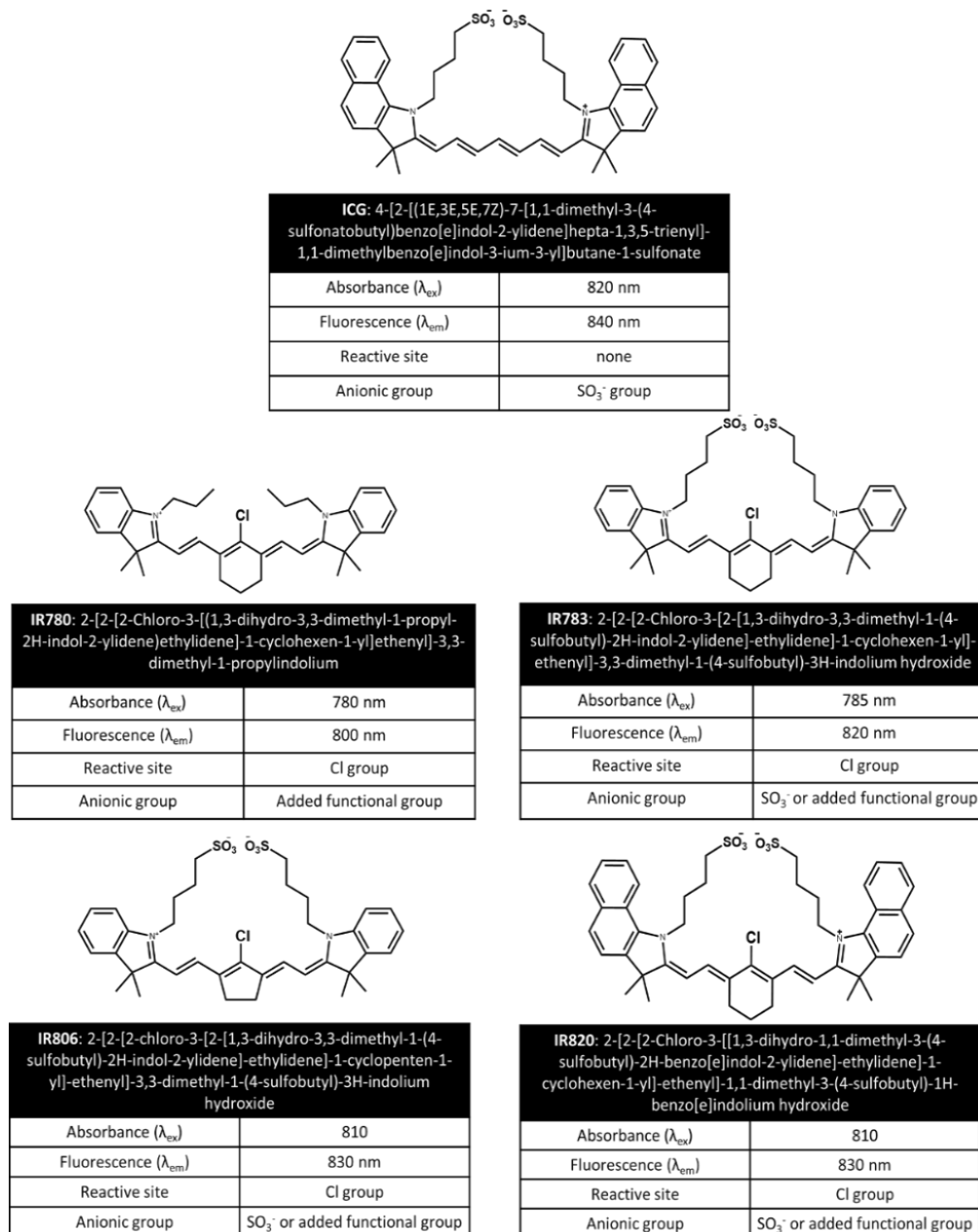


Figure 1.13. Commonly used heptamethine cyanine dyes used for dye-sensitization, with tabulated data on their optical properties, anionic groups and potential reactive sites.

surface of fluoride LnUCNPs.^{102–104} Notably, indocyanine green (ICG), one of the heptamethine cyanine dyes, has been approved by the U.S. Food and Drug Administration (FDA) for NIR fluorescence imaging in clinical ophthalmic retinal and choroidal angiography since the 1970s.¹⁰⁵ However, a major drawback of ICG is its low fluorescence emission efficiency due to ISC, susceptibility to photobleaching, and lack of modification sites.^{106,107}

1.5.2.2 IR820 Dye

One such heptamethine dye that bears a close resemblance to FDA-approved ICG is the IR820 dye. The versatile and widely utilized IR820 plays a significant role in upconversion sensitization. The key reason behind its popularity for dye-sensitized upconversion lies in its absorption band centered at 820 nm, coupled with a broad emission band at 850 nm which extends beyond 1000 nm.^{97,102,107,108} This unique feature ensures a favorable spectral overlap with Yb^{3+} ,⁵¹ resulting in efficient energy transfer. Moreover, the strategically positioned –Cl substituted aryl ring at the core of its heptamethine conjugation grants IR820 adaptability and ease of structural modifications. Modifications at this position enable the fine-tuning of both steric and optical properties, further enhancing the versatility and potential of this dye.¹⁰⁹

1.5.3 Method of Dye Linking

The mechanism of energy transfer, whether radiative or non-radiative (Förster or Dexter), is greatly impacted by the spatial distance between the NIR dye and the lanthanide ion. This distance is influenced by the method of linking, which refers to the various ways in which the dye can be associated with the surface of LnUCNPs. The interface engineering of LnUCNP/dye nanocomposites is a critical aspect that impacts both energy transfer efficiency and the stability of dye-sensitized nanoparticles. This involves considering three primary factors: (i) the binding interaction between the NIR dye and LnUCNP, (ii) the distance between them, and (iii) the spatial distribution of NIR dye molecules across the LnUCNP surface, relative to one another. Hence, it becomes imperative to understand the diverse approaches of dye linking onto the surface of the LnUCNPs.¹¹⁰

1.5.3.1 Electrostatic Method

The electrostatic method of dye linking involves the interaction between the positively charged surface of fluoride LnUCNPs, resulting from the dangling bonds⁴⁶, and NIR dyes containing anionic groups **Figure 1.14a**. This interaction is facilitated by electrostatic forces, allowing for the coordination of the dyes onto the nanoparticle surface. Typically, after the synthesis of ternary

fluoride LnUCNPs, the nanoparticles are coated with oleate or oleylamine ligands on their surface. To facilitate the linking of the dye, these ligands are usually removed through surface modification techniques. This allows the NIR dyes to coordinate directly with the lanthanide ions on the surface and ensures close contact between the dye and hence an efficient energy transfer.¹¹⁰

Generally, when the dye is directly coordinated to the lanthanide ions in the LnUCNP, the energy transfer is primarily non-radiative. The energy transfer can take place either through FRET or through Dexter energy transfer.^{111,112} This approach is straightforward to carry out and is commonly used for investigating energy transfer mechanisms and other optical properties.¹¹⁰ However, despite the potential advantages offered by electrostatic linking methods, there are significant drawbacks that need to be addressed.¹¹⁰ Firstly, the use of electrostatic forces to link NIR dyes to LnUCNPs often results in the dyes being fully exposed to the surrounding environment, which may be oxygen rich. This exposure can lead to issues such as degradation, photobleaching, and reduced stability, limiting the overall performance and longevity of the composite system. For this reason, to protect the NIR dyes specifically from molecular oxygen, dye-sensitization is often carried out in an inert atmosphere.^{111,113} Additionally, the weak nature of the electrostatic interaction can result in detachment of the NIR dyes from the LnUCNPs, leading to a loss of signal. These drawbacks highlight the need for alternative strategies to improve the stability and robustness of NIR dye linked LnUCNP systems, ensuring their reliability and effectiveness in various applications.

1.5.3.2 Encapsulation in Polymers or Mesoporous silica

To construct efficient and reliable nanocomposite comprising NIR dyes and LnUCNPs, encapsulation within a polymer matrix or mesoporous SiO₂ has emerged as the most effective and widely adopted approach.¹¹⁰

Prominent examples of such polymers include distearoylphosphatidylethanolamine-poly(ethylene glycol), Pluronic F127, phosphatidylcholine, and Tween[®]80.^{74,91,114–116} In this encapsulation process, the hydrophobic segments of the amphiphilic polymer interact with the capping ligands of LnUCNPs through hydrophobic interactions, while the hydrophilic segments are oriented towards the outer surface, enabling water dispersibility of the resulting nanocomposites (**Figure 1.14**).^{110,117} Several studies have also reported successful encapsulation of these dyes in a mesoporous silica matrix coated around the LnUCNPs (**Figure 1.14**).^{118, 119,120}

The encapsulation of NIR dyes within a polymer layer on LnUCNPs has shown promise for various applications. However, this approach is not without its drawbacks. Firstly, the interaction between the hydrophilic segments of the polymer and the NIR dye is often weak, leading to suboptimal dye encapsulation. The reliance on weak hydrophilic-hydrophilic interactions can result in inadequate stability and limited control over the encapsulation process. Secondly, the repeated use or exposure of the nanocomposite to harsh conditions can lead to the leaking of the encapsulated dye. This can compromise the performance and reliability of the nanocomposite, diminishing its effectiveness as a probe or sensor.

1.5.3.3 Covalent Linking

Covalent linking of the dye on the surface of the LnUCNPs refers to a chemical bonding process that involves the attachment of the dye molecule to the nanoparticle surface through the formation of strong and stable covalent bonds. This linking requires the presence of a functional group, such as COOH, NH₂, SH, azide, or terminal alkyne etc. on the dye molecule, which serves as the reactive site for the covalent attachment. Since the as-synthesized LnUCNPs do not possess any functional group, they must undergo surface modification with either porous or dense silica or polymer to introduce above mentioned functional groups capable of reacting with the dye molecule. Depending on the functional group on the nanoparticle surface, covalent linking can occur through various mechanisms, such as amide bond formation, disulfide linkage or click reaction, wherein the reactive functional groups on the dye and LnUCNP surface react together, resulting in a robust and stable attachment. This covalent linking strategy ensures a stable and long-lasting association between the dye and nanoparticles, offering enhanced retention and functionality in various applications.^{110,121}

In this type of system, the energy transfer process between the dye and the nanoparticle could be radiative, and this can be justified as follows. When a modified polymer or silica shell is introduced between the dye and the nanoparticle, it effectively creates a physical barrier that increases the distance between them. While this increased separation distance reduces the likelihood of non-radiative energy transfer pathways by protecting the nanoparticle from the external environment, it also reduces the efficiency of interaction between the dye and nanoparticle for the sensitization process (**Figure 1.14**). However, the issue of detachment of the sensitizing dye from the LnUCNP surface is effectively reduced.

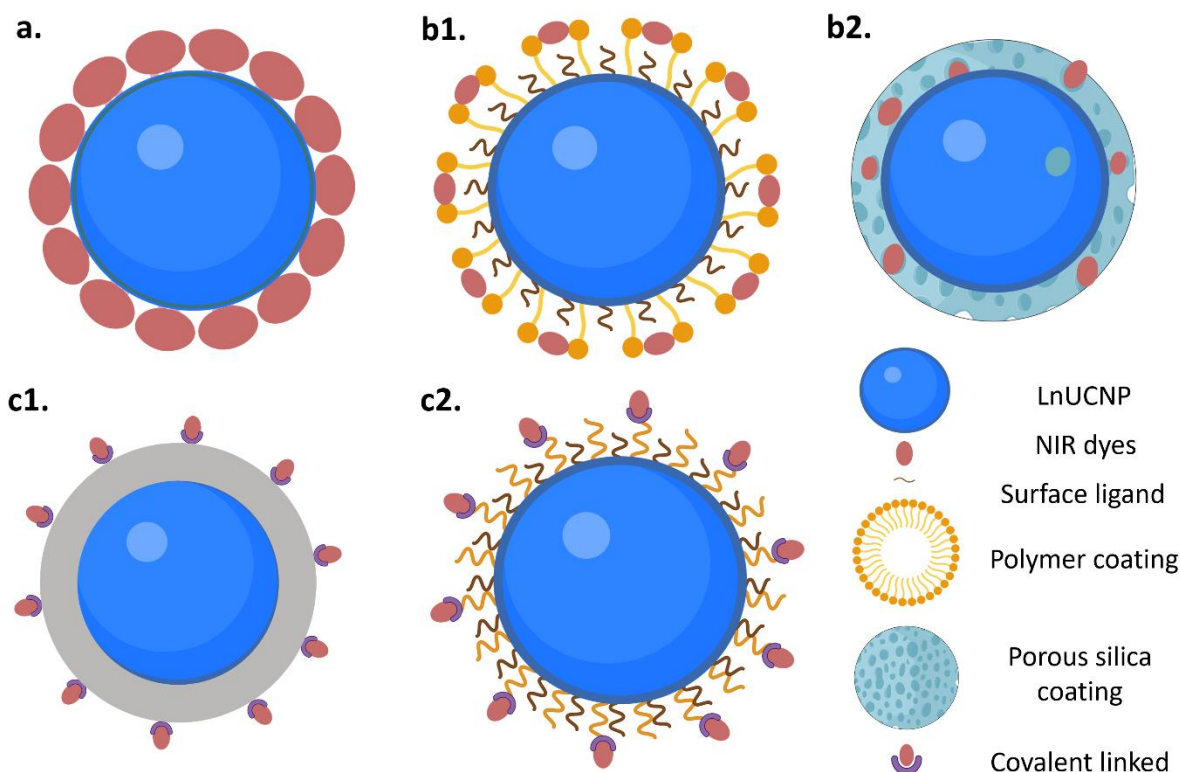


Figure 1.14. Schematic of different methods of dye linking on the surface on LnUCNP (a) Electrostatic method of direct coordination and encapsulation in (b1) polymer (b2) porous silica shell. Covalent linking by means of (c1) a functionalized silica shell and (c2) polymer coating. Created with BioRender

1.5.4 Disadvantages of Dye-sensitization

Although dye sensitization has presented itself as a promising method to enhance the upconversion luminescence of LnUCNPs, there are several challenging issues that need to be addressed before the full potential of dye sensitization can be realized. One major problem is the weak binding interaction between the dye molecules and LnUCNPs in the electrostatic systems, which leads to the low chemical stability of the dye-sensitized system, limiting their use in complex environments.^{110,122} Another major challenge is the low photostability of the dyes used to decorate LnUCNPs.^{46,109,123} Most organic dyes experience photobleaching, a photochemical alteration resulting from the permanent cleavage of covalent bonds in the fluorophores under strong or prolonged irradiation.¹²⁴⁻¹²⁶ Therefore, dye-sensitized LnUCNPs face a major challenge due to the poor photostability of NIR fluorescent dye molecules, which undergo photobleaching upon light exposure.

The degradation primarily occurs through photooxidation pathways, where the excited dye molecules interact molecular oxygen and generate singlet oxygen.¹²⁷ The subsequent reaction between these *in situ* generated singlet oxygen molecules and the NIR dye leads to the loss of sensitization properties.^{123,128,1} Specifically studies show that the photolysis of cyanine-based dyes results in the oxidative cleavage of the methine chain, producing carbonyl products.^{124–126,128}

In a study conducted by Nani *et al.*, they performed mass spectrometry to confirm the photodegradation mechanism of ICG (**Figure 1.15**). The reaction yielded two sets of compounds labeled as 1,2 and 3, 4. High-resolution mass spectrometry (HRMS) was used to analyze the reaction products, confirming oxidative cleavage at specific carbon positions (C₁/C₂ and C₃/C₄). Further investigation of the HRMS spectra showed no evidence of cleavage between other carbon positions or their hydrolysis products, indicating a high level of regioselectivity in the reaction. This confirms that singlet oxygen mediated the formation of dioxetanes as the main pathway in cyanine photooxidation. These findings provide valuable insights into the selective nature of the photooxidative C–C cleavage in heptamethine cyanines, emphasizing the critical role played by singlet oxygen in the formation of compounds 1-4 through the generation of dioxetanes. For all the above-mentioned reasons, the primary focus of the dye-sensitized LnUCNPs should be to improve the photostability of the sensitizing NIR dyes by reducing their reactivity toward O₂.^{124–126}

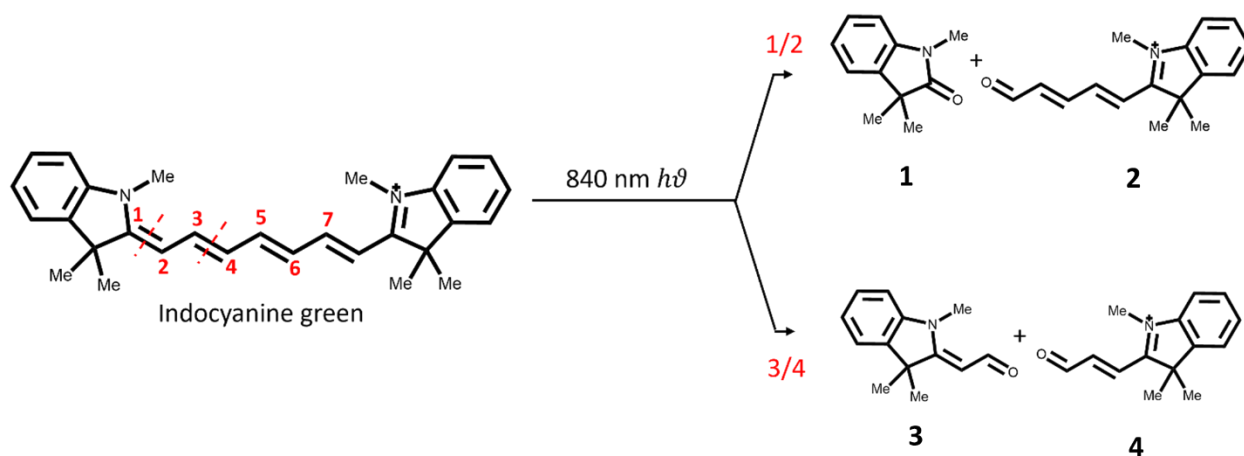


Figure 1.15. Reaction scheme of indocyanine green with possible cleavage sites undergoing photodegradation under 840 nm excitation. The formation of carbonyl compounds was confirmed by HRMS. Figure modified with permission from reference¹²⁶

1.6 State of the Field

Dye-sensitized upconversion was first observed in 2012 by the Hummelen research group. This study aimed to improve the brightness of $\text{NaYF}_4:\text{Er}^{3+}, \text{Yb}^{3+}$ by the antenna effect, using a NIR dye of a high absorption cross-section as previously discussed. In this study, they utilized IR780 and functionalized it with 4-mercaptobenzoic acid to yield carboxylic functionalized IR780, which they referred as IR806. The functionalization provides a carboxylic acid functionality to electrostatically coordinate on the nanoparticle and redshifts the absorption and emission of the dye to achieve greater spectral overlap with the Yb^{3+} sensitizer. The upconversion intensity from IR806-sensitized nanocrystals excited at ~ 800 nm was about 1100 times higher than that from non-dye-sensitized nanocrystals excited at ~ 980 nm. Moreover, considering a broad spectral response range of $\sim 720\text{--}830$ nm for upconversion, the dye-sensitized system exhibited brightness around 3300 times greater than the non-dye-sensitized system.¹¹³ While these values seem large, it is important to remember that the enhancement factors are highly dependent on the method used to calculate them, as discussed below.

This first study, however, did not address the surface quenching effects prevalent in the core-only dye-sensitized nanoparticles and the inefficient overlap between the emission of the dye and the absorption of the Yb^{3+} ion. To this end, the concept of energy cascade was introduced by Chen *et al.* in 2015. This system involves the use of IR783 functionalized with 4-mercaptobenzoic acid, which they referred as IR808 dye electrostatically linked on core/shell ($\text{NaYbF}_4:0.5\%\text{Tm}^{3+}/\text{NaYF}_4:\text{Nd}^{3+}$) nanoparticles, where Nd^{3+} ions act as an additional sensitizer in the shell layer, while Yb^{3+} and Tm^{3+} ions serve as corresponding lanthanide sensitizer and activator ions in the core. As mentioned in **section 1.3.1.2.**, Nd^{3+} can sensitize Yb^{3+} through resonant states. The NIR dye efficiently harvests excitation energy, which is then transferred to the Nd^{3+} ions in the shell layer and sequentially to the Yb^{3+} ions in the core, which can then undergo ETU with activator ion resulting in efficient multiphoton upconversion luminescence. The emission spectrum of IR808 and the absorption spectrum of Nd^{3+} ions incorporated in the shell exhibit significant overlap, allowing for non-radiative energy transfer across the organic/inorganic interface. This is followed by another non-radiative energy transfer process between Nd^{3+} and Yb^{3+} ions from the shell to the core across interface. As a result of this energy transfer, the dye-sensitized core/shell LnUCNPs consisting of ($\text{NaYbF}_4:0.5\%\text{Tm}^{3+}/\text{NaYF}_4:\text{Nd}^{3+}$), demonstrate a luminescence intensity that is approximately 14 times higher than that of the same LnUCNPs without dye sensitization. This

study addressed and improved the spectral mismatch between the dye and Yb³⁺ sensitizer and also minimized surface-related luminescence quenching problems associated with dye-sensitized core-only nanocrystals.⁹² However, the photostability of the dye was never discussed.

Work reported by Wu *et al.* in 2015, showed that highly tunable excitation advantages of NIR dyes had not been utilized in regard to LnUCNP sensitization. They used IR783, IR808, IR820, and IR820 functionalized with 4-mercaptobenzoic acid to yield IR845 having absorption and emission spectra in the ranges of 780-850 nm and 800-920 nm, respectively. Electrostatic coordination of the dye on the surface of NaYF₄: 20% Yb and 2% Er LnUCNPs was performed. Depending on the dye used, they reported 80-100-fold enhancement in emissions with respect to non-sensitized nanoparticles.¹²⁹

Wu *et al.* studied the effect of dye sensitization on inert and active shells coated over β-NaYF₄:20% Yb³⁺,2% Er³⁺ cores. Firstly, they studied the effect of varying thicknesses of β-NaYF₄ inert shells. They observed that as the shell thickness increased, the luminescence intensity of the dye-sensitized LnUCNPs decreased, indicating thicker β-NaYF₄ shell hindered the energy transfer from the dye to the core. However, by introducing Yb³⁺ ions into the shell, they achieved enhanced light emission under 800 nm excitation, confirming the distance between the dye and Yb³⁺ ions plays a crucial role. The dye-sensitized core/Yb³⁺ active shell nanoparticles exhibited approximately 8 times enhanced emission compared to only cores and approximately 70 times higher emission than LnUCNPs with core/inert shell of the same size. Furthermore, the enhancement in emission was approximately 1000 times greater for the IR-806-sensitized core/Yb³⁺ active shell LnUCNPs compared to the native core-Yb³⁺ active shell LnUCNPs without dye modification. While the enhancement factor detailed in the report is notably substantial, it is crucial to highlight that the excitation sources employed for the systems being compared vary. This variance does not establish the appropriate conditions necessary for valid comparative analysis.¹¹⁴

Another important study in 2018 by Shuck *et al.* reported the influence of the heavy atom in the LnUCNP on the spin-orbit coupling of the dye.¹¹¹ The heavy atom effect increases ISC rates between singlet and triplet states of the dye molecule, given by equation 6¹³⁰:

$$ISC \propto Z_{eff}^4 \quad (6)$$

The higher the value of Z_{eff} , the more effective the ISC, leading to a more populated triplet state, this effect plays an important role in photostability of the dye.¹³⁰ In this study, they reported when an organic polymethine dye is linked to the surface of heavy atom doped LnUCNP, such as one doped with Gd^{3+} , the triplet state of the dye becomes more efficiently populated. Because of this, the excited dye emits through phosphorescence at a wavelength that better overlaps with the Yb^{3+} absorption at 980 nm. This work showed that for 20% Yb^{3+} and 2% Er^{3+} doped LnUCNPs, the quantum yield (QY) shows a strong dependence on Gd^{3+} content, with a maximum QY of $5.3 \pm 0.4\%$ using 30% Gd^{3+} ($\lambda_{ex}=808\text{nm}$ at $5\text{W}/\text{cm}^2$). This represents an ~ 100 -fold increase over the same LnUCNPs without IR806 and provides clear evidence that ISC within the dye plays an integral role in LnUCNP sensitization.¹¹¹

The focus of research on dye-sensitized LnUCNPs has primarily been on studying energy transfer mechanisms, However, comparing enhancement values in these systems is challenging due to the lack of standardized methods and reference materials for comparison. Many studies compare newly reported dye-sensitized LnUCNPs to non-sensitized LnUCNPs under 800 nm or 976 nm excitation. Comparisons of dye-sensitized LnUCNPs to native Yb^{3+} -sensitized LnUCNP under 800 nm excitation often yield large enhancement values because the native nanoparticles do not absorb or emit at this excitation wavelength unless Nd^{3+} is used as a sensitizer (which is often not the case in the study). Moreover, the reported QY values are heavily influenced by experimental setups and cannot be easily compared to other reported values. Comparisons between bare LnUCNPs excited at 976 nm and dye-sensitized LnUCNPs excited at 800 nm are also common but present further challenges in interpreting reported improvements.^{114,129,131} Differences in photon flux, wavelength-solvent interactions, uncorrected signals for absorbance and/or scattering, and varying population dynamics during upconversion make meaningful comparisons of enhancement difficult in these scenarios.

As mentioned before, the electrostatic interactions used in the mentioned dye-LnUCNPs system still expose the dye to photodegradation and to detachment issues.¹¹⁰ The limited photostability of NIR dyes makes them unsuitable for applications that require excitation of the system for prolonged durations. Unfortunately, the photostability of NIR dyes with respect to dye-sensitized upconversion has been often overlooked in the myriad of reported dye-LnUCNP systems. Interestingly, some studies using covalent dye-embedded systems based on polymers or

mesoporous-silica materials have been published.^{115,120} This has proven to be an effective method to minimize photodegradation and detachment/leakage issues.

A polymer-based system, an "invisible ink" was created by combining a mixture of IR808-sensitized (NaYbF₄: 0.5%Tm³⁺/NaYF₄:Nd³⁺) core/shell LnUCNPs with a transparent polystyrene polymer. Polystyrene serves to stabilize the IR 808 dye on the surface of the LnUCNPs, act as a host for the luminescent dye-sensitized substance and protects it from environmental factors that may cause photobleaching. The system was reported to be photostable, showing no change in the emission under 5 minutes of continuous 800 nm irradiation, proving its suitability for use in anti-counterfeiting application.⁹²

A nanosystem composed of mesoporous silica-coated dye-sensitized LnUCNPs with the following structure: IR808-sensitized NaGdF₄:Yb³⁺,Er³⁺/NaGdF₄:Yb³⁺/NaNdF₄:Yb³⁺ was created for performing photodynamic therapy and tracked using upconversion, computed tomography, and magnetic resonance imaging techniques. The LnUCNPs have a core/shell/shell structure that enables efficient energy transfer from dye molecules to Yb³⁺/Er³⁺ in the core, resulting in effective green and red upconversion emissions.¹³² However, this study did not explore the photostability of dye-sensitized mesoporous system.

1.7 Photocatalysis

Photocatalysis offers a green solution for the removal of harmful organic compounds from the environment. This method often involves exposing semiconductor materials to a specific light source. As a result, free radicals with potent oxidation properties are generated, which break down organic contaminants into CO₂ and H₂O, among others.⁹ The ability to harness renewable solar energy for environmental remediation through photocatalysis has garnered significant interest. Fujishima and Honda highlighted this potential in 1972 when they observed water splitting on titanium dioxide (TiO₂) photoanodes under UV illumination.¹³³

The mechanism of photocatalysis can be described as the absorption of a photon of wavelength resonant with the band gap of the semiconductor, which generates electron-hole pairs. These created electron-hole pairs can undergo various processes: (i) they can recombine to emit light; (ii) the electrons produced can reduce electron acceptors; or (iii) the generated holes can oxidize electron donors.¹³⁴ Consequently, these generate ROS which could further photodegrade the organic contaminants and transform them into relatively harmless byproducts. This technology offers significant advantages, including cost-effectiveness, environmental friendliness, rapid degradation rates, low toxicity, and the ability to fully mineralize organic contaminants. It holds immense potential for diverse applications such as environmental remediation, water purification, and solar energy conversion.⁹ There has been a growing utilization of nanoscale semiconductor materials such as TiO₂, ZnS, ZnO, Ag₂WO₄, in various applications.¹³⁵

Most of these photocatalysts exhibit a wide band gap of 3.2-3.5 eV and thus are excited in the UV region. However, hematite (α -Fe₂O₃), which is the most stable form of iron oxide under ambient conditions exhibits a narrow band gap ranging from 2.0 to 2.2 eV. It can effectively harness visible light up to 600 nm.¹³⁶ As shown in **Figure 1.16**, upon visible irradiation, it generates electron-hole pair which catalyzes the dissociation of oxidizing agents into ROS through Fenton-type catalysis.¹³⁷

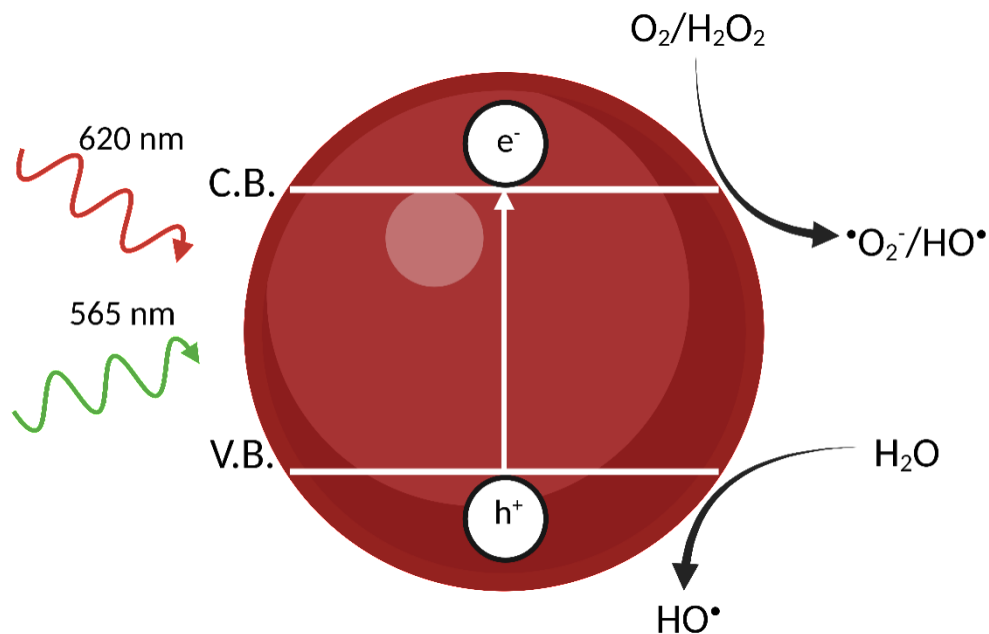


Figure 1.16. α -Fe₂O₃ (hematite) nanoparticle upon excitation at 565 and 620 nm, leading to the generation of electrons and holes in conduction (C.B.) and valence (V.B.) respectively, which subsequently produce superoxide and hydroxide radicals. Created with BioRender

1.7.1. Fenton-type Catalysis

The origins of the Fenton reaction can be traced back to 1894 when H.J.H. Fenton conducted an experiment involving the combination of iron ions and oxidizing agents.^{138–140} During his investigation, Fenton noted that the resulting mixture exhibited a significantly greater oxidative potential compared to the individual components.¹⁴¹ Fenton-type catalysis is widely used in the fields of biochemistry and photocatalysis.^{141,142}

1.7.2. NIR mediated Photocatalysis

TiO₂ and ZnO which are often regarded as highly efficient materials for photocatalysis.^{143–145} They are wide-band semiconductors and can only operate in the high-energy UV region, which represents a small portion, less than 5%, of the solar spectrum.¹⁴⁶ Conversely, the NIR region, which encompasses approximately more than 50% of the solar energy spectrum, can be employed to improve the effectiveness of photocatalysis.^{146,147} LnUCNPs have the potential to address these drawbacks to fulfill these requirements. By merging the benefits of LnUCNPs and the photocatalytic properties of semiconductor nanoparticles, LnUCNPs could potentially function as an intermediary agent to facilitate the use of NIR wavelengths.¹⁴⁸ Composite systems present a unique advantage by permitting excitation under various wavelengths. Not only can LnUCNPs be

excited in the NIR region to produce upconverted emissions in the UV, visible, and NIR – which can then sensitize the semiconducting photocatalyst to produce ROS – but the semiconductor itself can also be directly excited in the UV or visible region.

To harness the full potential of solar energy, researchers have been exploring innovative ways to enhance the light-harvesting efficiency of photocatalysts. This began with Qin *et al.*, who introduced a pioneering approach by utilizing $\text{YF}_3:\text{Yb}^{3+},\text{Tm}^{3+}/\text{TiO}_2$ core/shell nanoparticles. This synthesis used a modified hydrolysis method, resulting in uniform TiO_2 shells on the LnUCNPs. The decomposition of methylene blue under NIR irradiation exemplified the remarkable photocatalytic activity of these nanoparticles.¹⁴⁹ These findings not only showcased the potential of this structure for advanced photocatalyst modifications but also illuminated the prospects of harnessing NIR energy from sunlight, which could revolutionize the utility rate of solar energy for photochemical applications. Qi and Zhong's group further advanced the application of LnUCNPs by synthesizing a novel nanocomposite comprising upconverting material ($\text{YF}_3:\text{Yb}^{3+},\text{Tm}^{3+}$), TiO_2 , and graphene.¹⁵⁰ This composite showcased a vastly improved photocatalytic activity under sunlight as compared to the individual components.

However, the existing nanocomposite systems that integrate LnUCNPs or lanthanide ions with semiconductors have a major drawback associated with the limited upconversion efficiency of LnUCNPs. This inherently results in less efficient photocatalytic capability than directly exciting the semiconducting nanoparticles.⁹

1.8 Statement of Problem

Dye-sensitization is a technique that is frequently employed to make LnUCNPs more efficient by increasing the light absorption cross-section of the lanthanide ions by taking advantage of the antenna effect, which in turn enhances the overall upconversion process. This approach has been proven to be highly effective in improving the luminescence properties of LnUCNPs.

However, one significant drawback of dye-sensitized upconversion is the poor photostability of NIR dyes. The lack of photostability makes them unsuitable for applications that require prolonged excitation, as the benefits obtained from dye sensitization in terms of luminescence intensity are limited to a short period before the degradation of the dye. Unfortunately, the issue of photostability of NIR dyes has often been overlooked in the multitude of reported dye-LnUCNP systems. This scarcity of photodegradation studies makes it difficult to assess the efficiency of one reported dye-LnUCNP system compared to another and whether these systems are suitable for prolonged irradiation times. Additionally, despite numerous demonstrated dye-sensitized systems, there is no clear convention for reporting the improvements achieved by new dye-LnUCNP systems in terms of luminescence enhancement.

Therefore, to improve the limited photostability of NIR dyes, they are functionalized with sterically bulky groups in order to hinder the formation of the dioxetane intermediate, which is responsible for the dissociation of the sensitizing dye into carbonyl compounds. Although this approach extends the duration for which dye could be irradiated, it is still photostable for a limited period of time. As of now, the most common method for the linking of NIR dye molecules is through electrostatic coordination onto the surface of LnUCNPs^{92,111,113,129,131,151,152} or by encapsulation within mesoporous silica.^{120,153} However, both these approaches have the disadvantage of the dye molecules becoming exposed to atmospheric oxygen, leading to the subsequent *in situ* formation of deleterious singlet oxygen upon prolonged NIR irradiation. A promising avenue to further improve the photostability of the dye-sensitized system is through the coordination of the dye. Covalent embedding of NIR dyes into a silica framework has proven to be an effective method to overcome their limited photostability. NIR dyes are usually functionalized with various siloxane precursors and subsequently embedded into silica nanoparticles.⁶⁹⁻⁷⁶ The incorporation of the NIR dyes could be done by means of physical entrapment as well, but covalent encapsulation is preferred as it minimizes the leaching of the dye.^{77,78} This method is versatile enough to allow for different dyes to be incorporated.⁶⁹ This

method not only prevents the dye from forming the deleterious intermediate, but also relieves the detachment of the dye from the nanoparticle surface. While this is a well-established method to generate fluorescent silica nanoparticles embedded with dye with high photostability, this has not been studied for sensitizing the LnUCNPs.

1.9 Project Objectives

The objective of this thesis encompasses several aspects. Firstly, we investigated the role of singlet oxygen in the photodegradation of the IR820 dye and establishes a baseline for evaluating potential improvements through structural modifications to the dye to improve the photostability of the dye-sensitized LnUCNPs. This involved studying the photodegradation of IR820 under different conditions, such as varying atmospheres, solvents, and in the presence of singlet oxygen quenchers, in order to confirm the involvement of singlet oxygen in the degradation process.

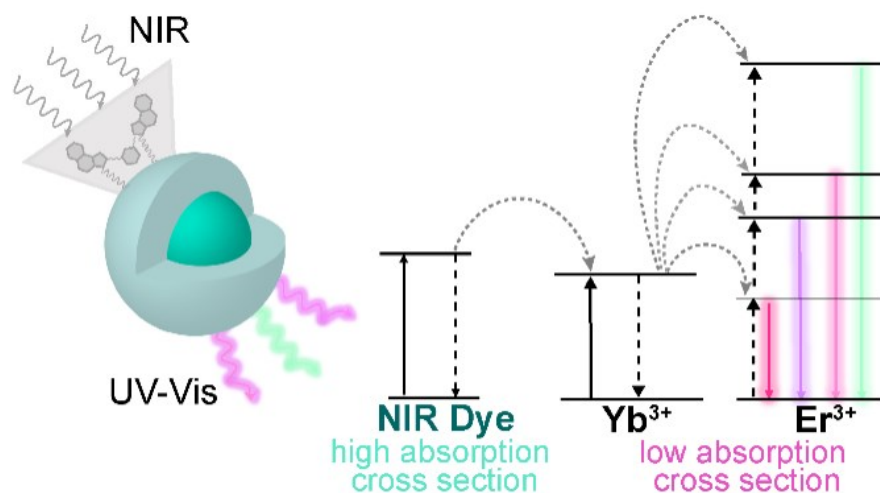
The second objective was to improve the photostability of the IR820 dye by preventing its reaction with singlet oxygen. This was achieved by modifying the -Cl group of the central aryl ring with various para-substituted phenylthioether groups having different electronegativities. The photostability of each modified dye was then assessed under 808 nm excitation. The effectiveness of these modified dyes for upconversion sensitization was evaluated using core/shell upconverting nanoparticles with a β -NaGdF₄: (2%) Er³⁺, (20%) Yb³⁺/NaGdF₄: (20%) Yb³⁺ architecture. Comparative kinetic studies were carried out on modified-IR820 sensitized NaYF₄: (2%) Er³⁺, (20%) Yb³⁺ and β -NaGdF₄: (2%) Er³⁺, (20%) Yb³⁺ to confirm potential occurrence of the heavy atom effect. Furthermore, luminescence lifetimes were analyzed to confirm the evidence of back-transfer from the nanoparticles to the coordinated dye molecules.

With this work, we also explored the covalent linking of IR820 dye to the LnUCNPs as a mode to enhance the photostability of the dye-sensitized system. To achieve this, IR820-COOH was covalently embedded in the silica shell around the NaGdF₄:Er³⁺, Yb³⁺/NaGdF₄:Yb³⁺ core/shell LnUCNPs. This was achieved by functionalizing IR820-COOH with aminopropyltrimethoxysilane (APTMS). The photostability and effectiveness of this new system were evaluated through spectroscopic comparisons with electrostatically and covalently linked dye systems in which IR820-COOH is covalently linked to amine-functionalized silica-coated LnUCNPs *via* an amide bond. A comparison of the optimum dye concentration, emission intensity, and photostability under NIR excitation confirmed the superiority of the embedded dye system.

QY measurements and luminescence lifetimes were conducted to compare the optimized dye-embedded system with similarly sized Nd³⁺-doped core/shell nanoparticles, which are commonly used as an alternative for 808 nm-sensitized upconversion systems. This study enabled a comparison of these two popular routes to 808-nm sensitized upconversion.

Finally, in this work, for the first time, we applied the optimized dye-embedded system for NIR-based dye-sensitized Fenton-type photocatalysis. For this purpose, a wide-pore silica shell was synthesized around the dye-embedded system, and various amounts of hematite nanoparticles were introduced into the pores. The nanocomposite displayed the great potential of a photocatalyst, as it degraded Rhodamine B, a known carcinogen and water pollutant discharged from textile industries.

Chapter 2: On the photostability and luminescence of dye-sensitized upconverting nanoparticles using modified IR820 dyes



Graphical Abstract: For dye-sensitized lanthanide upconverting nanoparticles

Abstract: Dye sensitization is a promising route to enhance luminescence from LnUCNPs by improving the photon harvesting capability of LnUCNPs through the use of dye molecules, characterized by higher absorption coefficients. The literature does not fully address the poor photostability of NIR dyes, hindering solution-based applications. The improvements achieved by dye-sensitized LnUCNPs are usually obtained by comparison with non-dye-sensitized LnUCNPs. This comparison results in exciting the LnUCNPs at different wavelengths with respect to the dye-sensitized LnUCNPs or at the same wavelengths, where, however, the non-dye-sensitized LnUCNPs do not absorb. Both these comparisons are hardly conclusive for quantification of the improvements achieved by dye sensitization. Both shortcomings were addressed by studying the photodegradation *via* thorough spectroscopic evaluations of a 4-nitrothiophenol-modified and unmodified IR820-LnUCNP system. The modified IR820 dye system exhibits a 200% enhancement in the emission of NaGdF₄:Er³⁺,Yb³⁺/NaGdF₄:Yb³⁺ nanoparticles relative to the unmodified IR820-sensitized LnUCNPs and emits for over twice the duration, demonstrating a substantial improvement over previous dye-LnUCNP systems. Upconversion dynamics between the dyes and Er³⁺ establish the importance of back-transfer dynamics in modulating the dye-LnUCNP luminescence. QY measurements further illustrate the mechanism of sensitization and increased efficiency of this new nanosystem.

2.1 Introduction

Upconversion is an anti-Stokes process in which the successive absorption of two or more low-energy photons results in the production of higher energy emissions. The long-lived intermediate energy states of some lanthanides enable them to emit in the UV, visible or NIR region when excited with NIR radiation, which makes them an ideal candidate for generating upconverting nanoparticles. LnUCNPs have narrow absorption and emission bands, high chemical stability, and are non-blinking and low toxicity nanomaterials.^{15,29,154,155}

Despite the promising properties of LnUCNPs, their practical applicability is still limited due to their low upconversion efficiencies. This drawback is, in part, caused by the low absorption cross-section of lanthanide sensitizer ions (on the order of 10^{-20} cm² in the NIR), usually based on the use of Yb³⁺ as a sensitizer.¹⁵⁶ Furthermore, Yb³⁺ is excited at 976 nm, which can cause significant heating of aqueous media. In contrast, Nd³⁺ has been used as a sensitizer and has a narrow absorbance band at 800 nm, which does not induce heating of water, however it has a low absorption cross-section at 976 nm.¹⁵⁷ Several structural manipulations have been studied to improve upconversion luminescence, such as controlling the crystal phase of the host lattice, tailoring the local crystal fields around lanthanide dopants or adopting core/shell structures, which can enhance upconversion luminescence by 10 to 20 times.^{77,85,158} In 1942, Weissman proposed to overcome the inherent low absorption cross-section of the lanthanides by encapsulating the lanthanide ion with a suitable organic ligand to harvest the light, which allows for an indirect excitation of the lanthanide ion *via* energy transfer.⁸⁶ In the early 1990s, lanthanide complexes were investigated as luminescent materials, and Lehn proposed that such complexes could be perceived as light conversion molecular devices and coined the term antenna effect.⁸⁷ This term denotes the absorption, the energy transfer and the emission sequence involving the ligand and the emitting lanthanide ion, thus surmounting the low absorption cross-section of the lanthanide ions. These concepts proposed by Weissman and Lehn form the basis for the concept of dye-sensitized upconversion for LnUCNPs.

Since 2012, several studies have proven the advantages in the use of dye sensitization for enhancing upconversion luminescence.^{92,113,129,131,151} According to this method, an organic NIR-emitting dye with a high absorption cross-section (on the order of 10^{-16} to 10^{-17} cm²)⁹² is coordinated to the nanoparticle surface, and the dye molecules act as an antenna to harvest the incoming radiation and transfer it to lanthanide sensitizer ions, after which upconversion

luminescence is observed.^{111,113,129,131} Apart from brighter upconversion luminescence, NIR dye-sensitized LnUCNPs can also be excited in the region of 780–830 nm, depending on the absorbance of the NIR dye used, in contrast to conventional Yb³⁺-doped LnUCNPs (excited at 976 nm), resulting in broadband absorption of LnUCNPs at different wavelengths.^{91,152}

In spite of the attractive nature of this approach, low photostability is a major drawback associated with the use of NIR dyes.^{46,109,123} The lack of photostability makes them unsuitable for applications which require excitation of the system for prolonged times, as the benefits obtained from dye sensitization, in terms of luminescence intensity, are restricted to the short period of time prior to the degradation of the dye. Unfortunately, the photostability of NIR dyes with respect to dye-sensitized upconversion has often been overlooked in the myriad of reported dye–LnUCNP systems.¹²² Because the drawback of photostability is rarely acknowledged, the practical applicability of these systems is at a disadvantage since there is a lack of knowledge of the duration for which these systems are effective. Additionally, despite the myriad of demonstrated dye-sensitized systems, there is no clear convention for reporting the improvements made by new dye–LnUCNP systems with respect to luminescence enhancement and again, photodegradation studies are lacking. Thus, it is difficult to gauge how efficient one reported dye–LnUCNP system is versus another and whether or not the systems are useful for prolonged irradiation times. Consequently, it is of the utmost importance to both properly study the photostability of NIR dyes and thoroughly investigate their dynamics upon coordination to the LnUCNPs. These studies are necessary in order to report a meaningful enhancement relative to previously reported systems, such that practical applicability can be realized and even greater improvements can be made.

IR820 is commercially available and is commonly utilized for upconversion sensitization.^{92,129,131} This dye belongs to the cyanine family, well-known for having high absorption cross-sections and low photostability.¹⁵⁹ IR820 is utilized because it exhibits good spectral overlap with Yb³⁺, facilitating energy transfer when excited at 800 nm.¹²⁹ Additionally, IR820 has a –Cl substituted aryl ring situated at the center of the heptamethine conjugation, allowing for versatile and facile structural modifications that can be used to modulate the steric and optical properties of the dye.^{91,92,113}

The structure of the dye also makes it attractive for use with LnUCNPs, owing to the pendant sulfonate moieties, which are crucial for obtaining strong electrostatic interactions to the

positively-charged surface of unfunctionalized fluoride nanoparticles.¹⁶⁰ It is well-established that the heptamethine conjugation of cyanine dyes can enhance the lifetime of the dye's triplet state when in the presence of a heavy atom such as Gd^{3+} . This phenomenon is known as the heavy atom effect and has been studied as early as 1949 by McClure *et al.*^{111,161} The enhancement of the lifetime of the triplet state is also known to be deleterious to the photostability of the dyes, as it results in an increased production of singlet oxygen, which is implicated in the photodecomposition of the dyes.^{111,128} Fortunately, the pendant sulfonate groups of IR820 can be used to anchor the dye to the LnUCNPs, without any electronic contribution to the heptamethine conjugation, hence avoiding the deleterious enhancement of the triplet state lifetime. Thus, these functional groups help to avoid the heavy atom effect and make these dyes applicable for different LnUCNP compositions, useful in situations where heavy atoms like Gd^{3+} may not be an option.

The photodegradation of NIR dyes occurs *via in situ* production of singlet oxygen, which further diffuses and reacts with the unsaturated bonds in the molecule. The use of dye-sensitized LnUCNPs embedded into a solid matrix, such as a polymer, has been proposed in order to prevent photodegradation that occurs at a greater rate in solution, owing to the increased diffusion efficiency of singlet oxygen in less-viscous media.¹⁶² Thus, currently reported systems are limited to solid-phase applications.^{74,114} Strategies aimed at preventing the degradation of cyanine dyes *via* structural modifications that sterically hinder the formation of deleterious dioxetane intermediates^{109,123,127} have shown great promise in enhancing their stability.

In this study, we proposed for the first time a structural modification of the IR820 dye with a sterically hindering 4-nitrothiophenol group (IR820- NO_2) onto the central aryl ring, with improved photostability and greater spectral overlap with Yb^{3+} . We also report the comparison of enhancement in emissions and QYs of $NaGdF_4:Er^{3+},Yb^{3+}/NaGdF_4:Yb^{3+}$ functionalized with modified and unmodified IR820, both excited at 808 nm. The functionalization of IR820 imparts resistance to photoinduced degradation, as proven by spectroscopic evaluation of the photodegradation dynamics. The enhancement of upconversion luminescence and photostability by using the modified NIR dye with LnUCNPs was demonstrated by linking the dye onto the surface of oleate-free $NaGdF_4:Er^{3+},Yb^{3+}/NaGdF_4:Yb^{3+}$ core/shell nanoparticles and recording the temporal evolution of their upconversion luminescence spectra. As the linking of the modified and unmodified IR820 dye is accomplished *via* the sulfonate pendants, we investigate the potential for

the heavy atom effect in Gd³⁺ and Y³⁺-based core/shell nanoparticle systems. A comprehensive study of the luminescence lifetimes provides further evidence of back-transfer from the LnUCNPs to the coordinated dye molecules. The proposed approach is the first, to our knowledge, to address the limitations in applicability of dye-sensitized LnUCNPs in the solution phase. The achieved prolonged stability and increased upconversion luminescence intensity and QYs demonstrate significant improvements toward practical utilization of dye-sensitized upconverting nanoparticles for solution-based applications or when embedded into a matrix.

2.2 Experimental Section

2.2.1 Material

Reagents. All reagents were used without further purification. Gd₂O₃ (99.999%), Yb₂O₃ (99.999%), Y₂O₃ (99.999%) and Er₂O₃ (99.999%) were purchased from Chemicals 101 Corp. Sodium trifluoroacetate (98%) and 4-(trifluoromethyl)thiophenol (97%) were purchased from Alfa Aesar. Oleic Acid (90%), 1-octadecene (90%), IR820 (80%), 4-mercaptobenzoic acid (99%), 4-nitrothiophenol (80%), 4-methylbenzenethiol (98%) and sodium azide (99.5%) were purchased from Sigma Aldrich. HCl (trace metal grade, 99.999%) was purchased from Fisher Scientific. Transmission electron microscopy grids (FCF300-CU) were purchased from Electron Microscopy Sciences Inc. For MALDI-MS analysis, 2,5-dihydroxybenzoic acid (DHB), was purchased from Sigma-Aldrich and used without further purification. Liquid chromatography grade solvents were purchased from VWR. ESI-MS low concentration tuning mix was purchased from Agilent Technologies.

2.2.2 Instrumentation and Method

2.2.2.1 Upconversion emission spectroscopy

Upconversion emission spectroscopy was performed using a SLOC Model IRM800T3-2500FC 808 nm infrared diode laser, operating at 2.5 W/cm² or 4.2 W/cm² as an excitation source. Emission spectra were recorded using a Princeton-Teledyne Instruments FERGIE BRXVR UV-NIR spectrograph equipped with a 250 grooves per mm grating blazed at 550 nm coupled to a 1 m 600 micron fiber (Ocean Optics) for detection, with an integration time of 2 seconds and a slit width of 25 microns. All spectra were recorded using a 450–750 nm band pass filter from Thorlabs placed between the sample and the optical fiber. Near-infrared emission spectroscopy of the modified and unmodified IR820 dyes was performed using a Spectral Products DK240 ¼ m monochromator with a 600 grooves per mm grating blazed at 1200 nm, and a slit width of 250 µm. The

monochromator was coupled to a Spectral Products AD131 silicon detector module. Emissions were detected perpendicular to the excitation source.

2.2.2.2 Lifetime measurements

Powder samples of LnUCNPs were excited using pulsed 976 nm excitation (Coherent 6-pin 15 fiber-coupled F6 series laser diode with a powder density of about 1.5 W/cm²) for upconversion lifetime measurements. The resulting emissions were dispersed using a Jarrell-Ash Czerny–Turner 25-102 1 m double monochromator (1180 grooves per mm) coupled to a cooled Hamamatsu R943-02 photomultiplier tube. Signals were processed through an SR440 Stanford Research Systems preamplifier and interpreted using an SR400 Stanford Research Systems gated photon counter, where the gate was varied to observe the emissions as a function of time.

2.2.2.3 Quantum Yield measurements

Colloidal solutions of IR820-LnUCNPs, IR820–NO₂-LnUCNPs, and undoped NaGdF₄ nanoparticles (10 mg/mL in methanol) were excited using the same 808 nm diode laser used for upconversion luminescence measurements, focused to a power density of ≈200 W/cm². Emissions were collected in an Avantes AvaSphere-30-REFL integrating sphere, fiber-coupled to a Thorlabs FOFMS/M-UV Filter Mount fitted with either a 400–750 nm bandpass filter or a 60% neutral density filter to record the emissions and absorptions, respectively. The filter mount was then fiber-coupled to an Avantes AvaSpec-ULS2048L spectrometer. The recorded absorption and emission signals were calibrated using an Avantes AvaLight-DH-CAL-ISP30 NIST calibrated lamp, converting the spectra from arbitrary units to Watts. Intensities were then converted to photons using the photon energy equation. The undoped NaGdF₄ solution, acting as a blank, was subtracted from the upconversion luminescent signals of the dye-functionalized LnUCNPs to provide the number of emitted photons (physical characterization Appendix 5, A5.1). The dye-functionalized LnUCNPs signal at 808 nm was subtracted from the blank solution to provide the number of absorbed photons. The quantum yield was then calculated by dividing the number of emitted photons by the number of absorbed photons.

2.2.2.4 UV-visible absorption spectroscopy

All UV-visible absorption spectra were collected on a Cary 5000 series UV-vis-NIR spectrophotometer from Agilent Technologies. Solutions were analyzed in a 1 cm path length quartz cuvette from Thorlabs. All ¹H-NMR spectra were recorded on a 500 MHz Varian Scientific NMR spectrometer at 25 °C in DMSO-d₆.

2.2.2.5 Powder X-ray diffraction

PXRD data was collected on a Scintag XDS-2000 diffractometer equipped with a Si(Li) Peltier-cooled solid state detector, Cu K α source operating at a power of 45 kV and 40 mA. The 2 θ scan range was set from 10–60° with a scanning step size of 0.01° and integration time of 2 s.

2.2.2.6 Transmission electron microscopy

TEM was performed using at 200 kV JEOL JSM2100F microscope. TEM samples were prepared on a 300mesh copper grid (3 mm in diameter) by depositing 10 μ L of 1 mg/mL LnUCNPs dispersed in hexanes. The images obtained were analyzed in ImageJ, a free software courtesy of the National Institutes of Health.

2.2.2.7 Fourier-transform infrared spectroscopy

FTIR was performed on a Nicolet iS50 FTIR spectrometer (Thermo Scientific). The instrument was used in its attenuated total reflectance (ATR) mode. The dried sample was placed against a diamond ATR crystal and the spectra were acquired from 500 to 4000 cm^{-1} with a resolution of 0.8 cm^{-1} and 64 scans.

2.2.2.8 Zeta potential measurements

Zeta potential was performed on a Malvern Zetasizer Nano ZSP at 20 °C.

2.2.2.9 Mass Spectrometry

MALDI-TOF-MS Analyses were performed on a MALDI TOF/TOF Ultraflextreme mass spectrometer equipped with a SmartBeam II Nd:YAG 355 nm laser operating at 2000 Hz, using the medium laser focus setting (Bruker Daltonics, Billerica, MA, USA). Samples were prepared by depositing 1 μ L of the dye solution on a MALDI target (MTP 384 target ground steel BC, Bruker Daltonics). 1 μ L of DHB matrix (20 mg/mL in 50% acetonitrile) was applied on the dried droplet. The data were acquired in positive mode in a mass range of 50–1500 Da. External calibration was carried out using a small molecule homemade mix and known matrix signals. The MALDI MS data were visualized using the FlexAnalysis 3.4 software (Bruker Daltonics). ESI-MS analysis was performed on an AmaZon SL ESI-ITMS (Bruker Daltonics, Billerica, MA, USA). The sample solutions were diluted 1000 \times in DMF prior to injection. The data were acquired in the positive mode in a mass range of 100–2000 Da. The following parameters were used during analysis: capillary: 4500 V, dry gas: 4.0 L min^{-1} , dry temperature: 180°C and flow rate: 4 μ L min^{-1} . MSⁿ was performed using the same MS parameters. External calibration was performed using the ESI tuning mix.

2.2.3 Synthesis of Material

2.2.3.1 Synthesis of β -NaGdF₄:Er³⁺,Yb³⁺/NaGdF₄:Yb³⁺ core/shell upconverting nanoparticles

Synthesis of core/active shell nanoparticles was done by double injection thermal decomposition method, as reported by Capobianco *et al.*⁷² In a typical thermal decomposition method of synthesis, 1.25 mmol lanthanide oxides Ln₂O₃ (78% Gd₂O₃; 20% Yb₂O₃; and 2% Er₂O₃ of mol%) reacted with 10 mL equal volume of CF₃COOH (5 mL) and distilled water (5 mL), this was refluxed at 80°C to get clear solution, and then was slowly evaporated at 60 °C to form dry Ln(CF₃COO)₃ precursors. The core nanoparticles of NaGdF₄:Er³⁺,Yb³⁺ are formed by decomposing the corresponding Ln(CF₃COO)₃ at 310°C for 60 min in a mixture of oleic acid and octadecene. Firstly, in a three-neck flask 12.5 mL of oleic acid and 12.5 mL of octadecene were degassed at 120 °C for 30 minutes. Meanwhile, in a separate flask, Ln(CF₃COO)₃ (Lanthanide = Gd³⁺, Yb³⁺, Er³⁺) along with 2.5 mmol of CF₃COONa (NaTFA) and 7.5 mL of each oleic acid and octadecene were degassed at 120°C for 30 minutes. The precursor solution was then injected into the solvents at rate of 1.5 mL min⁻¹, then heated to 310°C with a heating at rate of 10 °C min⁻¹. The resultant mixture was then stirred at 300 rpm for 60 min under Ar. To form the core-shell nanoparticles, 1.25 mmol of shell precursors were prepared by the above-mentioned procedure by taking 80% Gd₂O₃ and 20% Yb₂O₃. 2.5 mmol of NaTFA was added to shell precursors along with 2.5 mL of each oleic acid and octadecene, this mixture was degassed at 120 °C for 30 min. The shell precursors were injected at rate of 0.5 mL min⁻¹ to reaction vessel containing the core nanoparticles, keeping the final temperature at 310°C for 45 minutes. After a total of 1 hour 45 minutes, the solution was cooled to room temperature and it was divided in two equal parts. To each of the part 20 mL ethanol was added and was centrifuged at 3900 rpm for 15 minutes, resulting in white pellet. The resulting pellet was washed 3 times with 1 : 5 v/v mixture of hexane and ethanol and was precipitated by centrifugation.

2.2.3.2 Synthesis of IR820-COOH

Modification of the dye with each substituent was done by a nucleophilic substitution reaction, as reported in the literature.¹⁰⁸ In 5 mL anhydrous DMF, 0.11 mmol of IR820 dye was reacted with 0.58 mmol of 4-mercaptotoluene, under inert atmosphere at room temperature. DMF was evaporated, the resulting crude product was dissolved in dichloromethane and filtered through PTFE syringe filters, and the product was precipitated with anhydrous diethyl ether.

2.2.3.3 Oleate removal of core/shell nanoparticles

The oleate capping ligand from the surface of core/shell nanoparticles was removed by acid treatment, a well reported method from the literature.¹⁶³ In this method, 20 mg of oleate capped LnUCNPs were dispersed in 5 mL hexanes. 5 mL of pH 2 water (using HCl) was added to it and stirred for 2 hours. After 2 hours, nanoparticles were dispersed in water, 10 mL of acetone was added to precipitate the particles. The resulting dispersion was centrifuged at 12 000 rpm for 20 min and the pellet was collected and stored in ethanol.

2.2.3.4 Coordination of IR820 and IR820-NO₂ dyes to the LnUCNPs surface

10 mg of oleate free core/shell nanoparticles were dispersed in 1 mL methanol. 8, 12, 16 and 20 μ M of IR820/IR820-NO₂ solutions made in methanol were added to the 10 mg/mL nanoparticle solution. The resulting mixture was stirred for 12 hours in the dark. Nanoparticles coordinated with dye were precipitated by centrifuging at 10 000 rpm for 15 min. The pellet was washed with ethanol 3 times and kept for drying overnight for FT-IR and UV-vis calibration studies.

2.3 Results and Discussion

2.3.1 Effects of structural modifications on the photostability of IR820 dye

Singlet oxygen is a highly reactive species which is implicated in the photo-induced degradation of many cyanine dyes.^{109,123,128} However, to our knowledge, this has never been conclusively established for IR820 photodegradation. The photodegradation dynamics of IR820 were studied in order to ascertain the role of singlet oxygen in the decomposition mechanism of the dye, as well as to establish a baseline from which improvements (upon structural modification) could be evaluated. The changes in photostability of IR820 in different atmospheres and solvents, as well as in the presence of sodium azide (a singlet oxygen scavenger), were measured, and confirm the role of singlet oxygen in the photodegradation of the dye. This was evidenced by a decrease in IR820 absorbance (40–95%) within 30 minutes of irradiation under the different reported conditions (**Figure S2.1–S2.3**).

Investigations of the photodegradation products by mass spectrometry illustrate that the degradation of IR820 occurs primarily due to a bimolecular reaction of the heptamethine conjugation with photogenerated singlet oxygen. This is the first time, to our knowledge, that the photodegradation products of IR820 have been reported. As a result of this reaction, a strained dioxetane intermediate is formed, followed by decomposition of the dye into carbonyl compounds (**Figure S2.4** and **Table S2.2**). Therefore, by introducing steric hindrance to the region around the

heptamethine conjugation, the formation of the dioxetane intermediate can be inhibited, reducing the likelihood for photodegradation reactions to occur.¹²⁷

Structural modifications aimed at the inhibition of the bimolecular reaction of the dye with singlet oxygen were investigated as a route to improved photostability of the NIR dye. The –Cl group of the central aryl ring was modified with a variety of para-substituted phenylthioether groups with a range of different electronegativities at the para-position (**Figure 2.1a, S2.5, and S2.6**). The photostability of each modified dye under 808 nm excitation was evaluated. Irradiation time, laser power density and concentration of the functionalized dyes were identical to the photostability studies for IR820 discussed above (**Figure 2.1b**).

Upon comparing the photostability of the different functionalized dyes, the degradation was observed to follow a pseudo-first order reaction, due to the self-generation of singlet oxygen that is dependent on the concentration of dye.¹⁰⁹ IR820–NO₂ was found to be the most photostable, degrading 44% under ambient conditions after 60 min of irradiation, compared to the unmodified IR820, which exhibited 74% degradation and double the rate constant under the same conditions (**Figure S2.7**). In comparison, IR820–CF₃, IR820–COOH, and IR820–CH₃ exhibit decreasing photostability, respectively, with the –CH₃ modified dye exhibiting a 67% degradation (**Figure 2.1b and S2.7**).

The increase in photostability can be attributed to two main properties of the modification. Firstly, the bulkiness of the aromatic thioether group hinders the ability of singlet oxygen to approach the heptamethine conjugation, as previously discussed.^{123,152} Secondly, the strength of the electron withdrawing group at the para-position of the thiophenol alters the electron density within the conjugation, increasing photostability of the dye. Since the –CH₃ substituted thiophenol group is electron-donating, this results in electronic activation of the heptamethine conjugation towards electrophilic reaction with singlet oxygen by increasing the electron density.¹²⁷

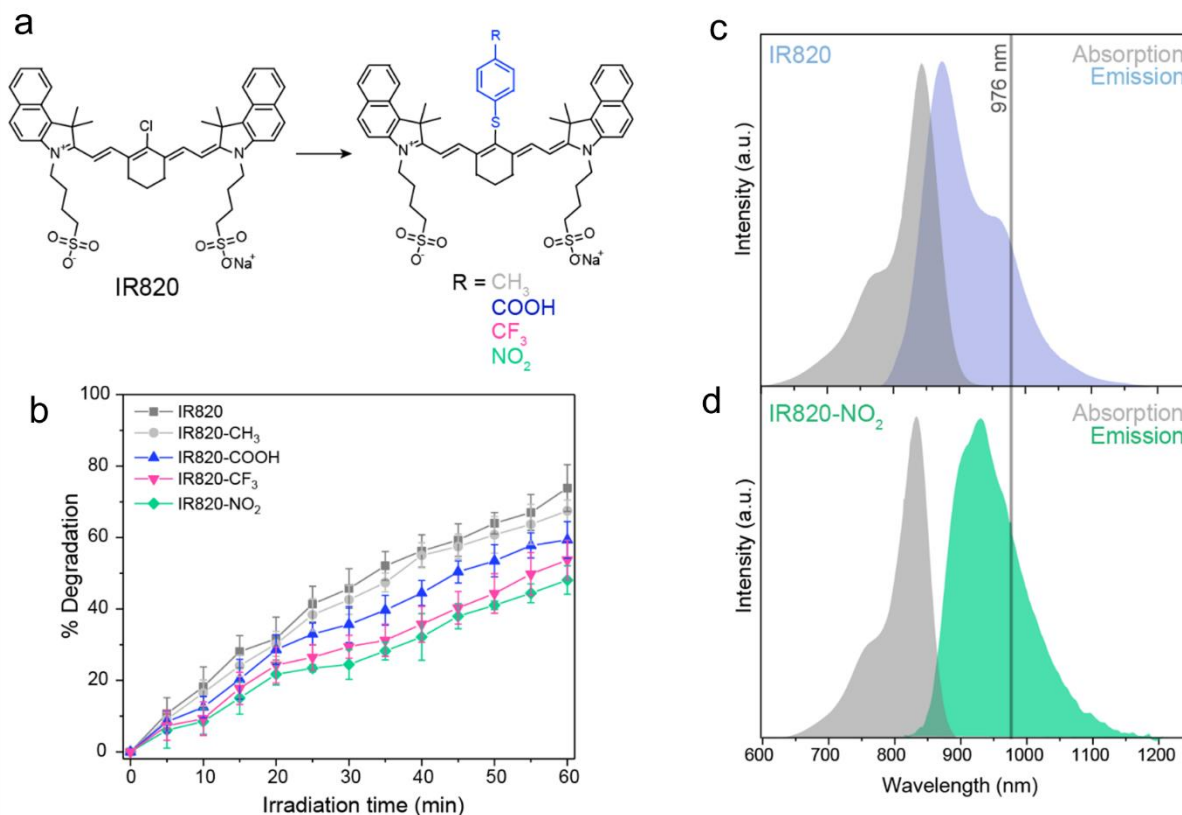


Figure 2.1 (a) Chemical structure of IR820 modified with a thiophenol group and corresponding studied groups placed at the para position. (b) Percentage photodegradation of the IR820 derivatives as a function of irradiation time (808 nm irradiation, 4.5 W/cm²) in methanol. Errors are established based on three repetitions. (c) Absorption (gray) and emission (blue) of IR820 dye in methanol (λ_{max} abs 820 nm, λ_{max} em 849 nm). (d) Absorption (gray) and emission (green) of IR820-NO₂ dye in methanol (λ_{max} abs 837 nm, λ_{max} em 924 nm).

For the CH₃-modified dye, the increased electron density of the conjugation is likely to facilitate the reaction with singlet oxygen in spite of the increased steric hindrance due to the thiophenol group, resulting in the highest degradation percentage among the studied functionalized dyes. Thus, introducing a strong electron withdrawing group at the *para*-position reduces the electron density within the conjugation, thereby reducing the likelihood of an electrophilic reaction with singlet oxygen.¹²⁷ These results illustrate that the combination of steric hindrance and strong electron withdrawing capability of the *para*-substituted group are necessary to improve the photostability of the IR820 dye, with IR820-NO₂ being the most photostable.

After confirming that the modified dyes were all more photostable than native IR820, shifts in the absorption and emission maxima of the modified IR820 dyes were evaluated in order to determine optimal suitability for energy transfer with Yb³⁺. Native IR820 has singlet-state absorption and

emission maxima at 820 and 850 nm, respectively (**Figure 2.1c**), which partially overlaps with Yb^{3+} absorption, between 910 and 1052 nm with a maximum at 976 nm. The functionalized dyes exhibited red shifts in absorbance and emission, which are desirable for increasing the spectral overlap of the singlet state of the dye with the Yb^{3+} sensitizer in the upconverting nanoparticles (**Table S2.3**). The Yb^{3+} sensitizer in $\beta\text{-NaGdF}_4\text{:Yb}^{3+}$, Er^{3+} is known to absorb between 910 nm and 1052 nm, with maximum absorption at 976 nm.⁵¹In particular, substitution with a 4-nitrothiophenol moiety allowed for a particularly good spectral overlap with Yb^{3+} as the emission maximum shifted to 950 nm (λ_{ex} 808 nm) for this functionalized dye (**Figure 2.1d**). Furthermore, it can be postulated that the red shift in the singlet emission band is also likely to mean a red shift occurs in the triplet state emission maxima, further reducing the efficiency of singlet oxygen production due to a mismatch in resonance with the energy gap of singlet oxygen, potentially also contributing to increased photostability. Thus, since IR820–NO₂ had the greatest photostability, and most optimal spectral overlap with Yb^{3+} , it was chosen as the ideal candidate to use for dye-sensitized upconversion.

2.3.2 Spectroscopic Characterization of dye-LnUCNP nanosystems

To evaluate the efficacy of the dyes for upconversion sensitization, $\beta\text{-NaGdF}_4\text{:Er}^{3+}, \text{Yb}^{3+}/\text{NaGdF}_4\text{:Yb}^{3+}$ core/shell upconverting nanoparticles were selected. A core/shell architecture was chosen because of the increased intensity of the Er^{3+} emissions in solution, as compared to the core-only particles, which often suffer from quenching due to interactions of solvent phonons with the nanoparticle surface.^{72,77,154} An “active” shell, containing Yb^{3+} as a sensitizer, was used to allow for non-radiative energy transfer between the dye molecules and the Yb^{3+} ions, which requires close proximity of the involved species to interact. These core/shell nanoparticles were synthesized by a double injection thermal decomposition method.⁷² The as-synthesized nanoparticles were physically characterized by PXRD and TEM (**Figure S2.8**), confirming a hexagonal crystal phase, uniform morphology, and an average nanoparticle size of 35 ± 2 nm.

IR820 and IR820–NO₂ were each coordinated to the nanoparticle surface *via* electrostatic interactions. To ensure a close contact between the dyes and nanoparticle surface to facilitate efficient energy transfer, the oleate capping ligand was removed from the nanoparticle surface.¹⁶³ Removal of the oleate ligand was confirmed by FT-IR (**Figure S2.9a**) and zeta potential (+29.5 mV for oleate-free LnUCNPs, +4.5 mV for dye-coated LnUCNPs). TEM was used to confirm

there was no aggregation post-oleate removal and dye linking (**Figure S2.10a and b**). Confirmation of the dye linking was obtained using FT-IR (**Figure S2.9b**) and subsequent spectroscopy experiments.

Functionalization of the LnUCNP surface with different concentrations of IR820 and IR820–NO₂ was performed in order to determine the optimal number of dyes per nanoparticle for luminescence enhancement with respect to the green Er³⁺ emissions. It is well-established that too high of a concentration of dye molecules can result in self-quenching, whereas too low of a dye concentration will not provide sufficient enhancement of the absorbed NIR light. Consequently, in both cases, the upconversion luminescence would be negatively affected.^{91,92,111,113,129,131} Therefore, upconversion emission spectra of the dye–LnUCNPs were recorded for varied amounts of dye molecules per nanoparticle (**Figure 2.2a**, **Table S2.1**, **Figure S2.11** and **S2.12**). Additionally, the dye-coating was stable for a minimum of 72 hours, with no observed leakage (**Figure S2.13**). Upconversion emission spectra of dye-functionalized LnUCNPs excited at 808 nm exhibit the characteristic Er³⁺ green and red emissions, as shown in **Figure 2.2b**. Green emissions were observed between 510–570 nm and ascribed to the ²H_{11/2}→⁴I_{15/2} and ⁴S_{3/2}→⁴I_{15/2} transitions (centered at 525 and 550 nm, respectively). Red emissions were observed between 630–680 nm from the ⁴F_{9/2}→⁴I_{15/2} transition. To evaluate the difference in intensity of Er³⁺ emissions from IR820 and IR820–NO₂ LnUCNPs with varying amounts of dye/LnUCNP, the Er³⁺ emissions sensitized by IR820 were normalized with respect to the most intense emission of IR820–NO₂ sensitized LnUCNPs (**Figure S2.12**). The emission spectra of the dye-functionalized LnUCNPs at different concentrations of dyes shows that approximately 94 IR820–NO₂ dye molecules/LnUCNP and approximately 99 IR820 dye molecules/LnUCNP constituted the optimum concentrations in each case (**Figure S2.12**). Furthermore, the photostability of the dye–LnUCNP constructs were evaluated using NaYF₄ (physical characterization Appendix 5, A5.2) as a host to evaluate the role of the heavy atom effect in dye degradation. Stabilization of the triplet state through the “heavy atom” effect should influence the emission from the dye-sensitized LnUCNPs if the triplet states overlap with the Yb³⁺ sensitizer ions. No contribution from the heavy atom effect was observed, as Y³⁺ is not considered a “heavy atom” and no change in upconversion luminescence was observed as a function of a change in host composition (**Figure S2.14**). This confirms the energy transfer occurs from the singlet state of the dye to Yb³⁺, as there is no spectral overlap of Yb³⁺ with the triplet state of the dye. As previously discussed, this is due to the alkyl chain length of the

pendant sulfonate moieties on the dye, which are used to conjugate the IR820–NO₂ to the LnUCNP surface. This is important, as it allows for versatile utilization of this photostable NIR dye with different LnUCNP compositions.

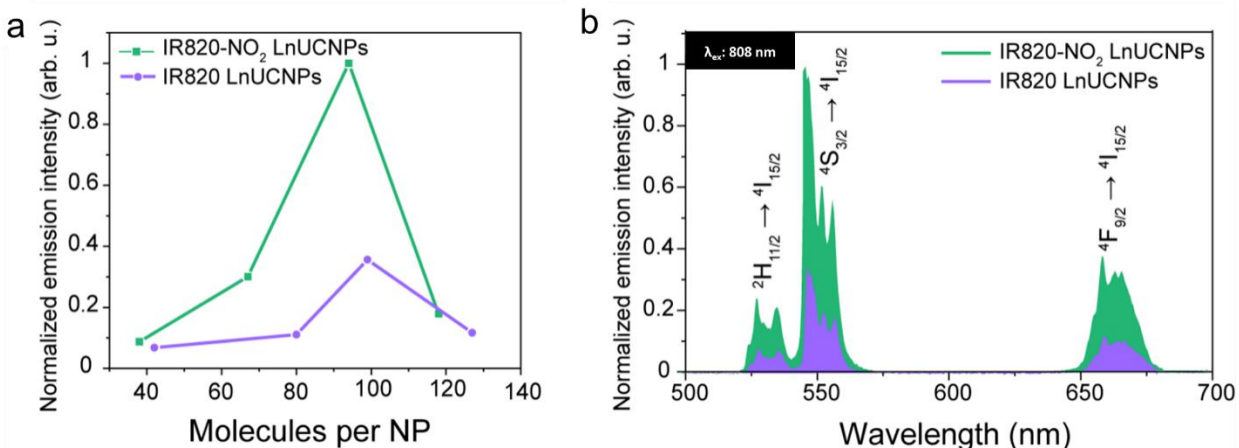


Figure 2.2 (a) Integrated emission intensities of the $4S_{3/2} \rightarrow 4I_{15/2}$ transition of colloidal dispersions of IR820–NO₂-LnUCNPs (green) and IR820-LnUCNPs (blue) as a function of the number of dye molecules per nanoparticle. (b) Upconversion emission spectra of IR820–NO₂-LnUCNPs and IR820-LnUCNPs (blue) with the optimum number of dye molecules per nanoparticle.

In order to assess the improvement imparted by the structural modification of IR820 upon 808 nm excitation, the enhancement of the upconversion luminescence had to be carefully analyzed, as the literature on dye-sensitized upconversion exhibits no standard methods of reporting enhancement values or a standard material/circumstance for which the enhancement values are compared to. It is especially difficult to compare improvements in newly reported dye-sensitized LnUCNP systems because many of them are evaluated with respect to the emissions of the non-sensitized LnUCNPs either upon 808 nm or 976 nm excitation.^{114,129,131} In the case of comparisons to LnUCNP emissions upon 808 nm, large enhancement values are reported since the native nanoparticles do not absorb (and therefore do not emit) at this excitation wavelength, unless Nd³⁺ is used as a sensitizer. Calculation of enhancement factors based on this method were carried out using the nanoparticles from this work, and a 3100-times enhancement was demonstrated (**Figure S2.15a**). This value is strongly influenced by the experimental setup, making it impossible to compare to other obtained values and easily manipulated by changing the recording parameters such as the integration time of the luminescence signal, underscoring the difficulty in comparing

to other systems. Comparison of bare LnUCNPs excited at 976 nm and dye–LnUCNPs excited at 808 nm are also commonly made in the literature, however, the reported improvements are even more difficult to contextualize under these conditions since, even under the same power densities of the different excitation wavelengths, the photon flux differs and the wavelengths interact with solvents differently in terms of transmittance and refraction, and signal are often not corrected for the relative absorbance at each wavelength. As a result of the differing photon flux, the QY of the system will vary drastically, making it virtually impossible to make a meaningful comparison between the two scenarios in terms of enhancement. More importantly, the population dynamics during upconversion when exciting at these two different wavelengths will differ. Upon 976 nm excitation of bare LnUCNPs, direct excitation of Yb^{3+} and energy transfer to Er^{3+} occurs, while upon 808 nm excitation of the dye-coated LnUCNPs, an indirect, two-step excitation must occur through the dye, then Yb^{3+} before exciting Er^{3+} . Despite this, the comparison was made to illustrate the “practical” difference between the dye-sensitized emissions upon 808 nm excitation, and Yb^{3+} -sensitized emissions upon 976 nm excitation, at the same power densities, from which a 1.7-times increase in the luminescence was observed for the IR820–NO₂ LnUCNPs (**Figure S2.15b**).

For the above-mentioned reasons, comparison between a previously established dye–LnUCNP system and the new dye–LnUCNP system reported herein allows for a clear evaluation of the improvements made to the field of dye-sensitized LnUCNPs since excitation dynamics are identical in both scenarios. The emission spectra of IR820-functionalized LnUCNPs and IR820–NO₂-functionalized LnUCNPs at their optimum loadings were compared by evaluating the integrated emission intensities over the entire visible region (400–750 nm). As shown in **Figure 2.2b**, the IR820–NO₂-functionalized LnUCNPs exhibit 200% enhancement in Er^{3+} emissions relative to the intensity of the IR820-functionalized LnUCNPs. Therefore, this result represents an enhancement over the baseline dye-sensitized upconversion system (IR820-LnUCNPs), indicating that significant and measurable progress has been demonstrated here in improving the luminescence of dye-sensitized upconversion nanosystems with respect to the commonly used IR820 dye.

In addition to observing enhanced luminescence from the IR820–NO₂ LnUCNPs upon 808 nm excitation, we also evaluated the dynamics of the dye-coated nanoparticles upon 976 nm excitation to establish the potential for deleterious back-transfer from Er³⁺ to the dye, resulting in luminescence quenching. The broad nature of the absorbance bands of organic dyes makes it likely that most currently employed dye–LnUCNP systems involving Er³⁺ have the potential for deleterious back-transfer processes. While this is likely the case for the majority of current dye–LnUCNP systems, to our knowledge, it has been seldomly explored or reported. By exciting the particles at 976 nm, the dye molecules are not expected to contribute to the population of the emitting states of Er³⁺. Contrarily, it provides insights into the dynamics of the depopulation of Er³⁺ in presence of the dye molecules, as both dyes have absorption bands that overlap with the Er³⁺ ⁴F_{9/2}→⁴I_{15/2} transition at 655 nm. As previously shown in **Figure 2.1c and d**, IR820 has an absorption coefficient of 8860 M⁻¹ cm⁻¹, while IR820–NO₂ has an absorption coefficient of 3340 M⁻¹ cm⁻¹ at 655 nm (**Figure S2.16**). Thus, both dyes have the potential for back-transfer from the Er³⁺ to the dye (**Figure 2.3a**). As shown in **Figure 2.3b**, evaluation of the upconversion emission spectra of both IR820–LnUCNPs and IR820–NO₂–LnUCNPs upon 976 nm excitation, there is a significant reduction in the overall red and green emission intensities from IR820 LnUCNPs. Considering the higher absorption coefficient of IR820 at 655 nm, the red-to-green emission ratio is significantly lower for the IR820 dye upconversion spectrum than for the modified IR820–NO₂ dye (0.625 for IR820, 0.833 for IR820–NO₂). However, the spectral overlap in the red region would not justify the decrease in the green emission intensities; thus upconversion lifetimes upon 976 nm excitation were performed to assess the interactions of the dyes and Er³⁺ (**Figure 2.3c**). When comparing unfunctionalized LnUCNPs to IR820 functionalized LnUCNPs, the dye coating shortens the decay time by about 50% for both the green and red emission bands. This is compared to IR820–NO₂ functionalized LnUCNPs, which only shortens the decay times by 36% for both the green and red emissions. The shortening of the red emission decay time is justified by the spectral overlap between both dyes and the Er³⁺ ⁴F_{9/2}→⁴I_{15/2} transition, resulting in a non-radiative energy transfer from the Er³⁺ to the dye. While this is consistent with their respective absorption coefficients, it does not explain the shortening of the green emission decay time, which follows the same trend. This is postulated to be, in part, a result of a known cross-relaxation mechanism occurring between the green and red emitting states of Er³⁺ (²H_{11/2} + ⁴I_{11/2}→⁴F_{9/2} + ⁴F_{9/2}).¹⁶⁴ The non-radiative depopulation of the red-emitting ⁴F_{9/2} state from the dye interaction results in

improved efficiency of this mechanism, consequently reducing the green emission intensity and decay time, relative to the unfunctionalized LnUCNPs. Moreover, the reported depopulation of the $^4I_{9/2}$ NIR intermediate state through back transfer from Er^{3+} to the dye molecules can further justify the observed trend for the green emitting states.¹⁶⁵ Quenching of any of the NIR intermediate states involved in the population of the upper states would further justify the observed trend. Considering that back transfer to Yb^{3+} ions has been known to often occur both from NIR transitions involving the $^4I_{11/2}$ and $^4S_{3/2}$ states, these transitions would also be resonant with the absorption of the dye, providing possible additional routes for the depopulation of the Er^{3+} excited states.^{166,167}

To summarize, due to the increased spectral overlap between IR820 and the Er^{3+} red emission, there is a slight quenching of the overall upconversion luminescence from Er^{3+} . This process is less efficient for IR820- NO_2 , due to its red-shifted absorbance band. As observed in **Figure 2.3b**, the IR820- NO_2 functionalized LnUCNPs exhibits a 60% increase in intensity relative to IR820 functionalized LnUCNPs, under 976 nm excitation. Back transfer occurs upon 808 nm excitation as well, since the Er^{3+} energy transfer to the dye is still expected, thus implying that up to 60% of the observed enhancement under 808 nm excitation is due to a decrease in back-transfer from the activator to the dye. This is an especially important finding, as it illustrates the importance of considering the back-transfer dynamics between the activator and dye when engineering dye-sensitized LnUCNPs.

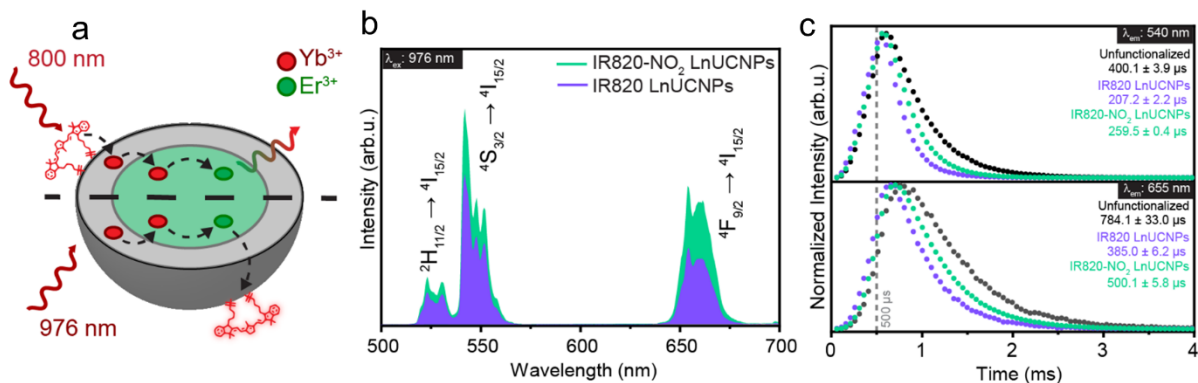


Figure 2.3 (a) Schematic of the interactions between the dye, sensitizer, and activator ions upon 808 and 976 nm excitation. (b) Upconversion emission spectra of IR820- NO_2 -LnUCNPs and IR820-LnUCNPs upon 976 nm excitation. (c) Upconversion lifetimes of the green (top) and red (bottom) emissions of Er^{3+} in unfunctionalized (black), IR820-functionalized (blue) and IR820- NO_2 -functionalized LnUCNPs upon 976 nm excitation.

As previously discussed, IR820–NO₂ dye exhibited increased photostability relative to IR820. Thus, kinetic studies were performed on the IR820 and IR820–NO₂ LnUCNPs to evaluate the photostability of the dye upon coordination to the nanoparticle surface. In particular, the luminescence intensity of the ⁴S_{3/2}→⁴I_{15/2} transition of Er³⁺ as a function of irradiation time was evaluated. As observed in **Figure 2.4a**, the green emissions of the IR820–NO₂-LnUCNPs are substantially more intense than the IR820-LnUCNPs, even after 30 minutes of irradiation, illustrating the vast improvement of the modified dye with respect to facilitating dye-sensitized upconversion luminescence. To quantify the results observed in **Figure 2.4a**, the emissions from IR820–NO₂ functionalized nanoparticles were observable for more than double the duration of the IR820 functionalized LnUCNPs. The emissions from the IR820–NO₂ functionalized LnUCNPs could be observed for over 1.5 hours, in comparison to only 30 minutes for IR820-LnUCNP emissions (**Figure 2.4b**). Interestingly, the dye-functionalized LnUCNPs follow the same pseudo-first order rate of degradation when observing the upconversion emissions. Since both the dye degradation kinetics, as discussed above, and the upconversion luminescence follow the same trend, it can be determined that the concentration of dye remaining on the surface of the nanoparticles (that is not degraded during irradiation) is related to the upconversion luminescence enhancement. The combination of the 200% enhancement in the luminescence and the more than doubled luminescence duration of this new nanosystem over the previous dye–LnUCNP system shows strong promise for practical use in a variety of applications, especially in solution.

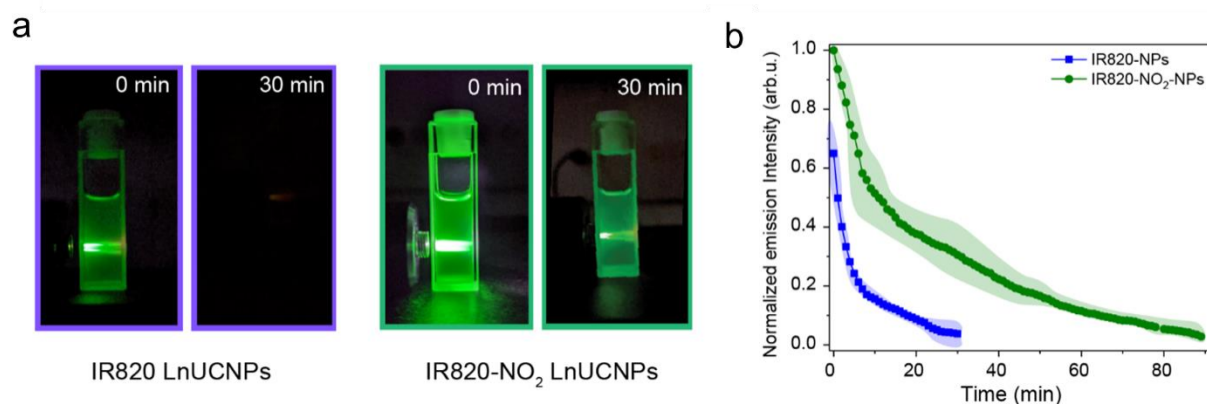


Figure 2.4 (a) Photographs of colloidal dispersions of IR820 LnUCNPs (top) and IR820–NO₂ LnUCNPs (bottom) at 0 and 30 minutes of irradiation with 808 nm excitation. (b) Overall emission intensities of IR820–NO₂-LnUCNPs (green) and IR820-LnUCNPs (blue) as a function of irradiation time upon 808 nm excitation (2.1 W/cm²). Light green and light blue regions around the curves represent the error margins. Errors are based on a minimum of two repetitions.

Because the modified IR820–NO₂ dye is characterized by a lower absorption cross-section than IR820 (**Figure S2.11**), quantum yield analyses on the ²H_{11/2}, ⁴S_{3/2}→⁴I_{15/2} transitions were carried out to evaluate the efficiencies of each system, as this method yields results which take into consideration the differences in the absorption cross-sections. QY measurements can also provide insight on the energy transfer mechanisms between the dyes and the Yb³⁺, and on the dynamics of the system. The QY of IR820–NO₂–functionalized LnUCNPs immediately after excitation was found to be over four times as efficient as IR820–functionalized LnUCNPs (**Figure S2.17**). This increase in efficiency can be credited to the improved energy transfer between IR820–NO₂ and Yb³⁺ compared to the unmodified IR820 dye, since IR820–NO₂ has improved spectral overlap with Yb³⁺ despite its slightly lower absorption coefficient (**Figure S2.11**).

The QY were measured as a function of irradiation time and both systems were found to be nearly constant (**Figure S2.17**). The quantum yields for both systems remained constant as a function of irradiation time, despite the occurrence of photodegradation. This implies that a decrease in absorbance due to the decomposition of the dye corresponds to a proportional decrease in emission; in other words, the upconversion luminescence is dependent only on the dye concentration. This excludes any direct population of Er³⁺ or energy transfer from Yb³⁺ ions when exciting at 808 nm, which would otherwise result in a non-constant trend in the quantum yields. Simply put, in the event of having direct population of Er³⁺ or through absorption from the Yb³⁺ ions, there would be a certain value of the QY directly dependent on these phenomena and, more importantly, independent of the irradiation time, since Yb³⁺ and Er³⁺ absorption and Er³⁺ emission would not be affected by the exposure time to the exciting source. Consequently, with decreasing of the absorption and emission due to the dye-sensitization process, an asymptotic trend would be expected, converging to the QY value obtained for the non-dye LnUCNPs, i.e. the value of the QY due to direct population of Er³⁺. The constant trend of the QY, contrarily, confirms the assumption that the Er³⁺ emissions achieved in the dye-sensitized LnUCNPs upon 808 nm excitation only arise from the dye energy transfer to the LnUCNPs.

2.4 Conclusion

For nearly a decade, NIR dyes have been used for upconversion sensitization. To our knowledge, studies on dye-sensitized LnUCNPs do not address the poor photostability of NIR dyes, and no significant measures have been taken to improve it. Furthermore, there is a lack of information on the dynamics between the dye, sensitizer and activator ions in these dye–LnUCNP systems. This calls for urgent attention towards this aspect, as the available dye-sensitized LnUCNPs systems are unsuitable for applications that require prolonged irradiation times, especially in solution, and there is little information on the degradation dynamics, and therefore a lack of knowledge on how to improve it.

In this study, for the first time, we report on the photostability of IR820 and the role of singlet oxygen in the photodegradation of this dye. To address the photostability of NIR dyes for upconversion sensitization, we introduced structural modifications to IR820 which were aimed at preventing the reaction of singlet oxygen with the heptamethine conjugation of the dye through steric and electronic effects. Of the modifications studied, IR820 functionalized with 4-nitrothiophenol group at the *para*-position was found to exhibit enhanced photostability relative to IR820 and possessed the greatest spectral overlap with Yb^{3+} .

IR820 and IR820–NO₂ were coordinated to NaGdF₄:Er³⁺,Yb³⁺/NaGdF₄:Yb³⁺ upconverting nanoparticles by electrostatic interaction and the emission enhancement, dynamics and photostability were studied. Significant attention was paid to providing a meaningful comparison between the dye-functionalized LnUCNP systems, as there is a lack of consistency in how these values are reported in the literature. The emission spectra of the IR820–NO₂-LnUCNPs exhibit 200% more intense emissions as compared to the IR820-sensitized LnUCNPs. The brighter emissions can be attributed to better spectral overlap between IR820–NO₂ and Yb^{3+} , which ensures a more efficient energy transfer, as well as a reduction in back-transfer from Er³⁺ to the dye, as proven by lifetime and QY measurements. Additionally, kinetic studies of the Er³⁺ ²H_{11/2}→⁴I_{15/2} and ⁴S_{3/2}→⁴I_{15/2} transitions illustrate that the IR820–NO₂-functionalized LnUCNPs exhibit more intense and observable emissions for more than twice the duration of IR820-sensitized LnUCNPs. The increased intensity, luminescence efficiency and duration of the emissions from IR820–NO₂-functionalized LnUCNPs represents a significant improvement in dye-sensitized upconverting nanoparticle properties.

These studies pave the way for dye-sensitized upconversion applications that require brighter emissions and prolonged irradiation times, especially with regard to solution-based and broadband absorbance applications. Future dye-sensitized upconversion systems should benefit from the knowledge gained from this work.

2.5 Supporting Information

2.5.1 Quantification of dye molecules per nanoparticle

Calibration curves were established for each dye sample in the range of 0.5 – 5 μM in methanol. The extinction coefficients for each dye were then obtained and utilized to calculate the observed dye concentrations in the nanoparticle samples which could then be utilized to obtain the number of molecules of dye in solution. The dimensions of the nanoparticles obtained from transmission electron microscopy images were utilized to calculate the volume of a single nanoparticle, and the density of the host material, NaGdF_4 (5.61 g/cm^3)¹⁶⁸ was obtained from the literature and combined, these values were utilized to estimate the mass of a single nanoparticle.

Table S2.1 Quantification of the number of dye molecules linked per nanoparticle.

Dye concentration added (μM)	Dye conc. linked on NPs $\times 10^{-3}(\mu\text{M})$		# dye molecules linked per particle	
	IR 820	IR 820- NO_2	IR 820	IR 820- NO_2
8	6	5	42	38
12	12	1	80	67
16	15	14	99	94
20	21	18	127	118

2.5.2 Photodegradation of IR820 in presence of different assays and in different solvents

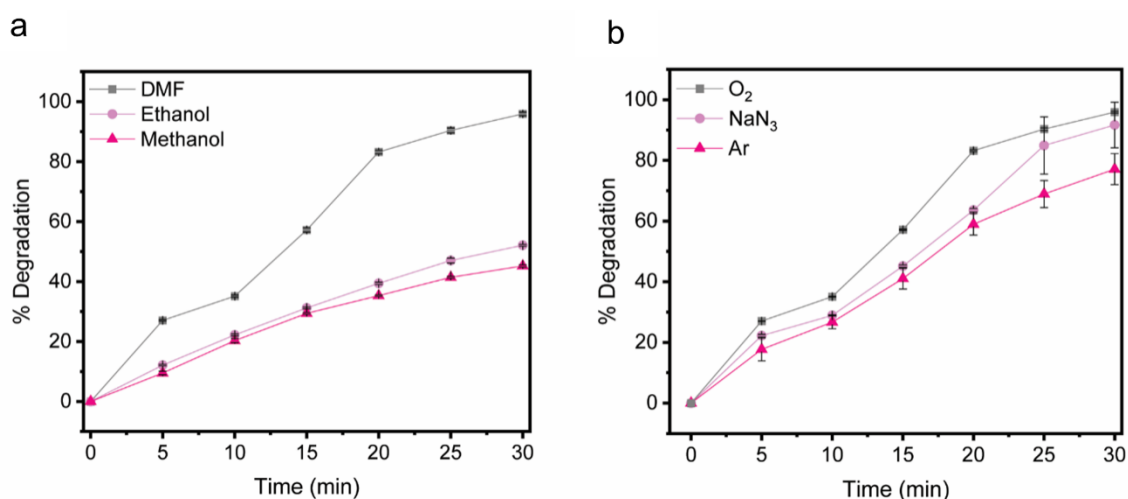


Figure S2.1 a) Percent degradation of IR820 dye versus time in ethanol (dark pink), and methanol (light pink). b) Percent degradation of IR820 (16 μM in DMF) dye versus time in ambient conditions (gray), in the presence of sodium azide (light gray) and under Ar atmosphere (pink). Errors based on a minimum of three repetitions.

Each assay was performed on a 16 μM solution in the corresponding solvent and a UV-visible absorption spectrum was measured at 5-minute intervals of irradiation with 808 nm light (4.2 W/cm^2). To obtain an inert atmosphere, the solution was purged with Argon for 10 minutes and sealed. Sodium azide was added at a concentration of 50 mM.

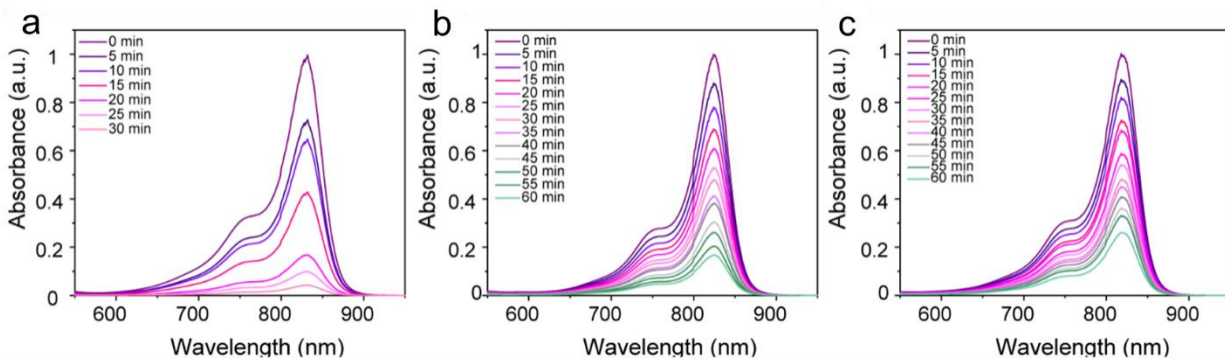


Figure S2.2 Decrease in absorbance of IR820 with irradiation time in a) DMF b) Ethanol c) Methanol

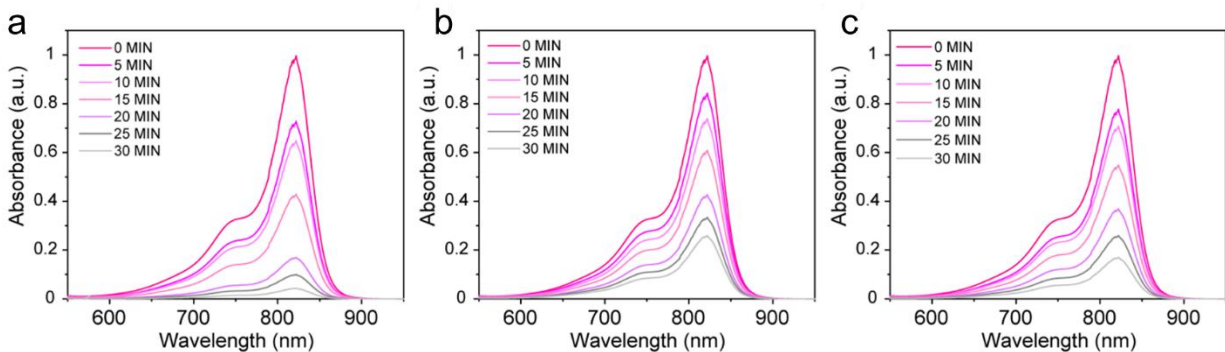


Figure S2.3 Absorbance of IR820 a) in air b) in Ar atmosphere c) with 50 mM sodium azide added in solution.

2.5.3 Analysis of photodegradation products of IR820 by ESI-MS

40ug/ml of IR820 dye was dissolved in DMF and irradiated at 808 nm for 15 minutes. The irradiated sample was analyzed for photoinduced degradation.¹²⁶

Table S2.2. Mass-to-charge ratio and molecular weight of peaks determined by ESI-MS analysis.

Peak	Molecular weight (MW)	Mass to charge ratio (m/z)
i	369.41[i]	368.03 [i-H+Na]
ii	394.45[iii]	392.01[ii-H+Na]
iii	509.01[ii]	508.17[iii-H+Na]
iv	535.05[iv]	534.21[iv-H+Na]
IR820	871.44[M]	435.58[M]/2

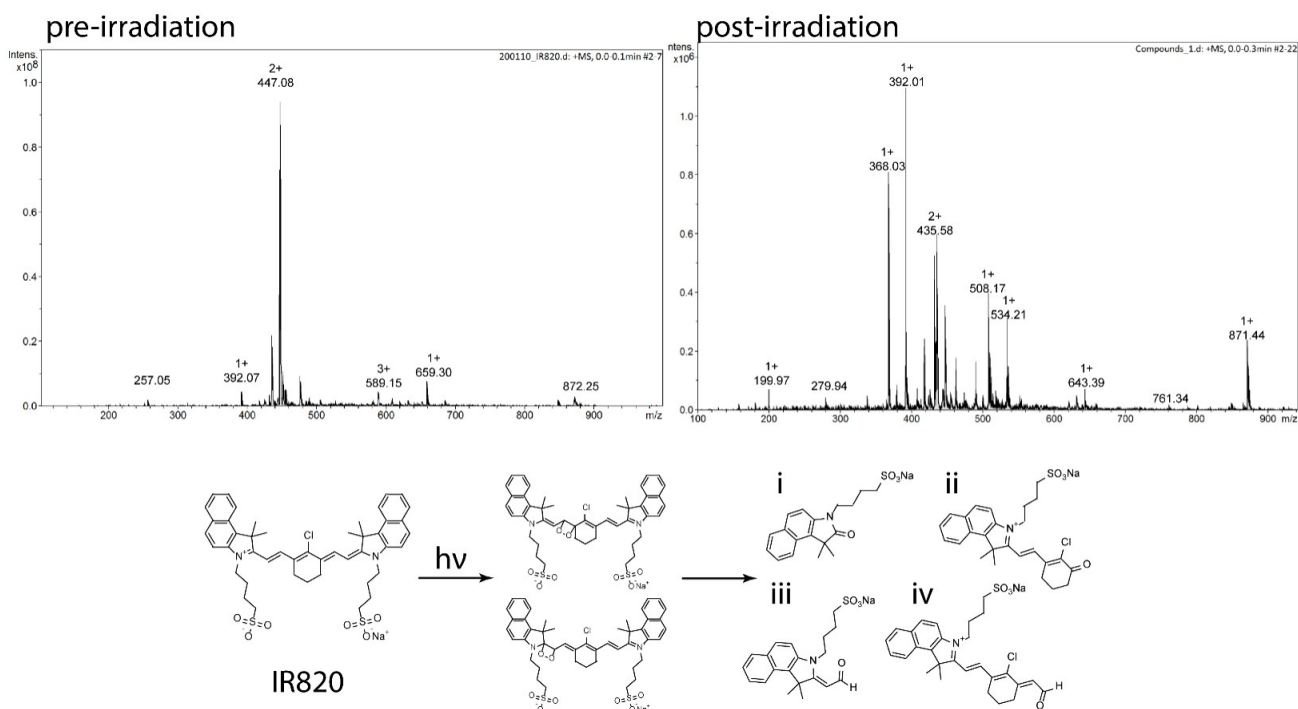


Figure S2.4 ESI-MS analysis of non-irradiated IR820 ESI-MS analysis and degradation mechanism of irradiated IR820 (at 808 nm 4.2 W/cm²)

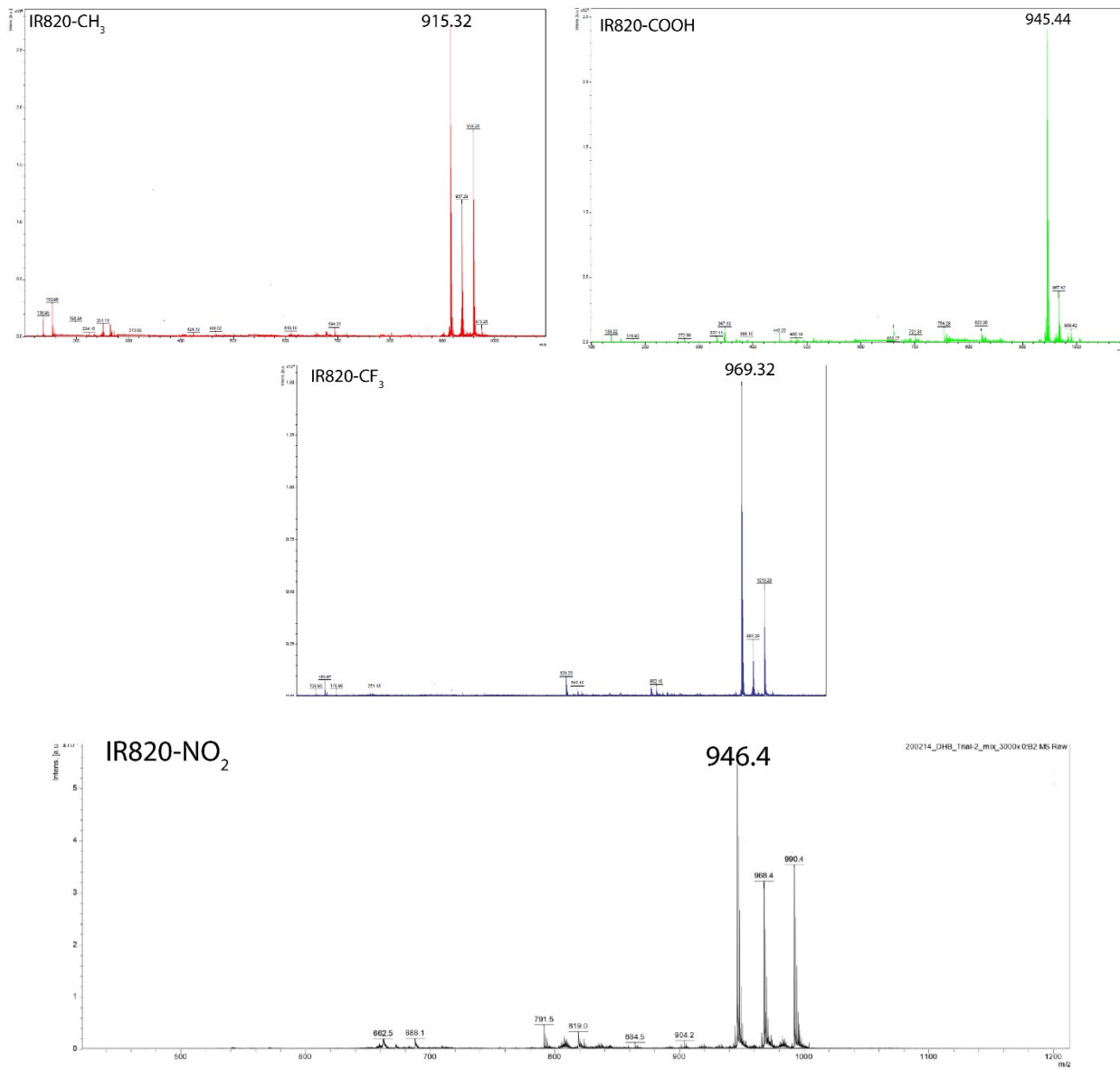
2.5.4 ¹H-NMR and MALDI-TOF-MS of IR820 derivatives

Synthesis of IR820-CH₃ yielded 87.5 mg (0.0975 mmol, 87%). ¹H NMR (500 MHz, d⁶-DMSO): δ 8.18(1H d), δ 8.05 (1H d), δ 7.95 (1H d), δ 7.93 (1H d), δ 7.92 (1H d), δ 7.61 (1H d), δ 7.54 (1H t), δ 7.52 (1H t), δ 7.47 (1H d), δ 7.45 (1H t), δ 7.29 (1H t), δ 7.07 (2H d), δ 7.06 (1H d), δ 6.89 (2H d), δ 6.55 (1 H d), δ 6.23 (1H d), δ 5.33 (1H d), δ 5.21 (1H d), δ 4.07 (4H t), δ 2.81 (4H d), δ 2.34 (3H s), δ 1.82 (6H s), δ 1.62 (6H s), δ 1.60 (2H p), δ 1.49 (4H t), δ 1.3 (4H t), MALDI-Calculated for C₅₃H₅₉N₂O₆S₃: 915.35; found 915.32.

Synthesis of IR820-COOH: Method same as above with 0.58mmol 4-mercaptobenzoic acid, IR820-COOH 92.5 mg (0.0979 mmol, 89%). ¹H NMR (500 MHz, d⁶-DMSO): δ 8.18(1H d), δ 8.05 (1H d), δ 8.05 (2H d), δ 7.95 (1H d), δ 7.93 (1H d), δ 7.92 (1H d), δ 7.61 (1H d), δ 7.60 (2H d), δ 7.54 (1H t), δ 7.52 (1H t), δ 7.47 (1H d), δ 7.45 (1H t), δ 7.29 (1H t), δ 7.06 (1H d), δ 6.55 (1H d), δ 6.23 (1H d), δ 5.33 (1H d), δ 5.21 (1H d), δ 4.07 (4H t), δ 2.81 (4H d), δ 1.82 (6H s), δ 1.62 (6H s), δ 1.60 (2H p), δ 1.49 (4H t), δ 1.3 (4H t). MALDI- Calculated for C₅₃H₅₇N₂O₈S₃: 945.32; found 945.33

Synthesis of IR820-CF₃: Method same as above with 4-(trifluoromethyl) thiophenol. Yield IR820-CF₃ 98 mg (0.101 mmol, 92%). ¹H NMR (500 MHz, d⁶-DMSO): δ 8.18(1H d), δ 8.05 (1H d), δ 7.95 (1H d), δ 7.93 (1H d), δ 7.92 (1H d), δ 7.61 (1H d), δ 7.54 (1H t), δ 7.52 (1H t), δ 7.47 (1H d), δ 7.45 (1H t), δ 7.29 (1H t), δ 7.23(2H d), δ 7.06 (1H d), δ 6.94 (2H d), δ 6.55 (1 H d), δ 6.23 (1H d), δ 5.33 (1H d), 5.21 (1H d), δ 4.07 (4H t), δ 2.81 (4H d), δ 1.82 (6H s), δ 1.62 (6H s), δ 1.60 (2H p), δ 1.49 (4H t), δ 1.3 (4H t).MALDI- Calculated for C₅₃H₅₆N₂O₆S₃F₃: 969.32; found 969.32.

Synthesis of IR820-NO₂: Method same as above with 4-nitrothiophenol. Yield IR820-NO₂ 96.8 mg (0.102 mmol, 93%). ¹H NMR (500 MHz, d⁶-DMSO): δ 8.18(1H d), δ 8.10 (2H d), δ 8.05 (1H d), δ 7.95 (1H d), δ 7.93 (1H d), δ 7.92 (1H d), δ 7.65 (3H t), δ 7.61 (1H d), δ 7.54 (1H t), δ 7.52 (1H t), δ 7.47 (1H d), δ 7.45 (1H t), δ 7.29 (1H t), δ 7.06 (1H d), δ 6.55 (1 H d), δ 6.23 (1H d), δ 5.33 (1H d), δ 5.21 (1H d), δ 4.07 (4H t), δ 2.81 (4H d), δ 1.82 (3H s), δ 1.62 (3H s), δ 1.60(2H p) δ 1.49 (4H t), δ 1.3 (4H t). MALDI- Calculated for C₅₂H₅₆N₃O₈S₃: 946.3; found 946.4.



2.5.5 UV-Visible Absorption spectra of IR820 derivatives and corresponding maxima

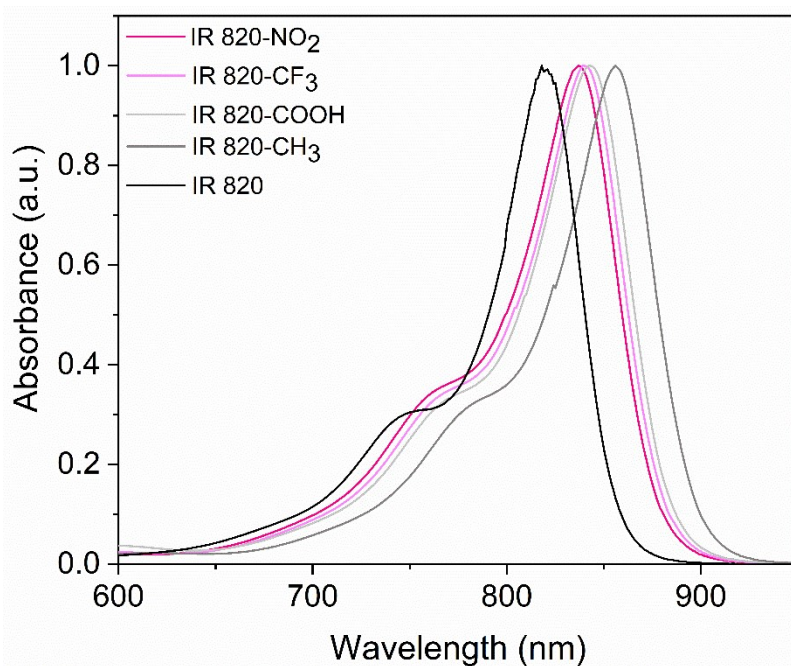


Figure S2.6 Absorbance of IR820 and IR820 functionalized with thiophenol with different para substituents: IR820 (black), IR820-NO₂(pink), IR820-CF₃(light pink), IR820-COOH(light gray), IR820-CH₃(gray)

Table S2.3. Absorbance and fluorescence (λ_{ex} 808 nm) of IR820 and functionalized dyes in methanol.

Dye	Absorbance $\lambda_{\text{max}}(\text{nm})$	Emission $\lambda_{\text{max}}(\text{nm})$
IR820	820	850
IR820-CH₃	850	900
IR820-COOH	845	920
IR820-CF₃	840	945
IR820-NO₂	837	950

2.5.6 Analysis of photodegradation of IR820 derivatives by UV-Visible absorption spectroscopy

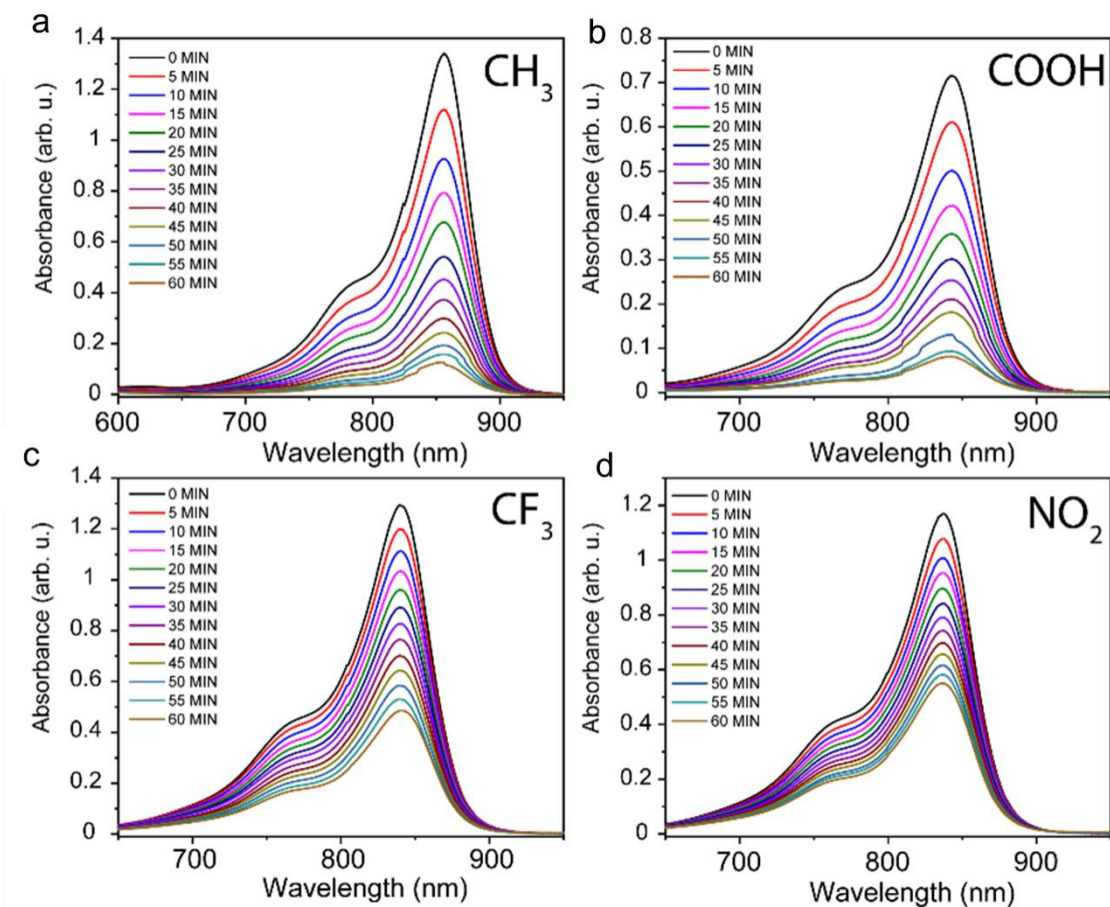


Figure S2.7 Decrease of absorbance of a) IR820-CH₃ b) IR820-COOH c) IR820-CF₃ and d) IR820-NO₂ with irradiation time under 808 nm irradiation.

2.5.7 Physical Characterization of core/shell NaGdF₄:Yb³⁺,Er³⁺/NaGdF₄:Yb³⁺ nanoparticles

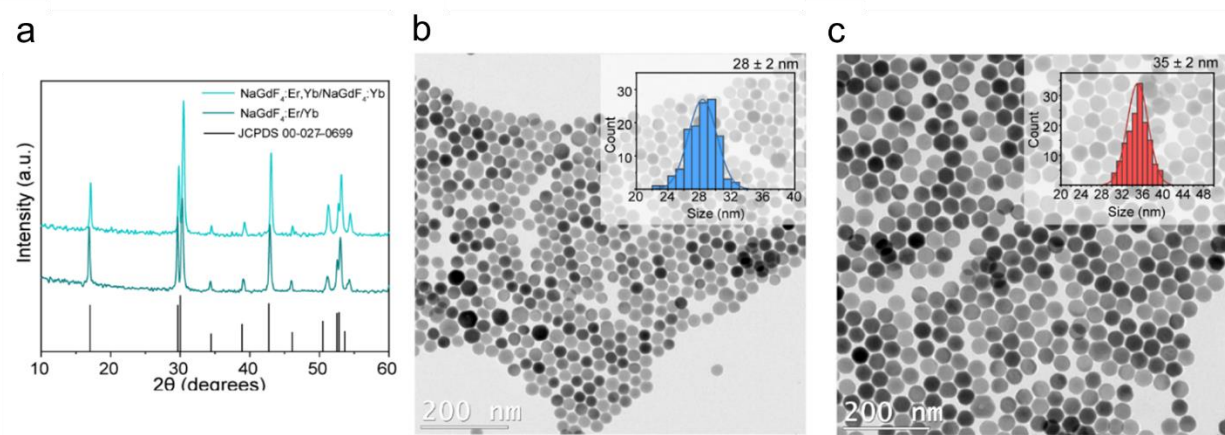


Figure S2.8. a) PXRD pattern of NaGdF₄:Er³⁺(2%),Yb³⁺(20%)/NaGdF₄:Yb³⁺(20%) (core/shell) and NaGdF₄:Er³⁺(2%),Yb³⁺(20%) (core) nanoparticles. TEM image of b) NaGdF₄:Yb³⁺,Er³⁺ (cores), with inset of size distribution c) NaGdF₄:Yb³⁺,Er³⁺/NaGdF₄:Yb³⁺ (core/shell) nanoparticles with inset of size distribution.

2.5.8 FT-IR spectra for characterization of nanoparticle surface

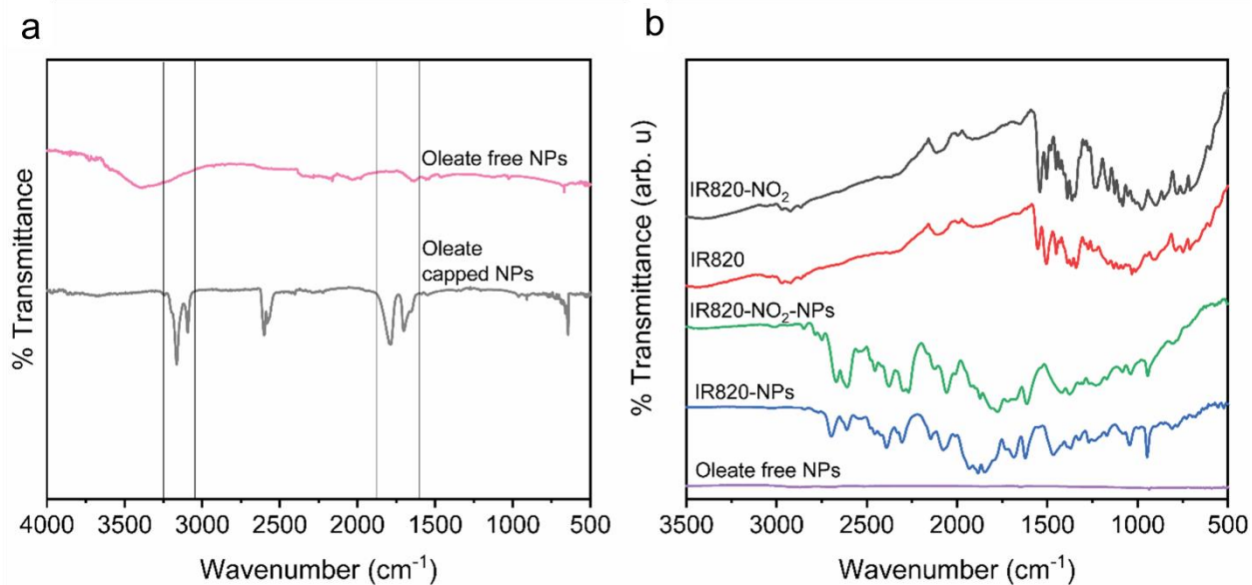


Figure S2.9 FT-IR of a) oleate capped and oleate free nanoparticles. The absence of peaks 3300 cm⁻¹ and 1700 cm⁻¹ in oleate free nanoparticles, confirms the removal of oleate b) Dye and nanoparticles conjugated with the respective dye.

The FT-IR reveals the emergence of bands at 3000 cm^{-1} (C=C from dye), 1375 cm^{-1} (C=C bending), 1260 cm^{-1} (C-N stretching), and 1100 cm^{-1} (S=O stretching) in LnUCNPs functionalized with dyes. Additionally, a slight red shift (70 cm^{-1}) is observed in the S=O stretching vibration (1170 cm^{-1}) upon conjugation of the dye to the LnUCNP surface, compared to the dye itself (1170 cm^{-1}), which indicates that the electron density of the sulfonate group is being shared with positively charged nanoparticle surface, thereby weakening the S-O bonds and shifting the vibration maximum to a lower wavenumber.¹²⁹

2.5.9 Transmission Electron Microscopy images of oleate free nanoparticles

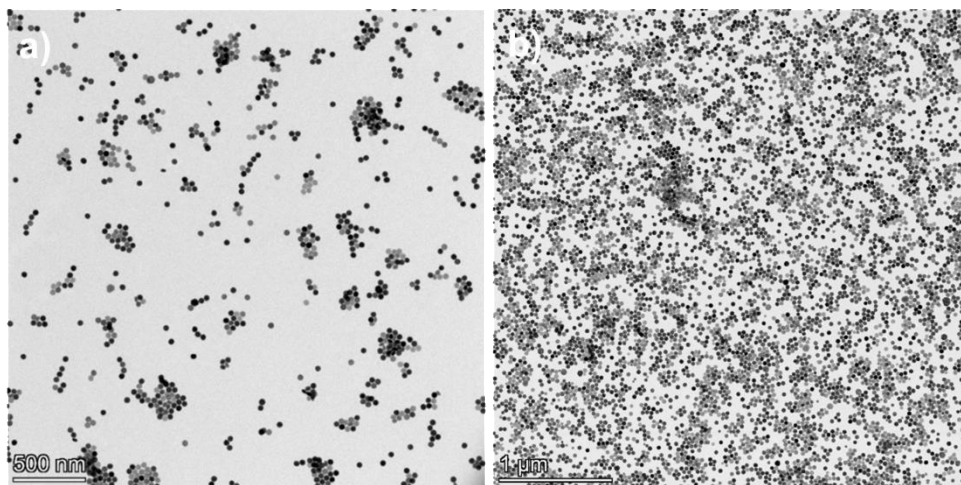


Figure S2.10 TEM images of a) oleate free LnUCNPs b) IR820-NO₂-LnUCNPs, 1 mg/ml dispersion in methanol.

2.5.10 Calibration curves for quantification of number of dye molecules per nanoparticle

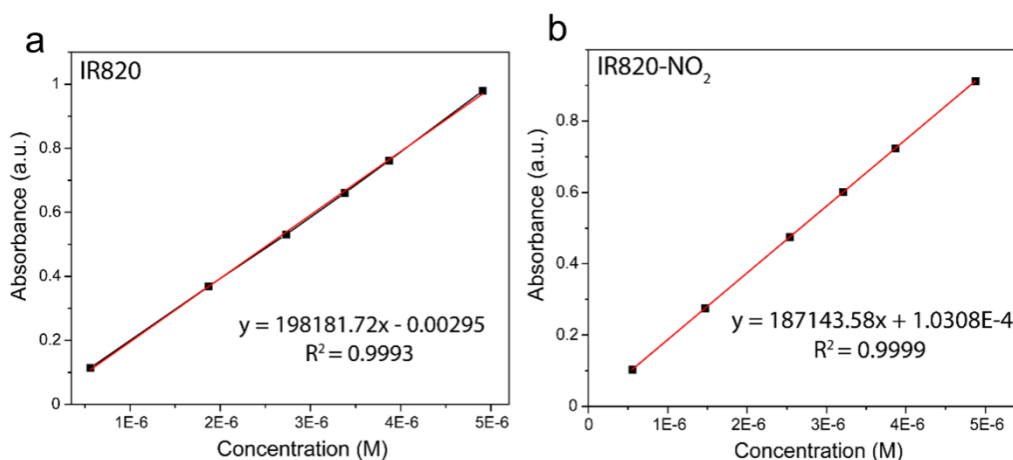


Figure S2.11 Calibration curve of a) IR820 and b) IR820-NO₂ having $198181\text{ M}^{-1}\text{ cm}^{-1}$ and $187143\text{ M}^{-1}\text{ cm}^{-1}$ molar extinction coefficients in methanol, respectively.

2.5.11 Emission Spectra of IR820 and IR820-NO₂ functionalized LnUCNPs at different dye concentrations

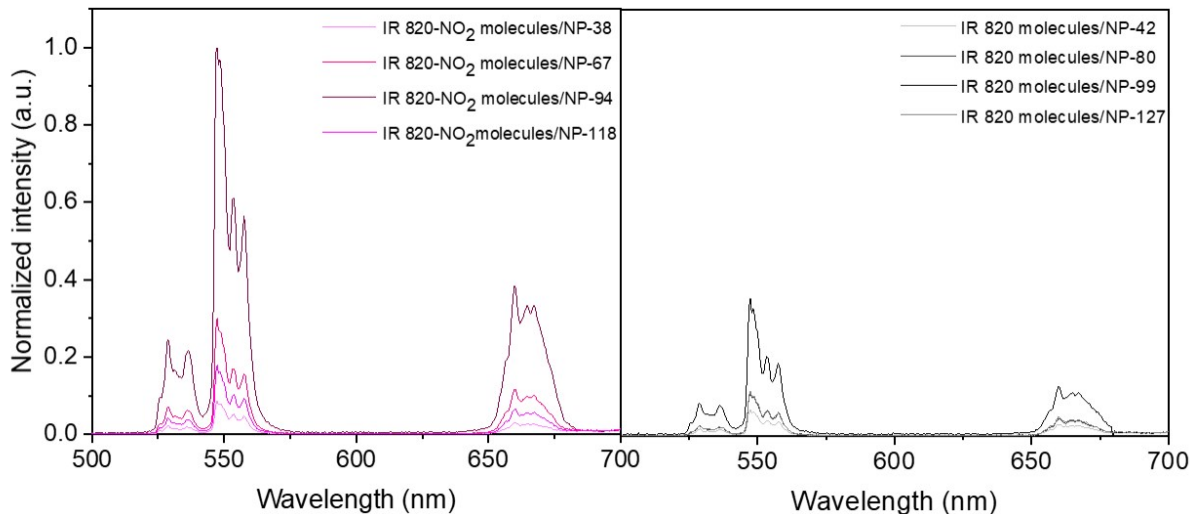


Figure S2.12 Emission spectra of IR820-NO₂ (pink) and IR820 (gray) functionalized LnUCNPs (in methanol) having different dye concentrations and 10mg/ml UCNPs excited at 808 nm (2.1 W/cm²)

2.5.12 Stability study on the electrostatic interaction of IR820-NO₂ dye with LnUCNP surface

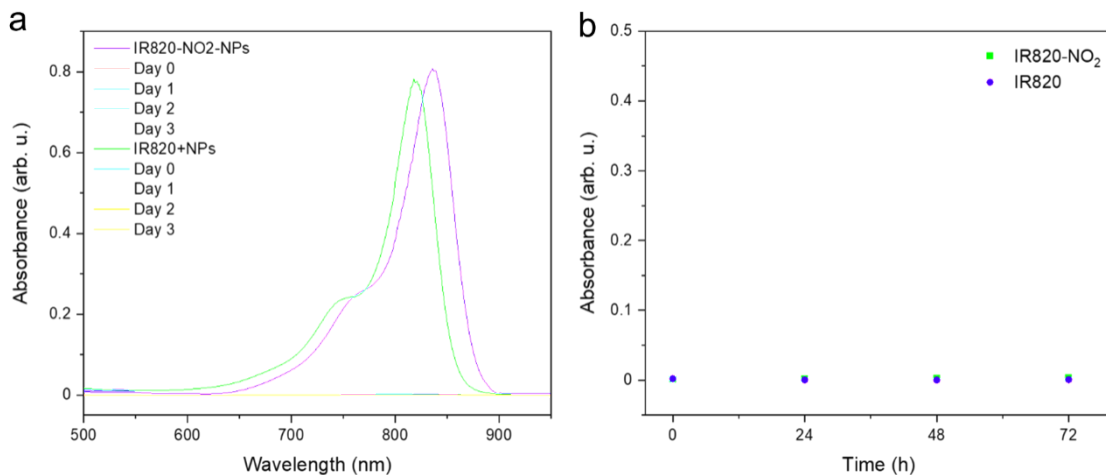


Figure S2.13 a) UV-visible absorption spectrum of supernatant collected after 24, 48 and 72 h from a dispersion of IR820-NO₂-LnUCNPs (10 mg/mL) in methanol. b) Absorption of supernatant of a dispersion of IR820-LnUCNPs at 820 nm and IR820-NO₂-LnUCNPs at 837 nm as a function of time. No leakage of dye from the nanoparticle surface was observed.

2.5.13 Kinetics of IR820-NO₂ degradation with NaGdF₄:Er³⁺/Yb³⁺ and NaYF₄:Er³⁺/Yb³⁺

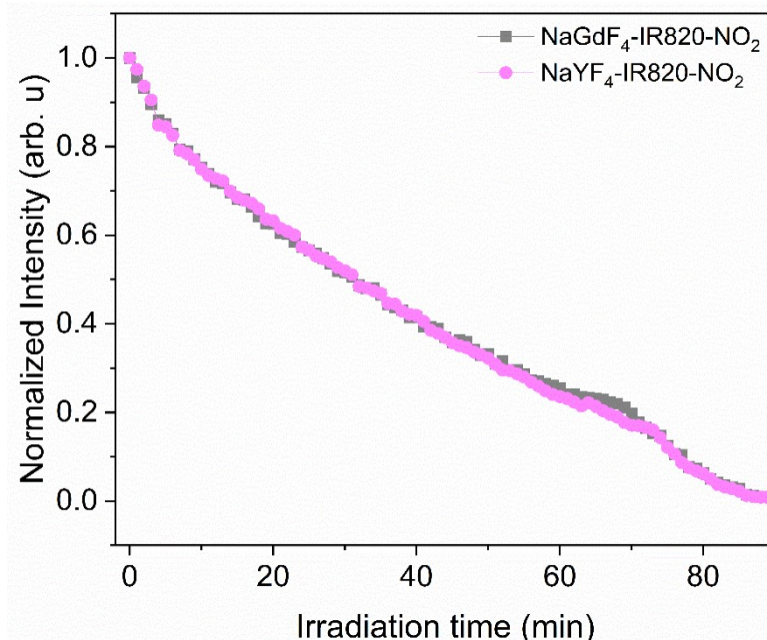


Figure S2.14 Normalized green emission intensity of LnUCNPs versus irradiation time for IR820-NO₂- NaGdF₄:Er³⁺, Yb³⁺-(gray) and IR820-NO₂-NaYF₄: Er³⁺, Yb³⁺ (pink) under 808 nm excitation (at 4.2 W/cm²).

2.5.14 Upconversion emission spectra comparisons upon different excitation wavelengths

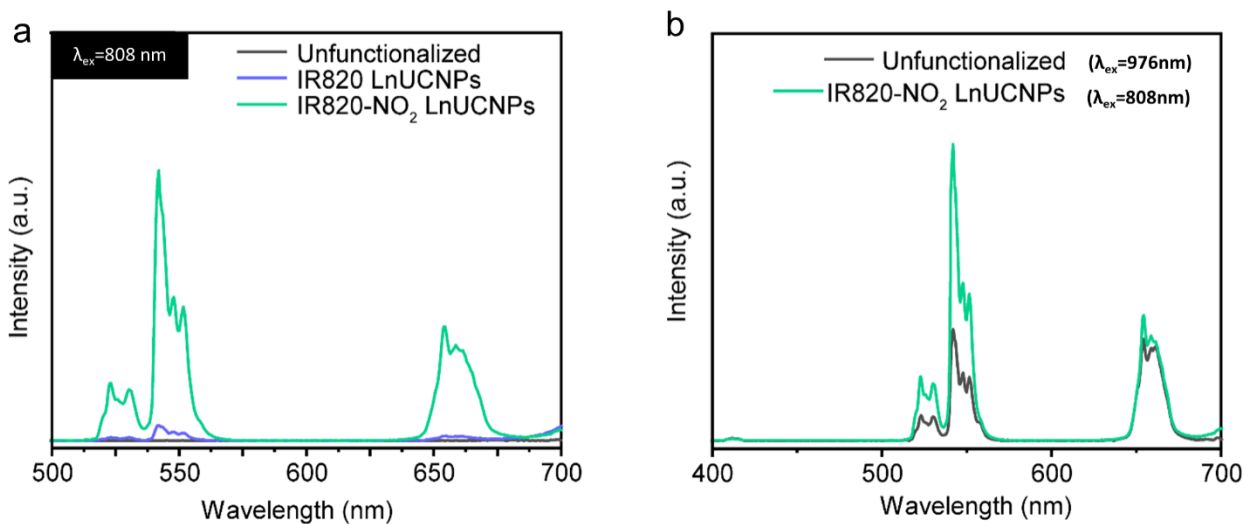


Figure S2.15 a) Upconversion emission spectra of colloidal dispersions of unfunctionalized LnUCNPs (gray), IR820-LnUCNPs (blue) and IR820-NO₂-LnUCNPs (green) upon 808 nm excitation (2.1 W/cm²). b) Upconversion emission spectra of colloidal dispersions of unfunctionalized LnUCNPs (gray) and IR820-NO₂ LnUCNPs (green) upon 976 nm excitation and 808 nm excitation, respectively (both at power densities of 4.2 W/cm²).

2.5.15 Calibration curves for absorption coefficients at 655 nm

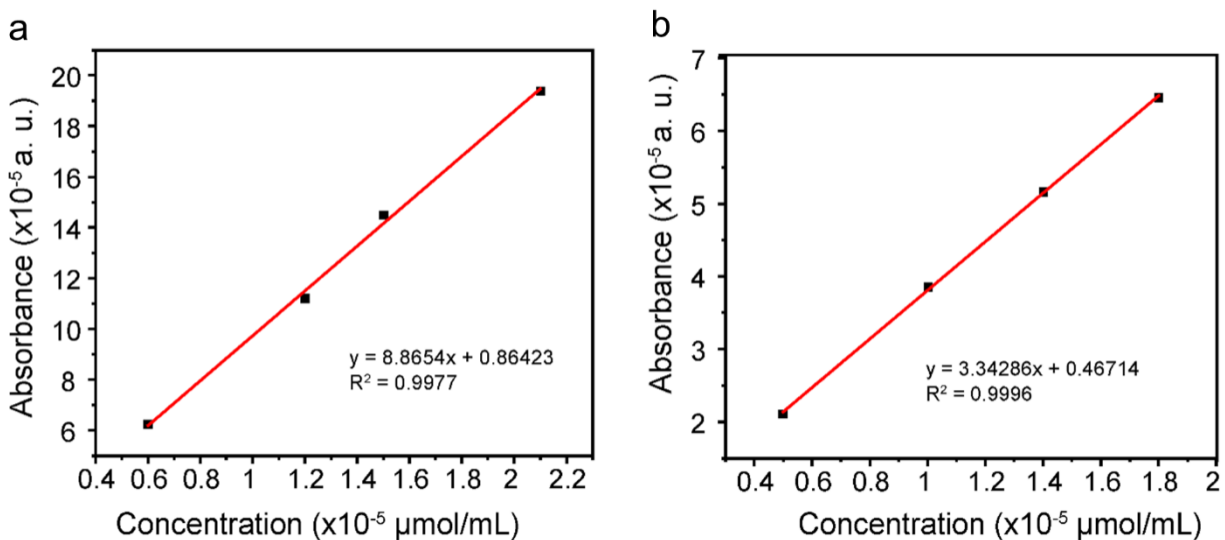


Figure S2.16 a) Calibration curve for IR820 at 655 nm in methanol b) Calibration curve for IR820-NO₂ at 655 nm in methanol.

2.5.16 Quantum Yield measurements

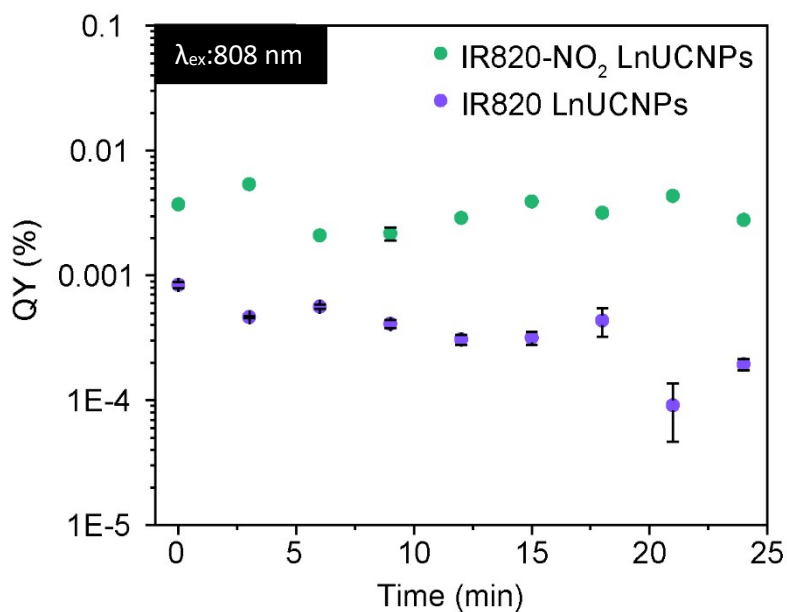
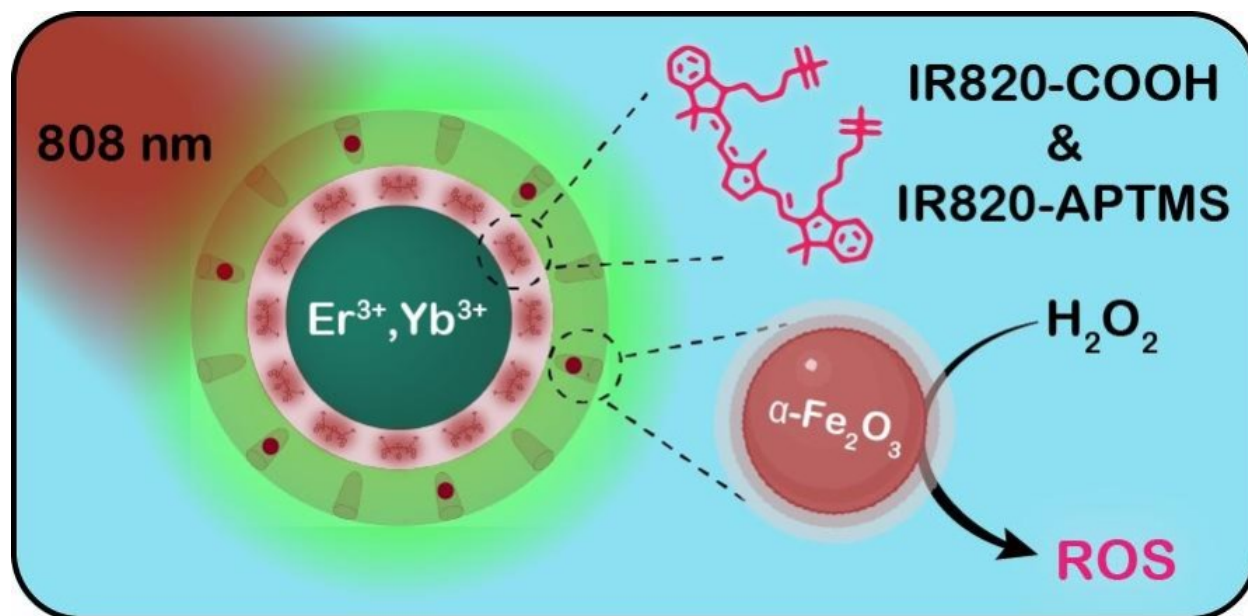


Figure S2.17 Quantum yields of IR820-NO₂-LnUCNPs (green) and IR820-LnUCNPs (blue) as a function of irradiation time upon 808 nm excitation. Errors for both measurements established based on a minimum of two repetitions

Chapter 3: Achieving photostability in dye-sensitized upconverting nanoparticles and their use in Fenton-type photocatalysis



Abstract: Dye sensitization is a promising approach to enhance the luminescence of LnUCNPs. However, the poor photostability of near-infrared dyes hampers their use in practical applications. To address this, commercial IR820 was modified for improved photostability and covalently bonded to amine-functionalized silica-coated LnUCNPs. Two methods of covalent linking were investigated: linking the dye to the surface of the silica shell and embedding the dye within the silica shell. The photostability of the dyes when embedded in the silica shell exhibited upconversion emissions from $\text{NaGdF}_4:\text{Er}^{3+}, \text{Yb}^{3+}/\text{NaGdF}_4:\text{Yb}^{3+}$ nanoparticles for over four hours of continuous excitation with no change in intensity. To highlight this improvement, the photostable dye-embedded system was successfully utilized for Fenton-type photocatalysis, emphasizing its potential for practical applications. Overall, this study presents a facile strategy to circumvent the overlooked limitations associated with photodegradation, opening up new possibilities for the use of dye-sensitized lanthanide-doped upconverting nanoparticles in a range of fields.

3.1 Introduction

The long-lived intermediate excited states of trivalent lanthanides have garnered considerable attention in the study of upconversion, where NIR irradiation is converted to UV, visible, or higher energy NIR emissions.^{29,154,169} Due to their narrow absorption and emission bands, high chemical and colloidal stability,¹⁷⁰ and low toxicity,¹⁷¹ LnUCNPs are used in many diverse applications such as photodynamic therapy,¹⁷² drug delivery,¹⁷³ optical encoding,¹⁷⁴ biosensing,¹⁷⁵ photovoltaics,¹⁷⁶ and bioimaging.¹⁷⁷ However, due to the forbidden nature of their intraconfigurational $4f-4f$ transitions, they have low absorption coefficients, leading to low upconversion efficiencies.¹⁵⁶ Consequently, the emission of light from LnUCNPs is commonly enhanced through an indirect sensitization technique involving an organic dye, known as the “antenna effect”,^{92,129,178,179} proposed by Weismann in 1942 to transfer energy from organic ligands to lanthanide ions.⁸⁶

Organic dyes possess considerably higher absorption cross-sections (3–4 orders of magnitude higher than that of lanthanide ions) and feature broad and tunable absorption bands, making them ideal light-harvesting agents.^{91,92,179,180} Moreover, the shift in absorbance relative to conventional Yb^{3+} (from 976 nm to around 800 nm) also reduces the absorption of NIR light by water in biological tissues and prevents laser-induced heating effects.⁵² This type of system has the advantage of protecting the activators from solvent-mediated quenching, as well as increasing the light absorption cross-section through the antenna effect.¹⁸¹ In recent years, numerous investigations have demonstrated the efficacy of dye sensitization in increasing the intensity of upconversion luminescence. This technique involves either electrostatically,^{111,115,182,183} or covalently¹⁸⁴ linking an organic NIR-emitting dye with a high absorption cross-section to the surface of a nanoparticle. Alternatively, the dyes can be encapsulated in a polymer or mesoporous silica shell.^{120,153,185,186} The photostability of dyes has also been successfully achieved through incorporation within silica nanoparticles to generate fluorescent silica nanoparticles.^{187–190}

The concept of dye-sensitized LnUCNPs was first introduced in 2012 by Zou *et al.* using carboxylic acid-modified cyanine dyes to enhance the upconversion luminescence of $\text{NaYF}_4:\text{Yb}^{3+},\text{Er}^{3+}$ LnUCNPs.¹¹³ Further, Prasad and co-workers demonstrated an energy-cascaded upconversion process where the energy is transferred from IR-808 to Nd^{3+} , and then to Yb^{3+} and Tm^{3+} , resulting in improved upconversion quantum yields.⁹² In 2019, Ju *et al.* designed core/shell/shell LnUCNPs with a core of $\text{NaYF}_4:\text{Gd}^{3+}$, an energy-concentrating shell of

NaYF₄:Yb³⁺,Er³⁺ and an outer shell of NaYF₄:Nd³⁺,Yb³⁺ to interact with a NIR dye and facilitate energy transfer.¹⁹¹

Unfortunately, while dye-sensitized LnUCNPs exhibited more intense upconversion luminescence, the release of the dyes from the surface^{110,122} and the limited photostability of NIR dyes still remains a challenge.^{109,123,125,126} Reports on the covalent linking of NIR dyes to silica-modified nanoparticles, or their encapsulation in polymers have alleviated the detachment issues.^{179,184,192,193} However, the photostability of NIR dyes still remains an obstacle since they are known to undergo bimolecular reactions with *in situ* generated singlet oxygen, resulting in degradation.^{1,109,123,125,126} While various steric and functional modifications have been explored to inhibit these bimolecular reactions,^{127,194,195} this has rarely been addressed with respect to dye-sensitized LnUCNPs. Our previous work took advantage of the steric modification of IR820, showing that the IR820–NO₂-functionalized LnUCNPs had brighter and considerably longer upconversion luminescence compared to IR820-sensitized LnUCNPs.¹ However, the issue of photostability was not fully resolved.

For the first time, to our knowledge, we have demonstrated a means of generating photostable dye-sensitized LnUCNPs. To achieve this, a modified version of commercial IR820 was covalently embedded in silica-coated NaGdF₄:Er³⁺,Yb³⁺/NaGdF₄:Yb³⁺ active-core/active-shell LnUCNPs. To assess the photostability and effectiveness of this system, spectroscopic comparisons were made between electrostatic and covalently linked dye-LnUCNP systems. Additionally, QY measurements and luminescence lifetimes were conducted to compare this system with Nd³⁺-doped core/shell nanoparticles, a commonly employed alternative for 808 nm-sensitized upconversion luminescence. Finally, we demonstrate the applicability of this photostable dye-sensitized system for Fenton-type photocatalysis.

3.2 Experimental

3.2.1 Material

All reagents were used without further purification. Gd₂O₃ (99.999%), Yb₂O₃ (99.999%), and Er₂O₃ (99.999%) were purchased from Chemicals 101 Corp. Sodium trifluoroacetate (98%) was purchased from Alfa Aesar. Oleic acid (90%), 1-octadecene (90%), IR820 (80%), 4-mercaptobenzoic acid (99%), tetraethylorthosilicate (99%), ammonium hydroxide solution (28-30%), 3-aminopropyltrimethoxysilane (97%), IGEPAL CO-520 (99%), N-(3-

dimethylaminopropyl)-N'-ethyl carbodiimide (EDC, 97%), N-hydroxysuccinimide (NHS, 98%), (3-aminopropyl)trimethoxysilane (97%), mesitylene (98%), L-arginine ($\geq 98\%$), iron(III) chloride hexahydrate ($\geq 98\%$), sodium acetate ($\geq 99.0\%$), and polyvinylpyrrolidone (PVP, average $M_w \sim 55,000$) were purchased from Sigma Aldrich. Trace metal grade hydrochloric acid (99.999%) was purchased from Fisher Scientific. Hexadecyltrimethylammonium chloride (CTAC, $>95.0\%$) was purchased from TCI Chemicals. For MALDI-MS analysis, 2,5-dihydroxybenzoic acid (DHB), was purchased from Sigma-Aldrich and used without further purification.

3.2.2 Synthesis of NaGdF₄:Er³⁺ (2%), Yb³⁺ (20%)/NaGdF₄: Yb³⁺ (20%) active core/active shell LnUCNPs

Core nanoparticles were synthesized using a previously established thermal decomposition method.⁷² 1.25 mmol of lanthanide oxides (78 mol% Gd₂O₃, 20 mol% Yb₂O₃, and 2 mol% Er₂O₃) were dissolved in 10 mL of 50% v/v aqueous trifluoroacetic acid under reflux conditions, generating the trifluoroacetate precursors. Once dried, the precursors were combined with 2.5 mmol of sodium trifluoroacetate, all dissolved in 7.5 mL oleic acid and 7.5 mL 1-octadecene and degassed under vacuum at 120°C for 30 min. In a separate flask, 12.5 mL of oleic acid and 12.5 mL 1-octadecene were degassed under vacuum at 120 °C for 30 min, followed by a temperature increase to 310°C, at a rate of 10°C/min, under argon atmosphere. The precursor solution was then injected into the solvents at a rate of 1.5 mL/min. This solution was left stirring at 300 rpm for 60 min. To synthesize the core/shell nanoparticles, 1.25 mmol of lanthanide oxides (80 mol% Gd₂O₃ and 20 mol% Yb₂O₃) were dissolved in 50% aqueous trifluoroacetic acid under reflux conditions, generating the shell precursor. Once dried, 2.5 mmol of sodium trifluoroacetate was added to the shell precursors and dissolved in 2.5 mL of oleic acid and 2.5 mL of 1-octadecene. This solution was degassed under vacuum at 120°C for 30 min. Once the full 60 min core synthesis was complete, the shell precursor solution was then injected into the reaction vessel, at a rate of 0.5 mL/min. This solution was maintained at 310°C for 45 min. Once the oleate-capped nanoparticles were synthesized, the solution was cooled to room temperature in ambient conditions and precipitated in 40 mL of ethanol. The resulting pellet was centrifuged at 3900 rpm for 15 min, and washed three times *via* dispersion in hexane and precipitation in ethanol, centrifuging between washes. Samples were stored as a solid pellet covered with ethanol.

3.2.3 Synthesis of NaGdF₄:Er³⁺, Yb³⁺/NaGdF₄: Yb³⁺/ NaGdF₄: (10-20%) Nd³⁺

In addition to the active-core/active-shell nanoparticles, a shell of Nd³⁺ was synthesized using the same protocol as the Yb³⁺ active shell. 1.25 mmol lanthanide oxides were dissolved in trifluoroacetic acid (90-80 mol% Gd₂O₃ and 10-20 mol% Nd₂O₃) to include the intended Nd³⁺ dopant concentration. Degassing was completed using the same methods as mentioned previously, and this solution was injected into the reaction vessel after the active-shell synthesis (t=105 min) at a rate of 0.5 mL/min. This full solution was then left at 310°C for 30 min. Once complete, the solution was cooled to room temperature under ambient conditions and precipitated/washed as mentioned previously.

3.2.4 Synthesis of IR820-COOH

A nucleophilic substitution reaction was used to functionalize the IR820 dye with 4-mercaptobenzoic acid.¹⁰⁸ 0.11 mmol of dye and 0.58 mmol acid were dissolved in 5 mL anhydrous DMF, under an argon atmosphere at room temperature. This solution was allowed to react for 12 h. Once complete, the DMF was evaporated under reduced pressure. The crude product was filtered through a PTFE syringe filter and precipitated with anhydrous diethyl ether, yielding 93.7 mg (92%) of IR820-COOH.

3.2.5 Synthesis of IR820-APTMS

The IR820-COOH dye (0.01 μmol) was dissolved in 10 mL of anhydrous DMSO, with 0.01 μmol EDC and 0.025 μmol NHS. This solution was stirred at room temperature, under nitrogen atmosphere for 8 h. 0.005 μmol APTMS was then added to the mixture and stirred for an additional 5 h. The crude product was filtered through a PTFE syringe filter and precipitated with anhydrous diethyl ether.

3.2.6 Synthesis of the Surface Silica Linked (SL system)

0.8 mL of IGEPAL CO-520 was mixed with 30 mg active-core/active-shell nanoparticles in 6 mL of hexane. After stirring for 30 min, 0.08 mL of ammonium hydroxide solution was added and sonicated for 20 min. Subsequently, 18 μmol of TEOS was added at a rate of 2.5 μL/15 min, followed by stirring for 48 h. 4 μmol of APTMS was then added at the same rate and stirred for an additional 24 h. Once complete, the newly amine-functionalized nanoparticles were precipitated with ethanol, collected by centrifugation at 8000 rpm for 10 min, and washed three times with 10 mL ethanol.

The covalent linking of IR820-COOH to the amine-functionalized surface of the nanoparticles was achieved using EDC/NHS amide coupling. IR820-COOH was dissolved in 20 mL of anhydrous DMSO, followed by the addition of varying amounts of EDC and NHS (Table S3.2). The mixture was stirred at 200 rpm at room temperature for 8 h. 25 mg of the amine-functionalized nanoparticles dispersed in 2 mL DMSO was then added to the IR820-COOH solution, and the mixture was stirred for an additional 5 h at room temperature. The completed SL system was isolated using centrifugation at 13000 rpm for 10 min, followed by three washes with 10 mL ethanol.

3.2.7 Synthesis of the Silica Embedded (SE system)

To synthesize the dye-embedded silica shell (with a thickness between 4-5 nm), 0.8 mL of IGEPAL CO-520 and 30 mg of oleate-capped nanoparticles were dispersed in 6 mL of hexane. After stirring for 30 min, 0.08 mL of ammonium hydroxide solution (28 wt% in water) is added and sonicated for 20 min. Subsequently, TEOS (**according to Table S3.3**) was added at a rate of 2.5 $\mu\text{L}/15$ min and stirred for 48 h. Following this, IR820-APTMS (**according to Table S3.3**) was added and stirred for an additional 24 h. Finally, the nanoparticles were precipitated with ethanol, collected by centrifugation at 8000 rpm for 10 min, and washed three times with 10 mL ethanol.

3.2.8 Transmission Electron Microscopy (TEM)

10 μL of 1 mg mL⁻¹ solutions of nanoparticles (in either hexane or methanol, depending on the hydrophilicity of the sample) were dropped on 300 mesh copper grids (3 mm, formvar/carbon film supported). Micrographs were recorded using a Talos L120C scanning transmission electron microscope operating at an accelerating voltage of 120 kV.

3.2.9 Energy dispersive X-ray spectroscopy (EDX)

EDX measurements were performed on a Jeol-JEM-2100F transmission electron microscope, operating at 200 kV. Scanning transmission electron microscopy (STEM) was used to record High Angle Annular Dark Field (HAADF) micrographs, which could then be used to acquire elemental mapping with an Oxford EDS detector (model Xplore).

3.2.10 Powder X-ray Diffraction (PXRD)

Diffraction patterns of dried upconverting nanoparticles were collected using a Bruker AXS D2 Phaser (30 kV, 10 mA), and dried hematite nanoparticles were collected using a Rigaku MiniFlex (40 kV, 15 mA). Both instruments are equipped with a Cu-K α source, and diffraction patterns were recorded with a resolution of 0.2° 2 θ .

3.2.11 Upconversion Emission Spectroscopy

Nanoparticle solutions in methanol (5 mg/mL) were excited using either 976 nm (Sky-laser, 0.8 W, 13 W/cm²) or 808 nm (SLOC Model IRM800T3-2500FC, 1.3 W, 5 W/cm²) irradiation. Upconverted emissions were collected at a right angle to the incident beam, using an optical fiber (Ocean Optics Inc, 600 μ m) coupled to a visible bandpass filter (Thorlabs, 400 – 750 nm), connected to a Princeton Instruments FERGIE BRX-VR UV-NIR spectrograph fitted with a 250 grooves/mm grating blazed at 550 nm, with a 50 μ m entrance slit.

3.2.12 Upconversion Lifetimes

Lifetime measurements were recorded on the same solution samples of nanoparticles as the emission spectra, excited using a 976 nm diode laser (Coherent 6-pin 15 fiber-coupled F6 series laser diode, 500 μ s pulse width, 1.5 W/cm²) or 808 nm diode laser (SLOC Model IRM800T3-2500FC, 500 μ s pulse width, 5 W/cm²). Emissions were collected using a Jarrell-Ash Czerny-Turner 25-102 1 m double monochromator (1180 grooves mm⁻¹), coupled to a Peltier-cooled Hamamatsu R943-02 photomultiplier tube. Signals were processed through an SR440 Stanford Research Systems preamplifier and interpreted using an SR400 Stanford Research Systems gated photon counter, varying the 50 μ s gate window to produce the lifetime profiles.

3.2.13 Upconversion Quantum Yield

Quantum yield measurements were completed on the same nanoparticle solutions used for the emission spectra and lifetime measurements. Samples were irradiated using the same excitation sources as the emission spectra (976 and 808 nm). Emissions were collected using an Avantes AvaSphere-30-REFL integrating sphere, fiber-coupled to a Thorlabs FOFMS/M-UV filter mount that was fitted with either a 400 – 750 nm bandpass filter or a 60% neutral density filter to record the emissions or absorptions, respectively. The filter mount was fiber-coupled to an Avantes AvaSpec-ULS2048L spectrometer. Emission and absorption intensities were recorded in units of Watts using a NIST calibrated AvaLight-DH-CAL-ISP30 lamp. These intensities were then converted to number of photons using the photon energy equation. Undoped NaGdF₄ nanoparticles (physical characterization Appendix 5, A5.4) were used as a control for Nd³⁺-doped nanoparticles, while undoped NaGdF₄ with an inert silica shell was used as a control for the SE system. Errors were calculated using triplicate measurements as well as the reported instrumental error.

3.2.14 Synthesis of Wide-pored silica shell

0.480 g of CTAC was mixed with 110 mL of water and 1.2 mL of mesitylene. 25 mg of SE nanoparticles were dispersed in 10 mL water and was added dropwise to the surfactant mixture. This solution was then sonicated for 30 min and stirred for an additional 30 min. 1.4 mL of butanol and 160 μL of TEOS was added to the solution at a rate of 0.5 mL/h. Afterward, 24 mg of L-arginine was dissolved in 1 mL water and added to the solution. This was allowed to stir for 17 h at 50°C under reflux.

Synthesis of the mesoporous silica shell was completed using the same method, omitting the addition of mesitylene.¹⁹⁶

3.2.15 Synthesis and incorporation of $\alpha\text{-Fe}_2\text{O}_3$ (hematite) nanoparticles

A previously reported hydrothermal method was used to synthesize the hematite nanoparticles.¹³⁷ 1.5 mmol of $\text{FeCl}_3 \cdot 6\text{H}_2\text{O}$, 45 mmol of sodium acetate, and 1.5 g of PVP were mixed together with 30 mL of water and stirred for 2 h at 40°C. The solution was then placed in a Teflon-lined stainless steel autoclave and heated at 200 °C for 18 h. After the reaction, the autoclave was cooled in ambient conditions, and the red solid product was collected by centrifugation and washed three times with water and ethanol. Finally, the red product was dried under vacuum at 70°C for 12 h. (Appendix 5, A5.6).

30 mg of wide-pore-functionalized SE nanoparticles were dispersed in 2 mL ethanol. 2, 3, or 5 mL of a hematite nanoparticle solution (5 mg mL^{-1} in ethanol) was then added dropwise, and this solution was stirred for 24 h at 2000 rpm.¹⁹⁷ The resulting nanocomposite (SE-WP-Fe) was collected by centrifugation and washed three times with ethanol. (Appendix 5, A5.7)

3.2.16 Diffuse Reflectance Spectroscopy

Reflectance data was collected for dried hematite nanoparticles using a Cary 5000 Series UV-Vis spectrophotometer (Agilent Technologies) with a single beam range between 360 – 800 nm using an EasiDiff reflectance accessory (PIKE Technologies, Inc.).

3.2.17 Electron Paramagnetic Resonance

Electron paramagnetic resonance (EPR) spectroscopy was performed at the McGill Chemistry Characterization facility (MC²) at McGill University in Montreal, Canada. Spectra were acquired on a Bruker Elexsys E580 X band EPR instrument using a high sensitivity resonator. The sample was analyzed in a flat cell (Suprasil, 150 μL , 0.3 mm wide) to minimize signal loss. A1G

modulation amplitude and 20 mW power were used for the acquisition. A polynomial baseline correction was applied to each spectrum before fitting. Fitting was performed using WinSim2002 version 0.98 developed by the National Institute of Environmental Health Sciences at the National Institutes of Health. 50 mM solutions of 5,5-dimethyl-pyrroline N-oxide (DMPO) in methanol were used within 1 h of their preparation. In all cases, 2 mg mL⁻¹ colloidal solutions of nanoparticles were used. In all samples involving H₂O₂, 10 μL of 30% H₂O₂ were added to a 2 mL dispersion of 2 mg/mL nanoparticles immediately before irradiation and/or signal acquisition. 808 nm irradiation was performed using the same laser previously discussed. 532 nm excitation was performed using a handheld diode laser (500 mW). For the irradiation experiments, samples were irradiated while inside the flat cell and the flat cell was immediately inserted into the EPR instrument for analysis after 15 min of irradiation. Control samples were treated identically to the irradiated samples.

3.2.18 Evaluation of the photocatalytic activity of SE-WP-Fe system

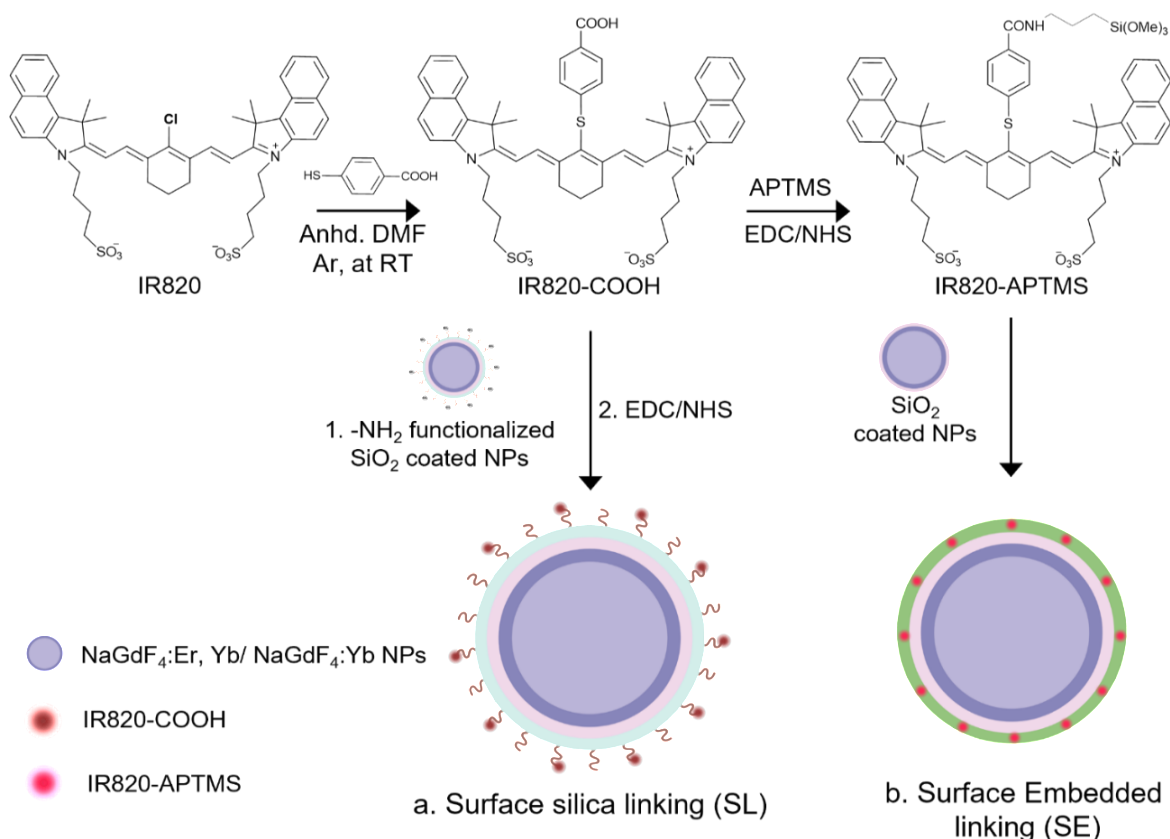
The photocatalytic activity of the SE-WP-Fe nanocomposites was evaluated by observing the degradation of Rhodamine B when exposed to 808 nm near-infrared laser irradiation. A mixture of 30 mg of the nanoparticles, 50 μL of 30% H₂O₂, and 10 mL of rhodamine B solution (4 × 10⁻⁶ M) was stirred for 1 h to reach the adsorption-desorption equilibrium of the dye with the catalyst. The stirred solution was then exposed to 808 nm irradiation and 1.5 mL aliquots were collected every 10 min. After removing any solid precipitate by centrifugation, an absorption spectrum (Agilent Technologies, Cary 5 Series UV–Vis–NIR Spectrophotometer) of each aliquot was recorded to evaluate the absorbance of the Rhodamine B.

3.3 Results and Discussion

The NaGdF₄:2% Er³⁺,20% Yb³⁺/NaGdF₄:20% Yb³⁺ active-core/active-shell nanoparticles used throughout this work were synthesized using a double-injection thermal decomposition method.⁷² The as-synthesized core and core/shell nanoparticles were characterized by TEM and PXRD. TEM micrographs display uniform size distributions, with an average core diameter of 19.8 ± 1.5 nm and core/shell diameter of 30.2 ± 3.0 nm, yielding a shell thickness of approximately 5.2 nm (**Figure S3.1a and b**). The PXRD diffractograms are consistent with the hexagonal NaGdF₄ structure (**Figure S3.1c**).¹⁹⁸ upconversion luminescence spectra upon 976 nm excitation, are displayed in (**Figure S3.1 d**). The characteristic green emissions of Er³⁺ from the ²H_{11/2}/⁴S_{3/2}→⁴I_{15/2} transitions are centered at 525 and 550 nm, respectively. Additionally, the red emission at 660 nm from the ⁴F_{9/2}→⁴I_{15/2} transition is also observed. As expected, a nine-times enhancement in the upconversion luminescence intensity for the core/shell LnUCNPs is observed relative to the core-only LnUCNPs.

Commercial IR820 dye was modified with 4-mercaptobenzoic acid at the central aryl ring of the dye (herein referred to as IR820-COOH), which is ideal for this study since it can be excited at wavelengths ranging from 780–830 nm (**Figure S3.2a**), with a broad emission band that overlaps with the absorption of Yb³⁺ (**Figure S3.2b, Table S3.1**).⁵¹ The structure of IR820-COOH was confirmed using absorption spectroscopy, ¹H-NMR spectroscopy, and MALDI-TOF mass spectrometry (**Figure S3.2-S3.4**).

In this study, two methods of covalent linking of the IR820-COOH dye to the LnUCNPs were investigated: surface silica linking (SL) and silica embedded linking (SE) (**Scheme 3.1**). Although the method of linking the dye to the surface of a silica shell has been previously reported, it helps us to establish a benchmark to assess the photostability and the enhancement factor for the covalent embedded system.^{184,199} The SL method employs covalently linking the carboxylic acid-functionalized dye onto the surface of amine-functionalized silica-coated LnUCNPs by EDC/NHS amide coupling reaction, after the silica shell has been formed (**Scheme 3.1a; Table S3.2**). The SE method involves first modifying IR820-COOH through EDC/NHS amide coupling with APTMS to produce IR820-APTMS, which results in the dye being embedded in the silica shell during polymerization on the LnUCNP surface (**Scheme 3.1b**).



Scheme 3.1. Scheme of the two types of nanoparticle systems investigated in this work, where IR820 is functionalized at the central aryl ring to generate IR820-COOH to generate (a) NaGdF₄:Er³⁺,Yb³⁺/NaGdF₄:Yb³⁺ coated with silica and IR820-COOH linked to the surface via the EDC/NHS amide coupling reaction (SL) and (b) the NaGdF₄:Er³⁺,Yb³⁺/NaGdF₄:Yb³⁺ coated with silica and IR820-APTMS embedded into the silica shell (SE). Created with BioRender

Silica shells with a thickness of 5 ± 1.5 nm and 4 ± 1.0 nm were obtained for the SL and SE systems, respectively (**Figure 3.1a and b**). The formation of the SL system was also characterized by FT-IR spectroscopy (**Figure S3.5**) confirming the presence of the amide bond between the dye and silica shell at the surface of the LnUCNPs.

Since it is essential to obtain a dye-sensitized system with maximal brightness to enable high sensitivity and lower detection limits for any application, various concentrations of the dye were studied in both methods to establish the optimum concentration of dye for improved upconversion luminescence under 808 nm excitation (**Figure S3.6-S3.7**). It is well-recognized that elevated concentrations of dye can lead to self-quenching, while low concentrations will not absorb sufficient NIR light.^{111,113,200} For the SL system, this was achieved by adding various concentrations of IR820-COOH to the EDC/NHS reaction. In contrast, modulating the dye content

in the SE system is difficult because of the distance-dependent nature of the energy transfer between the dye and the LnUCNP. Reagent quantities had to be carefully tailored (**Table S3.3**) to obtain similar-sized silica shells around the LnUCNPs in the range of 4-5 nm (**Figure S3.8**) such that a comparison can be made.

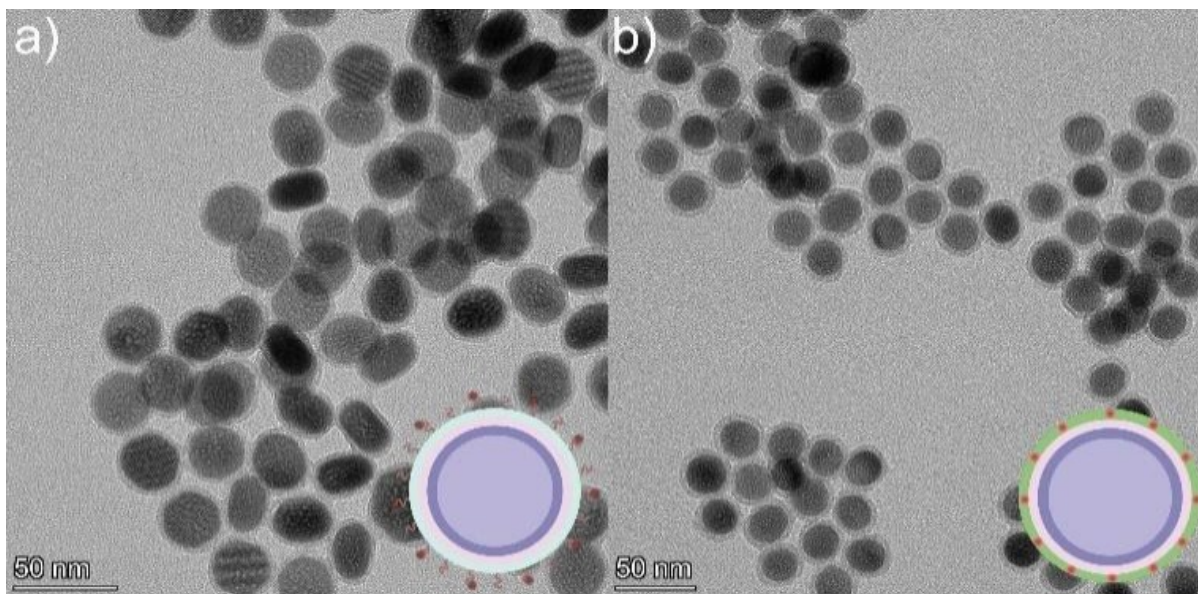


Figure 3.1 TEM micrographs of (a) LnUCNPs coated with amine-functionalized-SiO₂ for the SL system (b) LnUCNPs coated with IR820-APTMS embedded in the silica matrix in the SE system.

The upconversion emission spectra were recorded for both systems upon 808 nm excitation, showing characteristic Er³⁺ green and red emission bands (**Figure 3.2**). It is evident for both methods that as the concentration of the dye increases, the Er³⁺ emission intensity increases, however beyond 340 and 390 dye molecules per nanoparticle (for the SL and SE systems respectively), any further increase in dye concentration leads to quenching of the UCL. Since NIR dyes have a small Stokes shift, two of the same dye molecules that are in close proximity can experience FRET, resulting in the self-quenching observed, known as homo-FRET.^{201,202} Moreover, π -stacking could also contribute to quenching, though this is unlikely in the SE system since the dyes are spatially separated and their movement is restricted within the silica framework.

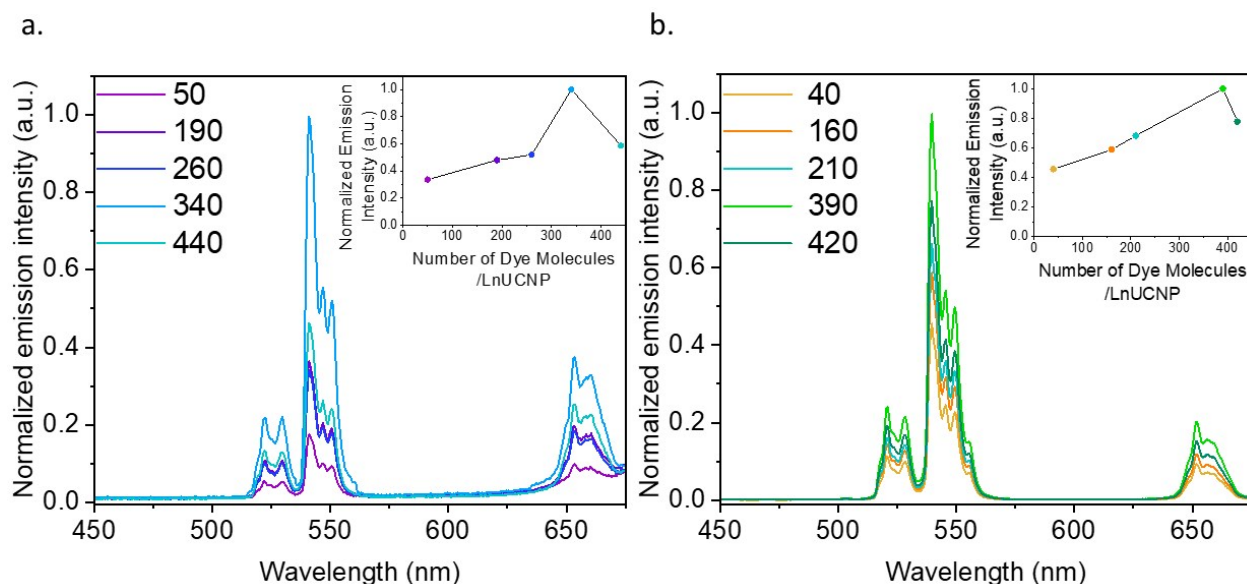


Figure 3.2 Upconversion emission spectra of the (a) SL system with the different number of dye molecules per LnUCNP. b) SE system with different numbers of dye molecules embedded into the silica shell per LnUCNP.

Comparing the upconversion luminescence intensities between the SL and SE system at their respective optimal dye concentrations are shown in **Figure 3.3**. As observed in **Figure 3.3a** and **Figure S3.9**, the SE system is 50% more intense than the SL system. The major difference between the two systems is the distance between the Yb^{3+} ions in the LnUCNP and the dye molecules. In the SL system, the dye molecules are spatially separated from the LnUCNPs due to the silica shell with a minimum distance of 5 nm as per the silica shell thickness. In contrast, in the SE system, the dye molecules are within the silica shell and therefore in closer proximity to the Yb^{3+} ions in the LnUCNP, with a maximum distance of 4 nm (from the LnUCNP surface to the edge of the 4 nm thick silica shell). As such, there should be a more efficient energy transfer between the dye molecules in the SE system and the Yb^{3+} ions.

For further comparison, the SL and SE systems were compared with a control sample where IR820-COOH was electrostatically linked to the surface of the LnUCNPs. Absorbance studies on both systems reveal no leakage of the dye even after 15 days, confirming this is not an issue for the covalently linked systems, whereas when the IR820-COOH dye is electrostatically linked there is a substantial release from the LnUCNP surface (**Figure S3.10**). The electrostatically-linked system also showed the least efficient upconversion

luminescence and complete degradation of the dye after 80 minutes of irradiation (**Figure S3.11**).

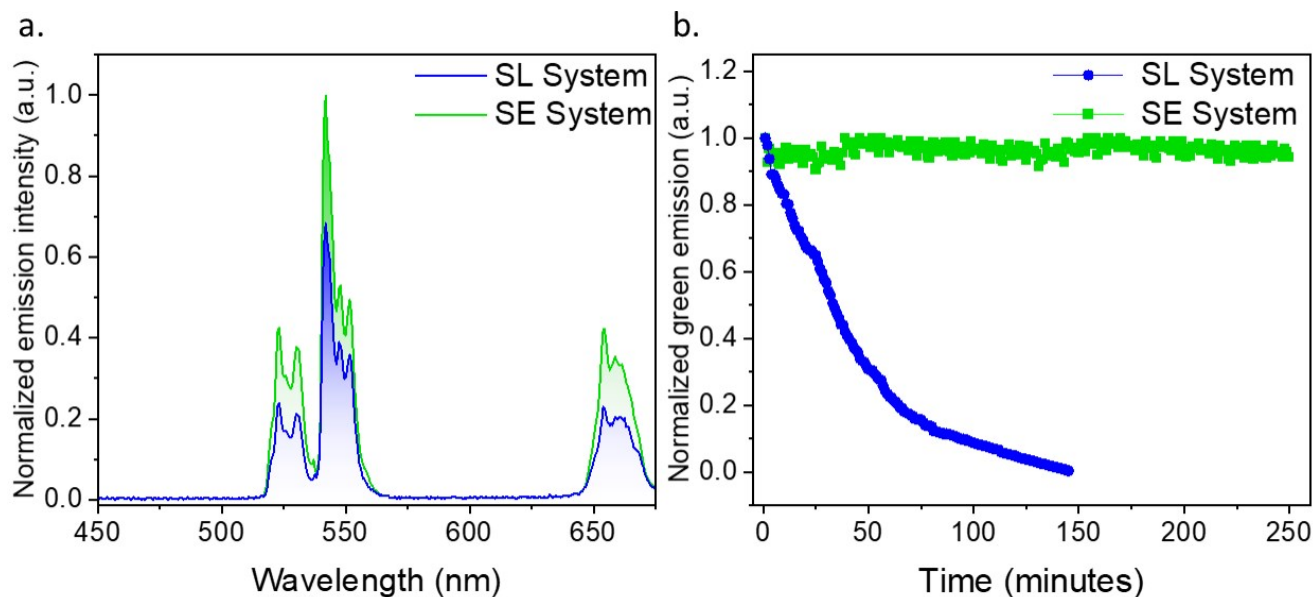


Figure 3.3 a) Normalized upconversion emission spectra of the SL and the SE systems under 808 nm excitation. b) Emission intensity of the $^4S_{3/2}, ^2H_{11/2} \rightarrow ^4I_{15/2}$ transition of Er^{3+} in the SL (blue) and SE (green) systems as a function of time under 808 nm excitation.

Kinetic studies were then completed on both systems (**Figure 3.3b**) to establish the photostability of the dye by evaluating the upconversion luminescence intensity of the $^4S_{3/2} \rightarrow ^4I_{15/2}$ transition of Er^{3+} as a function of irradiation time under 808 nm excitation. After 2.5 hours, the emission of the SL system was no longer observed, indicating that although leaching from the surface is not an issue, the dye molecules bound to the surface of the LnUCNPs were still susceptible to photodegradation. Finally, the emission of the SE system remained constant over four hours of irradiation, suggesting upconversion could be harnessed for extended periods of time. We attribute this improvement in photostability to the likelihood that covalent encapsulation of IR820-APTMS prevents oxygen from reaching the dye molecules, thus no singlet oxygen can be formed to cause degradation. Moreover, the dye in the SE system is fully isolated from the environment and has restricted rotational freedom, while the SL system, notwithstanding its structural stability, is still susceptible to the environment and to *in situ* generated singlet oxygen. Therefore, owing to its encapsulation, the photostability of the dye molecules is considerably enhanced, which

is a major advancement in terms of photostability over the past work in the dye-sensitized LnUCNPs.^{201–205} In summary, by embedding the IR820-APTMS dye into a silica network, it became possible to alleviate dye leaching and photodegradation, thereby generating a photostable dye-sensitized LnUCNP system capable of constant upconversion luminescence emission intensity for over four hours of excitation.

In addition to NIR dyes, the use of Nd³⁺ is common to facilitate upconversion using 808 nm excitation, due to the ⁴I_{9/2}→⁴F_{5/2} absorption band of Nd³⁺ which can transfer energy to Yb³⁺.^{206,207} While both NIR dyes and Nd³⁺ can be excited by the same wavelength, the NIR dyes have the additional benefit of having a higher absorption cross-section. In particular, the absorption cross-section of IR820 at 808 nm excitation is approximately 10⁻¹⁶ cm²⁹¹ while that for the Nd³⁺ ion is about 4x10⁻²⁰ cm².²⁰⁸

To explore the potential differences in Nd³⁺- and dye-sensitized LnUCNPs, we conducted a systematic evaluation of a group of similarly-sized NaGdF₄: Er³⁺, Yb³⁺/NaGdF₄: Yb³⁺/NaGdF₄: 10-20% Nd³⁺ nanoparticles. TEM micrographs for 10, 15, and 20% Nd³⁺ show all compositions have uniform particle sizes and morphology, and nanoparticle sizes and shell thicknesses that are comparable to the SE system (**Figure S3.12**). PXRD analysis confirms the hexagonal crystal structure for all samples (**Figure S3.13**). The upconversion luminescence spectra of the core, core/shell, and core/shell/shell LnUCNPs were recorded under 976 nm excitation to ensure their luminescent properties were similar to each other and with the corresponding SE system (**Figure S3.14**). Emission spectra under 808 nm excitation were recorded to determine the optimal concentration of Nd³⁺, showing that 15% Nd³⁺ exhibited the most intense upconversion luminescence (**Figure S3.15a**). Furthermore, on comparing the upconversion luminescence of the optimized core/shell/NaGdF₄:15% Nd³⁺ and the optimized SE system, under 808 nm excitation, the SE system exhibits 50% more intense emission (**Figure S3.15b**).

To evaluate the difference in energy transfer dynamics from Nd³⁺ or IR820-APTMS to Yb³⁺, upconversion lifetime measurements of Er³⁺ were recorded under 976 nm excitation (green ⁴S_{3/2}→⁴I_{15/2} transition shown in **Figure 3.4**, red ⁴F_{9/2}→⁴I_{15/2} transition shown in (**Figure S3.16a and b**). Using this excitation wavelength avoids absorption by Nd³⁺ or IR820-APTMS, exciting Yb³⁺ directly and allowing the study of potential “back-transfer” from the Er³⁺ ions in the core to the Nd³⁺ or IR820-APTMS in the outer shells. The addition

of Nd^{3+} results in shortening of the Er^{3+} decay times, indicative of FRET between these two species. A possible mechanism is $\text{Er}^{3+}:^4\text{F}_{9/2} + \text{Nd}^{3+}:^4\text{I}_{9/2} \rightarrow \text{Er}^{3+}:^4\text{I}_{15/2} + \text{Nd}^{3+}:^4\text{F}_{9/2}$, which results in quenching of the Er^{3+} upconversion luminescence, either directly or through a shift in the equilibrium of states.⁵⁹ In contrast, the addition of the IR820-APTMS dye results in an increase in lifetime. This, in all likelihood, is a consequence of the formation of the intermediate TEOS shell, which has been reported to encapsulate water more efficiently than APTMS, resulting in greater phonon quenching within the TEOS shell.²⁰⁹ Regardless, no FRET was observed between Er^{3+} and IR820-APTMS, which is likely a contributing factor to why the SE system exhibits brighter upconversion luminescence than Nd^{3+} -doped LnUCNPs.

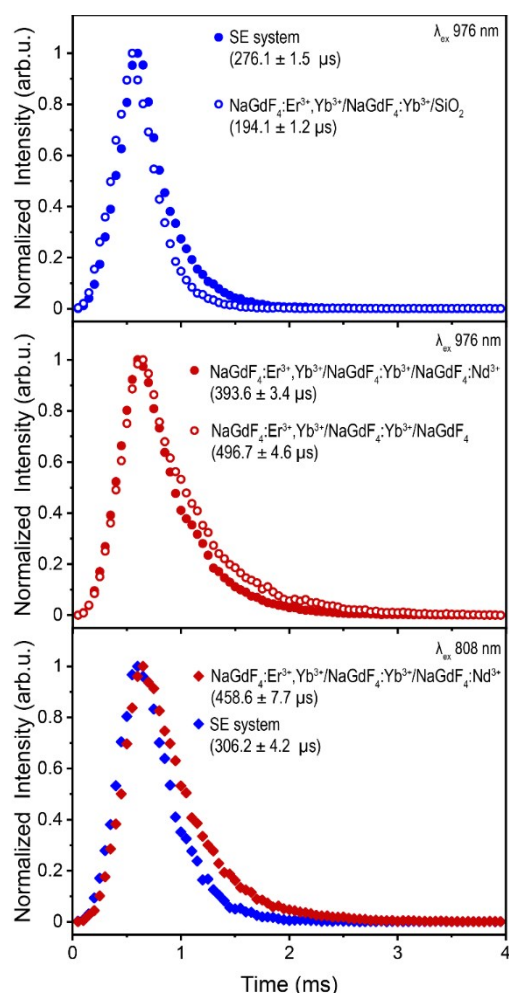


Figure 3.4 Upconversion lifetimes of the $^2\text{H}_{11/2} \rightarrow ^4\text{I}_{15/2}$ transition of Er^{3+} in (a) the SE system (filled circles) and $\text{NaGdF}_4:\text{Yb}^{3+},\text{Er}^{3+}/\text{NaGdF}_4:\text{Yb}^{3+}$ LnUCNPs coated with unfunctionalized silica (outlined circles) under 976 nm excitation. (b) $\text{NaGdF}_4:\text{Yb}^{3+},\text{Er}^{3+}/\text{NaGdF}_4:\text{Yb}^{3+}/\text{NaGdF}_4:15\% \text{Nd}^{3+}$ LnUCNPs (filled circles) and $\text{NaGdF}_4:\text{Yb}^{3+},\text{Er}^{3+}/\text{NaGdF}_4:\text{Yb}^{3+}/\text{NaGdF}_4$ LnUCNPs (outlined circles) under 976 nm excitation. (c) the SE system (blue) and $\text{NaGdF}_4:\text{Yb}^{3+},\text{Er}^{3+}/\text{NaGdF}_4:\text{Yb}^{3+}/\text{NaGdF}_4:15\% \text{Nd}^{3+}$ LnUCNPs (red) under 808 nm excitation.

Lifetime measurements under 808 nm excitation, shown in **Figure 3.4**, were undertaken to assess the dynamics when either Nd³⁺ or IR820-APTMS are excited directly. The resulting decay times are slightly longer than their 976 nm-excited counterparts, due to the additional energy transfer step from Nd³⁺ or IR820-APTMS to Yb³⁺. The decay time for Er³⁺ in the SE system is slightly shorter than in the Nd³⁺-doped LnUCNPs. This could be due to the vibrational modes of silica, resulting in phonon quenching that is not present in the Nd³⁺-doped NaGdF₄ shell. Moreover, there is likely a contribution from the longer sensitizer lifetime, since the forbidden electronic transitions of Nd³⁺ have considerably slower decay times than the allowed singlet transition of IR820-APTMS, also resulting in the SE system decaying faster. However, since the decay time of the IR820-APTMS dye is shorter than Nd³⁺, questions arise regarding its effectiveness as a sensitizer, since shorter decay times are inefficient for FRET.⁹³ Therefore, quantum yield measurements were performed to evaluate the FRET efficiencies from either Nd³⁺ or IR820-APTMS to sensitize Er³⁺. Interestingly, both systems exhibit quantum yields of the same magnitude under 808 nm excitation (Nd³⁺-doped LnUCNPs: $(7.3 \pm 0.87) \times 10^{-4}$ %, SE system: $(9.2 \pm 2.9) \times 10^{-4}$ %, indicating the energy transfer efficiency from excited Nd³⁺ ions or IR820-APTMS molecules to Yb³⁺ is similar, despite their drastically different decay times. While Nd³⁺ → Yb³⁺ was expected to have a greater FRET efficiency, owing to its longer decay time, the spectral overlap between these two species is quite weak, indicating that the energy transfer is phonon-assisted.^{51,210,211} In the case of the SE system, while the decay time is much shorter, the spectral overlap between the dye and Yb³⁺ is much greater, resulting in comparable FRET efficiencies from both these sensitizers. Therefore, considering the higher absorption cross-section of the NIR dye, the SE system exhibits more intense upconversion luminescence emissions.

There are several reports that utilize lanthanide-doped nanocrystals as efficient photocatalysts.^{212–214} However, due to the lack of structural architecture with dye-functionalized LnUCNPs, and the limited thermal and photostability of the NIR dyes, their incorporation with semiconducting photocatalysts has never been explored to our knowledge. In this work, we applied the SE system to facilitate Fenton-type photocatalysis, where 808 nm-sensitized upconversion luminescence can transfer energy to hematite nanoparticles and generate ROS in the presence of hydrogen peroxide. This was accomplished by synthesizing a wide-pore silica shell around the SE system and incorporating the hematite nanoparticles into the pores. We evaluated the photocatalytic activity

by examining the degradation of Rhodamine B, a known carcinogen and water pollutant discharged from textile industries.²¹⁵

The hematite (α -Fe₂O₃) nanoparticles were synthesized *via* a hydrothermal method and characterized by TEM, XRD, and diffuse reflectance.²¹⁶ The α -Fe₂O₃ nanoparticle sizes were measured to be 15.5 ± 5.7 nm by TEM (**Figure S3.17a**), with the expected rhombohedral crystal phase as confirmed by PXRD analysis (**Figure S3.17b**).²¹⁶ Diffuse reflectance confirms a bandgap energy of approximately 2.2 eV, in agreement with the reported value.²¹⁶(**Figure 3.5a and b**). A wide-pore silica shell was coated around the SE system (SE-WP) through a typical sol-gel method that uses mesitylene as a pore swelling agent (**Figure 3.5c**).¹⁹⁶ This method renders a pore size of about 20-25 nm.^{197,217} The hematite nanoparticles were inserted into the pores *via* the self-absorption method.¹⁹⁷ The insertion of hematite nanoparticles was confirmed using TEM, high-angle annular dark field-scanning transmission electron microscopy (HAADF-STEM), XRD, and energy dispersive X-ray spectroscopy (EDX). TEM micrographs demonstrated the random incorporation of hematite nanoparticles into the pores (**Figure 3.5d**), PXRD pattern for the composite nanoconstruct indicates that the diffraction peaks correspond to two distinct crystalline phases: β -NaGdF₄ and α -Fe₂O₃ (**Figure 3.5e**). HAADF-STEM imaging and EDX mapping of Gd, Si, and Fe provided confirmation of the LnUCNP core, silica shell, and hematite nanoparticles in the pores of the SE-WP system. (**Figure 3.5f**).

In this system, the emissions from Er³⁺ under 808 nm excitation correspond to the band gap of hematite and thus are absorbed by the α -Fe₂O₃ nanoparticles such that the Fe³⁺ ions should photocatalytically decompose H₂O₂ to ROS, which degrades Rhodamine B. Varied ratios of α -Fe₂O₃ to SE-WP (w/w) were studied (0.33, 0.50, and 0.83) to evaluate the effect of concentration on photocatalytic activity, herein the Fe₂O₃-loaded SE particles are referred to as SE-WP-Fe. The actual concentration of hematite nanoparticles incorporated in the LnUCNPs was established by UV-vis calibration curve (**Figure S3.18a and b**). As observed in **Figure 3.5g**, the decrease in upconversion luminescence upon increasing ratios of α -Fe₂O₃ to SE-WP indicates increased energy transfer accompanied by scattering, as expected.²¹⁷

To confirm the potential for ROS production *via* the Fenton reaction from this system, electron paramagnetic resonance spectroscopy (EPR) was performed. 5,5-dimethyl-1-pyrroline N-oxide (DMPO), a well-established spin-trapping agent, was used to capture the ROS and enable the

identification of the produced species. Shown in **Figure S3.19**, EPR spectra were obtained for each species in the presence and absence of H₂O₂, and the presence and absence of 808 nm excitation. As expected, in the absence of H₂O₂, in all cases weak or no EPR signal was obtained, confirming negligible ROS production, even under 808 nm excitation. A positive control was performed under direct excitation at 532 nm to excite α -Fe₂O₃ directly, from which the DMPO-X radical was generated; this is a well-established byproduct of substantial hydroxyl radical production.²¹⁸ This was the only species observed when exciting the α -Fe₂O₃ directly. In contrast, under 808 nm excitation, four ROS were identified from the activity of the full SE-WP-Fe system (**Table S3.4**). Specifically, hydroxyl radicals, superoxide radicals, and methylcarbonyl radicals were identified and their values are in agreement with what is observed for DMPO spin adducts in methanol and other Fenton-based systems.^{219,220} Notably, hydroxyl radicals are implicated in Fenton-reaction mediated degradation of Rhodamine B as described by Frindy *et al.*²²¹ The methylcarbonyl radicals are likely due to the decomposition and oxidation of methanol generated in the solution.²¹⁹

In summary, the EPR spectral data suggests the Fenton reaction can occur from excitation at 808 nm in this system. The photocatalytic activities of the SE-WP-Fe system when excited with NIR light, were evaluated by monitoring the degradation of rhodamine B in methanol. It is known that the photogenerated electrons and holes in the semiconductor will travel to the surface, but many electron-hole pairs recombine during this process and do not contribute to the photocatalytic reaction.^{213,214,222,223} Thus, although increasing the α -Fe₂O₃ nanoparticles improves the absorption rate of upconverted emission, it also aggravates the recombination of photogenerated charge carriers and thus affects the activity of the photocatalyst.²¹³ For this reason, several different ratios of α -Fe₂O₃ to LnUCNP (w/w) were evaluated for their photocatalytic activity. As shown in **Figure 3.5h**, no detectable change in the rhodamine B concentration was observed when the α -Fe₂O₃ nanoparticles were exposed to 808 nm light alone, confirming this low-energy wavelength does not excite the hematite. Similar results were observed when the SE system was studied in the absence of hematite in the pores (**Figure 3.5h**). The SE-WP-Fe nanoconstruct caused the successful degradation of rhodamine B under NIR irradiation for 100 minutes, with degradation of rhodamine B reaching 65%, 85%, and 75% when the hematite to SE-WP system mass ratios were 0.33, 0.50 and 0.83, respectively (**Figure 3.5h**). It was found that the ratio of 0.50 had the

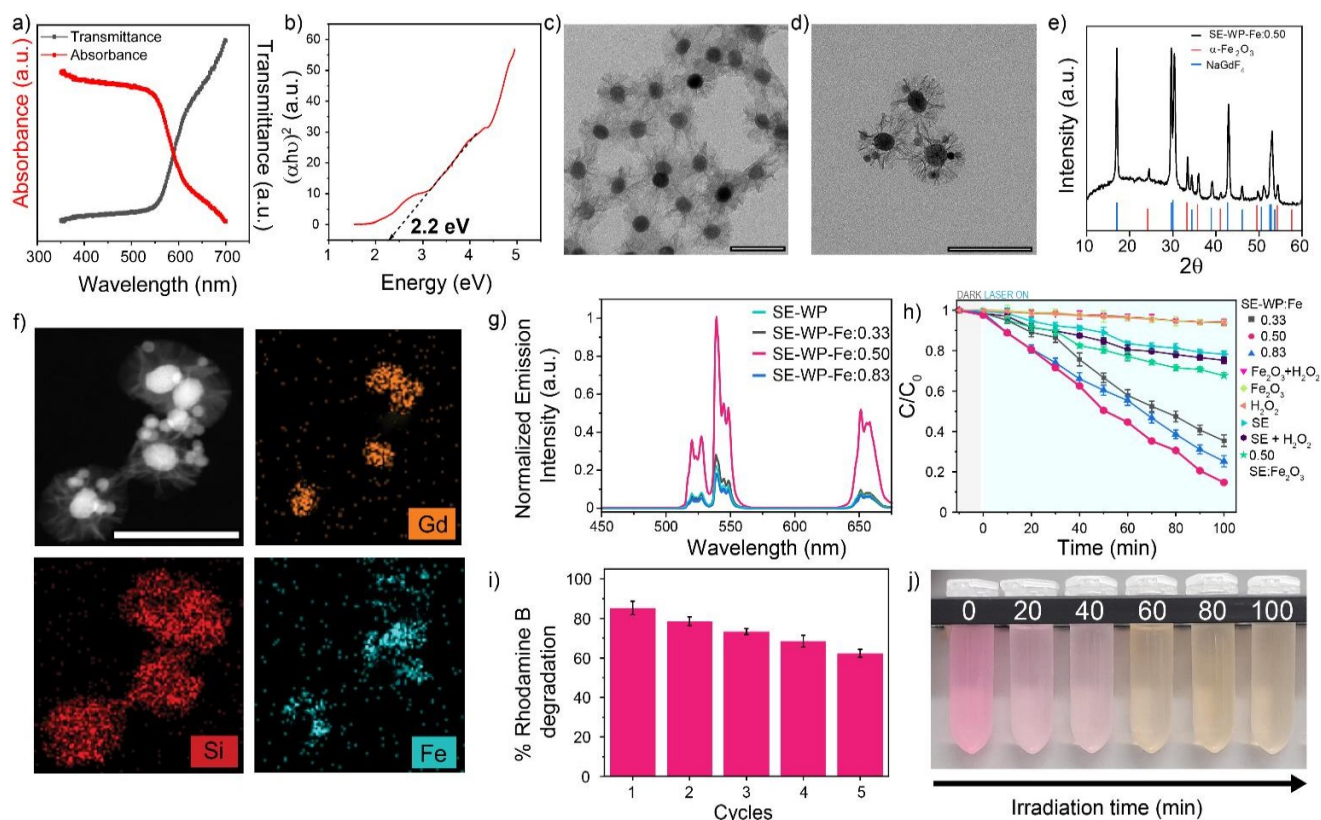


Figure 3.5 (a) Diffuse reflectance spectra for synthesized hematite nanoparticles and (b) the corresponding Tauc plot to determine the band gap energy. TEM micrographs for the wide-pored silica shell synthesized on the SE nanoparticles (c) before and (d) after the incorporation of hematite nanoparticles. (e) Powder XRD diffractogram and (f) HAADF and EDS mapping of the completed SE-WP-Fe system. (g) Upconversion emission spectra of the completed SE-WP-Fe system with varying concentrations of hematite nanoparticles. (h) Rhodamine B degradation measured from the relative absorbance spectra. (i) Repeated cycles of Rhodamine B photodegradation after 100 min, recycling the SE-WP-Fe system. (j) Photographs of the Rhodamine B solutions, illustrating the degradation of the dye after 100 min. All scale bars are 100 nm.

most efficient photocatalytic activity, suggesting that the photocatalytic efficiency is dependent on the ratio of the LnUCNP and Fe_2O_3 nanoparticles.

To assess the reusability of the photocatalyst, the 0.50 SE-WP-Fe system was recycled and used for repeated degradation experiments. After five consecutive cycles, 62% of the initial rhodamine B concentration could still be degraded under the same conditions, indicating the relatively high stability and recyclability of the photocatalytic system (**Figure 3.5i-j**). The decrease in photocatalytic efficiency may be attributed to the dissociation of hematite nanoparticles from the pores during the reaction and/or the recycling process.

To confirm the decrease in photocatalytic activity was not due to the degradation of the dye in the presence of H₂O₂ and hematite nanoparticles, we performed a time-dependent study on the upconversion luminescence of the SE-WP-Fe system under 808 nm excitation in the presence and absence of H₂O₂. As observed in **Figure S3.20**, there was no change in the upconversion luminescence intensity in the SE-WP-Fe system, even after 4 hours of 808 nm irradiation, indicating there is no dye degradation contributing to the loss of photocatalytic activity. In summary, the robust nature of the system presented herein has enabled dye-sensitized LnUCNPs for photocatalysis for the first time, to our knowledge. Embedding the dye within a silica framework prevents deleterious photodegradation, facilitating the use of these systems for long-term, repeated use under prolonged excitation.

3.4 Conclusion

This work addressed the photostability of dye-sensitized LnUCNPs, towards their use in solution-phase applications requiring prolonged and/or repeated irradiation. This was achieved by covalently embedding a modified IR820-APTMS dye into a silica matrix around the nanoparticles, to prevent interactions between the dye and oxygen present in the environment. Kinetic studies were conducted under 808 nm excitation, exhibiting no change in the upconversion luminescence intensity of the dye-embedded system after four hours of irradiation. This enabled the use of the established SE system as a promising candidate to study the photocatalytic capability of dye-sensitized LnUCNPs. A wide-pored silica shell was synthesized around the SE system to encapsulate hematite nanoparticles, which have Fenton-type photocatalytic activity. Degradation of Rhodamine B was observed under 808 nm irradiation, which was found to be efficient and reproducible across five cycles. As a result, the potential uses for dye-sensitized LnUCNPs can be expanded upon now that the limitation of dye photodegradation has been resolved.

3.5 Supplementary Information

3.5.1 Physical and Spectroscopic Characterization of core and core/shell NaGdF₄:Yb³⁺,Er³⁺/NaGdF₄:Yb³⁺ nanoparticles

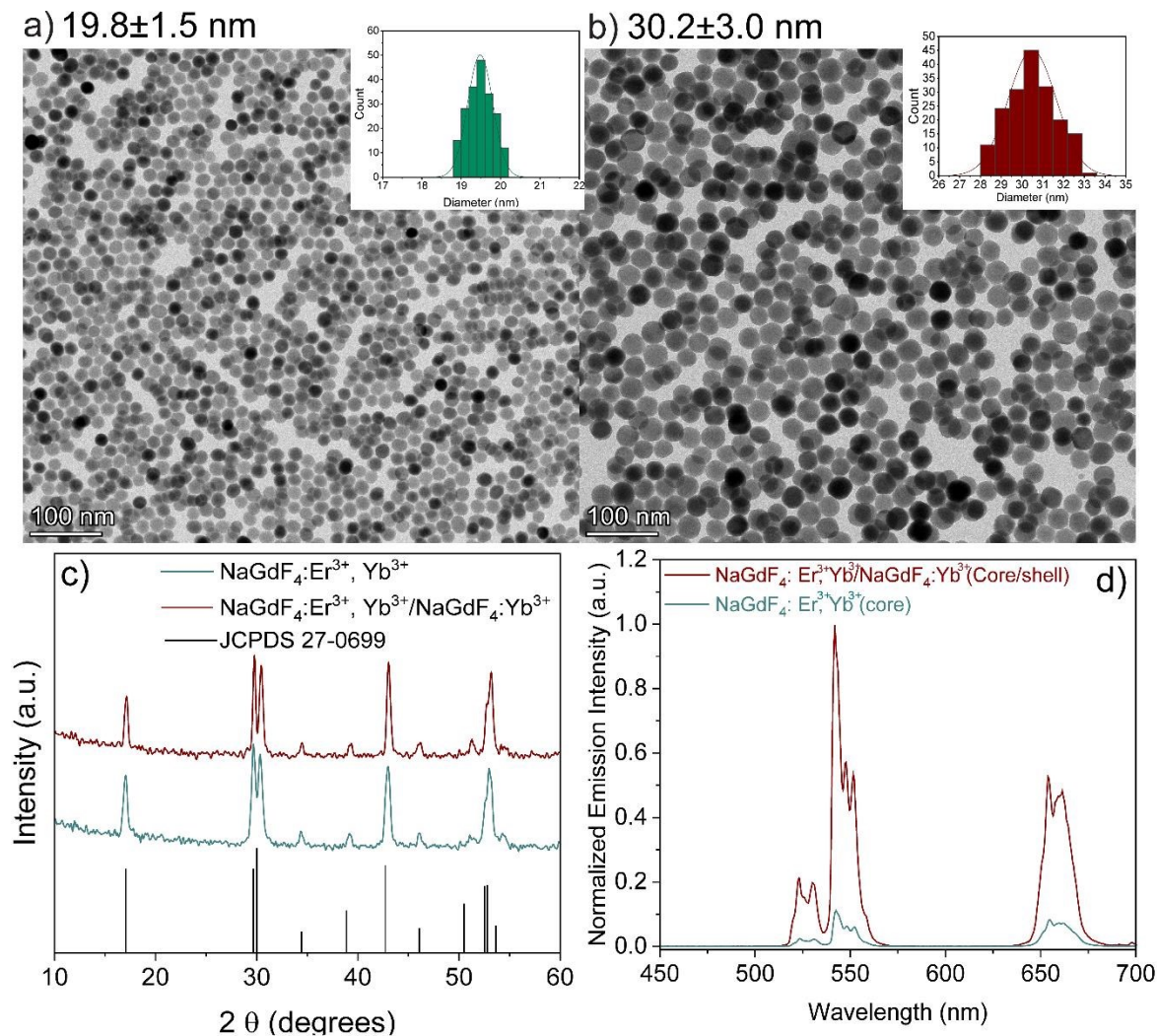


Figure S3.1 TEM micrographs of a) NaGdF₄:Er³⁺, Yb³⁺ (core nanoparticles) b) NaGdF₄:Er³⁺, Yb³⁺/NaGdF₄:Yb³⁺ (active core/active shell nanoparticles) with insets of their respective size distribution. c) Experimental XRD patterns of NaGdF₄:Er³⁺, Yb³⁺ (green) NaGdF₄:Er³⁺, Yb³⁺/NaGdF₄:Yb³⁺ (red) with a simulated line pattern for hexagonal phase NaGdF₄ (bottom plot) is shown for reference (black). d) Upconversion emission spectra of the 2 mg/ml NaGdF₄:Er³⁺, Yb³⁺ (green) and NaGdF₄:Er³⁺, Yb³⁺/NaGdF₄:Yb³⁺ (red) at 976 nm excitation.

3.5.2 Characterization of IR820-COOH and IR820-APTMS dye

3.5.2.1 UV-Visible Absorption and Fluorescence spectra

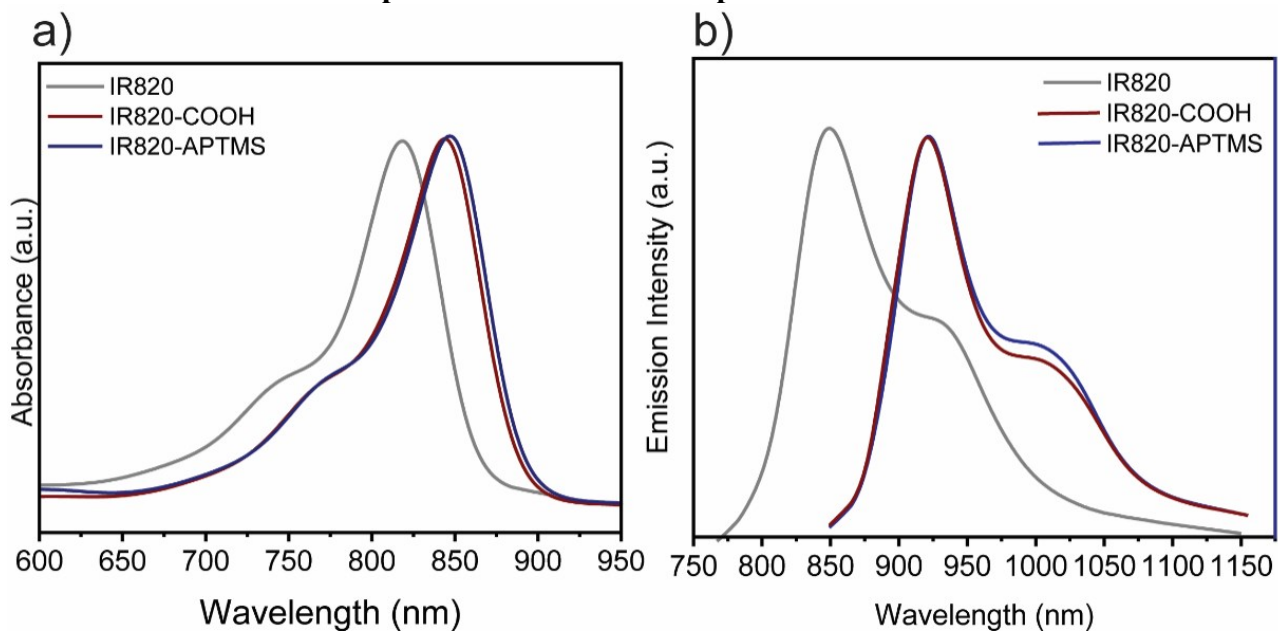


Figure S3.2 (a) Absorbance and (b) emission spectra of the synthesized IR820-COOH and IR820-APTMS, their comparison with IR820 dye (0.1 mg/ml in methanol).

Table S3.1 Absorbance maximum, emission maximum, and molar extinction coefficients for IR820, IR820-COOH, and IR820-APTMS dyes in methanol

NIR Dye	Absorbance maximum (nm)	Emission maximum (nm)	Extinction Coefficient ($M^{-1}cm^{-1}$)
IR820	820	850	198181.12
IR820-COOH	845	920	175625.58
IR820-CONH-APTMS	848	922	152256.89

3.5.2.2 ¹H-NMR Spectra of the Dyes

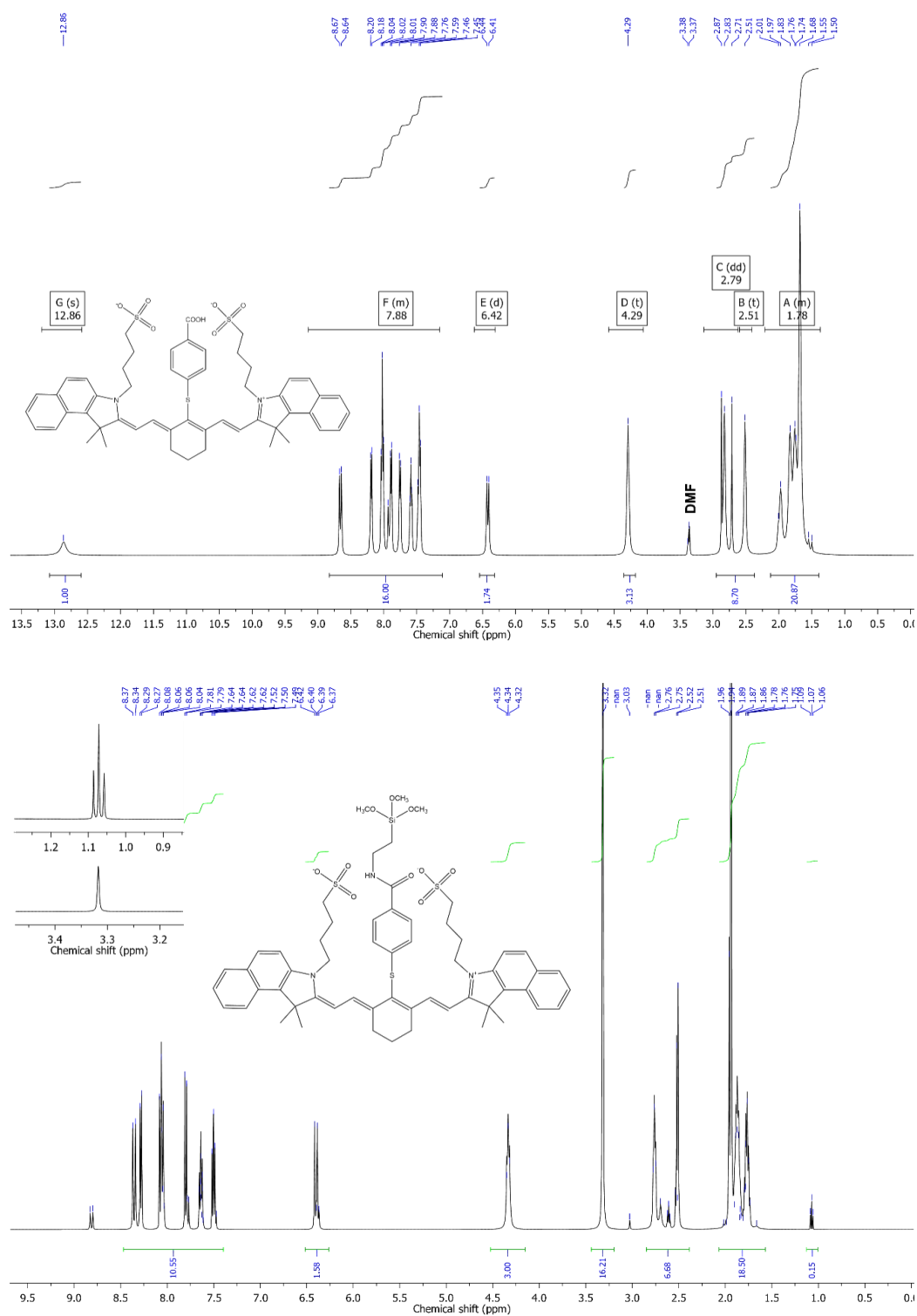


Figure S3.3 ¹H NMR spectra of IR820-COOH (top) and IR820-APTMS (bottom) in DMSO-d₆

3.5.2.3 MALDI-TOF analysis of the dyes

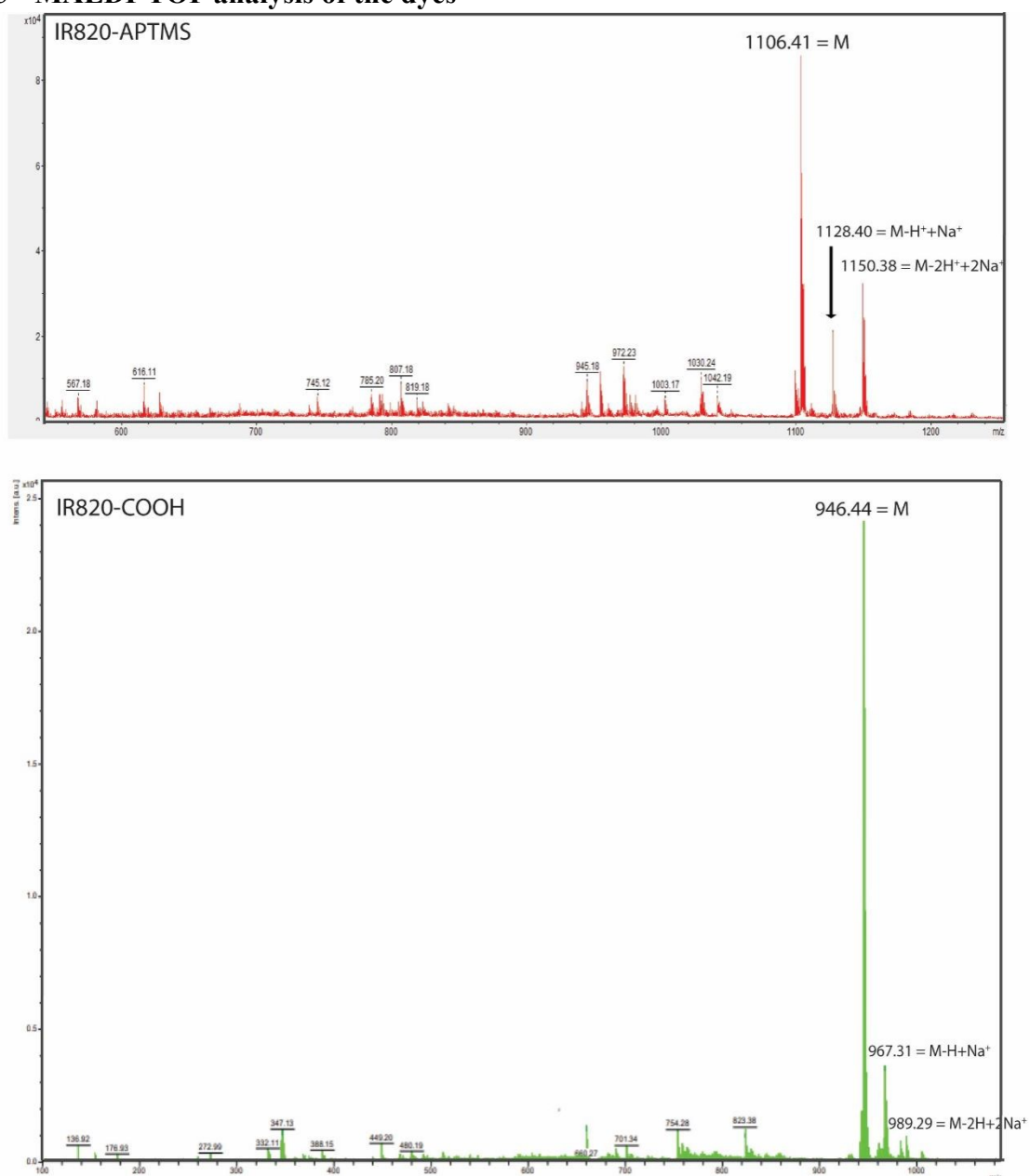


Figure S3.4 MALDI-TOF analysis of IR820-CONH-APTMS (MW=1106.41, top) and IR820-COOH (MW=946.44, bottom).

3.5.3 Surface Silica linking system

Table S3.2 Moles of IR820-COOH dye, EDC, and NHS were added to link different numbers of dye molecules in the SL system.

IR820-COOH (nmol)	EDC (nmol)	NHS (nmol)
10	10	25
20	20	50
28	28	70
34	34	85
42	42	105

3.5.3.1 FT-IR Analysis of LnUCNPs with and without Dye in the SL-System

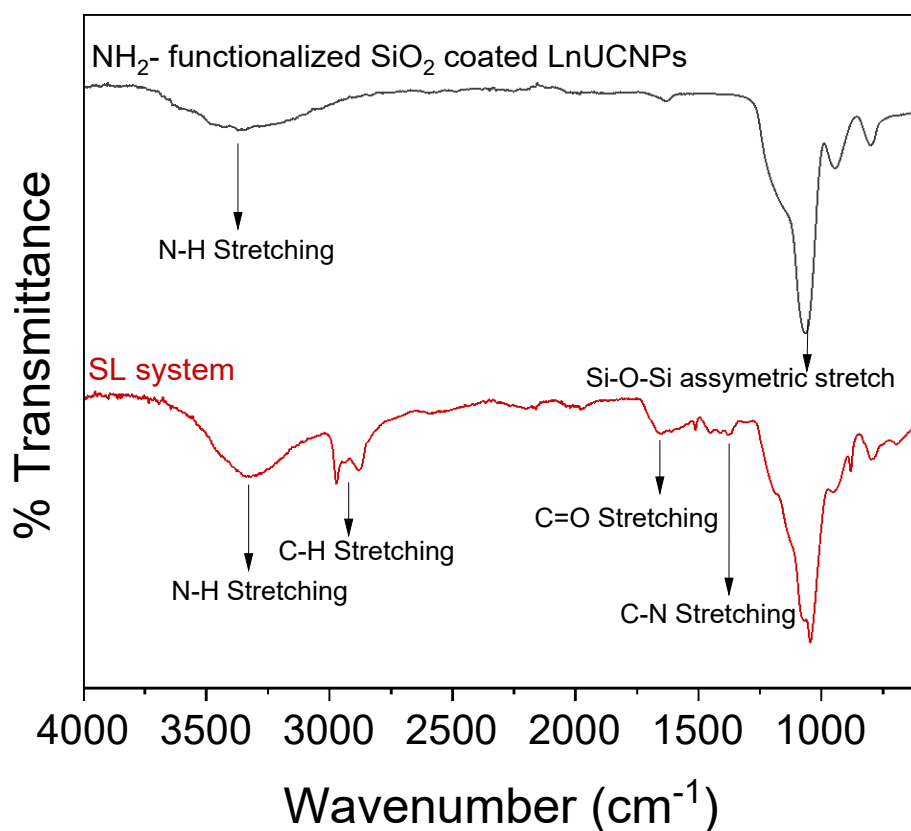


Figure S3.5 FT-IR of amine functionalized silica coated active-core/active-shell LnUCNPs (black) and IR820-COOH linked with amide coupling on the surface of the silica coated active-core/active-shell LnUCNPs (red).

3.5.3.2 Quantification of the dye linked in the SL system

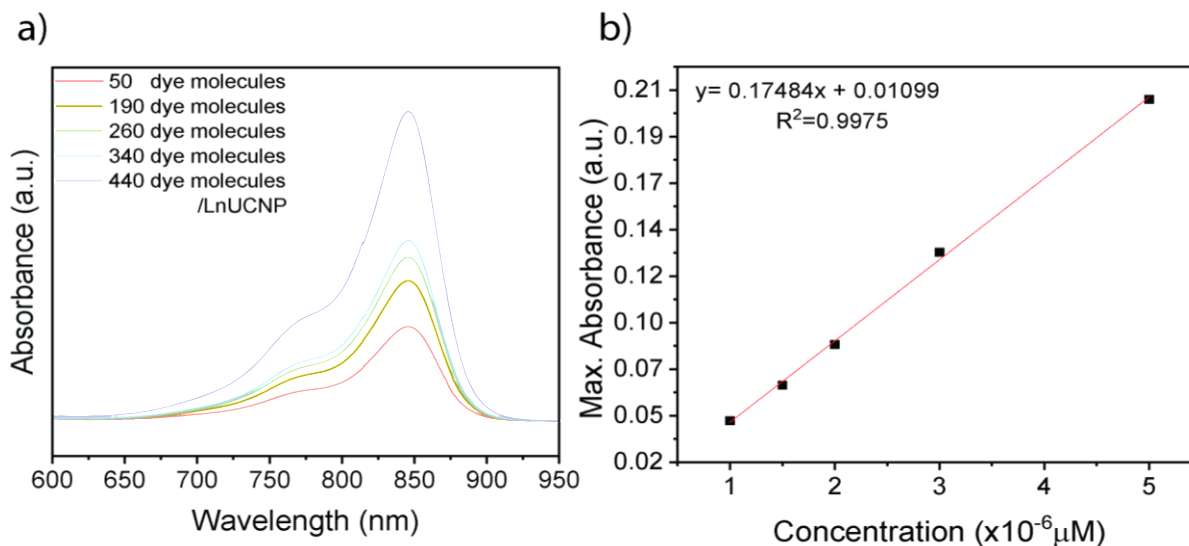


Figure S3.6 (a) UV-Vis absorption spectra for IR820-COOH dye molecules linked in SL system (b) UV-vis calibration curve to quantify the number of dye molecule.

3.5.4 Surface Embedded System

3.5.4.1 Quantification of the dye embedded in the SE system

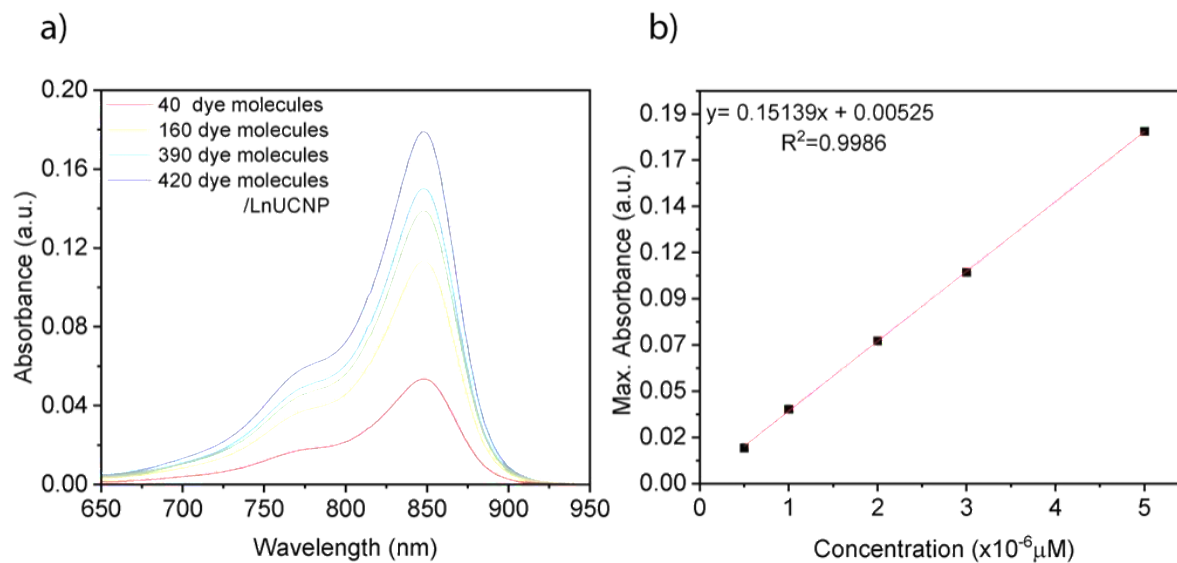


Figure S3.7 (a) UV-Vis absorption spectra for IR820-APTMS dye molecules embedded in SE system (b) UV-vis calibration curve to quantify the number of dye molecules.

Table S3.3 Moles of IR820-CONH-APTMS dye and TEOS added to embed different numbers of dye molecules in the SE system.

IR820-CONH-APTMS (nmol)	TEOS (μmol)
4	26
12	18
16	14
20	10
25	5

3.5.4.2 TEM of Dye-Embedded Silica Shell Samples in the SE System

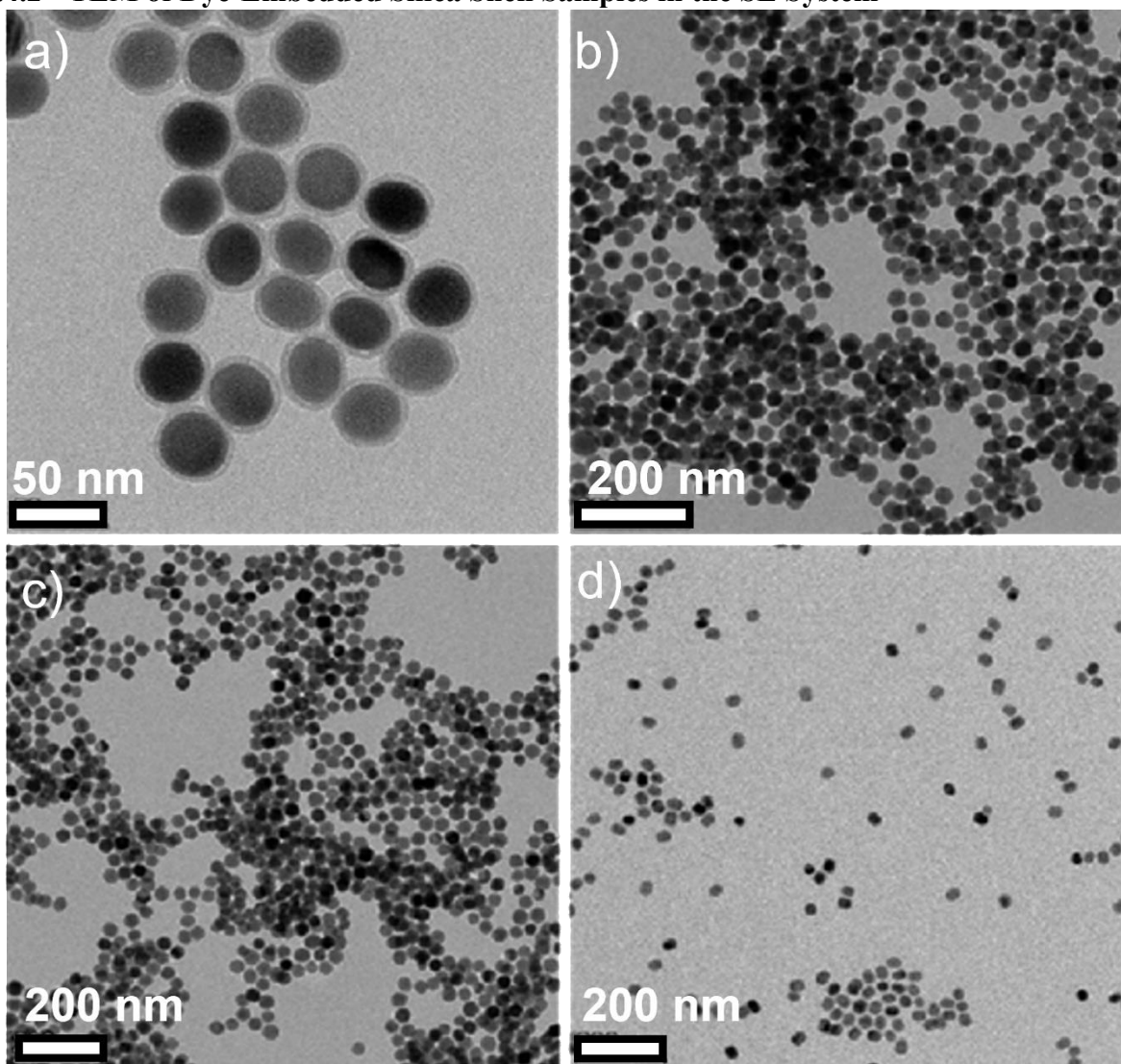


Figure S3.8 TEM micrograph of SE systems having varied amounts of dye embedded in the silica matrix with a thickness of a) 4 nmol dye, 4.2 ± 1.2 nm b) 12 nmol dye, 4.0 ± 0.7 nm c) 16 nmol dye, 4.5 ± 1.5 nm d) 25 nmol dye, 5.2 ± 1.0 nm. Amounts of dye correspond to those in Table S3.3.

3.5.5 Comparative Analysis of the Spectroscopic Properties and Stability between the SL, SE and Electrostatic system

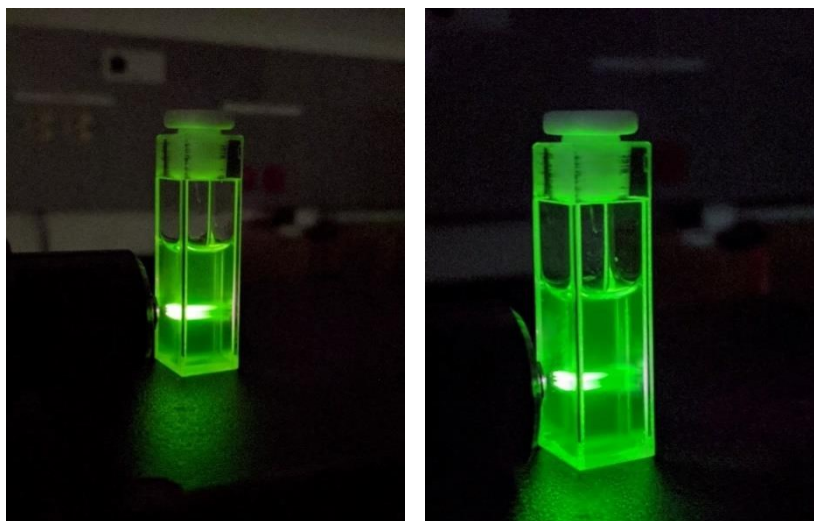


Figure S3.9 Photographs of 5 mg/mL solution in methanol of the (left) SL system and (right) SE system, under 808 nm irradiation.

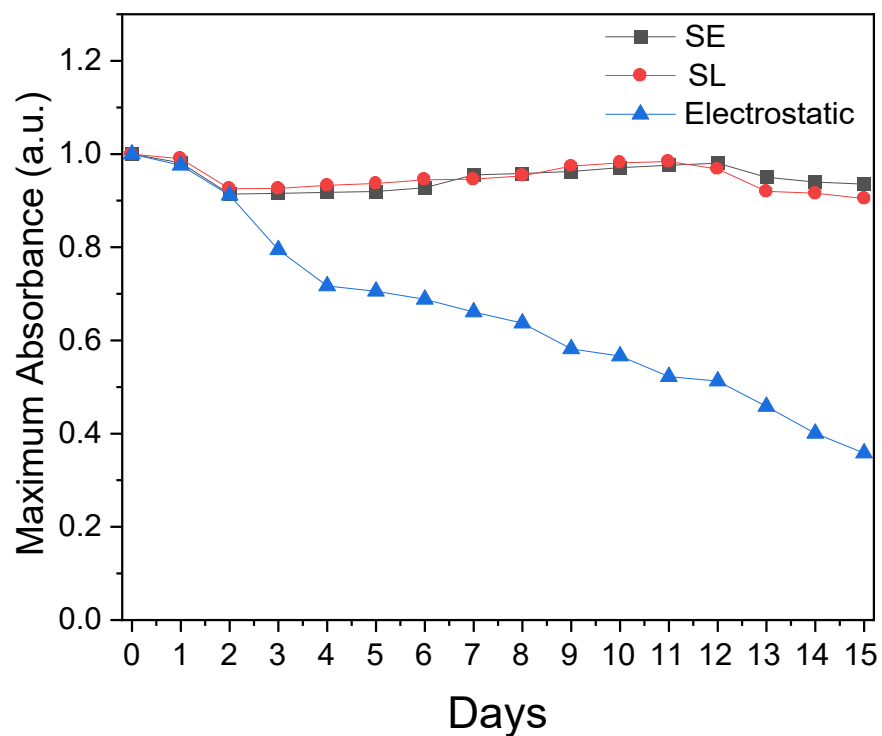


Figure S3.10 Absorbance as a function of incubation time for SE (black), SL (red), and electrostatic (blue) system to monitor leaking of dye from the nanoparticle surface. All samples are 5 mg/mL nanoparticles in methanol.

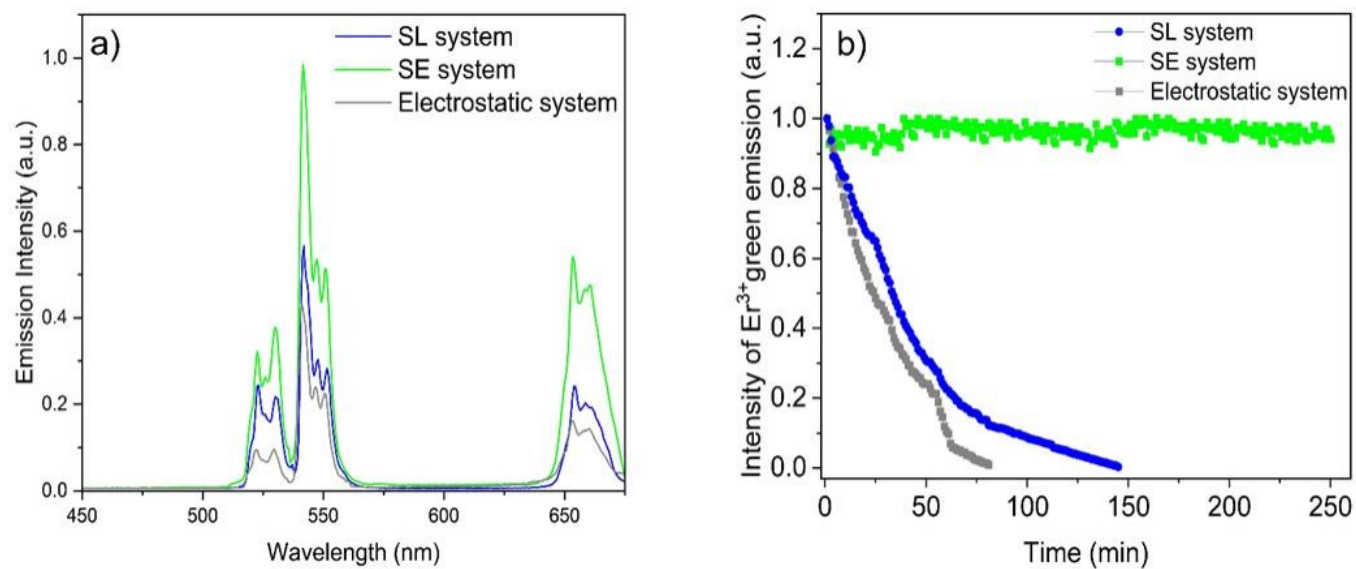


Figure S3.11 a) Comparison of UCL spectra of SL (green) SE (blue) and the electrostatic system (grey) with the dye coordinated to the oleate-free nanoparticle surface upon 808 nm excitation b) Overall emission intensities of SL (green), SE (blue) and electrostatic system (grey) as a function of irradiation time upon 808 nm excitation.

3.5.6 Physical and Spectroscopic Characterization of NaGdF₄: Er³⁺, Yb³⁺/NaGdF₄: Yb³⁺ /NaGdF₄: (10-20%) Nd³⁺

3.5.6.1 TEM images of core, core/shell and core/shell/shell for NaGdF₄: Er³⁺, Yb³⁺/NaGdF₄: Yb³⁺ /NaGdF₄: (10-20%) Nd³⁺

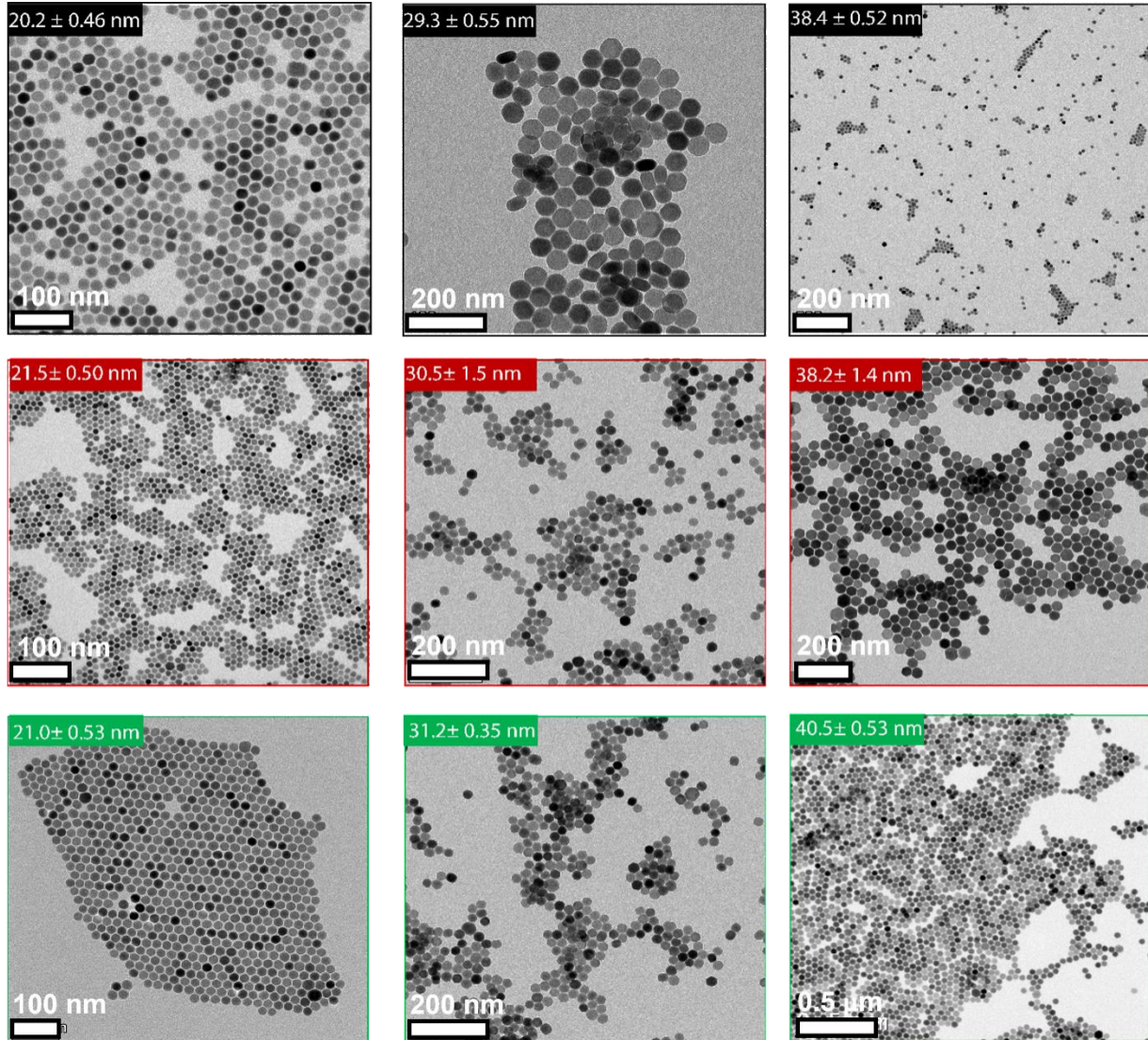


Figure S3.12 TEM micrographs of core, core/shell and core/shell/shell respectively for (a) NaGdF₄:Er³⁺, Yb³⁺/NaGdF₄:Yb³⁺/ NaGdF₄:10%Nd³⁺ (black), NaGdF₄:Er³⁺, Yb/NaGdF₄:Yb³⁺/ NaGdF₄:15%Nd³⁺ (red), NaGdF₄:Er, ³⁺ Yb³⁺/NaGdF₄:Yb³⁺/ NaGdF₄:20%Nd³⁺ (green).

3.5.6.2 PXRD of core, core/shell and core/shell/shell for NaGdF₄: Er³⁺, Yb³⁺/NaGdF₄: Yb³⁺/NaGdF₄: (10-20%) Nd³⁺

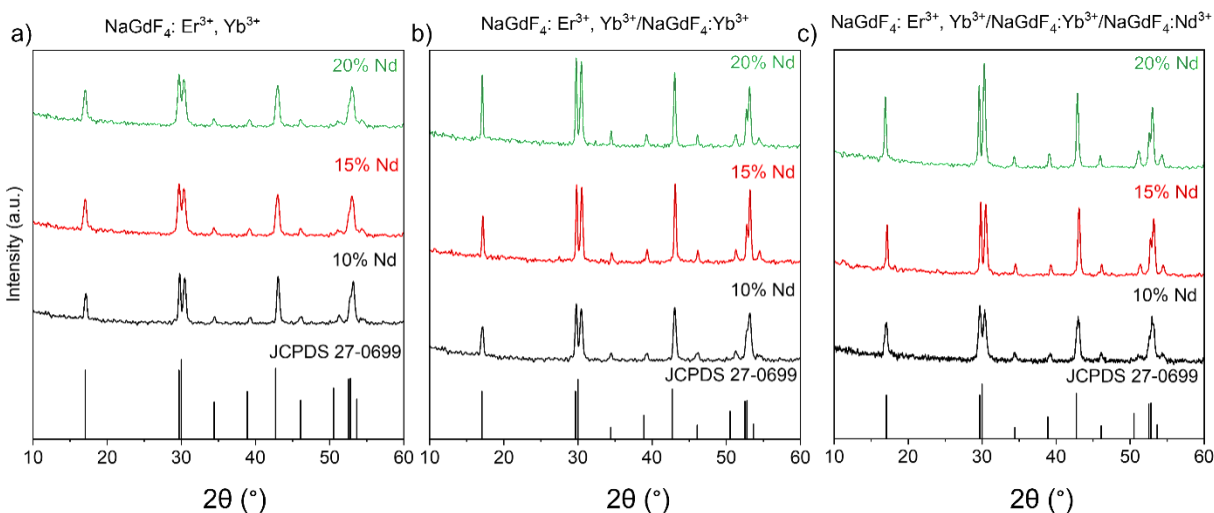


Figure S3.13 PXRD patterns of (a) NaGdF₄:Er³⁺, Yb³⁺ (cores), (b) NaGdF₄:Er³⁺, Yb³⁺/NaGdF₄: Yb³⁺ (core/shell), (c) NaGdF₄:Er³⁺, Yb³⁺/NaGdF₄: Yb³⁺/NaGdF₄: x%Nd³⁺ (core/shell/shell), for 10% (black), 15% (red), 20% (green) Nd³⁺-doped batches.

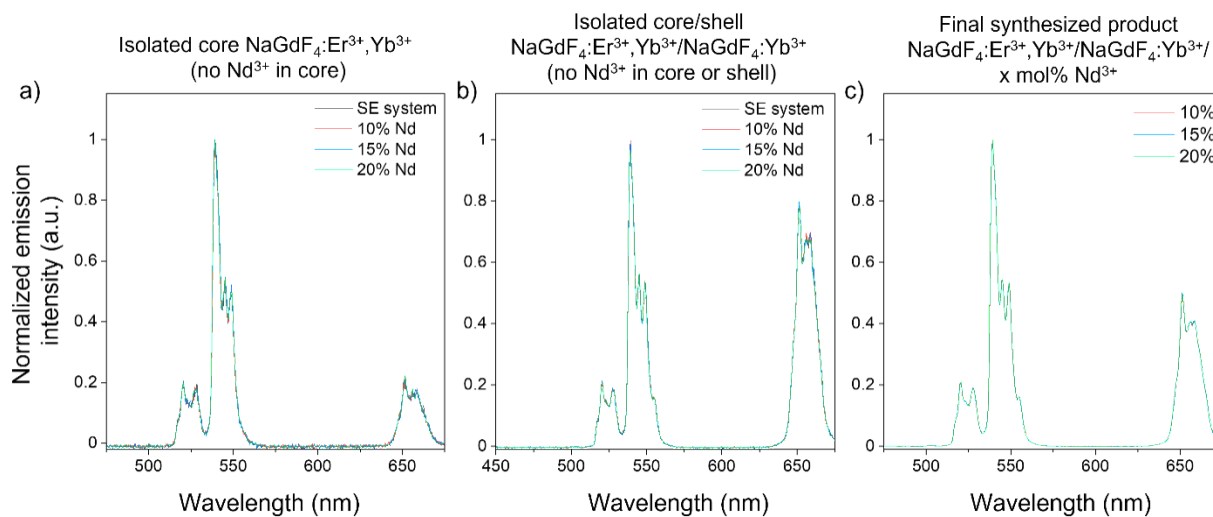


Figure S3.14 UCL spectra under 976 nm excitation of the (a) core and (b) core/shell nanoparticles isolated during the synthesis of (c) core/shell/shell LnUCNPs having 10 (red traces), 15 (blue traces) or 20 (green traces) mol% Nd³⁺ in the outer shell or the core and core/shell samples taken during the synthesis of the SE system (black). An aliquot of the cores and core/shells during the synthesis of the final product was taken and purified to obtain these spectra at 2 mg/mL nanoparticles dispersed in hexanes.

3.5.7 Comparative Analysis of Spectroscopic properties of the SE and the optimized Nd³⁺ system

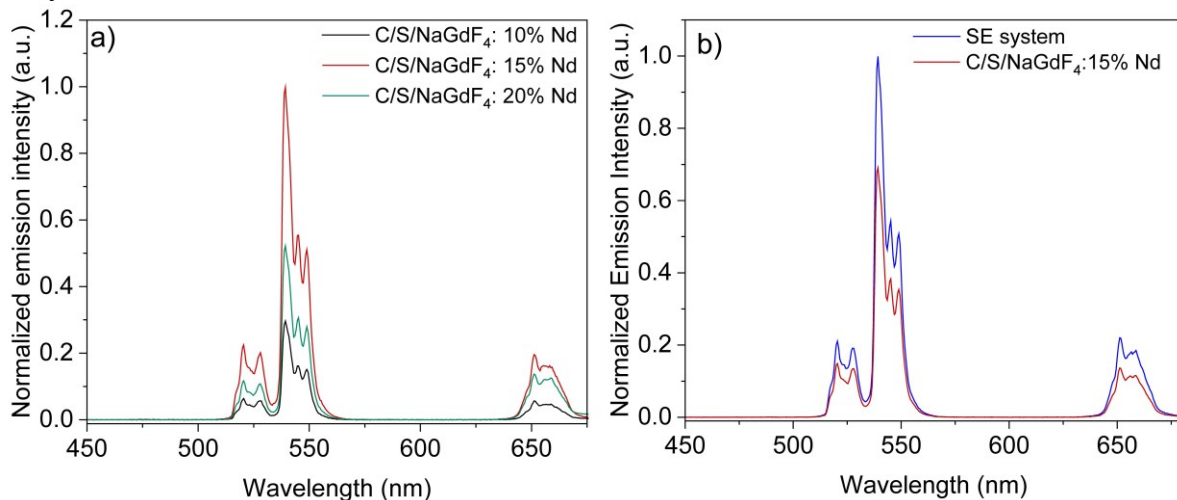


Figure S3.15 Normalized upconversion luminescence spectra under 808 nm excitation for a) (core/shell/shell) NaGdF₄:Er³⁺,Yb³⁺/NaGdF₄:Yb³⁺/NaGdF₄: x%Nd³⁺ x = 10, 15 or 20 mol% Nd³⁺ concentrations (hexanes, 2 mg/mL dispersions) b) upconversion luminescence spectra of oleate-free NaGdF₄:Er³⁺,Yb³⁺/NaGdF₄:Yb³⁺/NaGdF₄: 15% Nd³⁺ and the SE system (2 mg/mL dispersions in methanol)

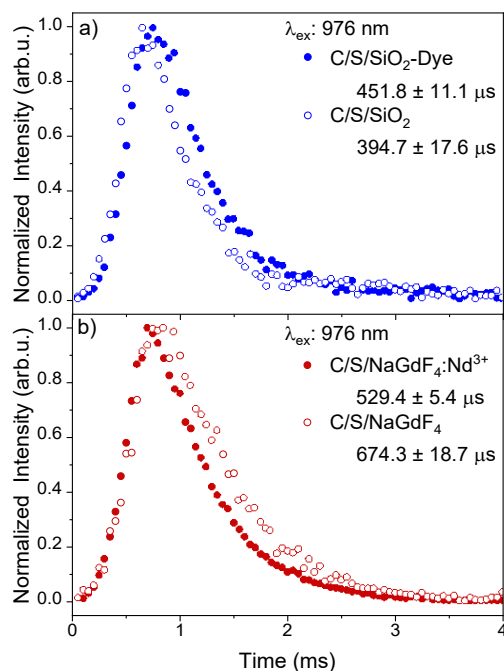


Figure S3.16 Upconversion lifetimes of the ⁴F_{9/2} → ⁴I_{15/2} transition of Er³⁺ in (a) the SE system (C/S/SiO₂-Dye, filled) and NaGdF₄:Yb³⁺,Er³⁺/NaGdF₄:Yb³⁺LnUCNPs coated with unfunctionalized silica (C/S/SiO₂, outlined) under 808 nm excitation. (b) NaGdF₄:Yb³⁺,Er³⁺/NaGdF₄:Yb³⁺/NaGdF₄:15% Nd³⁺ LnUCNPs (C/S/NaGdF₄:Nd³⁺, filled circles) and NaGdF₄:Yb³⁺,Er³⁺/NaGdF₄:Yb³⁺/NaGdF₄ LnUCNPs (C/S/NaGdF₄, outlined circles) under 976 nm excitation.

3.5.8 Evaluation and Quantification of Hematite Nanoparticles in the SE-WP System: A Physical and EPR Analysis

3.5.8.1 Physical Characterization of hematite nanoparticles

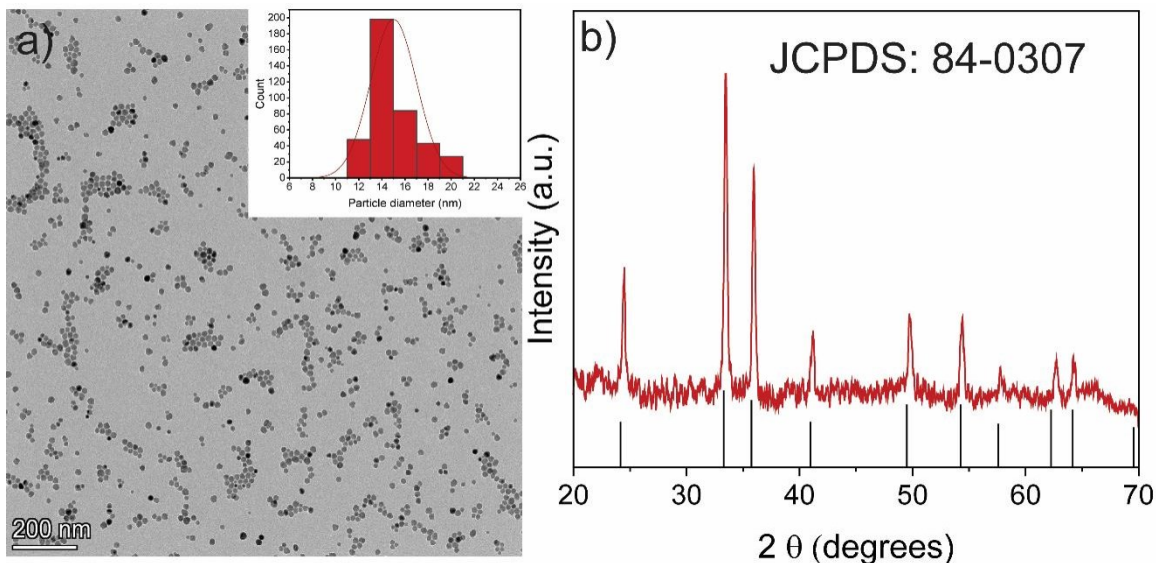


Figure S3.17 (a) TEM micrograph with the corresponding inset of the size distribution (15.5 ± 5.7 nm), (b) Experimental PXRD (red) and JCPDS 84-0307 reference pattern (black) of α - Fe_2O_3 nanoparticles.

3.5.8.2 Quantification of hematite NPs inserted in the wide-pored silica shell around the SE system

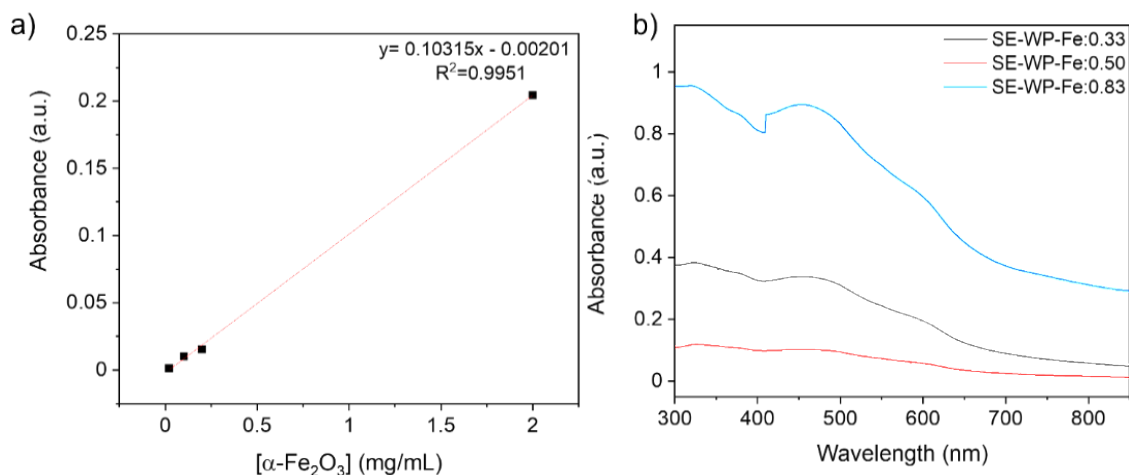


Figure S3.18 (a) Calibration curve generated from absorption spectra of dispersions of α - Fe_2O_3 NPs in ethanol. (b) Absorbance spectrum both used for quantification of the hematite nanoparticles inserted into the pores of the SE-WP nanoparticles (2 mg/mL in methanol).

3.5.8.3 EPR analysis

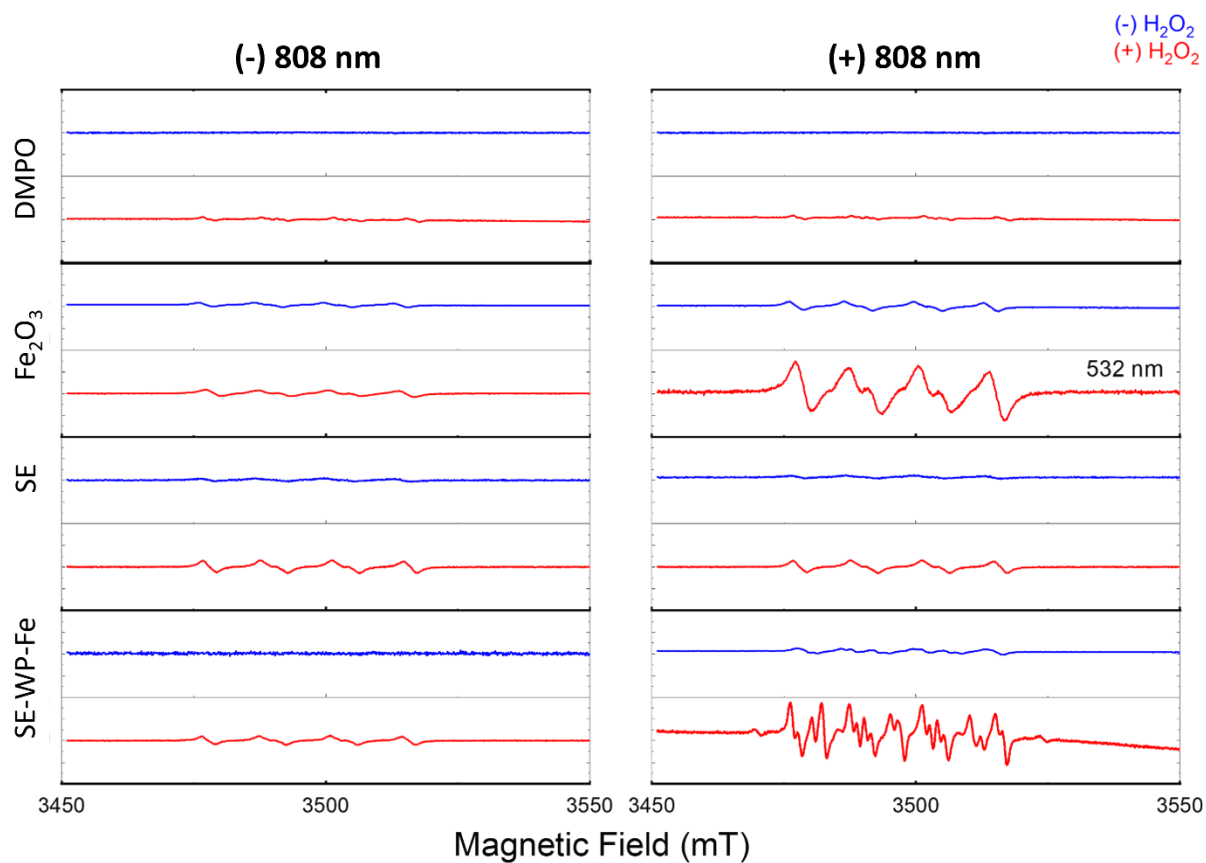


Figure S3.19 Electron paramagnetic resonance spectra of the SE-WP-Fe, SE, Fe₂O₃ with and without H₂O₂ (red and blue, respectively) with DMPO spin trapping agent with and without 808 nm excitation. All spectra were recorded using 2 mg/mL nanoparticles in methanol.

Table S3.4 EPR data corresponding to the spectra presented in Figure S3.19. All samples were recorded in methanol (2 mg/mL dispersions) at room temperature.

Sample	H ₂ O ₂	808 nm	aN	aH	aH2	aN/aH	Assignment ²¹⁹
DMPO	(-)	(-)	--	--	--		N/A
DMPO	(+)	(-)	--	--	--		N/A
DMPO	(-)	(+)	--	--	--		N/A
DMPO	(+)	(+)	13.8	11.1	1.2	1.24	DMPO-OOH (superoxide)
Fe ₂ O ₃	(-)	532 nm	13	12.2	--	1.09	DMPO-X (degradation)
Fe ₂ O ₃	(-)	(-)	13.1	10.3	--	1.27	DMPO-OH
Fe ₂ O ₃	(+)	(-)	--	--	--		
Fe ₂ O ₃	(-)	(+)	13.1	10.3	--	1.27	DMPO-OH
Fe ₂ O ₃	(+)	(+)	13.3	9.9	--	1.34	
SE system	(-)	(-)	--	--	--		
SE system	(+)	(-)	13.5	10.9	--	1.23	DMPO-OOH (superoxide)
SE system	(-)	(+)	--	--	--		
SE system	(+)	(+)	13.5	10.9		1.23	DMPO-OOH (superoxide)
SE-WP-Fe 0.50	(-)	(-)	--	--	--		--
SE-WP-Fe 0.50	(+)	(-)	--	--	--		--
SE-WP-Fe 0.50	(-)	(+)	13.7	9.8	0.7	1.39	DMPO-OH
SE-WP-Fe 0.50	(-)	(+)	13.9	6.7	--	2.07	DMPO-CH ₃ O
SE-WP-Fe 0.50	(-)	(+)	12.9	9.75	--	1.32	DMPO-OH
SE-WP-Fe 0.50	(+)	(+)	13.8	11.2	1.2	1.23	DMPO-OOH
SE-WP-Fe 0.50	(+)	(+)	12.9	9.9	--	1.30	DMPO-OH
SE-WP-Fe 0.50	(+)	(+)	13.9	14.6	--	0.95	DMPO-X (degradation)

3.5.8.4 Kinetic studies of the Photocatalyst in presence and absence of H₂O₂

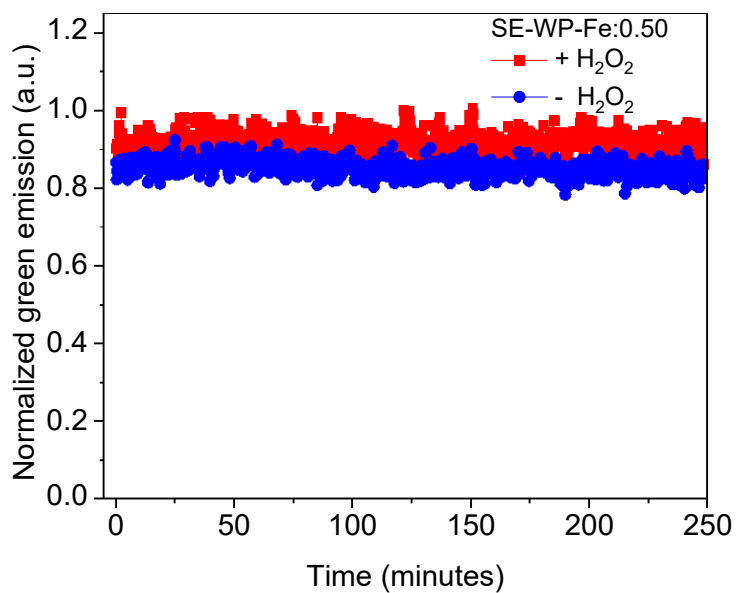


Figure S3.20 Emission intensity of the ${}^2\text{H}_{11/2} \rightarrow {}^4\text{I}_{15/2}$ transition of Er^{3+} in the SE-WP-Fe:0.50 system (2 mg/mL dispersion in methanol) as a function of irradiation time (808 nm excitation) in the presence and absence of H_2O_2 .

Chapter 4: Conclusion

Over the last decade, NIR dyes have become increasingly prevalent in the realm of upconversion sensitization. Nonetheless, there remained a pronounced uncertainty concerning their photostability, which hindered their practical applicability. Prior to the work described herein, there was a lack of detailed understanding regarding the complex interplay among the dye, the sensitizer, and the activator ions within dye-LnUCNP systems as well as their environment. This deficiency has curtailed the performance of dye-sensitized LnUCNP systems, particularly in scenarios demanding prolonged irradiation.

This work aimed to address the gap in knowledge and study the much-overlooked photostability characteristics of IR820 dye-sensitized NaGdF₄:Er³⁺,Yb³⁺/NaGdF₄:Yb³⁺ core/shell nanoparticles. We established the role of singlet oxygen in dye degradation through an in-depth examination of photostability across diverse solvents having varied lifetimes of singlet oxygen and under conditions with argon and sodium azide which prevent the presence of oxygen and scavenge the singlet oxygen, respectively. This brought to light the degradation mechanism of the IR820 dye and the role of the dioxetane intermediate formed during the reaction of oxygen with the dyes. Recognizing this issue, we introduced strategic structural alterations to the IR820 dye by functionalizing it with a sterically hindering thiophenol moiety having different electron-withdrawing capabilities. In this study, incorporating the 4-nitrothiophenol group offered a superior spectral overlap with Yb³⁺ to produce brighter upconversion luminescence, and led to enhanced photostability of the dye. This modified dye, IR820-NO₂, when electrostatically-coordinated to the surface of NaGdF₄:Er³⁺,Yb³⁺/NaGdF₄:Yb³⁺ core/shell nanoparticles, demonstrated an impressive 200% increase in emission intensity when compared to its unmodified counterpart. This enhancement can be credited to a combination of efficient energy transfer, reduced back-transfer, and the optimized overlap between the IR820-NO₂ and Yb³⁺. Our lifetime and quantum yield measurements corroborated these findings. Moreover, our system not only showcased enhanced emission intensity but also sustained these emissions for 90 minutes duration, which was almost double that of unmodified IR820 dye-sensitized systems. In summary, our initial efforts culminated in significant advancements in the capabilities of dye-sensitized upconverting nanoparticles, setting a new standard in the field.

We then moved toward addressing two important remaining challenges with regard to dye-sensitized upconversion. Specifically, we aimed to further improve the photostability of the dye-sensitized system, and the potential for detachment of the dye in systems with electrostatic linkages and the photodegradation in cases requiring extended and repeated irradiation remained areas of concern.

To this end, we improved the dye-sensitized LnUCNP systems even further by attaching the dye to the LnUCNPs using covalent interactions; this resolved the detachment of the dye prevalent in electrostatic systems and further improved the photostability of the dye-sensitized LnUCNP. Unlike the conventional electrostatic dye systems, which often expose the dye to environmental factors that compromise its stability, we devised the strategic step of covalently embedding this modified IR820-COOH dye within a protective silica matrix that surrounded the nanoparticles. This encapsulation was designed specifically to prevent any detrimental interactions between the dye and any environmental oxygen, which we established plays a primary role in dye degradation in the first part of the work. Such a strategy directly addresses one of the primary causes of dye degradation, thereby enhancing its resilience in extended-use scenarios. This was confirmed by the kinetic studies conducted on the embedded system and the conventional surface covalent linked system. These studies carried out under 808 nm excitation, provided empirical evidence of the enhanced durability of the dye-embedded system. Impressively, the upconversion luminescence intensity of the embedded dye system remained constant, even after four hours of continuous irradiation. This level of stability contrasts starkly with the covalent-surface and electrostatic dye-sensitized systems, for which no significant emissions are observed after 150 and 80 minutes, respectively under similar conditions. To assess the spectroscopic efficiency of the dye-embedded system, they were compared with a similar-sized Nd³⁺-doped system, for which photodegradation is not an issue. The lifetime, quantum yield, and luminescence spectra comparison of both systems established the dye-embedded system as more efficient, exhibiting enhanced emission and suggesting dye-sensitization is a truly viable alternative to Nd³⁺-doping as a route to prolonged upconversion sensitization.

Recognizing the potential of our dye-embedded system, we sought to explore further applications. Notably, dye-sensitized upconversion has been touted as a route for achieving enhanced upconversion luminescence but could not be used for photocatalysis due to the role of reactive

oxygen species in such processes, as they would inevitably cause degradation of the dye. This led to the development of a system capable of achieving photocatalysis by generating a silica shell with wide pores synthesized around the dye-embedded system. This shell was explicitly designed to encapsulate hematite nanoparticles, which are renowned for their Fenton-type photocatalytic activity. When this system was tested under 808 nm irradiation for the degradation of Rhodamine B, a successful dye-sensitized upconversion-mediated photocatalytic process was demonstrated. Not only was the degradation process efficient, but it was also consistently reproducible across multiple cycles, indicating the nanoparticles could be harvested and re-used without any additional purification steps, an important concept for sustainable practices in photocatalytic pollutant degradation.

In essence, our advancements have achieved two pivotal outcomes. Firstly, we've effectively addressed and mitigated the limitation of dye photodegradation, a long-standing impediment in the field of dye-sensitized LnUCNPs. Secondly, by doing so, we've opened the doors to an expanded range of applications for these nanoparticles. The breakthroughs from this thesis promise a brighter and more versatile future for dye-sensitized LnUCNPs in various applications.

Chapter 5: Future Work

The embedded dye system explored in this study represents a significant advancement in our understanding of their properties and their potential applications. As with any scientific endeavor, this research not only presents conclusive findings but also unveils new areas of exploration. Based on the outcomes and challenges identified, it is clear that multiple pathways can be pursued to further refine and apply our discoveries. For a structured approach to these possibilities, we categorize the future research avenues into immediate, short-term studies and broader, longer-term objectives.

5.1 Short-term fundamental studies

5.1.1 Environmental Adaptability

The performance and stability of any nanocomposite system can be significantly influenced by the environment in which it operates. The embedded dye system, as characterized in our study, was primarily examined in a colloidal dispersion in methanol. To assess the broader applicability and adaptability of this system, it is essential to evaluate its behavior under varied conditions. Understanding how the embedded dye system behaves across these varied environments will provide a broader view of its versatility, guiding future applications and potential modifications.

Water poses distinct challenges due to its polar nature. Studying the embedded dye system in aqueous conditions will help us understand potential interactions, stability concerns, and any resultant changes in optical properties. Water molecules can coordinate to the lanthanide ions, which may lead to dynamic changes in local coordination chemistry. This, in turn, can impact the emission profile of the LnUCNPs. Notably, LnUCNPs dispersed in water have been observed to exhibit different emission profiles when compared to those dispersed in non-polar solvents.¹⁶³ Understanding these solvent-dependent properties is crucial for optimizing dye-embedded LnUCNPs for specific applications, ranging from bioimaging to environmental sensing.

Transitioning from a colloidal system to a solid-state often impacts the nanocomposite's characteristics, such as aggregation behavior. Characterizing the dye-embedded system in powdered forms will provide data on how these transitions influence its performance. One of the key considerations when transitioning to a solid-state is the potential for different quenching mechanisms to come into play. In a colloidal system, solvents can act as a buffer to reduce inter-

particle concentration quenching.²²⁴ However, in a solid-state system, particles are in close proximity, and the absence of solvent molecules could facilitate or even exacerbate these quenching mechanisms, affecting the overall UCL efficiency.²²⁵ Moreover, thermal properties can vary greatly between colloidal and solid-state systems. In a colloidal system, the solvent often acts as a heat sink, effectively dissipating the generated heat.²²⁴ In contrast, the solid-state may have lower thermal conductivity, leading to heat accumulation and potential thermal quenching of the UCL, thereby affecting both the efficiency and stability of the system. Thus, understanding how the shift from a colloidal to a solid-state affects these two key parameters—quenching mechanisms and thermal properties—is essential for optimizing the system's performance.

5.1.2 Investigating properties under various excitations

The dye-embedded system, as currently characterized, has been primarily studied under coherent laser sources of 808 nm and 976 nm. However, a more exhaustive understanding mandates evaluating the system under diverse excitation conditions. Comprehensively probing the dye-embedded system under varied excitation conditions will not only provide insights into its robustness but also delineate optimal operational parameters for specific applications.

As a valuable avenue for future research, varying the power densities of the 808 nm excitation source could unveil complexities and capabilities within the system. Since the upconversion process strongly depends on the power of the excitation source. Lower power densities offer insight into baseline for activation barriers for dye-sensitization and generation of ROS, revealing the minimum energy requirements for effective photocatalysis. Conversely, higher power densities could be used to investigate the upper limits of ROS generation, as well as the potential for saturation effects, non-radiative decay, or electron-hole pair recombination, which could diminish the overall photocatalytic efficiency.²²⁶ The impact of power density on the thermal behavior of the nanoparticles is also worth investigating, as higher densities may induce localized heating, thereby altering reactivity and luminescence dynamics. By exploring a range of power densities, we could also ascertain whether different ROS species or ratios are favored at different power densities, offering another layer of control over the photocatalytic process. Hence, conducting systematic studies on the influence of power densities could greatly enhance our understanding and optimization of the dye-embedded system, potentially revealing new pathways for improved performance, efficiency, and adaptability.

For future work, it is crucial to explore the scope of the dye-embedded system's luminescent properties beyond the currently employed 808 nm laser excitation. While the lanthanide ions have narrow absorption bands, the NIR dye used herein has broad absorption. This could lead to exploring possibilities, particularly in terms of understanding how different characteristics of multiple excitation sources could influence the photocatalysis of the dye-embedded-based system. The integration of additional laser wavelengths or even broadband sources like sunlight into the system could offer unprecedented enhancements. A multi-wavelength approach holds promise of intriguing synergistic effects in Fenton-type reactions, optimized energy utilization, and more precise stoichiometric control over ROS. Additionally, such an approach could provide the system with adaptability to degrade various pollutants and quickly adapt to fluctuating environmental conditions. The resulting increased system complexity could open up new avenues for photocatalytic pathways and significantly elevate the throughput and sustainability of the photocatalytic process. Therefore, future research should aim to break free from the single-wavelength paradigm to embrace a more dynamic, multi-wavelength or broadband approach, thereby unlocking the full photocatalytic potential of the dye-embedded system.

5.1.3 Exploration of Other Lanthanide Dopants

Our current studies with dye-embedded system is based on $\text{Er}^{3+}/\text{Yb}^{3+}$ -doped LnUCNPs have demonstrated enhanced emission in the green and red regions, making them particularly efficacious in exciting semiconductors like $\alpha\text{-Fe}_2\text{O}_3$ within the visible spectrum. While the core work of this thesis has focused on the $\text{Er}^{3+}/\text{Yb}^{3+}$ doped LnUCNPs system in tandem with hematite for photocatalysis, alternative lanthanides in the series present exciting opportunities for further research. Since each lanthanide element has its unique emission profile, potentially offering diverse options for future investigations. Exploring a diverse range of these lanthanides could pave the way for new composite dye-sensitized systems across a more comprehensive array of spectral regions. The diverse emission profiles of different lanthanides could be exploited to tailor LnUCNPs for very specific pairings with semiconductors.

For example, dye-embedded $\text{Tm}^{3+}/\text{Yb}^{3+}$ doped LnUCNPs could provide interesting possibilities. Tm^{3+} ions have inherent emission characteristics that lie in the UV region. This distinct emission profile makes Tm^{3+} dopants compatible with a different class of photocatalysts, such as TiO_2 and ZnO , both of which have band gaps aligning well with UV emissions. This opens up the potential for achieving photocatalytic activity in novel spectral regions that were previously inaccessible

with the Er³⁺/Yb³⁺ system. Thus, the use of Tm³⁺ could not only extend the range of photocatalytic activity but also improve the efficiency in applications where UV-active photocatalysts are more effective.^{149,213}

Understanding the interaction between alternative lanthanides and semiconductors can significantly expand the applicability of LnUCNPs. Different dopant-semiconductor combinations could be optimized for specific tasks, ranging from the breakdown of particular pollutants to more specialized roles in industrial settings. This would not only advance the field of photocatalysis but also potentially open doors to new areas of application that have yet to be considered.

5.2 Long-term Goals in Material Development

5.2.1 Scalability and Commercial Viability

Our long-term goal entails the large-scale synthesis of dye sensitization, LnUCNP synthesis, and covalent bonding processes. Delving into this critical domain requires a thorough approach, emphasizing the importance of optimizing reaction conditions, ensuring the reproducibility of protocols, and flexibly adapting methodologies to suit several applications. To establish a foundation for this, it's crucial to commence with a thorough assessment of our existing synthesis techniques, both for LnUCNPs and dyes. Such an assessment can spotlight potential bottlenecks or inefficiencies that currently exist, providing the direction necessary for refinements.

This not only offers prospects for applications in different sectors but also emphasizes the broader economic and societal benefits that could materialize from successfully commercializing these techniques.

5.2.2 Dye Modification and Multi-dye Integration for Enhanced Photostability and Optical Performance

A crucial aspect of future research lies in systematically adjusting the number and positions of these anchoring points across different dye molecules to glean a deeper understanding of their influence on the system's photostability and optical properties. In particular, establishing connections with silica precursors at alternative sites, such as sulfonate groups functionalized through sulfonamide or di-sulfide linkages, or terminal structures of the added phenyl ring, could be instrumental.

The IR820 dye's successful modification serves as a precedent for the potential of applying similar strategies to diverse dye molecules. An emerging and promising avenue is the integration of

multiple dyes within the existing nanosystem. This multi-dye approach could yield a broader absorption spectrum and potentially improve energy transfer efficiencies. However, it will mandate thorough engineering and empirical research to discern the optimal dye combinations and understand their interactions with the underlying nanoparticles, ensuring the system's performance is maximized while maintaining stability and efficiency.

Appendix

Appendix 1: Mechanism of Anti-Stokes Luminescence

A1.1 Two-Photon Absorption Mechanism

The TPA mechanism, first proposed in the 1930s, involves the simultaneous absorption of two photons to elevate a molecule to a higher energy level (**Figure A1.1a**). Upon returning to its ground state, the molecule emits a single photon with higher energy. The TPA process requires a non-existent virtual state, leading to a low probability of TPA occurrence and an ultra-low absorption cross-section. To generate sufficient excitation photons for two-photon excitation luminescence, high power, ultra-fast, excitation source is required. The experimental confirmation of TPA was achieved in 1961 with the advent of lasers, and femtosecond pulse lasers are commonly used in commercial imaging systems for two-photon absorption. Despite efforts to optimize TPA fluorescence, the challenge of high excitation power density remains. As a result, alternative anti-Stokes luminescence mechanisms have emerged as potential solutions.^{227–229}

A1.2 Hot Band Absorption

For many decades, scientists have observed the phenomenon of anti-Stokes luminescence induced by hot band absorption, which dates back to 1928. In this process, additional energy is derived from the heat stemming from the fluorescent organic molecule's original Boltzmann distribution (as shown in **Figure A1.1 b**). The luminescence is generated when the excitation light, which has a longer wavelength than the emission, is absorbed by the molecules located at a higher vibrational energy level (also known as 'hot band') - this puts them in the excited state (1). The excited state then decays and produces the common fluorescence emission, which has a shorter wavelength than the excitation light. Despite being well-documented, there is still a lack of research in this area due to the difficulty of designing efficient dye molecules for generating this anti-Stokes luminescence.^{230,231}

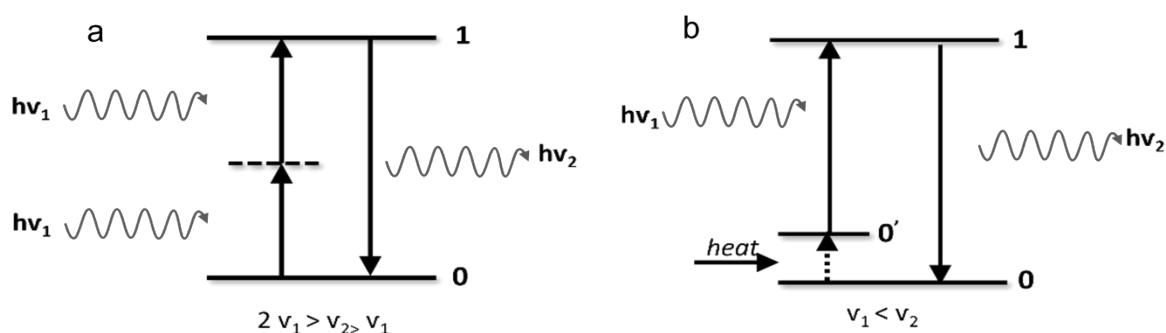


Figure A1.1 Schematic illustration of anti-Stokes luminescence by (a) Two-photon absorption and (b) Hot band absorption mechanism.

Appendix 2: Different Mechanisms of Upconversion

A2.1 Triplet-Triplet Annihilation

Triplet-triplet annihilation (TTA) utilizes the triplet state of dye molecules as an intermediate excited state. This system typically consists of two types of molecular dyes with matched triplet states. The sensitizer molecules absorb energy from the excitation light and transfer it to the emitter molecules, resulting in a long-lived excited triplet state ($^3T^*$). When two emitter molecules in the excited states come into contact, a highly efficient triplet-triplet annihilation process takes place, leading one emitter molecule to an excited singlet state (S_n) by consuming two triplet excited states. The sensitizers used in the TTA-based upconversion process should possess a large absorption cross-section at the excitation wavelength. Additionally, these sensitizers should exhibit high intersystem crossing efficiency to generate a substantial number of triplet states, and their phosphorescence decay rate should be slow enough to facilitate triplet-triplet energy transfer (TTET) to emitters. For effective TTET, the emitter utilized in the TTA process should have a triplet state with energy comparable to that of the sensitizer, and the lifetime of its triplet state should be sufficiently long to ensure energy transfer. Moreover, the emitter's fluorescence quantum yield should be high to achieve efficient upconversion emission.^{31,232–234}

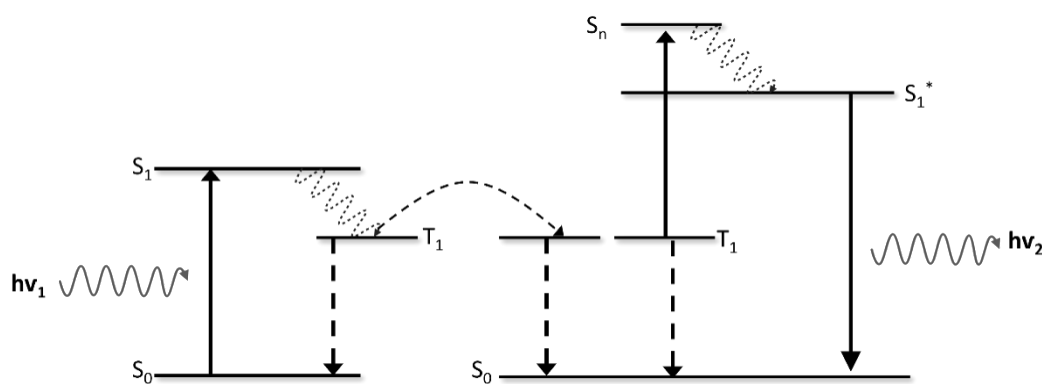


Figure A2.1 Schematic illustration of triplet-triplet annihilation.

A2.2 Cooperative Sensitized Upconversion

Cooperative Sensitized Upconversion (CSU) is a process that involves interactions between three different ion centers, typically labeled as ion 1, ion 2, and ion 3. In this process, ion 1 and ion 3 act as sensitizers. When exposed to excitation photons, both ion 1 and ion 3 are excited to an initial higher energy state, referred to as E_1 . After this, ion 1 and ion 3 engage with ion 2, which acts as the activator in this process. They simultaneously transfer their energy to ion 2, elevating it to a higher energy state, also denoted as E_1 . Following this energy transfer, ion 2 relaxes back to its ground state and, in the process, emits a photon with higher energy—this is the upconverted photon. One notable aspect of CSU is that its efficiency is typically much lower compared to other processes like ESA or ETU. This is due to the involvement of quasi-virtual pair levels during the transitions between energy states, which require a higher order of quantum mechanical perturbation to describe. Despite its lower efficiency, CSU offers a unique advantage: the potential for high-resolution imaging, as the need to tightly confine the excitation helps to compensate for this lower efficiency, which is a feature not available in other upconversion mechanisms.^{15,235–237}

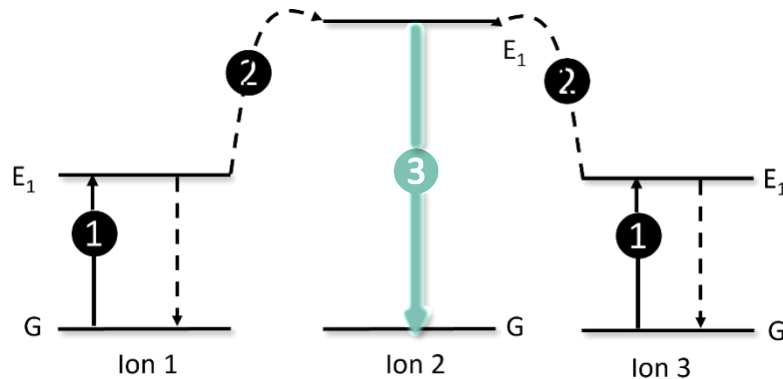


Figure A2.2 Upconversion process by Cooperative Sensitization.

A2.3 Photon Avalanche

The Photon Avalanche (PA) is a complex mechanism involved in upconversion, initially discovered by Chivian and colleagues in Pr³⁺-based infrared quantum counters. At the core of this mechanism is an unusual pump process that is highly dependent on the intensity of the pump source. Specifically, the PA process becomes significant only when the pump intensity exceeds a certain threshold value. Below this threshold, the system exhibits minimal upconverted luminescence. In contrast, once the pump intensity crosses this critical threshold, the photoluminescence intensity of the system increases dramatically, scaling by orders of magnitude.
15,238

In terms of its mechanism, it begins with the weak, non-resonant GSA of an ion, populating an initial excited state labeled as E₁. This is followed by a resonant ESA process, which promotes electrons to a higher, visibly emitting energy state, referred to as E₂. At this stage, an efficient cross-relaxation process takes place, specifically following the dynamics of E₂ (from ion 2) + G (from ion 1) transitioning to E₁ (in both ions 1 and 2). This CR process results in both ions occupying the intermediate level E₁. After both ions have transitioned to this intermediate state, they are quickly promoted to level E₂ again, and here is where the 'avalanche' effect indeed initiates. With both ions at E₂, further cross-relaxation processes occur in concert with additional ESA processes. These concurrent processes exponentially increase the population of ions in the E₂ energy state, creating a feedback loop that greatly amplifies the upconversion emission, much like an avalanche growing as it descends a slope.^{24,29,34,47,239}

It's worth noting two key characteristics of PA-induced upconversion. First, the process requires a rather long response time to the excitation source, with delays that can extend to several seconds. Second, the PA mechanism tends to result in limited emission output due to its reliance on weak, non-resonant GSA. Nevertheless, because of the cyclical, reinforcing nature of the ESA and CR processes under the right conditions, the PA mechanism can lead to significant upconversion emission, albeit with a notable dependence on the pump power to achieve sufficient inversion from the ground state to the excited states.

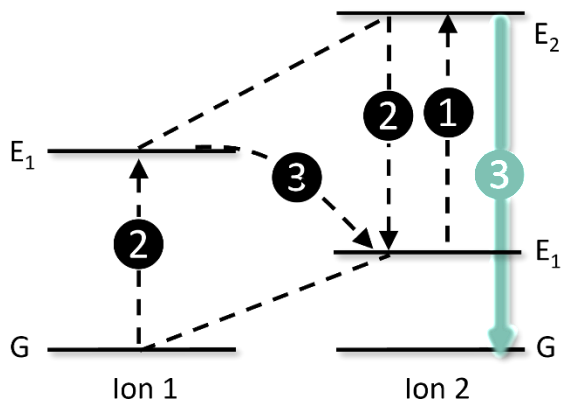


Figure A2.6 Upconversion process by Photon-Avalanche mechanism.

A2.4 Energy Migration Upconversion

Energy Migration Upconversion (EMU) is a unique process that enables the generation of upconverted photons without requiring activator ions to have long-lived metastable excited states. This feature allows for a higher degree of tunability in the resulting luminescence of the upconversion material. Systems designed to utilize EMU for photon upconversion are often structured as nanoparticles with a core/shell architecture. Within these systems, four distinct types of lanthanide ions play essential roles: sensitizers (ion 1), accumulators (ion 2), migrators (ion 3), and activators (ion 4). These ions are strategically positioned within specific regions of the crystalline host lattice of the material.^{28,81}

In these systems, sensitizer and accumulator ions are usually located in the core of the nanoparticle. Sensitizer ions are responsible for capturing pump photons through GSA. The energy absorbed by the sensitizers is then transferred to neighboring accumulator ions. This transfer results in the promotion of the accumulator ions to higher excited states, denoted as E₁. For the process to yield anti-Stokes emissions (emissions with a higher energy than the excitation source), the accumulator ions need to have long-lived metastable excited states, represented as G. This allows these ions to harvest energy from multiple sensitizer-absorbed pump photons. Common ions used as accumulators in this context include lanthanide ions like Ho³⁺, Tm³⁺, and Er³⁺, which are often used as activators in other upconversion mechanisms.^{28,81}

Meanwhile, activator ions are found exclusively in the shell of the nanoparticle. Migrator ions, on the other hand, serve a special function: they act as conduits for energy, facilitating the movement

of energy from the core of the nanoparticle to the shell. They are integrated throughout the host lattice of the material.

After the energy is stored within an accumulator ion in the core, a migrator ion takes over. The energy is then randomly passed through the migrator sub-lattice until it eventually reaches and is trapped by an activator ion residing in the shell of the nanoparticle. When this activator ion relaxes back to its ground state, an anti-Stokes photon is emitted, leading to the observable luminescence of the upconversion material. In essence, this intricate interplay among sensitizers, accumulators, migrators, and activators, and the precise structuring of these ions within the core/shell architecture, is central to the EMU process.²⁸

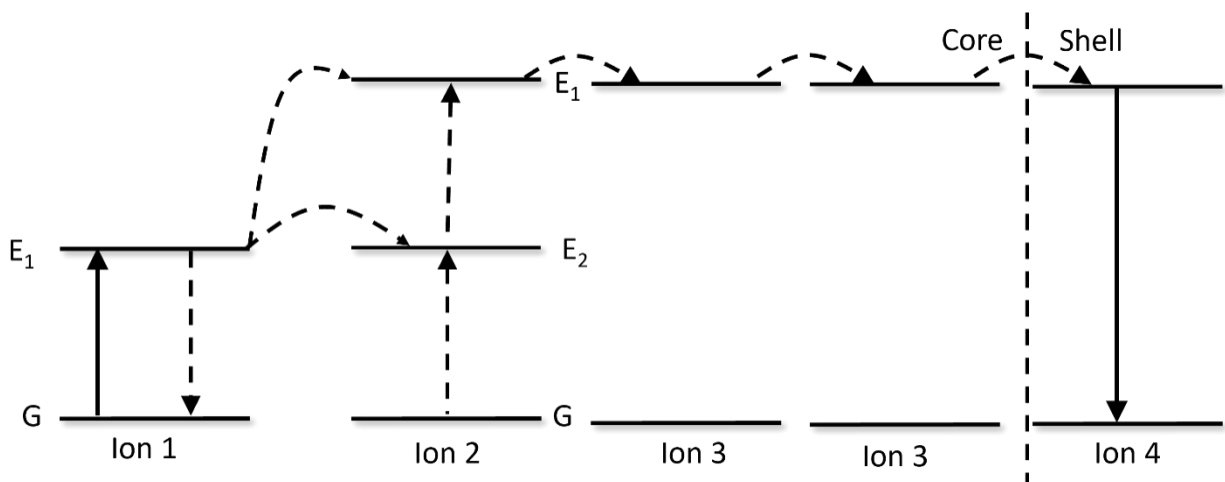


Figure A2.10 Upconversion process by Energy migration mechanism.

Appendix 3: Quenching Mechanisms in LnUCNPs

The presence of defects within the crystal structure of nanoparticles is widely recognized, and these defects are predominantly found near the surface.²⁴⁰ Consequently, as the ratio of surface area to volume increases, the defects generated during synthesis become significant factors contributing to the reduction of upconversion luminescence. Energy migration is the phenomenon where energy is transferred from emitting ions to defect sites either within the crystal or at its surface. This non-radiative transfer of energy can result in the quenching of luminescence. In the context of high-doping concentration, energy migration is particularly facilitated, allowing the energy to migrate through the excited levels within the sensitizer-sensitizer network towards the surface defects (as shown in **Figure A3.1**). Theoretical studies have revealed that energy migration can occur over an average distance of 28 nm, which, in practical scenarios, may exceed the diameter of the LnUCNPs.²⁴⁰

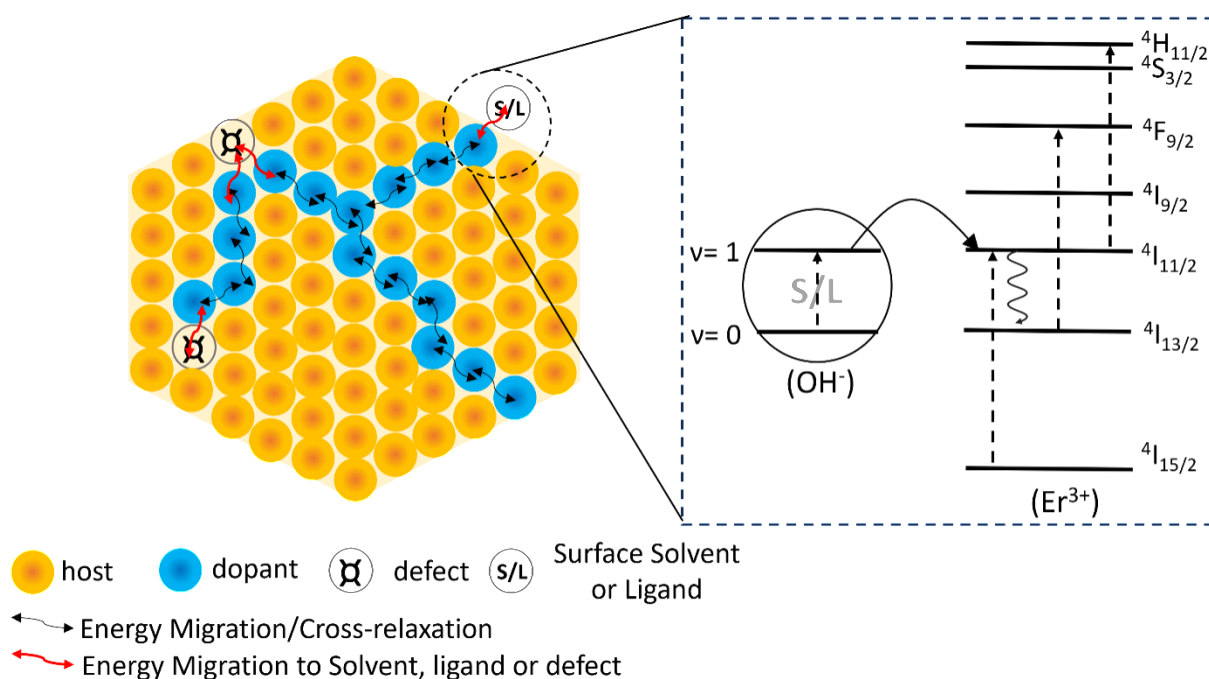


Figure A3.1 Quenching mechanism of LnUCNPs in presence of surface ligands and defects.

The surface quenchers in LnUCNPs are not limited to defects alone but also include solvent and ligand molecules.^{46,83,167} As the size of nanoparticles decreases, their surface-to-volume ratio increases, resulting in a greater number of ions located on the surface. These surface ions typically possess reactive dangling bonds, which are unsaturated and carry a partial charge, thereby

increasing the surface energy.²⁴¹ To minimize their free energy, these dangling bonds interact with the surrounding environment. Interaction of these dangling bonds with the solvent or ligand of vibrational energy resonant with the energy gap of the activator on the surface of nanoparticles results in the quenching of emission. The quenching mechanism is influenced by the nature of the solvent (polar or non-polar) and the phonon energy associated with it.⁴⁶ In the quenching process, a larger number of phonons is required to bridge the energy gap, resulting in a smaller probability of quenching (denoted by k_{nr}). For instance, in $\text{Yb}^{3+}/\text{Er}^{3+}$ co-doped LnUCNPs, the green-to-red ratio is affected by the surrounding environment. In the presence of -OH groups, whether in aqueous or organic solvents, the red emission of Er^{3+} increases at the expense of green emission due to population of $^4\text{F}_{9/2}$, by 2 photon absorption from $^4\text{I}_{13/2}$.²⁴²⁻²⁴⁵ Similar effects on the luminescence of LnUCNPs are observed in organic solvents containing -CH groups. However, the C-H stretching vibrations of aliphatic solvents exhibit a stronger quenching effect on the red emission of Er^{3+} compared to aromatic solvents due to greater energy overlap with the $^4\text{F}_{9/2} \rightarrow ^4\text{I}_{9/2}$ transition, leading to non-radiative decay of the red-emitting level.¹⁶⁷

Appendix 4: Strategies for enhancement of Upconversion efficiency

A4.1 Tailoring of Crystal Field

Tailoring the crystal structure can enhance luminescence emission intensity by lowering the symmetry around the lanthanides, which relaxes the selection rule and permits weakly allowed electric dipole transitions. However, once the host lattice is in a fixed state, it becomes unable to modify the immediate surroundings of the lanthanide ion any further. An alternative and promising approach to enhancing upconversion photoluminescence is to customize the local environment surrounding the lanthanide ion through intentional doping with non-luminescent cationic ions. These non-luminescent ions can replace the cationic ions at lattice points or occupy interstitial sites near the lanthanide ions. As a result, the local symmetry around the lanthanide dopants is reduced, which favors an increase in upconversion efficiency.^{232,246–248}

Often, Li^+ ions are employed to replace Na^+ ions in hosts of LnUCNPs. Several studies have observed differences in luminescence response and nanoparticle morphology by varying the concentration of Li^+ ions.^{249,250} Similar experiments have been conducted using K^+ ions as substitutes for Na^+ . Goldschmidt's rules, which describe an ionic substitution in a crystal lattice, stipulate that the replaced ion and the substituent should possess similar charges and ionic radii. Li^+ , Na^+ , and K^+ differ significantly in terms of their ionic radii, despite having the same coordination number. Li^+ ions, being smaller, can readily occupy interstitial sites without affecting the sample's crystallinity, although distortions may arise. Conversely, K^+ ions, being larger, are unable to efficiently occupy Na^+ sites within the LnUCNPs lattice. Their inclusion at interstitial sites severely compromises the crystal integrity and does not contribute to luminescence enhancement. Therefore, the substitution of Li^+ ions is preferred to achieve distortion-enhanced upconversion luminescence. The Li^+ , being the smallest metallic ion on the periodic table with an ionic radius of 0.9 Å, can be readily inserted into host lattices. Previous studies have showcased examples of lithium doping in oxide host lattices. Chen *et al.* conducted experiments where they incorporated lithium into $\text{Y}_2\text{O}_3:\text{Yb}^{3+}/\text{Er}^{3+}$ nanophosphors, resulting in significant enhancements in green and violet emissions.²⁵⁰

Furthermore, due to the similarity in ionic radii, the substitution of rare earth ions with Mn^{2+} at lattice sites is permissible. Extensive research has reported the use of Mn^{2+} to enhance red luminescence in LnUCNPs for biological applications. Recently, the overall improvements in

luminescence have been attributed to local distortions induced by the presence of Mn^{2+} ions. In β - $NaYF_4:Er^{3+}, Yb^{3+}, Mn^{2+}$ materials, the emission wavelengths favored by energy transfer depend on the relative concentrations of each dopant ion.²⁵¹

A4.2 Surface Plasmon Resonance

Another method reported in the literature that enhances the upconversion luminescence, is surface plasmon resonance (SPR) using noble metal nanoparticles. Metal nanoparticles are able to generate localized surface plasmons that vibrate at frequencies akin to those of incident photons, thus resulting in resonance. This phenomenon facilitates the propagation of surface plasmons along the metallic surface and leads to the formation of intense electromagnetic fields (Figure A4.1). Therefore, metal nanoparticles are considered useful light-capturing components that can be combined with LnUCNPs to augment the efficacy of the energy transformation process.

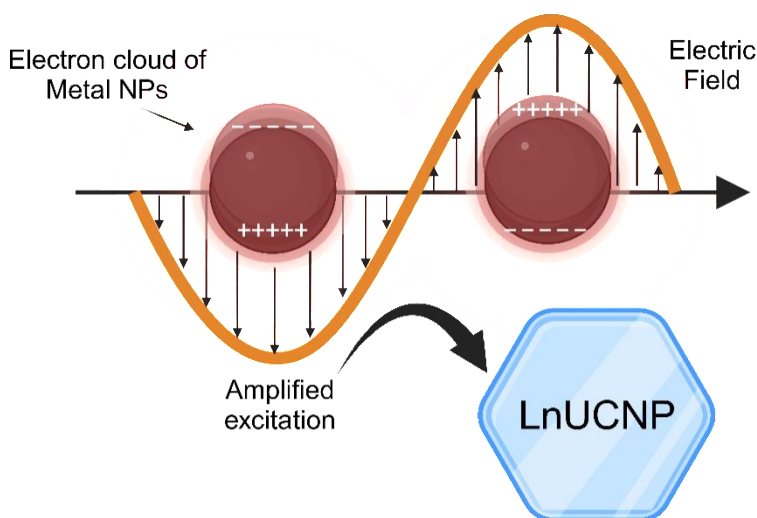


Figure A4.1 Diagram depicting the potential mechanism behind the plasmonic amplification of upconversion luminescence.

The intensity (I) of the upconversion emission from a typical lanthanide-doped nanocrystal can be calculated using following equation:

$$I = \phi \cdot \sigma_s \cdot \eta_{ET} \cdot \varphi$$

where ϕ symbolizes the photon flux of the irradiating radiation, σ_s represents the absorption cross-section of the sensitizing ion (it should be noted that the absorption of the activating ion is disregarded because of its very minimal absorption cross-section), η_{ET} stands for the energy-

transfer efficacy from the sensitizing ion to the activating one, and φ symbolizes the luminescence quantum yield of the activating ion.

Therefore, when a LnUCNP is brought close to a metal nanoparticle, the electric field of the plasmon should interact effectively with the transition dipole of the LnUCNP, thus leading to an increase in the light-harvesting capability of the sensitizer ions and ultimately an enhanced luminescence.²⁴⁸

Although SPR has been proposed as a method to improve upconversion luminescence, its effectiveness is dependent on the size, shape, and composition of the metal surface. Optimizing the plasmonic structure is therefore essential for boosting luminescence. Moreover, the commonly used 980 nm lasers have the downside of water absorption and heat, which can lead to cell and tissue damage in biological media. Furthermore, utilizing noble metals is costly and not cost-effective, and it requires precise control of the distance between the noble metal nanoparticles and the LnUCNPs.

Appendix 5: Additional Data

A5.1 Physical Characterization of undoped NaGdF₄ (in Chapter 2)

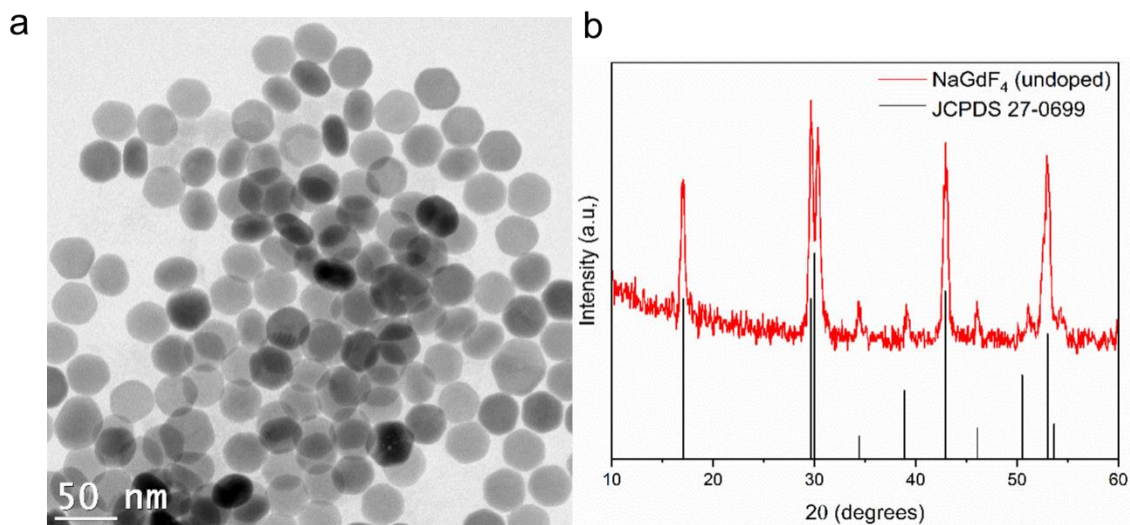


Figure A5.1 (a) TEM image of NaGdF₄ undoped nanoparticles of size 36.7 ± 3.5 nm (b) PXRD pattern confirming the hexagonal crystal phase.

A5.2 Physical Characterization of undoped NaYF₄ (in Chapter 2)

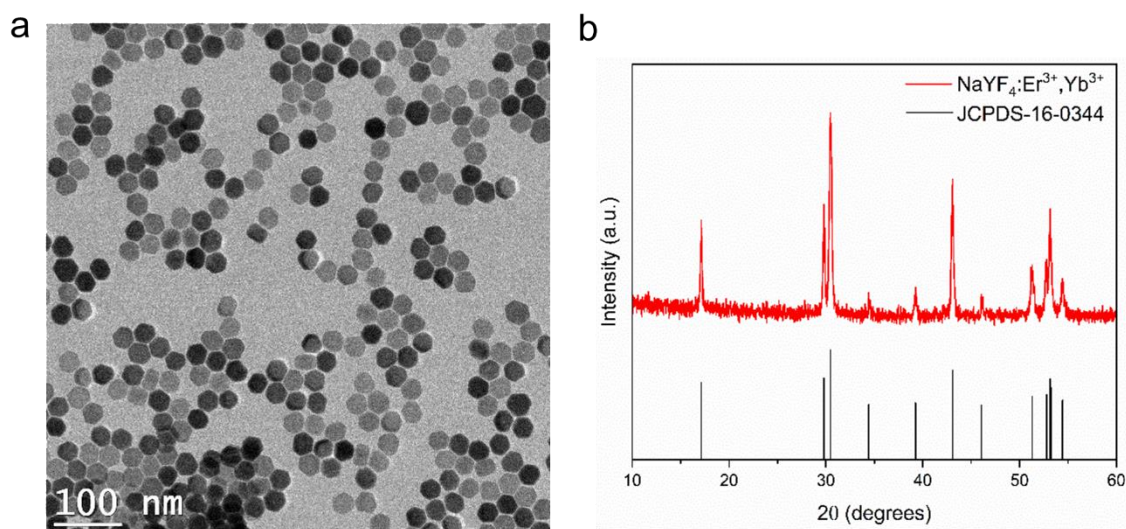


Figure A5.2 (a) TEM image of NaYF₄ undoped nanoparticles of size 26.2 ± 2.5 nm (b) PXRD pattern confirming the hexagonal crystal phase.

A5.3 Physical Characterization of NaGdF₄:Er³⁺,Yb³⁺/NaGdF₄:Yb³⁺/SiO₂ (in Chapter 3)

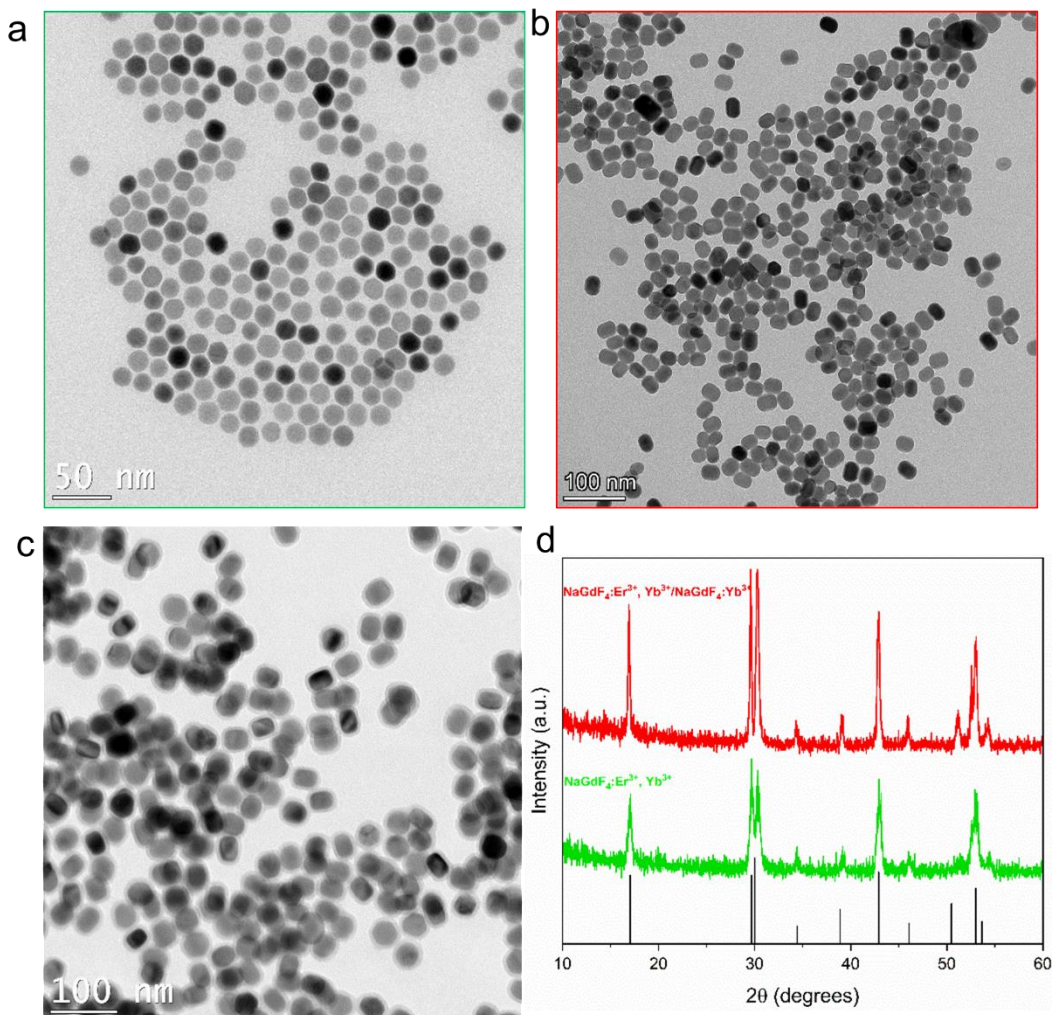


Figure A5.3 TEM image of (a) NaGdF₄:Er³⁺, Yb³⁺core nanoparticles of size 18.6±2.5 nm (green) (b) NaGdF₄:Er³⁺, Yb³⁺/ NaGdF₄:Yb³⁺core/shell nanoparticles of size 30.6±3.3 nm (red) (c) NaGdF₄:Er³⁺, Yb³⁺/ NaGdF₄:Yb³⁺/SiO₂ nanoparticles of size 30.6±3.3 nm with silica shell thickness of 3.5±1.2 nm (d)PXRD pattern confirming the hexagonal crystal phase of core (green) and core/shell (red) corresponding to JCPDS 27-0699.

A5.4 Physical Characterization of NaGdF₄:Er³⁺,Yb³⁺/NaGdF₄:Yb³⁺/NaGdF₄ (in Chapter 3)

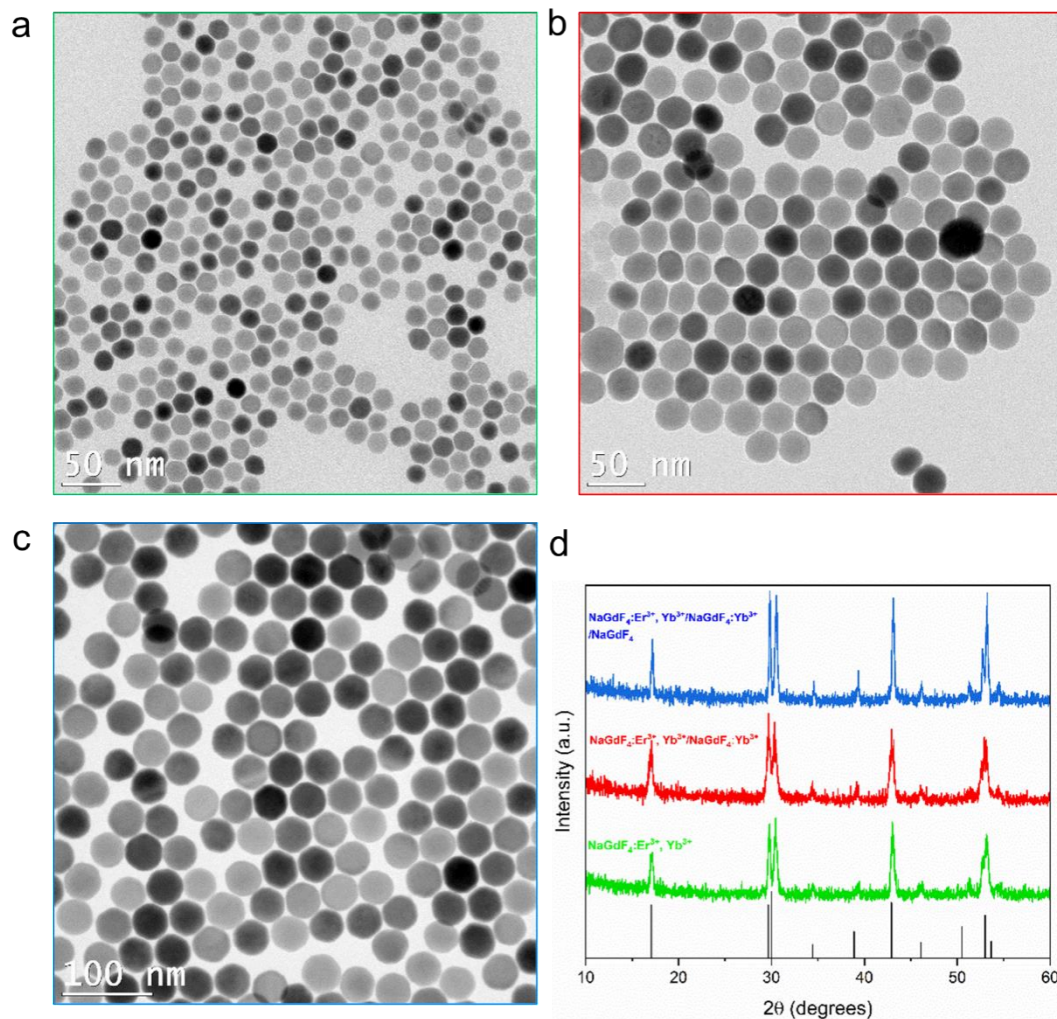


Figure A5.4 TEM image of (a) NaGdF₄:Er³⁺, Yb³⁺ core nanoparticles of size 19.2±1.7 nm (green) (b) NaGdF₄:Er³⁺, Yb³⁺/NaGdF₄:Yb³⁺ core/shell nanoparticles of size 29.8±2.0 nm (red) (c) NaGdF₄:Er³⁺, Yb³⁺/NaGdF₄:Yb³⁺/NaGdF₄ nanoparticles of size 37.6±3.3 nm (blue) (d) PXRD pattern confirming the hexagonal crystal phase of core (green), core/shell (red) and core/shell/shell (blue) corresponding to JCPDS 27-0699.

A5.5 Physical Characterization of NaGdF₄ undoped (in Chapter 3)

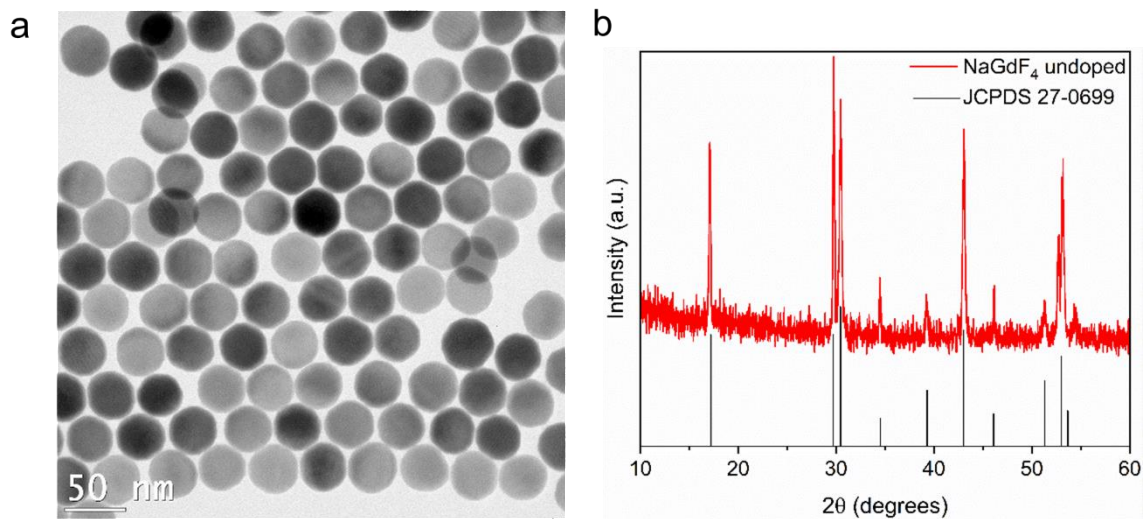


Figure A5.5 (a) TEM image of NaGdF₄ undoped nanoparticles of size 39.5±3.2 nm (b)PXRD pattern confirming the hexagonal crystal phase.

A5.6 Synthesis of Hematite Nanoparticles (in Chapter 3)

Table A5. 1 Trials for the synthesis of α -Fe₂O₃ Nanoparticles

Trial	Fe Precursor (FeCl ₃ .6H ₂ O) (mmol)	Precipitating Agent (CH ₃ COONa) (mmol)	Capping Ligand (Polyvinyl Pyrolidone) MW~55000 (g)	Cooking Temperature °C (18 hours)	Size of NPs (in nm)
1	3	20	0.5	250	37.9±5.2
2	3	25	0.5	250	36.4±4.3
3	3	20	0.5	200	35.3±5.5
4	3	20	0.5	250	37.8±6.2
5	2	40	1	200	25.0±4.5
6	1.5	45	1.5	200	15.5±5.7

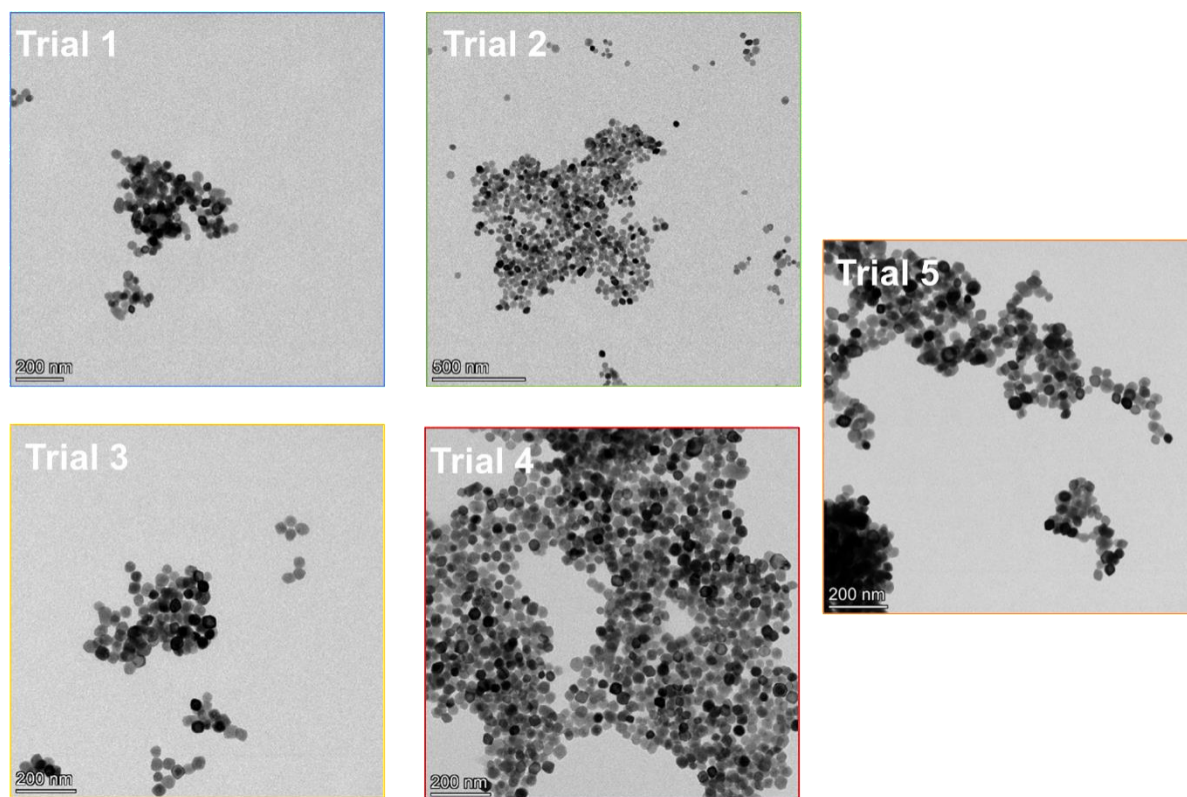


Figure A5.6 TEM images of α -Fe₂O₃ nanoparticles synthesized by different trials.

A5.7 Controls in the insertion of hematite in Wide pored silica on the Embedded system (in Chapter 3)

To validate the integration of hematite nanoparticles within the expansive pores surrounding the embedded structure, two reference batches were produced. The first involved the creation of a wide-pored silica shell, with pore dimensions approximately 20-25 nm, around the embedded system, into which α -Fe₂O NPs measuring 30 nm were introduced. In the second approach, a mesoporous silica shell was crafted around the embedded system, followed by the introduction of α -Fe₂O₃ NPs measuring 15 nm. The limited inclusion of hematite nanoparticles exceeding 25 nm, along with 15.5 nm hematite nanoparticles within the mesopores, aligns with our prior findings regarding the integration of hematite nanoparticles in the extensive pore silica shell surrounding the SE framework.

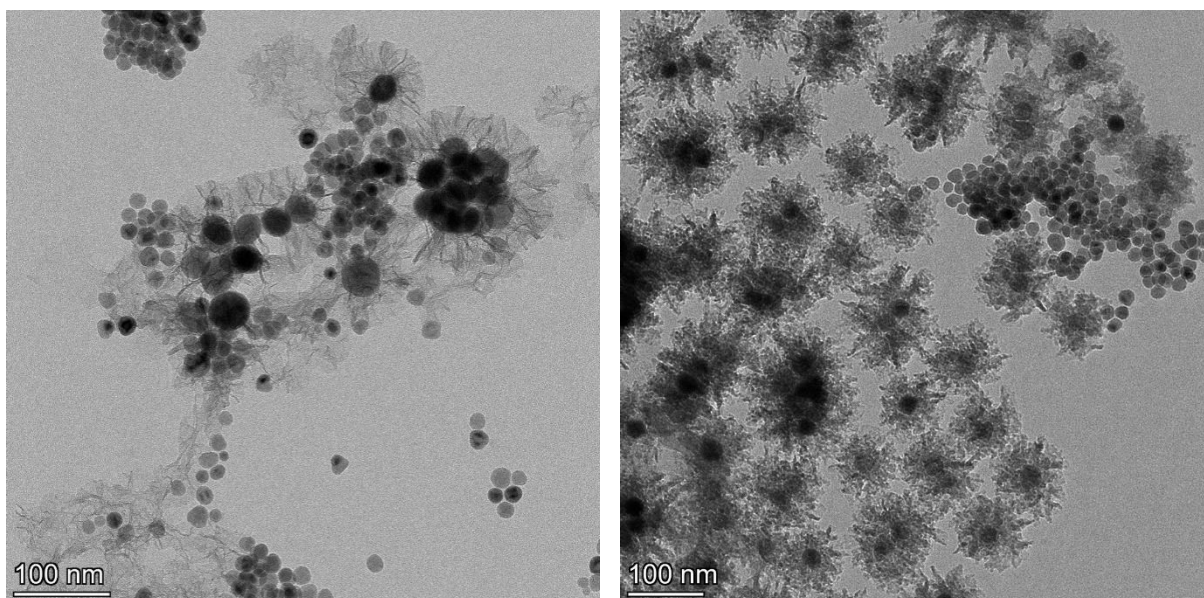


Figure A5.7 TEM images of (a) LnUCNP-WP with a large pore size of ~20-25 nm loaded with 30 nm α -Fe₂O₃ (b) LnUCNP coated with mesoporous silica loaded with 15 nm α -Fe₂O₃ nanoparticles.

References

- 1 M. Kaur, G. A. Mandl, S. L. Maurizio, G. Tessitore and J. A. Capobianco, *Nanoscale Adv*, 2022, **4**, 608–618.
- 2 M. Kaur, S. L. Maurizio, G. A. Mandl and J. A. Capobianco, *Nanoscale*, , DOI:10.1039/d3nr02845c.
- 3 G. Tessitore, G. A. Mandl, S. L. Maurizio, M. Kaur and J. A. Capobianco, *RSC Adv*, 2023, **13**.
- 4 B. Valeur, *Molecular Fluorescence - Principles and Applications*, 2001, vol. 8.
- 5 E. Wiedemann and J. B. Messerschmitt, *Ann Phys*, 1888, **270**, 463–469.
- 6 K. V. R. Murthy and H. S. Virk, *Defect and Diffusion Forum*, 2013, **347**, 1–34.
- 7 A. D. Mc Naught and A. Wilkinson, *IUPAC. Compendium of Chemical Technology*, 1997.
- 8 G. Blasse and B. C. Grabmaier, *Springer Series on Fluorescence, Vol. 7*, 1994.
- 9 F. Zhang, *Photon Upconversion Nanomaterials*, Springer , December 2014, Berlin Heidelberg, 2014.
- 10 G. G. Stokes, *Philos Trans R Soc Lond*, 1997, **142**, 463–562.
- 11 J. R. Lakowicz, *Principles of fluorescence spectroscopy, 3rd Edition*, Joseph R. Lakowicz, editor, 2006.
- 12 J. Zhou, Q. Liu, W. Feng, Y. Sun and F. Li, *Chem Rev*, 2015, **115**, 395–465.
- 13 X. Zhu, Q. Su, W. Feng and F. Li, *Chem Soc Rev*, 2017, **46**, 1025–1039.
- 14 J. Zhou, Z. Liu and F. Li, *Chem Soc Rev*, 2012, **41**, 1323–1349.
- 15 G. Chen, H. Qiu, P. N. Prasad and X. Chen, *Chem Rev*, 2014, **114**, 5161–5214.
- 16 J. C. G. Bünzli, *Chem Rev*, 2010, **110**, 2729–2755.
- 17 A. Jablonski, *Z. Physik*, 1935, **94**, 14.
- 18 A. Jablonski, *Nature*, 1933, **131**, 839–840.
- 19 Y. Masumoto and T. Takagahara, *Semiconductor quantum dots: physics, spectroscopy and applications*, Springer Science & Business Media, 2013.
- 20 S. F. Himmelstoß and T. Hirsch, *Methods Appl Fluoresc*, 2019, **7**, 022002–022053.
- 21 M. G. Bawendi, M. L. Steigerwald and L. E. Brus, *Annu Rev Phys Chem*, 1990, **41**, 477–496.
- 22 D. R. Gamelin and H. U. Güdel, *Acc Chem Res*, 2000, **33**, 235–242.
- 23 P. A. Tanner, *Chem Soc Rev*, 2013, **42**, 5090–5101.
- 24 M. Haase and H. Schäfer, *Angewandte Chemie - International Edition*, 2011, **50**, 5808–5829.
- 25 N. Bloembergen, *Phys Rev Lett*, 1959, **2**, 84.

- 26 F. Auzel, *CR Acad. Sci. Paris*, 1966, **262**, 1016–1019.
- 27 V. V Ovsyankin and P. P. Feofilov, *Soviet Journal of Experimental and Theoretical Physics Letters*, 1966, **3**, 322.
- 28 M. V. DaCosta, S. Doughan, Y. Han and U. J. Krull, *Anal Chim Acta*, 2014, **832**, 1–33.
- 29 F. Auzel, *Chem Rev*, 2004, **104**, 139–173.
- 30 Y. H. Chien, K. K. Chan, S. H. K. Yap and K. T. Yong, *Journal of Chemical Technology and Biotechnology*, 2018, **93**, 1519–1528.
- 31 R. Naccache, Q. Yu and J. A. Capobianco, *Adv Opt Mater*, 2015, **3**, 482–509.
- 32 S. Liu, Z. An and B. Zhou, *Chemical Engineering Journal*, 2023, 452, 139649–139667.
- 33 A. Nadort, J. Zhao and E. M. Goldys, *Nanoscale*, 2016, **8**, 13099–13130.
- 34 F. Wang and X. Liu, *Chem Soc Rev*, 2009, **38**, 976–989.
- 35 M. Betinelli, L. Carlos and X. Liu, *Phys Today*, 2015, **68**, 38–44.
- 36 S. Cotton, *Lanthanide and Actinide Chemistry*, 2006, 1–263.
- 37 B. Henderson and G. F. Imbusch, *Optical spectroscopy of inorganic solids*, Oxford University Press, 2006, vol. 44.
- 38 S. Hufner and B. R. Judd, *Phys Today*, 1979, **32**, 76–77.
- 39 J. H. Van Vleck, *Journal of Physical Chemistry*, 1937, **41**, 67–80.
- 40 G. H. Dieke, H. M. Crosswhite and B. Dunn, *J Opt Soc Am*, 1961, **51**, 820–827.
- 41 B. Zhou, B. Shi, D. Jin and X. Liu, *Nat Nanotechnol*, 2015, 10, 924–936.
- 42 G. E. Buono-core, H. Li and B. Marciniak, *Coord Chem Rev*, 1990, **99**, 55–87.
- 43 X. Cheng, D. Tu, W. Zheng and X. Chen, *Chemical Communications*, 2020, **56**, 15118–15132.
- 44 S. Wen, J. Zhou, K. Zheng, A. Bednarkiewicz, X. Liu and D. Jin, *Nat Commun*, 2018, **9**, 1–12.
- 45 D. L. Dexter and J. H. Schulman, *J Chem Phys*, 1954, **22**, 1063–1070.
- 46 G. Tessitore, G. A. Mandl, M. G. Brik, W. Park and J. A. Capobianco, *Nanoscale*, 2019, **11**, 12015–12029.
- 47 F. Wang, D. Banerjee, Y. Liu, X. Chen and X. Liu, *Analyst*, 2010, **135**, 1839–1854.
- 48 M. Lin, Y. Zhao, S. Q. Wang, M. Liu, Z. F. Duan, Y. M. Chen, F. Li, F. Xu and T. J. Lu, *Biotechnol Adv*, 2012, **30**, 1551–1561.
- 49 J. Chen and J. X. Zhao, *Sensors*, 2012, **12**, 2414–2435.
- 50 K. Venkata Krishnaiah, C. K. Jayasankar, V. Venkatramu, S. F. León-Luis, V. Lavín, S. Chaurasia and L. J. Dhareshwar, *Appl Phys B*, 2013, **113**, 527–535.

- 51 A. Aebischer, S. Heer, D. Biner, K. Krämer, M. Haase and H. U. Güdel, *Chem Phys Lett*, 2005, **407**, 124–128.
- 52 L. M. Wiesholler, F. Frenzel, B. Grauel, C. Würth, U. Resch-Genger and T. Hirsch, *Nanoscale*, 2019, **11**, 13440–13449.
- 53 K. Prorok, M. Pawlyta, W. Strek and A. Bednarkiewicz, *Chemistry of Materials*, 2016, **28**, 2295–2300.
- 54 J. Qiu, M. Shojiya, Y. Kawamoto and K. Kadono, *J Lumin*, 2000, **86**, 23–31.
- 55 N. Song, S. Liu, P. Zhang, J. He, Q. Zhang, F. Wang and B. Zhou, *Journal of Rare Earths*, 2021, **39**, 1506–1511.
- 56 D. T. Klier and M. U. Kumke, *RSC Adv*, 2015, **5**, 67419–67156.
- 57 J. Shen, G. Chen, A. M. Vu, W. Fan, O. S. Bilsel, C. C. Chang and G. Han, *Adv Opt Mater*, 2013, **1**, 644–650.
- 58 I. Mikalauskaitė, G. Pleckaitytė, L. Sinusaite, V. Plausinaitienė, A. Katelnikovas and A. Beganskiene, *J Lumin*, 2020, **223**, 117237–117246.
- 59 L. Tian, Z. Xu, S. Zhao, Y. Cui, Z. Liang, J. Zhang and X. Xu, *Materials*, 2014, **7**, 7289–7303.
- 60 L. Tu, X. Liu, F. Wu and H. Zhang, *Chem. Soc. Rev.*, 2015, **44**, 1331–1345.
- 61 D. Vennerberg and Z. Lin, *Sci Adv Mater*, 2011, **3**, 26–40.
- 62 S. Heer, K. Kömpe, H. Güdel and M. Haase, *Advanced Materials*, 2004, **16**, 2102–2105.
- 63 J. Ganem and S. R. Bowman, *Nanoscale Res Lett*, 2013, **8**, 455–466.
- 64 J. Shan, W. Kong, R. Wei, N. Yao and Y. Ju, *J Appl Phys*, 2010, **107**, 054901–054907.
- 65 R. K. Sharma, A. V. Mudring and P. Ghosh, *J Lumin*, 2017, **189**, 715531–715557.
- 66 X. Sun, Y. W. Zhang, Y. P. Du, Z. G. Yan, R. Si, L. P. You and C. H. Yan, *Chemistry - A European Journal*, 2007, **13**, 2320–2332.
- 67 Y. P. Du, Y. W. Zhang, L. D. Sun and C. H. Yan, *Dalton Transactions*, 2009, 8574–8581.
- 68 H. X. Mai, Y. W. Zhang, R. Si, Z. G. Yan, L. D. Sun, L. P. You and C. H. Yan, *J Am Chem Soc*, 2006, **128**, 6426–6436.
- 69 F. Wang, Y. Han, C. S. Lim, Y. Lu, J. Wang, J. Xu, H. Chen, C. Zhang, M. Hong and X. Liu, *Nature*, 2010, **463**, 1061–1065.
- 70 H. Dong, L. D. Sun and C. H. Yan, *Chem Soc Rev*, 2015, **44**, 1608–1634.
- 71 H. X. Mai, Y. W. Zhang, L. D. Sun and C. H. Yan, *Journal of Physical Chemistry C*, 2007, **111**, 13721–13729.
- 72 F. Vetrone, R. Naccache, V. Mahalingam, C. G. Morgan and J. A. Capobianco, *Adv Funct Mater*, 2009, **19**, 2924–2929.

- 73 H. Xiao, B. Liu, L. Qiu, G. Li, G. Zhang, D. Huang, Y. Zhao, C. Yang, F. Jiang, P. Dang, H. Lian, Z. Cheng and J. Lin, *Angewandte Chemie - International Edition*, 2022, **61**, e202115136.
- 74 X. Zou, M. Xu, W. Yuan, Q. Wang, Y. Shi, W. Feng and F. Li, *Chemical Communications*, 2016, **52**, 13389–13392.
- 75 H. Rabie, Y. Zhang, N. Pasquale, M. J. Lagos, P. E. Batson and K. B. Lee, *Advanced Materials*, 2019, **31**, 1806991–180699.
- 76 W. Feng, L. Zhang, Y. Zhang, Y. Yang, Z. Fang, B. Wang, S. Zhang and P. Liu, *J Mater Chem A Mater*, 2017, **5**, 10311–10320.
- 77 G. Chen, H. Ågren, T. Y. Ohulchanskyy and P. N. Prasad, *Chem. Soc. Rev.*, 2015, **44**, 1680–1713.
- 78 X. Chen, D. Peng, Q. Ju and F. Wang, *Chem Soc Rev*, 2015, **44**, 1318–1330.
- 79 G. Chen, H. Qiu, R. Fan, S. Hao, S. Tan, C. Yang and G. Han, *J Mater Chem*, 2012, **22**, 20190–20196.
- 80 H.-T. Wong, F. Vetrone, R. Naccache, H. L. W. Chan, J. Hao and J. A. Capobianco, *J Mater Chem*, 2011, **21**, 16589–16596.
- 81 F. Wang, R. Deng, J. Wang, Q. Wang, Y. Han, H. Zhu, X. Chen and X. Liu, *Nat Mater*, 2011, **10**, 968–973.
- 82 G. Chen, H. Ågren, T. Y. Ohulchanskyy and P. N. Prasad, *Chem Soc Rev*, 2015, **44**, 1680–1713.
- 83 S. Fischer, N. D. Bronstein, J. K. Swabeck, E. M. Chan and A. P. Alivisatos, *Nano Lett*, 2016, **16**, 7241–7247.
- 84 Z. Li, Y. Zhang and S. Jiang, *Advanced Materials*, 2008, **20**, 4765–4769.
- 85 E. M. Chan, E. S. Levy and B. E. Cohen, *Advanced Materials*, 2015, **27**, 5753–5761.
- 86 S. I. Weissman, *J Chem Phys*, 1942, **10**, 214–217.
- 87 J. M. Lehn, *Pure and Applied Chemistry*, 1994, **66**, 1961–1966.
- 88 J. Zhang, C. M. Shade, D. A. Chengelis and S. Petoud, *J Am Chem Soc*, 2007, **129**, 14834–14835.
- 89 J. Zhang, P. D. Badger, S. J. Geib and S. Petoud, *Angewandte Chemie - International Edition*, 2005, **44**, 2508–2512.
- 90 S. Petoud, G. Muller, E. G. Moore, J. Xu, J. Sokolnicki, J. P. Riehl, U. N. Le, S. M. Cohen and K. N. Raymond, *J Am Chem Soc*, 2007, **129**, 77–83.
- 91 X. Wang, R. R. Valiev, T. Y. Ohulchanskyy, H. Ågren, C. Yang and G. Chen, *Chem Soc Rev*, 2017, **46**, 4150–4167.
- 92 G. Chen, J. Damasco, H. Qiu, W. Shao, T. Y. Ohulchanskyy, R. R. Valiev, X. Wu, G. Han, Y. Wang, C. Yang, H. Ågren and P. N. Prasad, *Nano Lett*, 2015, **15**, 7400–7407.
- 93 Th. Förster, *Ann Phys*, 1948, **437**, 55–75.
- 94 D. L. Dexter, *J Chem Phys*, 1953, **21**, 836–850.

- 95 Z. Q. You, C. P. Hsu and G. R. Fleming, *Journal of Chemical Physics*, 2006, **124**, 044506–044517.
- 96 P. Agbo and R. J. Abergel, *Inorg Chem*, 2016, **55**, 9973–9980.
- 97 N. Narayanan and G. Patonay, 1995, **5**, 2391–2395.
- 98 J. H. Flanagan, S. H. Khan, S. Menchen, S. A. Soper and R. P. Hammer, *Bioconjug Chem*, 1997, **8**, 751–756.
- 99 G. Patonay, J. Salon, J. Sowell and L. Strekowski, *Molecules*, 2004, **9**, 40–49.
- 100 N. Tyutyulkov, F. Dietz, A. Ivanova and K. Müllen, *Dyes and Pigments*, 1999, **42**, 215–222.
- 101 M. Schreiber, V. Buß, M. P. Fülcher and M. P. Fülcher, *Physical Chemistry Chemical Physics*, 2001, **3**, 3906–3912.
- 102 N. S. James, Y. Chen, P. Joshi, T. Y. Ohulchansky, M. Ethirajan, M. Henary, L. Strekowski and R. K. Pandey, *Theranostics*, 2013, **3**, 692–702.
- 103 S. Luo, E. Zhang, Y. Su, T. Cheng and C. Shi, *Biomaterials*, 2011, **32**, 7127–7138.
- 104 J. Fabian, H. Nakazumi and M. Matsuoka, *Chem Rev*, 1992, **92**, 1197–1226.
- 105 J. Zhou, F. Yang, G. Jiang and J. Wang, *J Thorac Dis*, 2016, **8**, S738–S743.
- 106 L. Tarazi, A. George, G. Patonay and L. Strekowski, *Talanta*, 1998, **46**, 1413–1424.
- 107 T. Górecki, G. Patonay, L. Strekowski, R. Chin and N. Salazar, *J Heterocycl Chem*, 1996, **33**, 1871–1876.
- 108 L. Strekowski, C. J. Mason, H. Lee, R. Gupta, J. Sowell and G. Patonay, *J Heterocycl Chem*, 2003, **40**, 913–916.
- 109 A. Samanta, M. Vendrell, R. Das and Y. T. Chang, *Chemical Communications*, 2010, **46**, 7406–7408.
- 110 S. Lu, J. Ke, X. Li, D. Tu and X. Chen, *Aggregate*, 2021, **2**, e59–e76.
- 111 D. J. Garfield, N. J. Borys, S. M. Hamed, N. A. Torquato, C. A. Tajon, B. Tian, B. Shevitski, E. S. Barnard, Y. D. Suh, S. Aloni, J. B. Neaton, E. M. Chan, B. E. Cohen and P. J. Schuck, *Nat Photonics*, 2018, **12**, 402–407.
- 112 S. Han, R. Deng, Q. Gu, L. Ni, U. Huynh, J. Zhang, Z. Yi, B. Zhao, H. Tamura, A. Pershin, H. Xu, Z. Huang, S. Ahmad, M. Abdi-Jalebi, A. Sadhanala, M. L. Tang, A. Bakulin, D. Beljonne, X. Liu and A. Rao, *Nature*, 2020, **587**, 594–599.
- 113 W. Zou, C. Visser, J. A. Maduro, M. S. Pshenichnikov and J. C. Hummelen, *Nat Photonics*, 2012, **6**, 560–564.
- 114 X. Wu, Y. Zhang, K. Takle, O. Bilsel, Z. Li, H. Lee, Z. Zhang, D. Li, W. Fan, C. Duan, E. M. Chan, C. Lois, Y. Xiang and G. Han, *ACS Nano*, 2016, **10**, 1060–1066.
- 115 C. Hazra, S. Ullah, Y. E. Serge Correales, L. G. Caetano and S. J. L. Ribeiro, *J Mater Chem C Mater*, 2018, **6**, 4777–4785.

- 116 M. I. Saleh, I. D. Panas, F. Frenzel, C. Würth, B. Rühle, Y. L. Slominskii, A. Demchenko and U. Resch-Genger, *Methods Appl Fluoresc*, 2019, **7**, 014003–014013.
- 117 P. A. Rojas-Gutierrez, C. DeWolf and J. A. Capobianco, *Particle and Particle Systems Characterization*, 2016, **33**, 865–870.
- 118 J. Xu, A. Gulzar, P. Yang, H. Bi, D. Yang, S. Gai, F. He, J. Lin, B. Xing and D. Jin, *Coord Chem Rev*, 2019, **381**, 104–134.
- 119 J. Liu, Y. Liu, W. Bu, J. Bu, Y. Sun, J. Du and J. Shi, *J Am Chem Soc*, 2014, **136**, 9701–9709.
- 120 R. Lv, D. Wang, L. Xiao, G. Chen, J. Xia and P. N. Prasad, *Sci Rep*, 2017, **7**, 15753–15764.
- 121 T. Sabri, P. D. Pawelek and J. A. Capobianco, *ACS Appl Mater Interfaces*, 2018, **32**, 26947–26953.
- 122 S. Wilhelm, *ACS Nano*, 2017, **11**, 10644–10653.
- 123 E. Engel, R. Schraml, T. Maisch, K. Kobuch, B. Konig, R. M. Szeimies, J. Hillenkamp, W. Bäumlner and R. Vasold, *Invest Ophthalmol Vis Sci*, 2008, **49**, 1777–1783.
- 124 A. P. Gorka, R. R. Nani and M. J. Schnermann, *Acc Chem Res*, 2018, **51**, 3226–3235.
- 125 A. P. Gorka, R. R. Nani and M. J. Schnermann, *Org Biomol Chem*, 2015, **13**, 7584–7598.
- 126 R. R. Nani, J. A. Kelley, J. Ivanic and M. J. Schnermann, *Chem Sci*, 2015, **6**, 6556–6563.
- 127 D. H. Li, C. L. Schreiber and B. D. Smith, *Angew Chem Int Ed Engl*, 2020, **59**, 12154–12161.
- 128 A. P. Gorka and M. J. Schnermann, *Curr Opin Chem Biol*, 2016, **33**, 117–125.
- 129 X. Wu, H. Lee, O. Bilsel, Y. Zhang, Z. Li, T. Chen, Y. Liu, C. Duan, J. Shen, A. Punjabi and G. Han, *Nanoscale*, 2015, **7**, 18424–18428.
- 130 C. Du, H. Wang, F. Yang and P. C. Hammel, *Phys Rev B Condens Matter Mater Phys*, 2014, **90**, 140407–140412.
- 131 D. Yin, Y. Liu, J. Tang, F. Zhao, Z. Chen, T. Zhang, X. Zhang, N. Chang, C. Wu, D. Chen and M. Wu, *Dalton Transactions*, 2016, **45**, 13392–13398.
- 132 J. Xu, P. Yang, M. Sun, H. Bi, B. Liu, D. Yang, S. Gai, F. He and J. Lin, *ACS Nano*, 2017, **11**, 4133–4144.
- 133 A. Fujishima and K. Honda, *Nature*, 1972, **238**, 37–38.
- 134 A. L. Linsebigler, G. Lu and J. T. Yates, *Chem Rev*, 1995, **95**, 735–758.
- 135 Z. H. Jabbar and S. Esmail Ebrahim, *Environ Nanotechnol Monit Manag*, 2022, **17**, 100666.
- 136 Z. Lin, M. Ye and M. Wang, *Multifunctional Photocatalytic Materials for Energy*, 2018.
- 137 A. H. Asif, S. Wang and H. Sun, *Curr Opin Green Sustain Chem*, 2021, **28**, 100447–100455.
- 138 H. J. H. Fenton and H. J. Jackson, *Journal of the Chemical Society, Transactions*, 1899, **75**, 1–11.
- 139 H. J. H. Fenton, *Journal of the Chemical Society, Transactions*, 1894, **65**, 899–911.

- 140 H. J. H. Fenton and H. O. Jones, *Journal of the Chemical Society, Transactions*, 1900, 77, 69–76.
- 141 N. Thomas, D. D. Dionysiou and S. C. Pillai, *J Hazard Mater*, 2021, 404, 124082–124105.
- 142 W. H. Koppenol, *Free Radic Biol Med*, 1993, **15**, 645–651.
- 143 W. Q. Fang, X. Q. Gong and H. G. Yang, *Journal of Physical Chemistry Letters*, 2011, **2**, 725–734.
- 144 J. Augustynski, *Electrochim Acta*, 1993, **38**, 43–46.
- 145 K. M. Mohamed, J. J. Benitto, J. J. Vijaya and M. Bououdina, *Crystals (Basel)*, 2023, **13**, 1–26.
- 146 H. Q. Wang, M. Batentschuk, A. Osvet, L. Pinna and C. J. Brabec, *Advanced Materials*, 2011, **23**, 2675–2680.
- 147 Z. Zhang, W. Wang, W. Yin, M. Shang, L. Wang and S. Sun, *Appl Catal B*, 2010, **101**, 68–73.
- 148 D. Sarkar, S. Ganguli, T. Samanta and V. Mahalingam, *Langmuir*, 2019, **35**, 6211–6230.
- 149 W. Qin, D. Zhang, D. Zhao, L. Wang and K. Zheng, *Chemical Communications*, 2010, **46**, 2304–2306.
- 150 L. Ren, X. Qi, Y. Liu, Z. Huang, X. Wei, J. Li, L. Yang and J. Zhong, *J Mater Chem*, 2012, **22**, 11765–11771.
- 151 J. Xu, M. Sun, Y. Kuang, H. Bi, B. Liu, D. Yang, R. Lv, S. Gai, F. He and P. Yang, *Dalton Transactions*, 2017, **46**, 1495–1501.
- 152 M. D. Wisser, S. Fischer, C. Siefe, A. P. Alivisatos, A. Salleo and J. A. Dionne, *Nano Lett*, 2018, **18**, 2689–2695.
- 153 S. L. Lin, Z. R. Chen and C. A. Chang, *Nanotheranostics*, 2018, **2**, 243–257.
- 154 B. Chen and F. Wang, *Trends Chem*, 2020, **2**, 427–439.
- 155 X. Liu, C. H. Yan and J. A. Capobianco, *Photon upconversion nanomaterials*, 2015, vol. 44.
- 156 S. Banerjee, J. Koerner, M. Siebold, Q. Yang, K. Ertel, P. D. Mason, P. J. Phillips, M. Loeser, H. Zhang, S. Lu, J. Hein, U. Schramm, M. C. Kaluza and J. L. Collier, *Opt Express*, 2013, **21**, A726–A724.
- 157 Y. F. Wang, G. Y. Liu, L. D. Sun, J. W. Xiao, J. C. Zhou and C. H. Yan, *ACS Nano*, 2013, **7**, 7200–7206.
- 158 F. Vetrone, R. Naccache, V. Mahalingam, C. G. Morgan and J. A. Capobianco, *Adv Funct Mater*, 2009, **19**, 2924–2929.
- 159 C. Shi, J. B. Wu and D. Pan, *J Biomed Opt*, 2016, **21**, 050901–050913.
- 160 H. T. T. Duong, Y. Chen, S. A. Tawfik, S. Wen, M. Parviz, O. Shimoni and D. J. Ab, *RSC Adv*, 2018, **8**, 4842–4849.
- 161 D. S. McClure, *J Chem Phys*, 1949, **17**, 905–913.
- 162 I. Zebger, L. Poulsen, Z. Gao, L. K. Andersen and P. R. Ogilby, *Langmuir*, 2003, **19**, 8927–8933.
- 163 N. Bogdan, F. Vetrone, G. A. Ozin and J. A. Capobianco, *Nano Lett*, 2011, **11**, 835–840.

- 164 F. Vetrone, J. C. Boyer, J. A. Capobianco, A. Speghini and M. Betinelli, *Chemistry of Materials*, 2003, **15**, 2737–2743.
- 165 B. Xue, D. Wang, L. Tu, D. Sun, P. Jing, Y. Chang, Y. Zhang, X. Liu, J. Zuo, J. Song, J. Qu, E. J. Meijer, H. Zhang and X. Kong, *Journal of Physical Chemistry Letters*, 2018, **9**, 4625–4631.
- 166 R. H. Page, K. I. Schaffers, P. A. Waide, J. B. Tassano, S. A. Payne, W. F. Krupke and W. K. Bischel, *Journal of the Optical Society of America B*, 1998, **15**, 996–1008.
- 167 F. T. Rabouw, P. T. Prins, P. Villanueva-Delgado, M. Castelijns, R. G. Geitenbeek and A. Meijerink, *ACS Nano*, 2018, **12**, 4812–4823.
- 168 N. Liu, R. Marin, Y. Mazouzi, G. O. Cron, A. Shuhendler and E. Hemmer, *Nanoscale*, 2019, **11**, 6794–6801.
- 169 Y. Wang, K. Zheng, S. Song, D. Fan, H. Zhang and X. Liu, *Chem Soc Rev*, 2018, **47**, 6473–6485.
- 170 S. Wilhelm, M. Kaiser, C. Würth, J. Heiland, C. Carrillo-Carrion, V. Muhr, O. S. Wolfbeis, W. J. Parak, U. Resch-Genger and T. Hirsch, *Nanoscale*, 2015, **7**, 1403–1410.
- 171 A. Gnach, T. Lipinski, A. Bednarkiewicz, J. Rybka and J. A. Capobianco, *Chem. Soc. Rev.*, 2015, **44**, 1561–1584.
- 172 F. Lu, L. Yang, Y. Ding and J. J. Zhu, *Adv Funct Mater*, 2016, **26**, 4778–4785.
- 173 P. Lederhose, Z. Chen, R. Müller, J. P. Blinco, S. Wu and C. Barner-Kowollik, *Angewandte Chemie - International Edition*, 2016, **55**, 12195–12199.
- 174 S. Shikha, T. Salafi, J. Cheng and Y. Zhang, *Chem Soc Rev*, 2017, **46**, 7054–7093.
- 175 H. Yang, C. Han, X. Zhu, Y. Liu, K. Y. Zhang, S. Liu, Q. Zhao, F. Li and W. Huang, *Adv Funct Mater*, 2016, **26**, 1945–1953.
- 176 R. Naccache, F. Vetrone and J. A. Capobianco, *ChemSusChem*, 2013, **6**, 1308–1311.
- 177 H. Liu, M. K. G. Jayakumar, K. Huang, Z. Wang, X. Zheng, H. Ågren and Y. Zhang, *Nanoscale*, 2017, **9**, 1676–1686.
- 178 S. V. Eliseeva and J.-C. G. Bünzli, *Chem. Soc. Rev.*, 2010, **39**, 189–227.
- 179 T. Liang, Q. Wang, Z. Li, P. Wang, J. Wu, M. Zuo and Z. Liu, *Adv Funct Mater*, 2020, **30**, 1910765–1910773.
- 180 H. R. M. Silva, W. M. Faustino, E. E. S. Teotonio, H. F. Brito, O. L. Malta and M. C. F. C. Felinto, *J Lumin*, 2018, **207**, 182–187.
- 181 G. Bao, S. Wen, G. Lin, J. Yuan, J. Lin, K. L. Wong, J. C. G. Bünzli and D. Jin, *Coord Chem Rev*, 2020, **429**, 213642–213672.
- 182 G. Chen, W. Shao, R. R. Valiev, T. Y. Ohulchanskyy, G. S. He, H. Ågren and P. N. Prasad, *Adv Opt Mater*, 2016, **4**, 1760–1766.
- 183 S. Hao, Y. Shang, D. Li, H. Ågren, C. Yang and G. Chen, *Nanoscale*, 2017, **9**, 6711–6715.

- 184 S. Wang, L. Liu, Y. Fan, A. M. El-Toni, M. S. Alhoshan, D. Li and F. Zhang, *Nano Lett*, 2019, **19**, 2418–2427.
- 185 M. Zhao, B. Li, Y. Wu, H. He, X. Zhu, H. Zhang, C. Dou, L. Feng, Y. Fan and F. Zhang, *Advanced Materials*, 2020, **32**, 2001172–2001179.
- 186 Q. Chen, C. Wang, L. Cheng, W. He, Z. Cheng and Z. Liu, *Biomaterials*, 2014, **35**, 2915–2923.
- 187 V. Gubala, G. Giovannini, F. Kunc, M. P. Monopoli and C. J. Moore, *Cancer Nanotechnol*, 2020, **11**, 1–43.
- 188 M. Montalti, L. Prodi, E. Rampazzo and N. Zaccheroni, *Chem Soc Rev*, 2014, **43**, 4243–4268.
- 189 L. Jiao, F. Song, B. Zhang, H. Ning, J. Cui and X. Peng, *J Mater Chem B*, 2017, **5**, 5278–5283.
- 190 T. Ribeiro, S. Raja, A. S. Rodrigues, F. Fernandes, C. Baleizão and J. P. S. Farinha, *Dyes and Pigments*, 2014, **110**, 227–234.
- 191 X. Zhang, W. Chen, X. Xie, Y. Li, D. Chen, Z. Chao, C. Liu, H. Ma, Y. Liu and H. Ju, *Angewandte Chemie - International Edition*, 2019, **58**, 12245–12250.
- 192 D. Wang, D. Wang, A. Kuzmin, A. Pliss, W. Shao, J. Xia, J. Qu and P. N. Prasad, *Adv Opt Mater*, 2018, **6**, 1701142–1701151.
- 193 Z. Liu, F. Ren, H. Zhang, Q. Yuan, Z. Jiang, H. Liu, Q. Sun and Z. Li, *Biomaterials*, 2019, **219**, 119364–119375.
- 194 J. Cha, R. R. Nani, M. P. Luciano, G. Kline, A. Broch, K. Kim, J. M. Namgoong, R. A. Kulkarni, J. L. Meier, P. Kim and M. J. Schnermann, *Bioorg Med Chem Lett*, 2018, **28**, 2741–2745.
- 195 L. Feng, W. Chen, X. Ma, S. H. Liu and J. Yin, *Org Biomol Chem*, 2020, **18**, 9385–9397.
- 196 B. Ding, S. Shao, C. Yu, B. Teng, M. Wang, Z. Cheng, K. L. Wong, P. Ma and J. Lin, *Advanced Materials*, 2018, **30**, 1802479–1802489.
- 197 Y. Dai, D. Yang, D. Yu, S. Xie, B. Wang, J. Bu, B. Shen, W. Feng and F. Li, *Nanoscale*, 2020, **12**, 5075–5083.
- 198 A. Li, T. Guan and Z. Sun, *EPL*, 2014, **106**, 48001–48008.
- 199 H. Hu, L. Xiong, J. Zhou, F. Li, T. Cao and C. Huang, *Chemistry - A European Journal*, 2009, **15**, 3577–3584.
- 200 F. Zhao, D. Yin, C. Wu, B. Liu, T. Chen, M. Guo, K. Huang, Z. Chen and Y. Zhang, *Dalton Transactions*, 2017, **46**, 16180–16189.
- 201 I. Miletto, E. Botinelli, G. Caputo, S. Coluccia and E. Gianoti, *Physical Chemistry Chemical Physics*, 2012, **14**, 10015–10021.
- 202 G. Batistelli, A. Cantelli, G. Guideti, J. Manzi and M. Montalti, *Wiley Interdiscip Rev Nanomed Nanobiotechnol*, 2016, **8**, 139–151.

- 203 R. I. Nooney, C. M. N. McCahey, O. Stranik, X. Le Guevel, C. McDonagh and B. D. MacCraith, *Anal Bioanal Chem*, 2009, **393**, 1143–1149.
- 204 D. R. Larson, H. Ow, H. D. Vishwasrao, A. A. Heikal, U. Wiesner and W. W. Webb, *Chemistry of Materials*, 2008, **20**, 2677–2684.
- 205 H. Ow, D. R. Larson, M. Srivastava, B. A. Baird, W. W. Webb and U. Wiesner, *Nano Lett*, 2005, **5**, 113–117.
- 206 X. Xie, Z. Li, Y. Zhang, S. Guo, A. I. Pendharkar, M. Lu, L. Huang, W. Huang and G. Han, *Small*, 2017, **13**, 1602843–1602858.
- 207 N. Song, B. Zhou, L. Yan, J. Huang and Q. Zhang, *Front Chem*, 2019, **6**, 1–8.
- 208 B. M. Walsh, J. M. McMahon, W. C. Edwards, N. P. Barnes, R. W. Equall and R. L. Hutcheson, *Journal of the Optical Society of America B*, 2002, **19**, 2893–2903.
- 209 W. Y. D. Yong, Z. Zhang, G. Cristobal and W. S. Chin, *Colloids Surf A Physicochem Eng Asp*, 2014, **460**, 151–157.
- 210 E. van der Kolk, P. Dorenbos, K. Krämer, D. Biner and H. U. Güdel, *Phys Rev B*, 2008, **77**, 125110.
- 211 X. Li, R. Wang, F. Zhang, L. Zhou, D. Shen, C. Yao and D. Zhao, *Sci Rep*, 2013, **3**, 3536–3543.
- 212 S. Ullah, E. P. Ferreira-Neto, C. Hazra, R. Parveen, H. D. Rojas-Mantilla, M. L. Calegaro, Y. E. Serge-Correaes, U. P. Rodrigues-Filho and S. J. L. Ribeiro, *Appl Catal B*, 2019, **243**, 121–135.
- 213 L. Tan, D. Li, L. Zhang, L. Xu, Y. Zhao, L. Zhu and R. Qiao, *The Journal of Physical Chemistry C*, 2020, **124**, 18081–18090.
- 214 X. Han, L. Zhou, H. Zhuang, P. Wei, F. Li, L. Jiang and T. Yi, *ACS Appl Mater Interfaces*, 2022, **14**, 18031–18042.
- 215 L. Liang, L. Cheng, Y. Zhang, Q. Wang, Q. Wu, Y. Xue and X. Meng, *RSC Adv*, 2020, **10**, 28509–28515.
- 216 M. Zhu, Y. Wang, D. Meng, X. Qin and G. Diao, *Journal of Physical Chemistry C*, 2012, **116**, 16276–16285.
- 217 C. Xu, C. Lei, Y. Wang and C. Yu, *Angewandte Chemie - International Edition*, 2022, **61**, e202112752–e202112774.
- 218 A. Nsubuga, G. A. Mandl and J. A. Capobianco, *Nanoscale Adv*, 2021, **3**, 1375–1381.
- 219 G. R. Buettner, *Free Radic Biol Med*, 1987, **3**, 259–303.
- 220 K. M. Schaich and D. C. Borg, *Lipids*, 1988, **23**, 570–579.
- 221 S. Frindy and M. Sillanpää, *Mater Des*, 2020, **188**, 108461–108473.
- 222 S. Liang, Y. Chang, Y. Wang, D. Zhang and X. Pu, *Catal Sci Technol*, 2019, **9**, 2103–2110.

- 223 W. C. Oh, S. Ye, J. G. Park, S. H. Kang and C. S. Lim, *Journal of Industrial and Engineering Chemistry*, 2015, **32**, 225–232.
- 224 C. Pfeiffer, C. Rehbock, D. Hühn, C. Carrillo-Carrion, D. J. De Aberasturi, V. Merk, S. Barcikowski and W. J. Parak, *J R Soc Interface*, 2014, **11**, 1–13.
- 225 A. G. Joly, W. Chen, D. E. McCready, J. O. Malm and J. O. Bovin, *Phys Rev B Condens Matter Mater Phys*, 2005, **71**, 165304–165313.
- 226 I. Plesco, V. Ciobanu, T. Braniste, V. Ursaki, F. Rasch, A. Sarua, S. Raevschi, R. Adelung, J. Dutta and I. Tiginyanu, *Materials*, 2021, **14**, 1985–1998.
- 227 M. Pawlicki, H. A. Collins, R. G. Denning and H. L. Anderson, *Angewandte Chemie - International Edition*, 2009, **48**, 3244–3266.
- 228 K. D. Belfield, S. Yao and M. V. Bondar, *Advances in Polymer Science*, 2008, 213.
- 229 M. Rumi and J. W. Perry, *Adv Opt Photonics*, 2010, **2**, 451–518.
- 230 J. L. Clark, P. F. Miller and G. Rumbles, *Journal of Physical Chemistry A*, 1998, **102**, 4428–4437.
- 231 R. W. Wood, *The London, Edinburgh, and Dublin Philosophical Magazine and Journal of Science*, 1928, **6**, 310–312.
- 232 M. Betinelli, L. D. Carlos, X. X. X. Liu, Y. Il Park, K.-B. K. T. Lee, Y. D. Suh, T. Hyeon, X. Wu, Y. Y. Y. Y. W. Zhang, K. Takle, O. Bilsel, Z. Z. Li, H. H. H. Lee, O. Bilsel, Y. Y. Y. Y. W. Zhang, Z. Z. Li, T. T. Chen, Y. Y. Y. Y. Liu, C. C. Duan, J. Shen, A. Punjabi, G. Han, W. Zou, C. Visser, J. A. Maduro, M. S. Pshenichnikov, J. C. Hummelen, F. Zhang, R. Che, X. Li, C. Yao, J. Yang, D. D. Shen, P. P. Hu, W. Li, D. Zhao, A. Nadort, J. X. J. Zhao, E. M. Goldys, X. Li, F. Zhang, D. Zhao, S. S. Han, R. Deng, X. Xie, X. X. X. Liu, X. Wu, H. H. H. Lee, O. Bilsel, Y. Y. Y. Y. W. Zhang, Z. Z. Li, T. T. Chen, R. Naccache, Q. Yu, J. A. Capobianco, S. Wen, J. J. C. Zhou, K. Zheng, A. Bednarkiewicz, X. X. X. Liu, D. Jin, C. C. Duan, L. Liang, L. M. L. Li, R. Zhang, Z. P. Xu, M. V. DaCosta, S. Doughan, Y. Y. Han, U. J. Krull, A. Dong, X. Ye, J. J. Chen, Y. Kang, T. Gordon, J. M. Kikkawa, C. B. Murray, W. Zou, C. Visser, J. A. Maduro, M. S. Pshenichnikov, J. C. Hummelen, D. J. Garfield, N. J. Borys, S. M. Hamed, N. A. Torquato, C. A. Tajon, B. Tian, B. Shevitski, E. S. Barnard, Y. D. Suh, S. Aloni, J. B. Neaton, E. M. Chan, B. E. Cohen, P. J. Schuck, F. Vetrone, R. Naccache, V. Mahalingam, C. G. Morgan, J. A. Capobianco, A. S. Editor, H. Search, C. Journals, A. Contact, M. Iopscience, I. P. Address, A. M. Nocolak, T. A. Manuscript, I. O. P. Publishing, A. A. Manuscript, A. A. Manuscript, C. C. By-nc-nd, A. A. Manuscript, W. Stober, A. Fink, Q. Q. Liu, C. C. C. C. Li, T. Yang, T. Yi, F. F. Li, P.-J. P. Huang, W. Zheng, S. Zhou, D. Tu, Z. Z. Chen, H. Zhu, R. Li, W. Li, D. Zhao, A. U. Intensity, P. Hamm, J. Helbing, G. Y. G. Liu, B. Jacquier, Thermo Spectronic, H. C. Swart, J. J. Terblans, O. M. Ntwaeaborwa, R. E. Kroon, E. Coetsee, I. M. Nagpure, V. V. V. Kumar, V. V. V. Kumar, V. V. V. Kumar, M. A. Wear, L. Blackburn, M. W. Nowicki, H. Peng, E. N. S. Cachan, P. Wilson, E. N. S. Cachan, P. Wilson, C. Cnrs, G. Urbain, F. Iufm, J. Mac, X. Ge, L. L. L. D. Sun, L. Shi, R. Wei, S. I. Text, S. Plus, U. Es, P. Rp, A. Hplc, Q. N. Superflow, A. S. Cell, F. F. Liu, Q. Zhao, H. You, Z. Z. Z. Y. Wang, E. Sections, R. Dna, P. Dna, T. Dna, D. Biotech, E. D. Goddard-Borger, R. V. Stick, F. F. Wang, R. Deng, J. J. J. Wang, Q. Wang, Y. Y. Han, H. Zhu, X. X. X. Chen, X. X. X. Liu, F. F. Liu, Q. Zhao, H. You, Z. Z. Z. Y. Wang, J. J. J. Wang, R. Deng, M. A. Macdonald, B. B. Chen, J. Yuan, F. F. Wang, D. Chi, T. S. Andy Hor, P. Z. P. Zhang, G. Y. G. Liu, Y. Y. Han, X. X. X. Liu, H. Hu, L. Xiong, J.

J. C. Zhou, F. F. Li, T. Cao, C. Huang, Y. Y. Y. F. Wang, G. Y. G. Liu, L. L. L. D. Sun, J. W. Xiao, J. J. C. Zhou, C. C. C.-H. H. Yan, N. Bogdan, F. Vetrone, G. A. Ozin, J. A. Capobianco, K. D. Wegner, N. Hildebrandt, W. Li, Y. Y. Xu, Y. Zhou, W. Ma, S. S. S. Q. Wang, Y. Dai, S. L. Chia, D. T. Leong, W. Li, Y. Y. Xu, Y. Zhou, W. Ma, S. S. S. Q. Wang, Y. Dai, J.-J. J. J.-N. J. J. Liu, W. W.-B. Bu, J. J.-L. Shi, X. Li, F. Zhang, D. Zhao, M. Prieto, A. Y. Rwei, T. Alejo, T. Wei, M. T. Lopez-Franco, G. Mendoza, V. Sebastian, D. S. Kohane, M. Arruebo, S. Xiao, X. Yang, Z. Z. Liu, X. H. Yan, S. Xiao, X. Yang, Z. Z. Liu, X. H. Yan, G. G. Chen, H. Qiu, P. N. Prasad, X. X. X. Chen, O. Dukhno, F. Przybilla, M. Collot, A. Klymchenko, V. Pivovarenko, M. Buchner, V. Muhr, T. Hirsch, Y. Mély, I. a. M. Ibrahim, A. a. F. Zikry, M. a. Sharaf, P. Vinicius, C. Garcia, M. Walker, S. Vasconcelos, K. Results, D. a Larsen, S. b Holyer, J. c Eckstein, A. d Kirjavainen, O. e Sorje, M. A. Sganderla, G. S. Lacerda, M. D. Tegner, E. L. Daronco, Á. A. Roberto, H. P. Fernandes, M. A. Gonçalves, D. Paula, A. Henrique, A. Barranqueiros, G. Travassos, D. Gurov, E. Amaral, M. G. Dias, S. Easterbrook, J. Singer, M.-A. Storey, D. Damian, J. Silva, C. Manager, X. X. X. Liu, C. C. C.-H. H. Yan, J. A. Capobianco, P.-J. P. Huang, W. Zheng, S. Zhou, D. Tu, Z. Z. Chen, H. Zhu, R. Li, E. Ma, M. Huang, X. X. X. Chen, C. C. Wang, L. Cheng, Z. Z. Liu, J. V. Frangioni, N. M. Sangeetha, P. Moutet, D. Lagarde, G. Sallen, B. Urbaszek, X. Marie, G. Viau, L. Ressler, D. Ban, J. J. Chen, J. Tao, M. G. Helander, Z. Z. Z. Y. Wang, J. Qiu, Z. Lu, F. F. Wang, R. Deng, J. J. J. Wang, Q. Wang, Y. Y. Han, H. Zhu, X. X. X. Chen, X. X. X. Liu, J. Fabian, H. Nakazumi, M. Matsuoka, Z. Z. Z. Y. Wang, J. J. J. Zhang, X. Wu, M. Birau, G. Yu, H. Yu, Y. Qi, P. Desjardins, X. Meng, J. P. Gao, E. Todd, N. Song, Y. Bai, A. M. R. Beaudin, G. Leclair, W. Feng, X. Zhu, F. F. Li, Z. Z. Li, Y. Y. Y. Y. Y. W. Zhang, X. Ye, J. E. Collins, Y. Kang, J. J. Chen, D. T. N. Chen, A. G. Yodh, C. B. Murray, A. Aebischer, F. Gumy, J.-C. G. Bünzli, I. Rodrigues, J. Sanches, D. S. Conceição, D. P. Ferreira, L. F. Vieira Ferreira, S. S. Xu, B. Dong, D. Zhou, Z. Yin, S. Cui, W. Xu, B. B. Chen, H. Song, A. Diaspro, G. Chirico, C. Usai, P. Ramoino, J. Dobrucki, J.-J. J. J.-N. J. J. Liu, W. W.-B. Bu, L. Pan, J. J.-L. Shi, N. L. Olteanu, C. A. Lazăr, A. R. Petcu, A. Meghea, E. A. Rogozea, M. Mihaly, S. A. Hilderbrand, R. Weissleder, D. Yin, F. Zhao, C. Wu, B. Liu, T. T. Chen, M. Guo, K. Huang, Z. Z. Chen, Y. Y. Y. Y. Y. W. Zhang, A. Haque, M. S. H. Faizi, J. A. Rather, M. S. Khan, S. Shah, J.-J. J. J.-N. J. J. Liu, N. Pasquale, J. Lai, H. McGowan, Z. P. Pang, K.-B. K. T. Lee, H. X. Mai, Y. Y. Y. Y. Y. W. Zhang, R. Si, Z. G. Yan, L. L. L. D. Sun, L. P. You, C. C. C.-H. H. Yan, H. A. Shindy, X. Zhai, P. Lei, P. Z. P. Zhang, Z. Z. Z. Y. Wang, S. Song, X. Xu, X. X. X. Liu, J. Feng, H. Zhang, S. Hussain, L. Fodor, Y. Ullmann, M. Elman, B. K. Sodipo, A. A. Aziz, C. C. C.-H. H. Yan, H. H. Zhao, D. F. Perepichka, F. Rosei, S. Br-br, J. Shen, L. Zhao, G. Han, A. Bagheri, H. Arandiyani, C. Boyer, M. Lim, Q. Q. Liu, C. C. C. C. Li, T. Yang, T. Yi, F. F. Li, R. Naccache, F. Vetrone, V. Mahalingam, L. a Cuccia, J. A. Capobianco, V. Kale, M. Lastusaari, J. Hölsä, T. Soukka, Y. Li, J. J. Tang, L. He, Y. Y. Y. Y. Liu, Y. Y. Y. Y. Liu, C. C. Chen, Z. Tang, S. Brasselet, P. Ferrand, A. Kress, A. Schlossbauer, D. Schaffert, J. Kecht, E. Wagner, T. Bein, C. Chemistry, J. V. B. Kanth, M. Periasamy, N. S. James, Y. Y. Y. M. Chen, P. Joshi, T. Y. Ohulchanskyy, M. Ethirajan, M. Henary, L. Strekowski, R. K. Pandey, A. A. Manuscript, O. M. Imaging, R. Scheps, R. D. Badley, W. T. Ford, F. J. McEnroe, R. A. Assink, X. Wu, Y. Y. Y. Y. Y. W. Zhang, K. Takle, O. Bilsel, Z. Z. Li, H. H. H. Lee, Z. Z. Zhang, D. Li, W. Fan, C. C. Duan, E. M. Chan, C. Lois, Y. Xiang, G. Han, M. Laurenti, M. Paez-Perez, M. Algarra, P. Alonso-Cristobal, E. Lopez-Cabarcos, D. Mendez-Gonzalez, J. Rubio-Retama, C. C. Chen, C. C. C. C. Li, Z. Shi, J. Wen, K. Yang, F. F. Liu, H. H. Li, Y. Y. Xu, S. Sun, S. S. Han, S. Beack, S. Jeong, B. W. Hwang, M. H. Shin, H. M. H. H. Kim, S. Kim, S. K. Hahn, Z. Feng, H. Xia, C. C. Wang, Z. Z. Zhang, D. Jiang, J. J. J. Zhang, S. He, Q. Tang, Q. Sheng, X. Gu, Y. Y. Y. Y. Y. W. Zhang, B. B. Chen, H. Jiang, S. Luo, E. Zhang, Y. Su, T. Cheng, C. C. Shi, S. S. S. Q. Wang, L. L. L. Zhang, C. C. Dong, L. Su, H. H. H. Wang, J. Chang, Z. Z. Li, Y. Y. Y. Y. Y. W. Zhang, J. J. J. Wang, T. Ming, Z. Jin, J. J.

J. Wang, L. L. L. D. Sun, C. C. C.-H. H. Yan, Y. L. Y. Zhao, J. Fraser Stoddart, D. V. Okhrimenko, A. Budi, M. Ceccato, M. Cárdenas, D. B. Johansson, D. Lybye, K. Bechgaard, M. P. Andersson, S. L. S. Stipp, E. D. Goddard-Borger, R. V. Stick, T. J. Sminia, D. S. Pedersen, J. J. Bloomfield, S. L. S. Lee, X. Huang, J. Lin, H. H. Li, R. Wei, G. H. Yan, J. Sun, C. C. C. C. Li, H. H. H. Wang, L. Shi, J. A. Capobianco, L. L. L. D. Sun, J. J. C. Zhou, Q. Q. Liu, W. Feng, Y. Sun, F. F. Li, A. Agarwal, S. R. Bakshi, D. Lahiri, M. Meyyappan, M. Sunkara, Y. Yang, F. An, Z. Z. Liu, X. X. X. Zhang, M. Zhou, W. Li, X. Hao, C. S. Lee, X. X. X. Zhang, F. Auzel, S. L. Westcott, S. J. Oldenburg, T. R. Lee, N. J. Halas, V. Kale, J. J. C. Zhou, S. Wen, J. Liao, C. Clarke, S. A. Tawfik, W. Ren, C. Mi, F. F. Wang, D. Jin, A. Gnach, T. Lipinski, A. Bednarkiewicz, J. Rybka, J. A. Capobianco, F. N. I. R. Fluorescent, J. L. Lakshmi, S. Bin Dolmanan, S. Tripathy, B. Zhou, B. Shi, D. Jin, X. X. X. Liu, G. G. Chen, H. Ågren, T. Y. Ohulchanskyy, P. N. Prasad, G. Y. G. Liu, A. Sedlmeier, H. H. Gorris, L. L. L. D. Sun, Y. Y. Y. F. Wang, C. C. C.-H. H. Yan, G. G. Chen, J. Damasco, H. Qiu, W. Shao, T. Y. Ohulchanskyy, R. R. Valiev, X. Wu, G. Han, Y. Y. Y. F. Wang, C. Yang, H. Ågren, P. N. Prasad, L. Tu, X. X. X. Liu, F. Wu, H. Zhang, E. Hemmer, M. Quintanilla, F. Légaré, F. Vetrone, W. Zheng, P.-J. P. Huang, D. Tu, E. Ma, H. Zhu, X. X. X. Chen, S. Mourdikoudis, L. M. Liz-marza, M. A. Evans, P.-J. P. Huang, Y. Iwamoto, K. N. Ibsen, E. M. Chan, Y. Hitomi, P. C. Ford, S. Mitragotri, R. Si, Y. Y. Y. Y. W. Zhang, L. P. You, C. C. C.-H. H. Yan, A. D. Ostrowski, E. M. Chan, D. J. Gargas, E. M. Katz, G. Han, P. J. Schuck, D. J. Milliron, B. E. Cohen, Y. Hitomi, Y. Iwamoto, M. Kodera, S. C. Singh, H. Zeng, X. X. Peng, Q. Q. Liu, H. H. H. Wang, Y. Y. Y. F. Wang, P.-J. P. Huang, W. Zheng, S. Zhou, D. Tu, Z. Z. Chen, H. Zhu, J. S. Venkataraman, C. Subramaniam, R. R. Kumar, S. Priya, T. R. S. Kumar, R. V. Omkumar, A. John, T. Pradeep, A. Sedlmeier, H. H. Gorris, F. He, N. Niu, L. L. Wang, J. J. J. Xu, Y. Y. Y. F. Wang, G. Yang, S. Gai, P. P. Yang, D. Baziulyte-paulaviciene, V. Karabanovas, M. Stasys, G. Jarockyte, F. Zhang, R. Che, X. Li, C. Yao, J. Yang, D. D. Shen, P. P. Hu, W. Li, F. F. Wang, J. J. J. Wang, X. X. X. Liu, H. Dong, L. L. L. D. Sun, L. M. L. Li, R. Si, R. Liu, C. C. C.-H. H. Yan, A. A. Manuscript, N. J. J. Johnson, W. Oakden, G. J. Stanisiz, R. S. Prosser, F. C. J. M. Van Veggel, D. Yin, K. Song, Y. Ou, C. C. Wang, B. Yong, I. Park, J. H. Kim, K.-B. K. T. Lee, K. Jeon, H. Bin Na, J. H. Yu, H. M. H. H. Kim, N. Lee, S. H. Choi, S. Baik, H. M. H. H. Kim, S. P. Park, B. Park, Y. W. Kim, H. H. H. Lee, S. Yoon, I. C. Song, W. K. Moon, Y. D. Suh, T. Hyeon, C. E. T. Al, Y. Il Park, J. H. Kim, K.-B. K. T. Lee, K. Jeon, H. Bin Na, J. H. Yu, H. M. H. H. Kim, N. Lee, S. H. Choi, S. Baik, H. M. H. H. Kim, S. Pyo, I. B. Excited, J. Rocha, L. D. Carlos, F. A. A. Paz, D. Ananias, D. Jaque, F. Vetrone, X. X. X. Chen, C. C. Dong, J. Pichaandi, T. Regier, F. C. J. M. Van Veggel, R. Wu, L. Lei, S. Zhang, J. J. J. Zhang, S. S. Xu, Z. Xiao, J. J. J. Zhang, S. S. Xu, V. Mahalingam, R. Naccache, F. Vetrone, J. A. Capobianco, O. A. Savchuk, J. J. Carvajal, P. Haro-Gonzalez, M. Aguiló, F. Díaz, M. Fang, L. Fu, R. A. S. Ferreira, L. D. Carlos, A. A. Manuscript, P. Modification, Q. Control, Q. Q. Liu, Y. Sun, T. Yang, W. Feng, C. C. C. C. Li, F. F. Li, X. M. Kaur, M. Oh, J. Yi, U. Seo, H. H. H. Lee, H. Cho, M. Hwang, K. Kim, L. D. Carlos, R. A. S. Ferreira, V. De Zea Bermudez, S. J. L. Ribeiro, M. M. S. Ibrahim Khaleelullah, A. Tanaka, T. Dheivasigamani, K. Sugimoto, Y. Shimura, W. Inami, Y. Kawata, Y. Hayakawa, F. F. Li, C. C. C. C. Li, X. X. X. Liu, Y. Y. Y. M. Chen, T. Bai, L. L. Wang, Z. Shi, S. Feng, F. Edition, F. F. Wang, Y. Y. Han, C. S. Lim, Y. Lu, J. J. J. Wang, J. J. J. Xu, H. Chen, C. C. Zhang, M. Hong, X. X. X. Liu, F. Benetollo, G. Bombieri, L. Calabi, S. Aime, M. Botta, H. P. Austin, M. D. Allen, B. S. Donohoe, N. A. Rorrer, F. L. Kearns, R. L. Silveira, C. Pollard, G. Dominick, R. Duman, K. El Omari, V. Mykhaylyk, A. Wagner, W. E. Michener, A. Amore, M. S. Skaf, M. F. Crowley, A. W. Thorne, C. W. Johnson, H. L. Woodcock, E. John, G. T. Beckham, M. B. Laboratories, B. Sciences, U. Kingdom, N. Renewable, N. Renewable, U. States, S. Paulo, D. L. Source, H. Science, I. Campus, U. Kingdom, W. M. Bulleit, J.-J. J. J.-N. J. J. Liu, H. Rijckaert, M. Zeng, K. Haustraete, B. Laforce, L. Vincze, I. Van Driessche, A. M. Kaczmarek, R. Van

- Deun, C. Zhao, L. L. L. Zhang, Y. Hang, X. He, J. Yin, P. P. Hu, G. G. Chen, M. He, H. Huang, Y. Zhu, V. Ter-Mikirtychev, N. Vaccines, S. S. Deshpande, J. J. Chen, J. X. J. Zhao, P. I. V. E. Chemistry, F. Vetrone, R. Naccache, V. Mahalingam, C. G. B. Del Rosal, E. Ximendes, U. Rocha, D. Jaque, T. Ma, Y. Ma, S. Liu, L. L. L. Zhang, T. Yang, H. Yang, D. Yin, Y. Y. Y. Y. Liu, J. J. Tang, F. Zhao, Z. Z. Chen, T. Zhang, X. X. X. Zhang, N. Chang, C. Wu, D. T. N. Chen, M. Wu, A. You, M. A. Y. Be, I. In, G. G. Chen, J. Damasco, H. Qiu, W. Shao, T. Y. Ohulchanskyy, R. R. Valiev, X. Wu, G. Han, Y. Y. Y. F. Wang, C. Yang, H. Ågren, N. Paras, Q. S. Qin, P. Z. P. Zhang, L. L. L. D. Sun, S. Shi, N. X. Chen, H. Dong, X. Y. Zheng, L. M. L. Li, C. C. C.-H. H. Yan, C. D. S. Brites, P. P. Lima, N. J. O. Silva, A. Millán, V. S. Amaral, F. Palacio, L. D. Carlos, X. X. X. Chen, Z. Z. Chen, C. C. Zhang, J. Y. Lee, A. Nadort, J. X. J. Zhao, E. M. Goldys, F. F. Wang, X. X. X. Liu, A. Berger, C. F. Gainer, M. Romanowski, E. D. Braunstein, E. Duijnste, S. L. S. Lee, M. Lin, A. Lee, Y. Il Park, E. Alcalde, I. Dinarès, A. Ibáñez, N. Mesquida, A. Gnach, A. Bednarkiewicz, B. Del Rosal, A. Pérez-Delgado, M. Misiak, A. Bednarkiewicz, A. S. Vanetsev, Y. Orlovskii, D. J. Jovanović, M. D. Dramićanin, U. Rocha, K. Upendra Kumar, C. Jacinto, E. Navarro, E. Martín Rodríguez, M. Pedroni, A. Speghini, G. A. Hirata, I. R. Martín, D. Jaque, C. Cao, M. Xue, X. Zhu, P. P. Yang, W. Feng, F. F. Li, M. Lin, Y. L. Y. Zhao, S. S. S. Q. Wang, M. Liu, Z. F. Duan, Y. Y. Y. M. Chen, F. F. Li, F. Xu, T. J. Lu, K. V. R. Murthy, H. S. Virk, A. Bednarkiewicz, D. Wawrzynczyk, M. Nyk, W. Strek, V. V. Chalapathi, V. K. Ramiah, L. Marciniak, A. Pilch, S. Arabasz, D. Jin, A. Bednarkiewicz, K. Elzbieciak, D. Wawrzynczyk, A. Bednarkiewicz, M. Nyk, W. Strek, M. Samoc, J. J. J. Xu, A. Gulzar, P. P. Yang, H. Bi, D. Yang, S. Gai, F. He, J. Lin, B. Xing, D. Jin, I. J. Gomez, B. Arnaiz, M. Cacioppo, F. Arcudi, M. Prato, X. Wang, R. R. Valiev, T. Y. Ohulchanskyy, H. Ågren, C. Yang, G. G. Chen, Y. Mita, H. Yamamoto, K. Katayanagi, S. Shionoya, P. S. Peijzel, A. Meijerink, R. T. Wegh, M. F. Reid, G. W. Burdick, N. Narayanan, G. Patonay, L. Xia, X. Kong, X. X. X. Liu, L. Tu, Y. Y. Y. Y. W. Zhang, Y. Y. Chang, K. Liu, D. D. Shen, H. H. Zhao, H. Zhang, A. Samanta, M. Vendrell, Y. Y. Chang, A. Teitelboim, B. Tian, D. J. Garfield, A. F. Bravo, A. Gotlin, J. Schuck, B. E. Cohen, E. M. Chan, F. F. Wang, R. Deng, X. X. X. Liu, D. Press, C. Nps, A. Meoh, C. C. Shi, S. G. Awuah, J. Polreis, V. Biradar, Y. You, L. Zhou, G. Zhao, J.-J. J. J.-N. J. J. Liu, K. Han, Y. Wu, F. Of, T. H. E. Problem, F. Song, X. X. Peng, E. Lu, Y. Y. Y. F. Wang, W. Zhou and J. Fan, *Chem. Soc. Rev.*, 2015, **44**, 1–13.
- 233 C. Gao, W. W. H. Wong, Z. Qin, S. C. Lo, E. B. Namdas, H. Dong and W. Hu, *Advanced Materials*, 2021, **33**, 2100704–2100710.
- 234 P. Bharmoria, H. Bildirir and K. Moth-Poulsen, *Chem Soc Rev*, 2020, **49**, 6529–6554.
- 235 A. A. Pushkar', T. V. Uvarova and V. V. Kiiko, in *Optics and Spectroscopy (English translation of Optika i Spektroskopiya)*, 2011, vol. 111.
- 236 Y. Dwivedi, S. N. Thakur and S. B. Rai, *Appl Phys B*, 2007, **89**, 45–51.
- 237 H. Liang, G. Chen, L. Li, Y. Liu, F. Qin and Z. Zhang, *Opt Commun*, 2009, **282**, 3028–3031.
- 238 M. F. Joubert, *Opt Mater (Amst)*, 1999, **11**, 181–203.
- 239 F. E. Auzel, *Proceedings of the IEEE*, 1973, **61**, 758–786.
- 240 L. Cademartiri, G. A. Ozin and J.-M. Lehn, in *Concepts of Nanochemistry*, 2009.
- 241 J. J. H. A. Van Hest, G. A. Blab, H. C. Gerritsen, C. De Mello Donega and A. Meijerink, *Journal of Physical Chemistry C*, 2017, **121**, 19373–19382.

- 242 M. Kraft, C. Würth, V. Muhr, T. Hirsch and U. Resch-Genger, *Nano Res*, 2018, **11**, 6360–6374.
- 243 I. Hyppänen, N. Höysniemi, R. Arppe, M. Schäferling and T. Soukka, *Journal of Physical Chemistry C*, 2017, **121**, 6924–6929.
- 244 C. Würth, M. Kaiser, S. Wilhelm, B. Grauel, T. Hirsch and U. Resch-Genger, *Nanoscale*, 2017, **9**, 4283–4294.
- 245 D. Yuan, M. C. Tan, R. E. Riman and G. M. Chow, *Journal of Physical Chemistry C*, 2013, **117**, 13297–13304.
- 246 G. A. Mandl, D. R. Cooper, T. Hirsch, J. Seuntjens and J. A. Capobianco, *Methods and applications in fluorescence*, 2019, **7**, 012004–012028.
- 247 A. Gnach and A. Bednarkiewicz, *Nano Today*, 2012, **7**, 54–66.
- 248 S. Han, R. Deng, X. Xie and X. Liu, *Angewandte Chemie - International Edition*, 2014, **53**, 11702–11715.
- 249 Q. Cheng, J. Sui and W. Cai, *Nanoscale*, 2012, **4**, 779–784.
- 250 S. Fan, G. Gao, S. Sun, S. Fan, H. Sun and L. Hu, *J Mater Chem C Mater*, 2018, **6**, 5453–5461.
- 251 B. Zhou, B. Xu, H. He, Z. Gu, B. Tang, Y. Ma and T. Zhai, *Nanoscale*, 2018, **10**, 2834–2840.